

**Parylene-C Neural Probes with Nanolaminate-sealed and Protruding  
Electrodes, and *In Situ* Microactuation**

Submitted in partial fulfillment of the requirements for

the degree of

Doctor of Philosophy

in

Department of Electrical and Computer Engineering

Xiao Chuan Ong

B.S., Electrical Engineering, National University of Singapore  
M.S., Electrical and Computer Engineering, Carnegie Mellon University

Carnegie Mellon University  
Pittsburgh, PA

December, 2017

© Xiao Chuan Ong, 2017

All Rights Reserved

# Acknowledgements

A PhD turned out to be a tougher endeavor than I expected when I first joined. Writing this section gives me an opportunity to evaluate how much I have developed throughout my PhD years and I can safely say that I have improved so much in conducting research, developing a research problem and using creative ways to solve the problem. I have also improved tremendously in writing and presentations when is evident when I compare my writing and presentations at the beginning of my PhD to now. For all this, I have to thank my advisor, Prof. Gary K. Fedder, for being so patient and spending so many hours in giving great feedback, ideas and suggestions, and being flexible and allowing me to try many of my ideas throughout the PhD.

In addition, I also thank Dr. Peter Gilgunn, who was also my advisor for the first few years of my PhD for his feedback and time spent in editing my writing, and also, importantly, for emphasizing the need to be aware of minute details that might seem mundane to many. It is often these small details that make a presentation or paper good or a process successful. Prof. Burak Ozdoganlar, who I worked closely with throughout my thesis, is also instrumental with his ideas and expertise on the different methods of fabrication of biodissolvable needles. I have learnt so much about micromachining using various approaches from all the meetings.

For reading my thesis and giving great suggestions for my thesis work, I thank my thesis committee, Prof. Gary K. Fedder, Prof. Aryn Gittis, Prof. Michael Bockstaller, Prof. Maysam Chamanzar and Prof. Burak Ozdoganlar.

The fabrication focus of my thesis means that I have spent a large portion of my time in the cleanroom. This has allowed me to interact and see, first hand, devices fabricated from a wide range of fields. There are too many people who I have met

in the cleanroom that have helped me one way or another to list but I want to especially thank, Prof. Wee-Liat Ong, Prof. Wei-Chen Huang, and Dr. Haosheng Wu who guided me on choosing the correct equipment, trained me on the equipment and confirmed my analysis based on the results of my experiments. In addition, I want to thank Dir. Joel Gillespie from the University of Pittsburgh who allowed me to use the XPS machine in the Materials Characterization Laboratory for free and trained me for an entire day on the theory and operation of XPS. The machine has proved to be extremely useful in my work. I would also like to thank Wei Chen for helping me so much on the AFM.

The fabrication focus of my research also means that I rely a lot on the cleanroom staff in process development and machine maintenance. For that, I thank Dir. Matthew Moneck, Carsen Kline, Norman Gottron, James Rosvanis and Mark Weiler.

I thank Dr. Yi Luo, Changho Oh, Suresh Santhanam and many others for various useful discussions about fabrication. I will also like to thank Prof. Chris Bettinger, Prof. Wei-Chen Huang, Dr. Burak Ozdoganlar, Rakesh Khilwani, Prof. Aryn Gittis, Amanda Willard, Prof. Tracy Cui, Dr. Takashi D. Yoshida Kozai and Prof. Rob Gaunt for the collaborative effort in various projects.

The people working in MEMS such as Prof. Gianluca Piazza, Prof. Tamal Mukherjee have also been a great help. I will like to thank Dr. Yu-Jen (Dylan) Fang, Prof. Kristen Dorsey, Dr. Sean Yen, Dr. Lionel Wong, Albert Patterson, Dr. Congzong Guo, Dr. Erdinc Tatar, Metin Guney, Marybeth Galanko, Mats Forsell, Metin Guney, Vincent Chung, Anthony Lin and Dr. Jason Gao for being great labmates.

As the superuser of a very tough-to-maintain machine (the device bonder) throughout my PhD, I thank Steve Einhorn and Miroslav Sokol who helped me to fix many problems that arose with the machine.

I thank my family and friends, including many who I met in CMU, for the moral support. Of course, I also thank DARPA (HR0011-15-2-0009 and N66001-11-1-4025), the Richard King Mellon Foundation Presential Fellowship and the Department of ECE for the financial support.

# Abstract

Neural probes are a promising tool in understanding the brain, alleviating symptoms of various diseases like Parkinson's Disease and allowing for applications like controlling prosthetics directly using the mind. However, current probes suffer from deleterious glial tissue buildup, poor insulation and low electrode yield. In this work, to improve upon current probes, ultra-compliant probes are fabricated and integrated with biodissolvable needles. Mechanically compliant probes allow for reduction in the body's immune response chronically whereas biodissolvable needles provide sufficient stiffness during insertion.

To achieve this, contributions are made in the categories of probe design concepts, device level processes, and processes in support of final probe assembly. Major contributions include incorporation of interleaved atomic layer deposited ceramics to create hybrid materials that provide better insulation properties, reducing the distance between the electrode and the site-of-interest by developing a gray scale lithography based technique to fabricate protruding electrodes and creating probes that improve electrode yield by integrating liquid crystal polymers into the parylene-C probe structure, which allows the parylene-C probe to actuate.

To allow for integration of the biodissolvable needle with the probe, a peel-based process is developed that controls the adhesion between parylene-C to Si using different HMDS conditions and a transfer based process is developed that enables high-temperature annealing.

In addition, a generalized design of neural probes using meandering interconnect structures is developed, allowing for rapid mechanical design of probes. This is key for neural probes because of the application specific nature of neural probe design.



# Contents

<b>Acknowledgements</b>	<b>iii</b>
<b>Abstract</b>	<b>v</b>
<b>List of Figures</b>	<b>x</b>
<b>List of Tables</b>	<b>xxvi</b>
<b>1 Introduction</b>	<b>1</b>
1.1 Neural probes and their applications . . . . .	1
1.2 Motivation . . . . .	2
1.3 Neural probes . . . . .	4
1.3.1 Mechanically compliant neural probes . . . . .	6
1.3.2 Structure of nerves and neurons . . . . .	7
1.3.3 Extracellular recording of action potentials . . . . .	8
1.3.4 Stimulation of neurons . . . . .	11
1.4 Outline and contributions . . . . .	16
<b>2 Fabrication of parylene-C probes with integration of dissolvable needles</b>	<b>21</b>
2.1 Insulation materials for flexible neural probes . . . . .	22
2.1.1 Biocompatibility . . . . .	23
2.1.2 Mechanical Properties . . . . .	24
2.1.3 Electrical Properties . . . . .	24

2.1.4	Processability . . . . .	26
2.1.5	Chemical properties of parylene-C . . . . .	26
2.2	Fabrication of peelable structures . . . . .	31
2.2.1	Contact angle measurements . . . . .	33
2.2.2	Work of adhesion from contact angle measurements . . . . .	33
2.2.3	Peel test analysis . . . . .	37
2.2.4	Peel force measurement . . . . .	41
2.3	Processing of Electrodes . . . . .	49
2.3.1	Processing of Pt electrodes for flexible neural probes . . . . .	54
2.3.2	Processing of IrO <sub>2</sub> electrodes for flexible neural probes . . . . .	59
2.4	Summary . . . . .	66
<b>3</b>	<b>A transfer process to fabricate probes strongly-adhered to silicon substrates</b>	<b>67</b>
3.1	Introduction . . . . .	67
3.1.1	Embedding ultra-compliant probes in a biodissolvable needle . . . . .	68
3.1.2	Bonding ultra-compliant probes on a biodissolvable needle . . . . .	69
3.2	Fabrication of Parylene-C probes on Si substrate . . . . .	71
3.3	Transfer of Strongly Adhered Structures . . . . .	74
3.4	Molding . . . . .	76
3.5	Adhesives for the transfer process . . . . .	78
3.5.1	PDMS (Sylgard 184) . . . . .	79
3.5.2	Photoresist (AZ4620) . . . . .	81
3.5.3	Crystal Bond 509 . . . . .	82
3.5.4	BGL7080 . . . . .	88
3.6	Compatibility of process with CMC-glucose . . . . .	94
3.7	Impedance experiment results . . . . .	98
3.8	Bonding of needles to probes transferred on to BGL7080 . . . . .	103
3.9	Summary . . . . .	106

<b>4</b>	<b>Atomic layer deposited ceramic nanolaminates for sealing</b>	<b>109</b>
4.1	Improving adhesion of parylene-C for flexible neural probes . . . . .	111
4.1.1	Quantification of encapsulation capability by EIS . . . . .	113
4.1.2	Parylene-C to parylene-C adhesion . . . . .	114
4.2	ALD ceramics for flexible neural probes . . . . .	130
4.2.1	Test structures to investigate ALD ceramics . . . . .	133
4.2.2	Determination of stoichiometry of TiO <sub>2</sub> by XPS . . . . .	148
4.3	Nanolaminates for flexible neural probes . . . . .	150
4.3.1	Al <sub>2</sub> O <sub>3</sub> -TiO <sub>2</sub> nanolaminates as a barrier material . . . . .	150
4.4	Three layer hybrid encapsulation scheme . . . . .	152
4.4.1	Analysis of Crosstalk . . . . .	152
4.4.2	Analysis of mechanical properties of hybrid encapsulation . . .	157
4.5	Summary . . . . .	159
<b>5</b>	<b>Protruding electrodes</b>	<b>161</b>
5.1	Vias and interconnects . . . . .	162
5.1.1	Existing processes for fabrication of vias . . . . .	162
5.2	A metal-fill based process to fabricate vias . . . . .	162
5.2.1	Fabrication of Vias . . . . .	166
5.3	Protruding Electrodes . . . . .	169
5.3.1	Existing processes for fabrication of protruding electrodes . . .	169
5.3.2	Sloped sidewalls of parylene-C to fabricate vias or protruding electrodes . . . . .	170
5.3.3	Grayscale lithography . . . . .	173
5.3.4	Analysis of pattern transfer for anisotropic etch processes . . .	177
5.3.5	Implementation of pattern transfer . . . . .	181
5.3.6	Fabrication of Protruding Electrodes . . . . .	182
5.3.7	Roughening of electrodes . . . . .	190
5.4	Summary . . . . .	194

<b>6</b>	<b>Design of probes and <i>in vivo</i> experiments for specific applications</b>	<b>195</b>
6.1	Meanders to improve axial compliance in implantable probes . . . . .	196
6.1.1	Analysis of circular meanders for probes . . . . .	196
6.1.2	Simulation of spring constants . . . . .	202
6.1.3	Constrained optimization of $k_y$ for a single electrode wire . . .	204
6.1.4	Constrained optimization of $k_y$ for multiple electrode wires . .	206
6.2	Design of probe cabling . . . . .	211
6.3	<i>In vivo</i> experiments of implantable Si neural probes and ultra-compliant probes integrated with biodissolvable needles . . . . .	216
6.3.1	Fabrication of Si probes . . . . .	216
6.3.2	<i>In vitro</i> experiments . . . . .	219
6.3.3	<i>In vivo</i> experiments . . . . .	221
6.4	Actuation of neural probes using light-sensitive liquid crystals . . . . .	225
6.4.1	Controlling orientation of liquid-crystal molecules on parylene-C	225
6.4.2	Actuation experiments . . . . .	230
6.5	Summary . . . . .	232
<b>7</b>	<b>Conclusions and Future Work</b>	<b>233</b>
7.1	Future Work . . . . .	238

# List of Figures

Figure 1-1	Structure of (a) myelinated nerve fiber, (b) fascicle, (c) nerve and (d) myelinated neuron. . . . .	9
Figure 1-2	Hodgkin and Huxley model representing the membrane of a neuron. . . . .	9
Figure 1-3	Waveform of (a) transmembrane voltage and (b) currents in the $\text{Na}^+$ and $\text{K}^+$ branches during an action potential . . . . .	11
Figure 1-4	Typical strength-duration curve. . . . .	12
Figure 1-5	Distributed model of a nerve fiber. . . . .	13
Figure 1-6	$S$ against $x$ for a point source of current. $I_{el}$ , $\rho_e$ and $z$ are set to 1 A, 1 $\Omega\text{mm}$ and 1 mm respectively. $S$ is in $\text{V}/\text{mm}^2$ and $x$ is in mm. . . . .	16
Figure 1-7	Cartoon showing contributions of this thesis in different parts of a neural probe. . . . .	17
Figure 2-1	(a) Microscope image of a probe attached to a biodissolvable needle (b) Assembled probe with connection to omnetics . . . . .	22
Figure 2-2	Experimental load versus extension for a 6.5 $\mu\text{m}$ thick, 10 mm wide sample of parylene-C. . . . .	25
Figure 2-3	(a) Chemical structure of dimer used to deposit parylene-C. (b) Chemical structure of monomer used to deposit parylene-C. (c) Chemical structure of parylene-C . . . . .	27

Figure 2-4	(a) Reaction between A174 and silicon or silicon oxide. (1) A174 and H <sub>2</sub> O reaction. (2) Product of reaction between A174 and H <sub>2</sub> O. (3) Hydrogen bond formation between silane and surface of Si. (4) Formation of covalent bonding between adsorbed A174 and the surface of Si. (b) Reaction between HMDS and silicon or silicon oxide surface. (1) unreacted HMDS and silicon surface. (2) Surface after reaction between HMDS and silicon surface. . . . .	30
Figure 2-5	(a) Contact angle of DI water and ethylene glycol. Inset: representative result from one measurement using the Goniometer. (b) Setup for contact angle test using the goniometer. . . . .	34
Figure 2-6	Work of adhesion for parylene-C on Si, and the polar and dispersive energies derived from measured contact angles versus HMDS vapor prime time . . . . .	38
Figure 2-7	Schematic cross-section of a film being peeled from a substrate. The final position of the applied force after $\Delta x$ of film is peeled is $P'$ . . . . .	38
Figure 2-8	(a) Setup for peel test. Inset: Zoomed in image of clamp region of instron. (b) Sample used for peel test after completion of peeling test. Width of peeled film is indicated by $w$ . (c) Representative peel force measurement result. The peel region is indicated on the graph. . . . .	42
Figure 2-9	Peel force per unit width versus HMDS vapor prime time in minutes. Error bars are one standard deviation from the mean. . . . .	43
Figure 2-10	Peel force per unit width versus surface energy and work of adhesion for parylene-C film on HMDS-treated Si substrate. Error bars represent 1 standard deviation from the mean. . . . .	46
Figure 2-11	(a) Device prior to peeling. (b) Device after initiation of peeling. (c) Device mounted onto Instron machine for peel test measurement. . . . .	48
Figure 2-12	(a) Cartoon illustrating formation of a double-layer capacitance when an electrode is immersed in an electrolyte. Red and green dots represent oppositely charged particles. (b) Electrical model of an electrode. . . . .	50

Figure 2-13 Process flow to fabricate test devices to investigate effect of processing on Pt electrodes. . . . .	55
Figure 2-14 XPS results on Pt electrodes after O <sub>2</sub> RIE deinsulation process performed to remove parylene-C covering it (a) without Ar <sup>+</sup> etch and (b) with Ar <sup>+</sup> etch. . . . .	57
Figure 2-15 EIS result on 80 μm by 80 μm electrodes with and without Ar <sup>+</sup> etch. (a) Magnitude of measured impedance and (b) phase of measured impedance. Sample numbers are indicated in the legend. EIS is performed by Mats Forssell. . . . .	58
Figure 2-16 (a) Surface morphology of a Pt electrode using AFM over a 6 μm by 20 μm scan region, (b) SEM of a Pt electrode, (c) Optical microscope showing exposed Pt electrodes. . . . .	60
Figure 2-17 Surface morphology of Pt coated on parylene-C using AFM over a 10 μm by 10 μm scan region . . . . .	61
Figure 2-18 Observed non-uniformity in deposited film with pressure during deposition. Thicknesses were measured using a profilometer. (a) Wafer with IrO <sub>2</sub> deposited at 14.5 mT. (b) Wafer with IrO <sub>2</sub> deposited at 6.95 mT. . . . .	63
Figure 2-19 EDX performed on (a) film deposited at 14.5 mT, 100 W DC and (b) film deposited at 6.95 mT, 100 W RF to determine stoichiometry of oxygen to iridium in deposited film. . . . .	64
Figure 2-20 200 μm by 200 μm test electrode fabricated on glass to test charge injection capacity. . . . .	64
Figure 2-21 Evolution of the charge storage capacity of the IrO <sub>2</sub> electrodes during the CV activation. The periodic dips in the activation are artifacts of the CV measurement and do not indicate a change in the charge storage capacity. CV test is performed by Mats Forssell. . . . .	65

Figure 3-1	Neural probe fabrication process. (a) Deposition of parylene-C (Px) on a Si wafer. (b) Pt is patterned using lift-off. (c) A second layer of Px is deposited (d) Parylene-C RIE. . . . .	71
Figure 3-2	(a) Optical microscope image of the needle region of a fabricated probe. (b) Zoomed-in optical image of the interconnect region. (c) Zoomed-in optical image of the electrode region. (d) A fabricated chip	73
Figure 3-3	Transfer process. (a) Adhesive is spin coated on glass receiving substrate. (b) After pressing the substrates together, the combined donor Si substrate and receiving substrate are heated. Pressure is applied. (c) Donor Si substrate is removed by RIE followed by XeF <sub>2</sub> . (d) Adhesive is partially etched to produce an undercut is performed for some processes. . . . .	75
Figure 3-4	Molding process flow. (a) A top mold is mounted onto the transferred device. (b) CMC-glucose solution is applied and the device is centrifuged. (c) The molded device is released in isopropyl alcohol.	77
Figure 3-5	(a) Optical image of a probe transferred onto PDMS coated glass. (b) Microscope image of needle portion of probe transferred onto PDMS coated glass. (c-d) Images of dissolvable needles molded over probes and released using Dynasolve 220. . . . .	80
Figure 3-6	Optical images of (a) Si chip with fabricated probe mounted on glass using AZ4620 photoresist as an adhesive. (b) Despite an extended softbake, gas pockets are formed during the reflow process. (c) Prebaking the resist before mounting eliminates formation of gas pockets. However, adhesion is insufficient as seen by the observed delamination while etching Si. Glass side refers to the image being taken with the glass on top (viewing through the glass) and top side refers to the image being taken with the glass at the bottom. . . . .	83
Figure 3-7	DSC of Crystal Bond 509. The measured glass transition temperature from the sample is 116°C. . . . .	84

Figure 3-8	Thickness versus spin speed for Crystal Bond 509 dissolved in acetone at 20% and 40% by weight. Spin time is 60 s. Error bars represent the standard deviation of the measured thicknesses. . . . .	86
Figure 3-9	Probe transferred using Crystal Bond 509. (a) Optical image of a probe transferred onto the receiver substrate. (b) Microscope image of a transferred probe. (c) Microscope image after performing the undercut using acetone. (d) A molded and released probe embedded in CMC-glucose. . . . .	87
Figure 3-10	DSC of BGL7080. The measured glass transition temperature is approximately 98°C. A melting point of approximately 129°C is also detected. . . . .	89
Figure 3-11	BGL7080 spin curves for two spin times (30 s and 60 s). Each test case is performed with three samples. Error bars represent the standard deviation of the measured thickness. . . . .	90
Figure 3-12	Probe transferred using BGL7080 as an adhesive. (a) Optical image of a probe transferred onto BGL7080 coated glass. (b) Microscope image of a molded and released probe embedded in a CMC-glucose needle. (c) Zoomed-in microscope image of a molded and released probe. Some residual amount of CMC-glucose remaining from the molding process is seen on the electrode surface. . . . .	92
Figure 3-13	Optical images of transferred two and four shank probes using BGL7080 as an adhesive. The successful transfer of large devices demonstrates the versatility of this process. . . . .	93
Figure 3-14	Width of the CMC-glucose extent at 30 s time intervals relative to initial width after insertion into agar. The width is measured at the midpoint along the shank. . . . .	95
Figure 3-15	Snapshots at 30 s time intervals of needles treated for 48 h with various solvents inserted into agar. . . . .	96
Figure 3-16	FTIR spectra of untreated CMC, and of CMC immersed in IPA, acetone, and Dynasolve 220 for 48 h. . . . .	97

Figure 3-17 Impedance magnitude of $Z^{measured}$ and $Z^{loop}$ at 1 kHz of a molded probe versus time. Test is performed by Mats Forssell. . . . .	100
Figure 3-18 Diagram showing the various impedances ( $Z^{loop}$ , $Z^{wire}$ , $Z^{electrode}$ that are measured or derived. . . . .	100
Figure 3-19 Impedance magnitude of $Z^{measured}$ and $Z^{loop}$ at 1 kHz of transferred probes without CMC molding versus time. The geometric average of $n = 3$ tests is plotted with solid lines. The impedance one geometric standard deviation apart from the geometric average is represented in dashed lines. Test is performed by Mats Forssell. . . . .	102
Figure 3-20 Impedance of completely insulated test structures at 0.1 Hz in PBS under different conditions. The drying of CMC in air or in a centrifuge degrades the insulation of the test structure as seen by the lower impedance compared with a sample not exposed to CMC. . . . .	104
Figure 3-21 Contact angle of DI water on as deposited parylene-C and parylene-C treated with $O_2$ plasma . . . . .	104
Figure 3-22 Initial <i>in vitro</i> impedance of recording probe in three different assembly configurations: 1) molded CMC needle (full line), 2) low stress bonded attached CMC needle (dashed line), and 3) no CMC needle (dotted lines). The self-test loop does not have exposed metal and its impedance is indicative of insulation quality. Test is performed by Mats Forssell. . . . .	106
Figure 4-1 Different means of insulation failure . . . . .	110
Figure 4-2 Electrochemical Impedance Spectroscopy. (a) Test setup for electrodes and insulation tests. (b) Model for encapsulation with degradation or electrode on an encapsulated wire. . . . .	115
Figure 4-3 Process flow to fabricate test devices to investigate different methods of improving encapsulation properties of parylene-C . . . . .	117

Figure 4-4 Optical images of fabricated test structure chips. (a) After Pt lift-off. (b) Zoomed-in image of test structures after lift-off. (c) After patterning of parylene-C. (d) Zoomed-in image of test structure after patterning of parylene-C. (e) Image of a fabricated test structure chip showing the location of the pads, counter electrode and test electrodes. (f) Image of another test structure with an exposed electrode. . . . . 118

Figure 4-5 XPS of as-deposited parylene-C. (a) Survey scan of sample. (b) Detailed C 1s scan. (c) Detailed Cl 2p scan. The green lines are the fitted background spectrum. The orange lines are the fitted individual peaks. The dark blue lines are the fitted summed peaks. The red lines are the measured spectra. The light blue lines are a graphical plot, in arbitrary units, showing the variation in the difference between the fit and the measured values across binding energies. . . . . 121

Figure 4-6 XPS of fluorinated parylene-C. (a) Survey scan of sample. (b) Detailed O 1s scan. (c) Detailed F 1s scan. (d) Detailed C 1s scan. (e) Detailed Cl 2p scan. The green lines are the fitted background spectrum. The orange lines are the fitted individual peaks. The dark blue lines are the fitted summed peaks. The red lines are the measured spectra. The light blue lines are a graphical plot, in arbitrary units, showing the variation in the difference between the fit and the measured values across binding energies. . . . . 123

Figure 4-7 XPS of oxygenated parylene-C. (a) Survey scan of sample. (b) Detailed C 1s scan. (c) Detailed Cl 2p scan. (d) Detailed O 1s scan. The green lines are the fitted background spectrum. The orange lines are the fitted individual peaks. The dark blue lines are the fitted summed peaks. The red lines are the measured spectra. The light blue lines are a graphical plot, in arbitrary units, showing the variation in the difference between the fit and the measured values across binding energies. . . . . 125

Figure 4-8	Magnitude of impedance measured at 0.1 Hz over time in hours to determine encapsulation properties using various treatments. P-n, P-a, P-f, P-i indicates parylene-C only encapsulation with various treatments (regular oxygen plasma descum treatment, A174 treatment, fluorination treatment and ion mill treatment respectively). PA-n, PA-a, PA-i indicate similar surface treatments with a parylene-C-alumina hybrid encapsulation scheme. Measurement is performed by Mats Forssell. . . . .	128
Figure 4-9	Test results comparing annealed and unannealed chips for test structures with 2.2 $\mu\text{m}$ thick, 50 $\mu\text{m}$ wide insulation. . . . .	130
Figure 4-10	Description of ALD process. . . . .	132
Figure 4-11	Microscope images showing residue left after BHF etch of the nanolaminate. (a) Optical image showing residue in a chip that has completed fabrication (parylene-C layer is also patterned). (b) Differential Interference Contrast (DIC) image showing residue in a chip that has completed fabrication. (c) Optical image showing residue just after the nanolaminate etch. (d) Optical image showing test structure processed using $\text{Cl}_2$ ICP-RIE. . . . .	136
Figure 4-12	Process flow to fabricate test devices to investigate different methods of improving encapsulation properties of ceramics . . . . .	138
Figure 4-13	Optical images of test structures to test $\text{TiO}_2$ at different points of processing. (a) Glass wafer after second layer of $\text{TiO}_2$ deposition. (b) Glass wafer after $\text{TiO}_2$ etch and resist removal. (c) Test structure after photoresist patterning of $\text{TiO}_2$ . (d) Other test structures after photoresist patterning of $\text{TiO}_2$ . (e) Test structures such as those in (c) after $\text{TiO}_2$ etch and resist removal. . . . .	138

Figure 4-14 Optical images at different points of processing for the nanolaminate test structures. (a) After 1 minute of etching in BHF (b) After etching of the nanolaminate is completed and photoresist is stripped. (c) Microscope image of fabricated test electrodes and encapsulated test structures after completion of fabrication. . . . . 139

Figure 4-15 Magnitude of impedance versus time at 0.1 Hz versus of time of samples aged at 60°C. The increased temperature accelerates the time to failure. P-n refers to the sample with parylene-C insulation only. A-n refers to the sample with ALD alumina insulation only. T-n refers to the sample with titania insulation only. N-n refers to the sample with TiO<sub>2</sub>/Al<sub>2</sub>O<sub>3</sub> nanolaminate (NL) insulation only. PA-n refers to the sample with parylene-C/alumina hybrid encapsulation only. PN-n refers to the sample with parylene-C/nanolaminate hybrid encapsulation only. PNT-n refers to parylene-C/nanolaminate/TiO<sub>2</sub> triple encapsulation. Measurement is performed by Mats Forssell. . . 141

Figure 4-16 Process flow to fabricate test devices with parylene-C and alumina (PA) and with parylene-C and nanolaminate (PN). (a) Parylene-C and a ceramic is deposited. (b) Ti-Pt-Ti is deposited and patterned. (c) A second layer of ceramic is deposited. (d) The ceramic is patterned and a second layer of parylene-C is deposited. Cr is deposited and patterned for use as a hard mask. (e) parylene-C is etched and any remaining Cr is removed. . . . . 144

Figure 4-17 Process flow to fabricate test devices with parylene-C, TiO<sub>2</sub> as an adhesion layer and nanolaminate (PNT). (a) Parylene-C is deposited followed by TiO<sub>2</sub> and NL. (b) Ti-Pt-Ti is deposited and patterned. (c) A second layer of NL is deposited followed by TiO<sub>2</sub>. (d) TiO<sub>2</sub> and NL layers are patterned. (e) A second layer of parylene-C is deposited followed by Cr. Cr is patterned and used as a hard mask. (f) Parylene-C is patterned and any remaining Cr is removed. . . . . 145

Figure 4-18 Optical images at different points of processing of hybrid encapsulation test structures. (a) After first Pt layer lift-off. (b) After patterning of ceramic layer. (c) After parylene-C outline patterning. The image is taken with a protective photoresist layer is on the structures after dicing. (d) A sharpened version of (c) with increased contrast so that the encased ceramic is more visible. . . . .	146
Figure 4-19 XPS Spectra of TiO <sub>2</sub> . (a) Survey spectra of TiO <sub>2</sub> sample. (b) Detailed scan around O 1s region. (c) Detailed scan around Ti 2p region. Red line is measured spectra. Green line is fitted background spectra. Orange line is fitted spectra of each peak. Dark blue line is combined fitted spectra. The light blue lines are a graphical plot, in arbitrary units, showing the variation in the difference between the fit and the measured values across binding energies. . . . .	149
Figure 4-20 XPS spectra of the nanolaminate. (a) Survey spectra of the nanolaminate sample. (b) Detailed scan around O 1s region. (c) Detailed scan around Ti 2p region. Red line is measured spectra. Green line is fitted background spectra. Orange line is fitted spectra of each peak. Blue line is combined fitted spectra. The dark blue lines are combined fitted spectra. The light blue lines are a graphical plot, in arbitrary units, showing the variation in the difference between the fit and the measured values across binding energies. . . . .	151
Figure 4-21 Cartoons and schematics of the proposed encapsulation schemes. (a) Interconnect scheme with electrode. (b) Simulation setup in COMSOL. (c) Proposed lumped parameter model. (d) Reduced circuit from (c) based on symmetry. (e) Setup for crosstalk analysis. (f) Setup for more realistic model of the input and output circuits. (g) Lumped parameter model of titania only scheme. . . . .	154
Figure 4-22 Simulation results from SPICE simulation based on lumped parameter model. Lighter dashed line is the phase. Solid line is the magnitude in voltage. . . . .	155

Figure 4-23 Simulation results from COMSOL Multiphysics finite element analysis. . . . .	156
Figure 4-24 Stress in MPa versus radius of curvature (mm) based on theoretical calculations. Various elastic limits are also plotted to indicate point of failure. . . . .	159
Figure 5-1 A. Condensed process flow to fabricate vias using an etch and metal-fill kind of process. A description of each step depicted in the process flow is found in the text. B. An optical image of test structures fabricated using described process flow. C. Zoomed-in image of a fabricated via. . . . .	163
Figure 5-2 SEM of a fabricated via showing signs of delamination at the edges. EDX is performed at points 1,2 and 3 labelled on the figure. No material is detected at point 1. Only Pt is detected at points 2 and 3.	165
Figure 5-3 Optical image and profilometer measurement of sloped sidewall fabricated using grayscale lithography. . . . .	167
Figure 5-4 SEM of side of a via fabricated using grayscale lithography. (a) Zoomed-out SEM showing extent of slope. (b) Zoomed-in SEM showing microstructures formed by grayscale lithography. . . . .	168
Figure 5-5 Profilometer scan of a parylene-C probe. . . . .	170
Figure 5-6 Process flow to fabricate neural probes with sloped sidewalls. (a) Deposition of parylene-C. (b) Patterning and deposition of Pt by lift-off. (c) Deposition of second layer of parylene-C. (d) Grayscale lithography to fabricate sloped sidewalls in photoresist. (e) Transfer of slope sidewall pattern from photoresist to parylene-C followed by patterning and deposition of second layer of Pt by lift-off. . . . .	172

Figure 5-7	(a) Profilometer scan to show variation in height for four different doses used in the test structure. (b) Optical image of grayscale test structures after development. Percentages indicate transmission ratio used. (c) Graph of height of photoresist versus transmission ratio. Photoresist used is AZ4620. . . . .	175
Figure 5-8	Effect of process variations on the pattern transfer process from photoresist to parylene-C. (a) In the ideal case where both photoresist and top layer parylene-C are just etched. (b) Case where parylene-C is overetched. (c) Case where photoresist is thinner than the ideal case. (d) Case where photoresist is thicker than the ideal case. . . . .	180
Figure 5-9	Layout of a protruding electrode. Grayscale tones are obtained by using a subpattern of 4 squares. . . . .	183
Figure 5-10	Optical images at different points of processing of protruding electrodes. (a) After first Pt layer lift-off. (b) After patterning of ceramic layer (a description of the use of ceramics is found in chapter 4. (c) After parylene-C outline patterning and grayscale patterning of parylene-C in electrode regions. (d) After second layer Pt deposition and lift-off. . . . .	185
Figure 5-11	Images of protruding electrodes. (a) Optical image of 9 protruding electrodes in a penetrating neural probe. (b) SEM of a protruding electrode. . . . .	187
Figure 5-12	Zygo measurement of the profile of a protruding electrode in a 4.5 $\mu\text{m}$ -thick probe. The contrast in slope between a typical and sloped sidewall is evident here. The slope obtained is approximately 0.15 $\mu\text{m}/\mu\text{m}$ (a) 3D profile of a protruding electrode. (b) extracted 2D profile across dotted white line seen in (a). . . . .	187
Figure 5-13	(a) 3D profile of a protruding electrode in a 4.5 $\mu\text{m}$ -thick probe obtained using the Alicona microscope. (b) extracted 2D profile across red line seen in (a). . . . .	188

Figure 5-14 Zygo measurement of the profile of a protruding electrode in a 9 $\mu\text{m}$ probe. (a) 3D profile of a protruding electrode. (b) extracted 2D profile across dotted white line seen in (a). . . . .	188
Figure 5-15 (a) 3D profile of a protruding electrode in a 9 $\mu\text{m}$ probe obtained using the Alicona microscope. (b) Extracted 2D profile across red line seen in (a). (c) Extracted 2D profile across green line seen in (a). . . . .	189
Figure 5-16 AFM of protruding electrode. . . . .	191
Figure 5-17 Comparison of the impedance of electrodes with and without protrusion. . . . .	191
Figure 5-18 AFM of 4.5 $\mu\text{m}$ -thick parylene-C (a) with no treatment (b) after 2 min etch in $\text{O}_2$ RIE (c) after 5 min etch in $\text{O}_2$ RIE. Measured roughness, $R_a$ is 4 nm for (a), 7 nm for (b) and 22 nm for (c). . . . .	192
Figure 5-19 AFM of Pt on 4.5 $\mu\text{m}$ -thick parylene-C (a) with no treatment of parylene-C (b) with parylene-C etched for 2 min in $\text{O}_2$ RIE (c) with parylene-C etched for 5 min etch in $\text{O}_2$ RIE. Measured roughness, $R_a$ is 3 nm for (a), 5 nm for (b) and 18 nm for (c). . . . .	193
Figure 5-20 AFM of positive photoresist (AZ4210) spun on 4.5 $\mu\text{m}$ -thick parylene-C (a) with no treatment (b) after 2 min etch in $\text{O}_2$ RIE (c) after 5 min etch in $\text{O}_2$ RIE. Measured roughness, $R_a$ is 0.3 nm for (a), 2 nm for (b) and 6 nm for (c). . . . .	193
Figure 6-1 Schematic representing the mechanical model of a probe implanted in a brain. . . . .	197
Figure 6-2 (a) Meanders formed using circular segments with (a) $\theta_s = \pi$ , (b) $\theta_s < \pi$ and (c) $\theta_s > \pi$ . . . . .	198
Figure 6-3 Calculated displacements in the $x$ , $y$ and $z$ directions when $R = 100 \mu\text{m}$ , $t = 2.5 \mu\text{m}$ , $w = 10 \mu\text{m}$ for different $\theta_s$ and $N$ under a test force of $10^{-10}$ N in the respective directions. . . . .	201

Figure 6-4	Ratio of spring constant under the fixed-guided boundary condition to the fixed-free boundary condition when $\theta_s = \pi$ . The ratio approaches 1 as $N$ increases. Non-monotonicity results from different equations for odd $N$ and even $N$ . . . . .	203
Figure 6-5	Error in simulations of $k_y$ as compared with theoretical analysis. Meanders which are less curved (small $R$ and $\theta_s$ ) have larger errors because the analysis does not include axial strain energy. . . . .	203
Figure 6-6	(a) Constraints imposed by a delivery vehicle of length $L = 1500 \mu\text{m}$ and width $W_{max} = 110 \mu\text{m}$ . (b) Fixed-free $k_y$ under the constraint of $L = 1500 \mu\text{m}$ and $W_{max} = 110 \mu\text{m}$ . Increasing $N$ reduces the spring constant. No stationary point exists. . . . .	205
Figure 6-7	Three probes satisfying the conditions $L = 1500 \mu\text{m}$ and $W_{max} = 110 \mu\text{m}$ . $w$ is set to $10 \mu\text{m}$ . (a) $N = 12$ , (b) $N = 22$ and (c) $N = 42$ . Large $N$ results in more compliant probes but is limited by the need to avoid meander overlap. In addition, a minimum spacing is required because of lithographic resolution. (d) Minimum spacing for the probe with $N = 42$ . . . . .	207
Figure 6-8	(a) Maximum probe density arises when probes are arrayed with no vertical displacement. Segment with limiting spacing is shown with dotted red lines. (b) Minimum spacing, $g$ , between two identical circular probes shifted horizontally by distance $d$ . (c) shows the case of 3 probes in the delivery vehicle ( $M = 3$ ) . . . . .	209
Figure 6-9	(a) Maximum probe density arises when probes are arrayed with no vertical displacement. Segment with limiting spacing is shown with dotted red lines. (b) Minimum spacing, $g$ , between two identical circular probes shifted horizontally by distance $d$ . (c) shows the case of 3 probes in the delivery vehicle ( $M = 3$ ) . . . . .	211
Figure 6-10	Design of a peripheral probe . . . . .	213
Figure 6-11	Parameterized design of transition region. . . . .	213

Figure 6-12 Mechanical simulation of two transition region designs within the proposed design parameter space. (a) $\theta = \pi/4$ . (b) $\theta = \pi/2$ . . . .	214
Figure 6-13 Mechanical simulation of fabricated design with needle. . . . .	215
Figure 6-14 Fabrication steps to pattern Si needle using BGL7080 as an adhesive. (a) Parylene-C is deposited. Pt is patterned by lift off. (b) Second layer of parylene-C is deposited. Cr is deposited and patterned. (c) Parylene-C is etched with O <sub>2</sub> plasma. Si is bonded to glass using BGL7080 adhesive. (d) Cr is deposited and patterned. (e) Si is etched using DRIE. Device is released in IPA. . . . .	218
Figure 6-15 (a) Optical image of a fabricated probe. (b) Zoomed-in image of the tip of a fabricated probe. . . . .	220
Figure 6-16 Bode plot of Electrochemical Impedance Spectroscopy (EIS) performed on 115 $\mu\text{m}$ by 15 $\mu\text{m}$ electrodes in saline ( $n = 2$ ). Measured impedance at 1 kHz is $\sim 80 \text{ k}\Omega$ . The red circles denote the average phase and the blue crosses the average magnitude. Standard deviations are indicated by the dashed lines. Measurement is performed by Mats Forssell. . . . .	220
Figure 6-17 Insertion setup for acute <i>in vivo</i> experiment in a mouse. . . .	223
Figure 6-18 (a) Image of mouse brain after post-insertion histology. (b) Image of histology with annotations. Dotted lines represent the substantia nigra region. Probe trace is marked by bold lines. Histology indicates that probe is inserted successfully into target region. . . . .	223
Figure 6-19 Recorded spike data from three different electrodes. (a-c) are data from 3 separate electrodes. (d-f) are plots that are zoomed-in to individual spikes. . . . .	224
Figure 6-20 Optical image of mask used to fabricate groove patterns. . . .	228

Figure 6-21 POM images of azobenzene on grooved hydrophillic parylene-C with (a) sample oriented $0^\circ$ with respect to polarizer and (b) sample oriented $45^\circ$ with respect to polarizer. The orientation of the polarizer (the first polarizer) and the analyzer (the second polarizer) is denoted by P and A. . . . .	229
Figure 6-22 POM images of azobenzene on grooved hydrophobic parylene-C with (a) sample oriented $0^\circ$ with respect to polarizer and (b) sample oriented $45^\circ$ with respect to polarizer. The orientation of the polarizer (the first polarizer) and the analyzer (the second polarizer) is denoted by P and A. . . . .	229
Figure 6-23 A liquid crystal on parylene-C sample exposed to UV laser in air. (a) Sample prior to UV laser exposure. Sample after (b) 7 min, (c) 16 min, and (d) 49 min of UV exposure. . . . .	231
Figure 6-24 A liquid crystal on parylene-C sample exposed to UV from an LED lamp in 0.5% agar. (a) Sample prior to UV exposure. (b) Sample after 5 s of UV exposure. (c) Images of (a) and (b) overlaid to show movement. . . . .	231

# List of Tables

Table 2.1	Mechanical properties of various polymers . . . . .	25
Table 2.2	Electrical properties of various polymers . . . . .	25
Table 2.3	Summary of properties of various polymers . . . . .	27
Table 2.4	Measured peel force per unit width in mN/cm for four different surface treatments of Si over 3 parylene-C deposition runs . . . . .	32
Table 2.5	Surface energy components of DI water and ethylene glycol [1]	36
Table 2.6	Mean peel force per unit width in mN/cm for four different surface treatments of Si over four parylene-C deposition runs. $SS_B$ is the standard deviation between groups, $SS_W$ is the standard deviation within groups and $SS_T$ is the total standard deviation. . . . .	44
Table 2.7	<i>In situ</i> peel force per unit width in mN/cm for 3 neural probe structures . . . . .	47
Table 2.8	Warburg capacitance per unit area( $\mu\text{F}/\text{cm}^2$ ) of metals in contact with 0.9% saline (Reproduced from [2]) . . . . .	52
Table 4.1	Quantitative Analysis of XPS performed on parylene-C . . . . .	122
Table 4.2	Quantitative Analysis of XPS performed on fluorinated parylene-C124	
Table 4.3	Quantitative Analysis of XPS performed on oxygenated parylene-C . . . . .	124
Table 4.4	Measured etch rates of different ALD ceramics . . . . .	135
Table 4.5	Quantitative Analysis of XPS performed on $\text{TiO}_2$ . . . . .	148
Table 4.6	Quantitative Analysis of XPS performed on the nanolaminate.	150
Table 4.7	Mechanical properties of various ceramic layers . . . . .	158

Table 5.1	Measured resistances of different vias . . . . .	164
Table 5.2	Measured etch rate of various materials in O <sub>2</sub> plasma RIE and calculated selectivities based on the etch rates . . . . .	182

# Chapter 1

## Introduction

### 1.1 Neural probes and their applications

The nervous system is one of the least understood organ systems in the body. However, it is also one of the most important systems since it is involved in cognitive function, emotion, vision, hearing, balance and consciousness among many other functions. Furthermore, all organs in the body are controlled by nerves. Hence, by understanding the nervous system, it is possible for us to treat various diseases and symptoms, even those that might not be directly related to the nervous system. Apart from informing new therapies, understanding the nervous system can also give rise to better ways to interface with machines.

Great strides have been made in understanding the nervous system, such as the work by Cajal [3], who established the neuron doctrine - that the neuron is an individual cell and is the unit of the nervous system; Sherrington who established the concept of the synapse [4]; and Hodgkin and Huxley [5] who established the model of an action potential. However, the interactions of neurons and their effects within the brain and peripheral nervous system are far from fully understood.

Much of the progress in understanding the nervous system is due to the development of tools. For example, the invention of the electron microscope and development of better optical microscopes allowed for confirmation of certain aspects of the neuron doctrine such as the physical presence of synapses[6]. Similarly, the development of

various neuroimaging methods, in particular magnetic resonance imaging (MRI), led to various advancements in the Human Connectome Project[7]. Different methods to measure activity and interface to the brain have emerged including electroencephalography (EEG), electrocorticography (ECoG) and penetrating neural probes, allowing recording and stimulating at different time and spatial scales. In addition, non-electrical methods of imaging such as calcium imaging and optogenetics have emerged but require loading the neurons of interest with dyes[8], using transgenic subjects[9] or genetically modifying the neurons[10].

Apart from understanding the brain, the development of these probes allows an interface with the nervous system which opens up a host of new applications. Brain machine interfaces have been demonstrated in research labs to allow tetraplegics to control robotic arms[11], allow the blind to partially regain sight[12] and allow people to control a computer cursor with their minds[13]. Deep brain stimulation has been approved by the FDA as a treatment for essential tremor or Parkinson's disease[14] and is also used to treat dystonia and depression. Depending on the requirements of the application, different types of probes are required.

## 1.2 Motivation

This thesis aims to realize neural probes a) with mechanical compliance using patterned parylene-C shanks less than 10  $\mu\text{m}$ -thick, b) protruding electrodes that are at least flush with the insulation and c) with improved encapsulation compared with parylene-C only probes through the use of ceramic materials. This is determined by the ability to fabricate these probes with at least greater than 50% yield.

Despite the demonstration of a myriad of possibilities with the use of neural probes, problems still exist which prevent large scale use of the neural probes. In particular, chronic neural recordings tend to fail over longer periods because of both biotic and abiotic mechanisms. Biotic mechanisms include gliosis, bleeding and abiotic mechanisms include insulation degradation and delamination and mechanical damage to the neural probes. These issues need to be resolved in order to achieve reliable

neural probes that can be safely implanted for long-term use without the need for excessive invasive implantations over the patient's lifetime.

Gliosis has been identified as a major biotic cause of recording failure. Gliosis occurs as a foreign body reaction to the inserted neural probes. A sheath of glial cells (i.e. scar tissue) can form around the neural probes, which increases the distance between the electrodes on the neural probe and the neurons of interest, hence resulting in reduced signal-to-noise ratio of recordings. The mechanical mismatch between Si (with Young's modulus,  $E = 169$  GPa) and neural tissue ( $E \sim 10$  kPa) has been shown to be a factor in glial formation. Hence, by using softer materials such as parylene-C ( $E \sim 4$  GPa) and appropriate designs, compliance can be achieved to reduce the mechanical mismatch between the brain and the neural probe. For penetrating probes that are inserted into the brain, glial scarring can form due to immune reaction of the brain tissue to the implanted neural probes. This has been identified as a major chronic failure mechanism [15]. It is suggested that the mechanical mismatch between the neural probes and the brain tissue is an important driver for sustained immune reaction [16].

Insulation degradation/delamination is another cause of recording failure. Degradation of insulation results in loss of spatial selectivity because the interconnects are essentially exposed. Neural probes are exposed to a variety of ions and water which can often degrade the probe. In order to achieve longevity in neural probe recordings, new encapsulation schemes that can still allow mechanical flexibility and also provide improved encapsulation for the neural probes are important research areas.

The stochastic nature of the location of neurons in the brain results in electrodes that are often located further away from neurons than desired. As a result, some electrodes tend to not detect any neurons. Thus, having the ability to actuate the neural probe to bring the electrodes closer to the neurons will result in improved performance of the neural probes.

## 1.3 Neural probes

The development of electrical neural probes is a key development in neuroscience. Neural probes provide a direct way of detecting signals from neurons since they acquire electrical signals and depending on architecture, allow for both detection of signals and stimulation of neurons at different spatial scales.

For the brain, probes can either be placed on the scalp (electroencephalogram, EEG), on the surface of the brain (electrocorticography, ECoG) or be inserted into the brain (single-unit or field potential recording). There are different engineering considerations for each of the different types of probes.

For EEG probes, the electrodes are typically large (radius on the order of cm) because the signals are attenuated and spatially filtered by the skull. The electrodes measure the synchronous activity of a large population of neurons[17] and can be used for the study of epilepsy and sleep. Since EEG probes are often designed as a wearable device, the probes have to be attached to the scalp in a comfortable way and yet provide a low enough contact resistance which is typically achieved using gels[18].

ECoG probes are typically planar and sheet like with electrode radius in the order of mm[19]. The mechanical compliance of ECoG probes is an important consideration - compliance has to be high to ensure that the electrodes conform well to the surface of the brain to ensure good contact[20]. The placement of the ECoG arrays on the surface of the brain just above the dura (for an epidural ECoG) or below the dura (subdural ECoG) results in better spatial localization compared to EEG since the effect of signal attenuation and spatial filtering of the skull is eliminated. However, the signal is still spatially averaged as the neurons are still separated by brain tissue, the pia mater, cerebrospinal fluid, the arachnoid and for an epidural ECoG, the dura[21]. Hence, ECoG arrays typically measure the local field potentials of the cortical pyramidal cells which are located closer to the surface of the brain or stimulate neurons along the surface of the brain.

For penetrating probes, the electrodes are typically small in size (radius in the order of 10  $\mu\text{m}$ ). The proximity of the electrodes to the neurons means that single

unit activity can be recorded, spatially specific stimulation can be achieved and very high temporal resolution can be achieved[22] compared with EEG or ECoG. However, since each recording site can only detect neuron firing events in a volume of radius approximately 100 to 150  $\mu\text{m}$ [22], the number of electrodes has to be large to collect information on a large neuronal population.

Similarly, probes meant to connect to the peripheral nervous system, various types of designs are meant to record or stimulate at different spatial scales. Cuff probes are placed on the surface of the nerve and can be used to stimulate or record but are less selective than penetrating electrodes. To ensure mechanically robust placement and good contact, cuff probes are usually closed using sutures or other means of applying a force between the nerve and the probe which can cause mechanical damage. Penetrating probes cause damage during insertion and might break the fascicles since they are aligned perpendicular to the probe. Sieve probes are one way of mitigating this by allowing regrowth of the fascicles through the sieves.

Many applications require penetrating probes either because of the need for single-unit recordings or the need to stimulate deep within the brain or nerve. The most common penetrating neural probes that are in use are developed by the University of Utah[23], the University of Michigan[24] and MicroProbes for Life Science[25]. These probes are made of rigid materials like Si (166 GPa) or metal (168 GPa) which result in large mechanical mismatch with neural tissue. Furthermore, evidence of mechanical damage to rigid arrays explanted after *in vivo* experiments are performed suggests that there are also a number of abiotic mechanisms causing poor reliability of current neural probes[26][27].

The Utah probes are fabricated using a combination of dicing and isotropic etching of Si using 5% HF and 95% nitric acid to create sharp needle arrays[23]. The Michigan probes are fabricated using an anisotropic EDP (an aqueous solution of ethylene diamine and pyrocatechol) etch with highly boron doped Si as an etch stop to create 15  $\mu\text{m}$  thick Si needles[24]. MicroProbes needle probes are made out of various metals (tungsten, iridium, platinum/iridium, stainless steel, and nickel-chromium), insulated with parylene-C and have tips that are sharpened electrochemically[25].

### 1.3.1 Mechanically compliant neural probes

Compliant neural probes, which lower the mechanical mismatch between brain tissue and the neural probe, are shown to reduce the brain tissue response[28]. Polymers such as parylene-C and polyimide are usually used in neural probes as they are mechanically compliant ( $\sim 1$  GPa), electrically insulating and biocompatible polymers. Parylene-C and polyimide are also inert, making it easier to integrate the materials with various processes although poor adhesion to most materials poses challenges. In addition, fabrication of ultra-compliant neural probes poses important challenges arising from difficulties in handling and manipulation of such probes after release.

Mechanical compliance for neural probes presents a problem for the failure-free and precise implantation of neural probes into the brain as buckling can occur during insertion with insufficient axial stiffness as seen from the Euler buckling equation for a fixed-pinned beam:

$$P_{cr} = \frac{2\pi^2 EI}{L^2} \quad (1.1)$$

where  $P_{cr}$  is the critical force above which the beam will buckle,  $E$  is the Young's modulus of the material used in the beam,  $I$  is the area moment of inertia of the beam, and  $L$  is the length of the beam.

In order to insert the neural probes into the brain successfully while preserving mechanical compliance in the long term, temporary methods of stiffening are employed during the insertion process. This temporary rigidity can be achieved using a wide range of novel methods are employed such as the use of shape memory polymers that are rigid at room temperature and soften at body temperature[29], application of biocompatible dissolvable materials such as extracellular matrix[30], polyethylene glycol (PEG)[31], maltose[32], tyrosine-derived terpolymer[33], chitosan[34] or silk[31], temporarily attaching a stiff silicon needle to a compliant probe using PEG[35] or filling microfluidic channels with PEG to stiffen a compliant probe[36]. The choice of material is often limited by practical issues including softening time. The use of materials like carboxymethyl-cellulose (CMC) and PEG requires fast insertion because of rapid dissolution times as opposed to the use of silk, which softens in the time scale

of hours[37]. Another approach is to only have locally flexible regions[38][39], where silicon is still used in the needle but certain regions of the needle are flexible or to effectively shorten the probe during insertion by stiffening with dissolvable material only the regions above the part that is inserted initially[40].

In this thesis, probes are embedded in blends of CMC and various sugars that are molded as described in[41]. The dissolvable needle is either spin-coated onto the probes on a Si substrate with an attached mold[41] or the needle is premolded before being bonded onto the probe as will be described in chapter 3. This technique allows a wide design space of possible needle geometries, which can affect insertion force[42].

Apart from the reduction of immune response in penetrating probes, mechanically compliant neural probes are also important for applications which require conformal coverage over the nerve (cuff electrodes) or brain (ECoG). Having stiff probes makes it difficult to achieve the radius of curvatures necessary to conformally cover the tissue and result in an increased distance between the electrode and the tissue.

### **1.3.2 Structure of nerves and neurons**

The structure of a typical myelinated neuron is shown in Figure 1-1(d). It consists of a number of dendrites, which carry signal towards the cell body or the soma. The axon which is shown to be myelinated carries the signal away from the soma. The myelin sheath around the axon is an electrical insulator that serves to increase conduction speed[43]. The myelin sheath is formed by Schwann cells, which are a type of glial cell. The small 1  $\mu\text{m}$ -long breaks in the myelin sheath are known as the nodes of Ranvier[44]. During electrical conduction, the signal jumps from one node of Ranvier to the next. The exposed neuronal membranes at the nodes of Ranvier allow for electrical sensing and stimulation at these points. In the brain, the spatial distribution and orientation of the neurons are dependent on the area within the brain.

The structure of a peripheral nerve is shown in Figure 1-1(c). It consists of a number of fascicles(Figure 1-1(b)) embedded in connective tissue (the epineurium). Blood vessels are also embedded in the connective tissue. Each fascicle consists of a

number of axons bundled together as shown in (Figure 1-1(a)).

### 1.3.3 Extracellular recording of action potentials

The main reason for recording failure due to gliosis is the formation of highly resistive scar tissue between the neuron and the probe. The scar tissue increases the distance between the neurons of interest and the electrodes. The effect of this can be approximated by considering the models used for intracellular and extracellular recording.

#### 1.3.3.1 Generation of an action potential across a cell membrane

The Hodgkin and Huxley model shown in Figure 1-2 describes the generation of an action potential[5]. The circuit models the membrane of a neuron. The bilipid layer is represented by  $C_m$ , the capacitance due to the lipid bilayer,  $g_{Na}$  is the conductance of the voltage gated sodium channels in the membrane of the neuron,  $g_K$  is the conductance of the voltage gated potassium channels in the membrane of the neuron,  $g_l$  is the conductance of the leakage channel where chloride and other ions can pass. Due to a difference in concentration of the various ions inside and outside of the neuron, a potential is formed across the membrane. The contribution of each ion to the potential across the membrane is represented by  $V_{Na}$ ,  $V_K$  and  $V_l$  for the sodium, potassium and other ions respectively and is derived using the equation for the Nernst potential which considers that at equilibrium, the drift and diffusion currents cancel:

$$V_n = \frac{RT}{zF} \ln \frac{[n^{z+}]_{outside}}{[n^{z+}]_{inside}} \quad (1.2)$$

where  $n$  is the relevant species,  $R$  is the universal gas constant,  $T$  is the absolute temperature in Kelvin,  $F$  is the Faraday constant,  $z$  is the charge of the species,  $[n^{z+}]_{outside}$  and  $[n^{z+}]_{inside}$  is the concentration of the species outside and inside of the cell.

The Hodgkin and Huxley model further considers the change in  $g_K$  and  $g_{Na}$  over time and voltage by experimentally fitting the respective conductances to various dif-

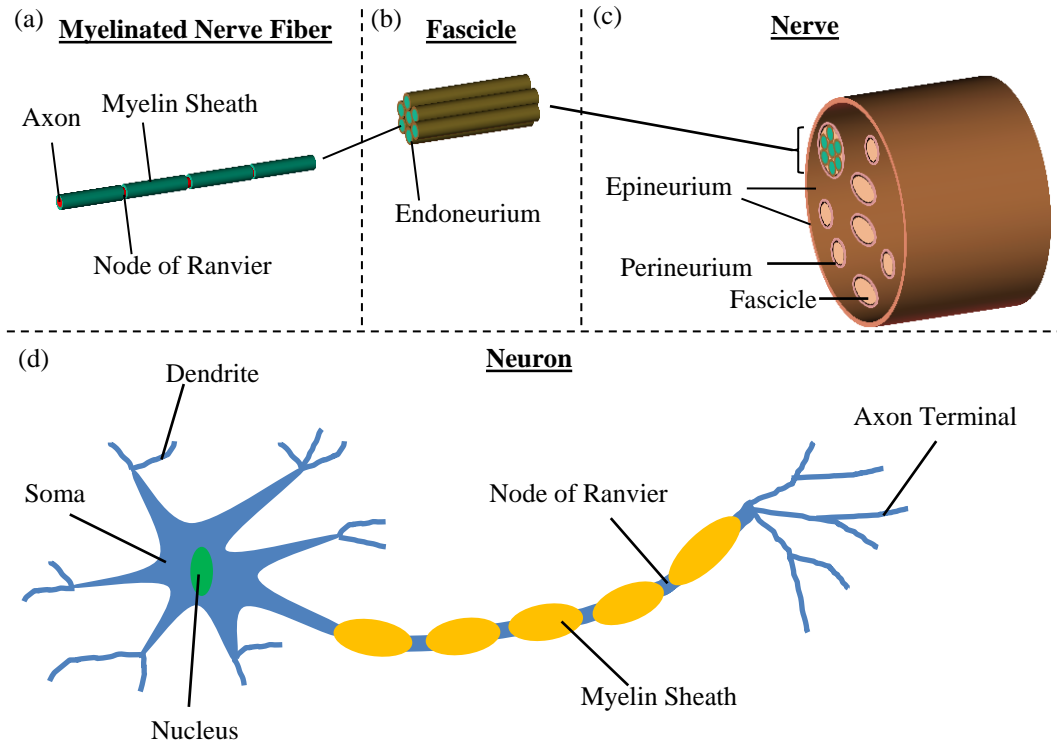


Figure 1-1: Structure of (a) myelinated nerve fiber, (b) fascicle, (c) nerve and (d) myelinated neuron.

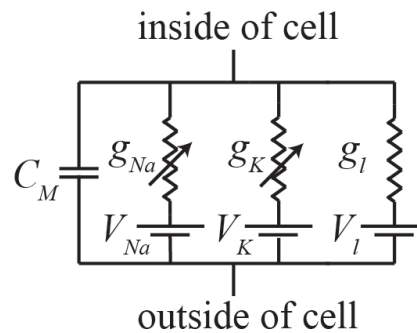


Figure 1-2: Hodgkin and Huxley model representing the membrane of a neuron.

ferential equations representing the probability of the opening and closing of various channels. The model predicts that if a stimulus results in a transmembrane voltage exceeding a threshold, an action potential is generated. The resulting voltage potential waveform across the membrane and respective current in the  $\text{Na}^+$  and  $\text{K}^+$  branches of the model after a stimulus exceeding the threshold is shown in Figure 1-3. The voltage outside the cell is taken to be zero.

### 1.3.3.2 Effect of distance between the neuron and the electrode on extracellular recordings

Using the theory of volume conduction, the relationship between the current across a point on the membrane of a nerve and the potential at a point away from the nerve is:

$$\phi = \frac{\rho I}{4\pi r} \quad (1.3)$$

assuming purely ohmic conductivity which is shown to be valid for 1-3000 Hz[45] where  $\rho$  is the resistivity of the medium,  $I$  is the current,  $r$  is the distance from the point on the membrane to the point of measurement and  $\phi$  is the potential at that point of measurement.

For the case of a myelinated nerve, each of the Nodes of Ranvier is represented by a point source. Hence, the potential at a point is represented using the sum of (1.3). For unmyelinated nerves, a line source approximation takes the form of the line integral of (1.3):

$$\phi = \frac{\rho}{4\pi} \int_{-\Delta s}^0 I \frac{ds}{\Delta s} \sqrt{r^2 + (h-s)^2} = \frac{\rho I}{4\pi \Delta s} \log \left| \frac{\sqrt{h^2 + r^2} - h}{\sqrt{l^2 + r^2} - l} \right| \quad (1.4)$$

where  $r$  is the perpendicular distance from the line,  $\Delta s$  is the length of the nerve fiber,  $h$  is the longitudinal distance from the end of the line and  $l = \Delta s + h$ .

From (1.3) and (1.4), increasing distance reduces the signal amplitude rapidly. For the line source approximation case, for large  $l$  and  $h$ ,  $l \approx h$  which makes the potential zero. Similarly, if  $r$  is large compared to  $h$  and  $l$ , the potential approaches

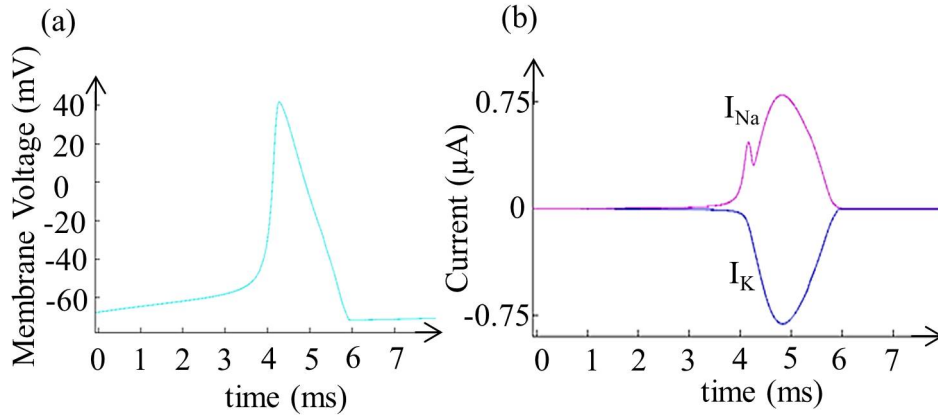


Figure 1-3: Waveform of (a) transmembrane voltage and (b) currents in the  $Na^+$  and  $K^+$  branches during an action potential

zero. Hence, there is a small volume, dependent on the length of the nerve, where the signal amplitude is sufficiently high for detection. In addition, the impedance of the electrode at the extracellular site should be kept sufficiently low to ensure high signal to noise ratio. This is discussed in chapter 2.

Based on simulations performed in [45] which are also corroborated with experimental results, the measured signal amplitude drops by half approximately every  $20 \mu m$ . Hence, it is important to keep the electrodes in close proximity to the neuron to ensure good signal to noise ratio.

### 1.3.4 Stimulation of neurons

Given the electrochemical basis of nerve function, it is also possible to stimulate a neuron to fire. When a stimulus current is applied, the potential across the cell membrane increases as predicted by the model shown in Figure 1-2 until the threshold voltage is reached. The required current to stimulate a nerve is also dependent on the duration of the current pulse and on the type of neuron or nerve fiber that is intended to be stimulated. This dependence is given by the strength-duration curve as shown in Figure 1-4. At very long durations, the required current to stimulate the neuron remains constant with time. The value of this current is known as the rheobase. The time required to stimulate at two times the rheobase is known as the chronaxy.

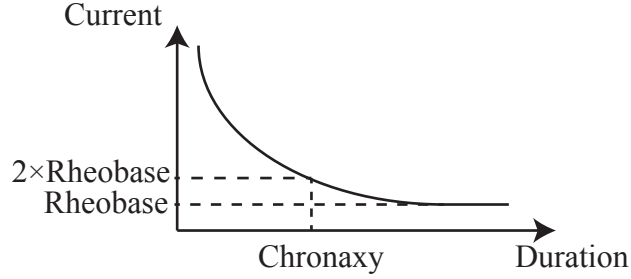


Figure 1-4: Typical strength-duration curve.

A commonly used experimentally derived equation for the strength-duration curve is[46]:

$$I_{th} = \frac{I_{rh}}{1 - e^{-\frac{W}{\tau_M}}} \quad (1.5)$$

where  $I_{th}$  is the current required to reach threshold,  $I_{rh}$  is the rheobase,  $W$  is the stimulation time and  $\tau_M$  is the membrane time constant.

Typically, the charge per phase required to stimulate the nerve is lower for smaller pulse durations [47][48]. Hence, to minimize the charge injected, shorter pulse durations should be used. The minimum pulse duration is limited by the maximum allowable current (especially in battery operated devices) and other physiological considerations such as the time constants of the opening and closing of the various ion channels[48]. Other considerations for stimulation include the maximum charge that can be transferred in a single pulse which is dependent on the electrode material properties and electrode size which will be discussed in chapter 2.

In order to avoid corrosion and for safe stimulation, a biphasic stimulation waveform is usually used where the initial cathodal current pulse (the electrode acting as a current sink) is followed by an anodic current pulse. The initial cathodal pulse initiates the action potential and the second pulse reverses the electrochemical reactions that occur during the initial pulse[48]. It is important to ensure that the reactions that occur during the initial cathodal current pulse are reversible.

### 1.3.4.1 Effect of distance between the neuron and the electrode on stimulation

For stimulation, a distributed model of the neuron as shown in Figure 1-5 is used for analysis[49][50] to determine the effect of distance between the nerve and the electrode on stimulation. If the fiber is myelinated, each node represents a Node of Ranvier and  $G_a$  is the internodal conductance. For unmyelinated fibers, each node represents a small segment of the membrane and  $G_a$  is the conductance between two of these small segments. Each node, as shown in Figure 1-5, also contains a membrane element represented by a voltage source,  $V_n$ , a variable conductance,  $g_n$ , and a membrane capacitance,  $C_M$  which is a condensed version of Figure 1-2.  $V_{e,n}$  and  $V_{i,n}$  are the voltages outside and inside the cell membrane respectively.

Using Kirchoff's current law and substituting the Hodgkin and Huxley model for the ionic currents, it is shown in [50][51] that

$$I_{ion} + C_m \frac{\partial V_m}{\partial t} - \frac{1}{r_i} \frac{\partial^2 V_m}{\partial x^2} = \frac{1}{r_i} \frac{\partial^2 V_e}{\partial x^2} \quad (1.6)$$

where  $I_{ion}$  is the magnitude of ionic current,  $r_i$  is the resistivity of the material inside the fiber,  $C_m$  is the membrane capacitance and  $V_m$  is the transmembrane voltage. Since the only term external to the nerve is  $\frac{\partial^2 V_e}{\partial x^2}$ , this is defined as the activating

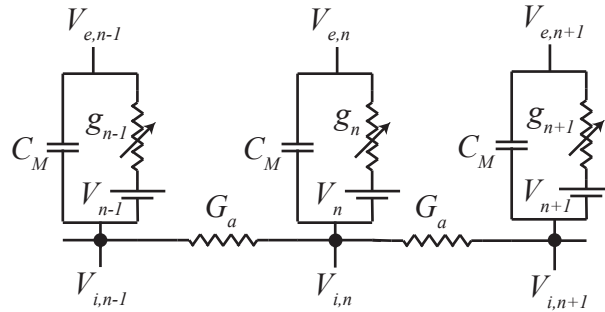


Figure 1-5: Distributed model of a nerve fiber.

function,

$$S = \frac{\partial^2 V_e}{\partial x^2} \quad (1.7)$$

and is responsible for the activation of the neuron during electrical stimulation.

When the neuronal membrane is at rest,  $I_{ion}$  and all the spatial derivatives of  $V_m$  are zero[51] and hence, (1.6) reduces to:

$$C_m \frac{\partial V_m}{\partial t} = \frac{1}{r_i} S \quad (1.8)$$

In order to depolarize a membrane beyond the threshold voltage to trigger an action potential,  $V_m$  should increase and hence,  $S$  should be greater than zero. If  $S$  is less than 0, the membrane will be hyperpolarized. The actual value of  $S$  required for stimulation is dependent on the type of nerve and stimulation protocol such as the duration of the cathodic pulse.

For a point source of current at a distance  $r$  away from an axon, the potential is

$$V_e = \rho_e \frac{I_{el}}{4\pi r} = \rho_e \frac{I_{el}}{4\pi} (z^2 + x^2)^{-\frac{1}{2}} \quad (1.9)$$

where  $I_{el}$  is the magnitude of the current,  $\rho_e$  is the resistivity of the extracellular medium,  $z$  is the perpendicular distance away from the neuron and  $x$  is the longitudinal distance between the point on the neuron and the point source of current. The activating function is then,

$$S = \frac{\partial^2 V_e}{\partial x^2} = \rho_e \frac{I_{el}}{4\pi} (z^2 + x^2)^{-\frac{5}{2}} (2x^2 - z^2) \quad (1.10)$$

A plot of  $S$  against  $x$  is shown in Figure 1-6. From (1.10),  $I_{el}$  has to be negative (the electrode has to be a current sink) in order to elicit a positive activating function at  $x = 0$ . Stimulation occurs when  $S$  is greater than zero; i.e., when

$$|x| < \frac{z}{\sqrt{2}}. \quad (1.11)$$

Hence, having an electrode placed close to the neuron results in a more selective

stimulation and, as seen from (1.10) requires a lower amplitude of current.

In another stimulation model, the relationship between threshold current,  $I_{th}$  and distance of the neuron from the stimulating electrode,  $r$  is proposed to be[52]:

$$I_{th} = I_r + kr^2 \tag{1.12}$$

where  $I_r$  is the minimum current required to stimulate the neuron and  $k$  is an experimentally determined constant. Requiring a larger current means requiring a larger charge which possibly results in damage to the tissue if the safe charge injection limit is reached.

This again highlights the importance of keeping the electrode close to the neuron that is to be stimulated. Hence, for reliable stimulation, it is important to reduce glial response to ensure minimal scar tissue formation between the neuron and the electrode.

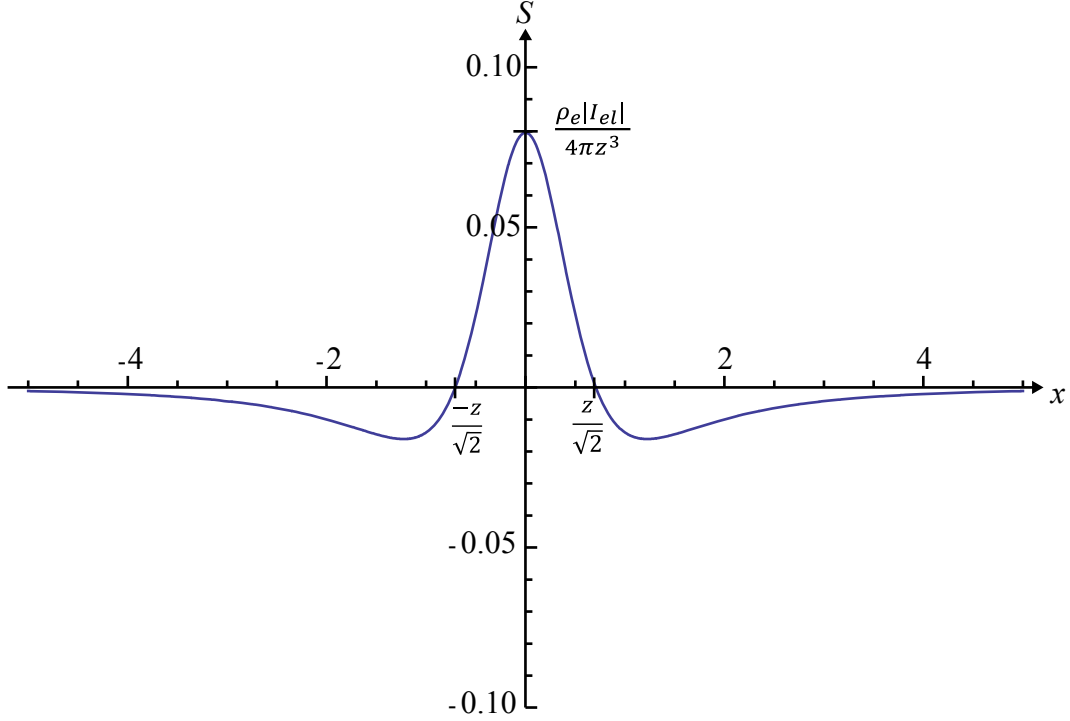


Figure 1-6:  $S$  against  $x$  for a point source of current.  $I_{el}$ ,  $\rho_e$  and  $z$  are set to 1 A, 1  $\Omega\text{mm}$  and 1 mm respectively.  $S$  is in  $\text{V}/\text{mm}^2$  and  $x$  is in mm.

## 1.4 Outline and contributions

This thesis focuses on the fabrication of mechanically compliant neural probes to reduce the mechanical mismatch between the probe and the brain, and reduce the distance between the neuron and the electrodes by using various fabrication techniques to create flexible neural probes with various features as shown in Figure 1-7. The transfer process removes the requirement of mechanical force to peel the probes and manual handling, hence allowing for the fabrication of parylene-C neural probes less than 10  $\mu\text{m}$ -thick that are embedded in a biodissolvable needle. The biodissolvable needle allows for reliable insertion of the probe without compromising long-term flexibility of the probe. Actuation and protruding electrodes reduce the distance between the neuron and the electrodes, which can help to track neurons for long term recording stability. Nanolaminate ceramic sealing serves to improve the encapsulation properties of parylene-C by introducing a ceramic material, which has better water vapor transmission properties than a polymeric material like parylene-C. Given the

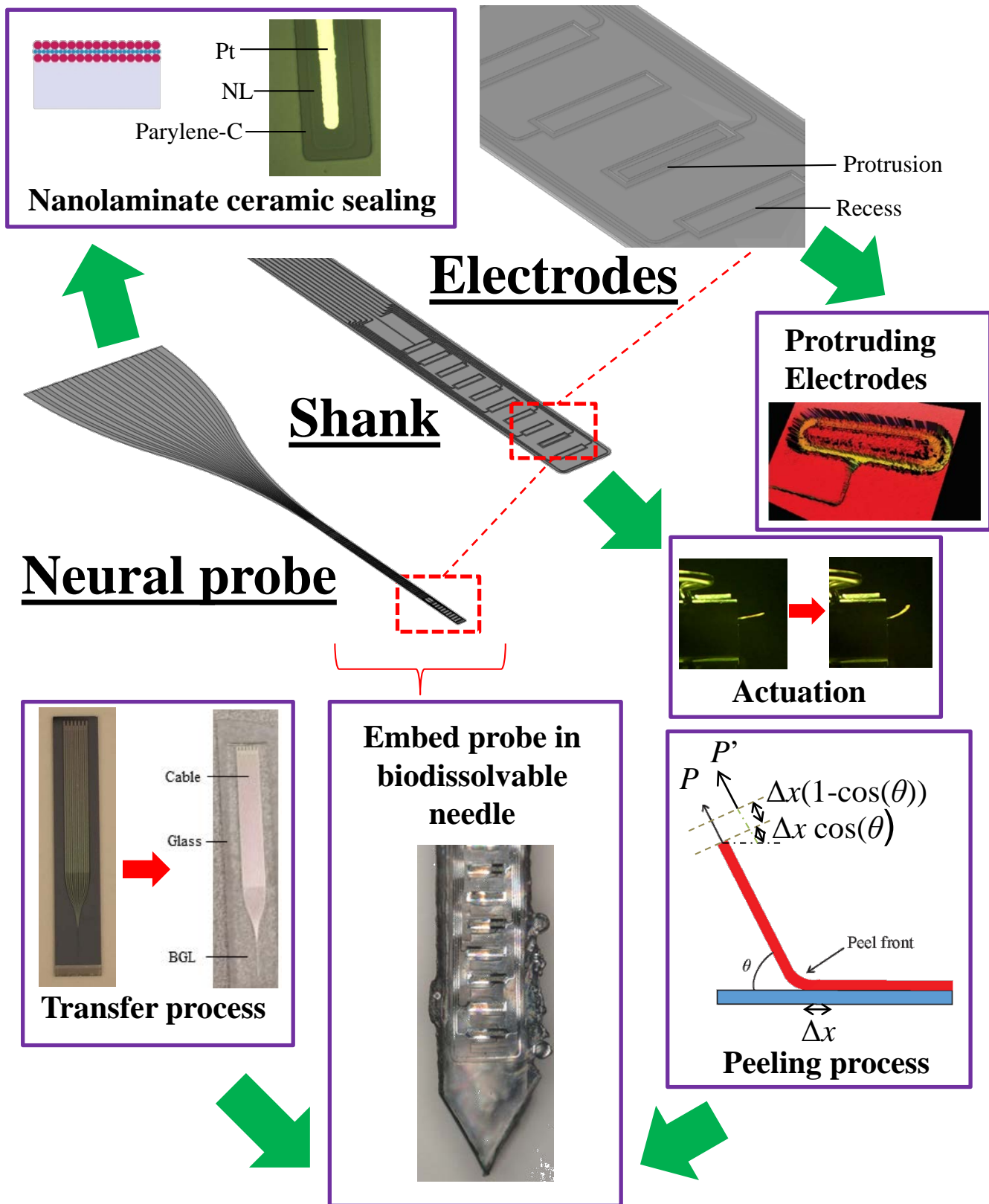


Figure 1-7: Cartoon showing contributions of this thesis in different parts of a neural probe.

wide range of applications for neural probes, the requirements for different applications are typically very different. To address the different requirements, different aspects of fabrication are discussed in chapters 2 to 5. In chapter 6, devices fabricated for various applications which integrate some of the aspects of neural probes discussed in chapters 2 to 5 are discussed. Each chapter includes a short literature review relevant to each topic.

In chapter 2, a fabrication flow is presented which focuses on key aspects of fabricating parylene-C neural probes. In this chapter,

1) the adhesion between the Si substrate and the probe is engineered in order to ensure that the flexible probe survives the fabrication process and can be peeled from the substrate;

2) the surface chemistry of Pt electrodes in parylene-C probes is controlled; and a process to develop IrO<sub>2</sub> electrodes in parylene-C probes is developed. The surface chemistry of Pt electrodes is found to affect the impedance of the electrode which is important as it determines the signal to noise ratio of the acquired signal. The typical process flow of using O<sub>2</sub> plasma to etch the parylene-C to create electrode openings is found to create a layer of PtO<sub>2</sub> on the surface of the Pt electrode which degrades performance of the electrode. Including an Ar<sup>+</sup> etch step removes this layer of PtO<sub>2</sub> and improves the performance of the electrode. Reactive sputtering of Ir in an O<sub>2</sub> environment is used to create IrO<sub>2</sub> electrodes. The use of IrO<sub>2</sub> is expected to improve the charge storage capacity (CSC) of the electrode because of the electrochemical properties of the IrO<sub>2</sub>.

Chapter 3 describes a process to transfer the completed probe to a handle for eventual assembly with a biodissolvable needle:

3) The fabrication flow presented in chapter 2 imposes constraints on the maximum temperature allowed as heating parylene-C beyond its melting point of 290°C increases adhesion between the Si substrate and the parylene-C such that the probe cannot be removed from the wafer without inflicting damage. By performing the transfer of the neural probe to a handle wafer with an adhesive, the requirement of low adhesion between parylene-C and Si is removed. This development involves the

investigation of different adhesives and solvents and appropriate choice of process parameters (i.e., adhesive thickness and appropriate choice of sacrificial silicon substrate removal (e.g., SF<sub>6</sub> reactive ion etching (RIE), XeF<sub>2</sub>, potassium hydroxide (KOH)) in order to achieve a transfer that is compatible with the water soluble needles. It is found that BGL7080, an isopropyl alcohol dissolvable backgrinding liquid wax has suitable properties as an adhesion layer. In addition, the process of transferring the probes onto an IPA dissolvable adhesive enables another transfer process to flip-chip bond biodissolvable needles directly on probes which makes the process scalable and is also found to improve the encapsulation properties of the probe.

Chapter 4 focuses on the electrical insulation of parylene-C neural probes:

4) Surface modifications of parylene-C are performed to investigate the effect of surface hydrophobicity and various functional groups on the adhesion between parylene-C layers in saline which mimics body fluid. It is found that of the different plasma treatments used, O<sub>2</sub> plasma improves the adhesion between parylene-C layers the most. The lack of correlation between hydrophobicity and adhesion indicates that the improvement in adhesion is likely to be due to the introduced functional groups rather than surface hydrophobicity;

5) In addition, various atomic-layer-deposited ceramics (i.e., Al<sub>2</sub>O<sub>3</sub>, TiO<sub>2</sub>, nanolaminates of Al<sub>2</sub>O<sub>3</sub> and TiO<sub>2</sub>) are explored for sealing the Pt wiring, including the development of etching techniques to process these ceramics. These ceramics have a lower water vapor transmission ratio as opposed to polymers like parylene-C and is expected to improve the encapsulation of the probes. It is found that ICP-RIE Cl<sub>2</sub> etch is much cleaner compared to buffered HF etch of nanolaminates, which leaves surface residue. Test devices are fabricated to investigate the effect of various ceramics on the insulation of the probe. It is found that Al<sub>2</sub>O<sub>3</sub> corrodes in saline but TiO<sub>2</sub> does not corrode appreciably in saline and has low resistivity. Nanolaminates of Al<sub>2</sub>O<sub>3</sub> and TiO<sub>2</sub> have high resistivity and do not corrode appreciably in saline. The successful design of the best encapsulation scheme requires both electrical and mechanical considerations. The conductivity of TiO<sub>2</sub> requires analysis of electrical crosstalk to explain a lower impedance seen for the bilayer Al<sub>2</sub>O<sub>3</sub>/TiO<sub>2</sub> combination.

The results suggest separation of the ceramic layer between electrode interconnect is important for reduction of crosstalk. Mechanical analysis is also performed to determine the maximum extent of flexion possible for flexible probes with ceramic encapsulation.

In chapter 5, a process flow to fabricate protruding electrodes is developed:

6) Conventional thin-film fabrication techniques result in recessed electrodes that increase the distance between the electrode and the neuron. The development of protruding electrodes requires electrical connectivity between the top of the protrusion and the probe interconnect located at the bottom of the protrusion, which is being achieved with the use of gently sloped parylene-C sidewalls to enable continuous thin-film coverage. The gently sloped parylene-C sidewalls is developed using gray-scale lithography followed by a controlled etch step that increases the electrode roughness and hence, lowers the impedance of the electrode. This technique can also be expanded to fabricate vias which allow for high electrode densities.

In chapter 6, tests of various devices are presented:

7) Probes attached to dissolvable needles and probes fabricated on Si are compared *in vivo*. A process flow to fabricate parylene-C probes with Si as an insertion vehicle is developed to emulate the encapsulation properties of parylene-C based compliant probes. This is used as a means to help eliminate the causes for the lack of neural recordings of parylene-C probes inserted with a dissolvable carboxy-methyl-cellulose (CMC)/glucose needle. The CMC needle swells upon insertion and may create extensive damage at the insertion site. *In vivo* implantation and neural recordings are performed to see if single-unit signals are detected without the effect of the dissolvable needle;

8) In addition, preliminary work is presented on probes that can actuate which reduces the distance between the electrode and the neuron by moving the electrode near to the neuron.

A conclusion and proposals for future work is provided in chapter 7.

## Chapter 2

# Fabrication of parylene-C probes with integration of dissolvable needles

Neural probes typically consist of three main components. The electrode region detects currents or transfers charge depending on whether the electrode is meant for recording or stimulation; the interconnect provides an electrical connection between the electrode and the pads; and the insulation provides control of the spatial extent of recording or stimulation by electrically isolating the interconnects. Depending on the application, the requirements of the probes can be very different and hence, the design and shape of the probes can vary significantly. For example, ECoG probes are typically flat and planar and are made to be very mechanically compliant so as to conform to the shape of the brain. In this chapter, a fabrication flow for flexible probes meant for insertion into the brain is developed. In order to overcome the insertion forces, a biodissolvable needle is incorporated with the probe. An optical image of a fabricated probe integrated with a biodissolvable needle is shown in Figure 2-1(a). A probe assembled with connectors is shown in Figure 2-1(b).

In the literature, for the majority of flexible probes, fabrication is performed on a rigid substrate, which is necessary to ensure ease of handling and compatibility with fabrication equipment. Following fabrication on the rigid substrate, the probe is then released either by peeling or by etching a sacrificial material. For probes with a biodissolvable needle attached to the probe, using a sacrificial material is

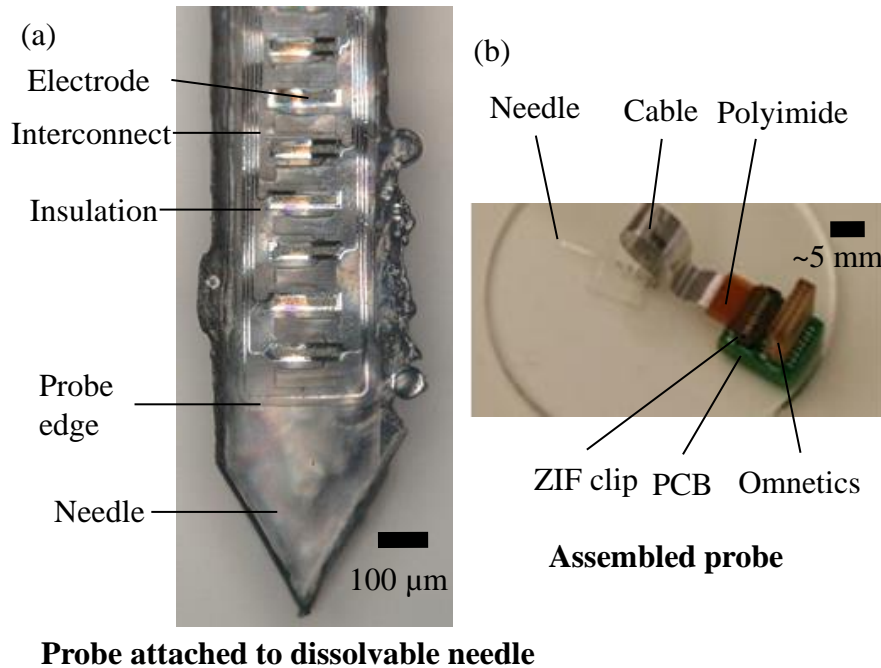


Figure 2-1: (a) Microscope image of a probe attached to a biodissolvable needle (b) Assembled probe with connection to omnetics

not straightforward because of material compatibility problems. The biodissolvable needles are often incompatible with numerous solvents and using a release material that is compatible with mild solvents like isopropyl alcohol are not compatible with the various processes and rigorous cleaning steps required in even the most basic of fabrication flows. Hence, a peelable process flow is developed for this application.

This chapter describes the fabrication flow in three sections: The choice and processing techniques of the insulation is discussed in Section 2.1, the control of adhesion between the insulation and the substrate is described in Section 2.2 and the choice of electrodes and processing techniques of the electrode is described in Section 2.3.

## 2.1 Insulation materials for flexible neural probes

For flexible neural probes, the insulating material usually forms the bulk of the probe. Hence, the most important properties of the insulating material are biocompatibility,

high electrical resistance and high resistance to water penetration. In addition, a high yield strength and low Young's modulus are desired. Polymers such as parylene-C, polyimide, SU-8[53] and PDMS are predominantly used for compliant neural probes and will be evaluated in this section.

### 2.1.1 Biocompatibility

The biocompatibility of SU-8 is tested in the literature but the results are mixed. The major concern for SU-8 is the leaching of antimony. In [54], SU-8 is shown to be toxic for neurons with less than 10% neurons cultured on SU-8 2000 surviving although the authors suggested coating the SU-8 with parylene-C to improve cell viability. However, in [55], SU-8 is found to be biocompatible although the *in vivo* experiments are not done on neurons but are performed subcutaneously. However, devices are successfully fabricated using SU-8, implanted into a mouse model and recorded neural activity for at least 4 months [53].

On the other hand, the other commonly used polymers (parylene-C, polyimide and PDMS) are regarded as biocompatible. Parylene-C is classified as a USP Class VI biocompatible material, is used for decades in medical devices and has also been tested in the brain. In [56], no adverse effect on surrounding tissue was reported after implanting microelectrodes coated with parylene-C in a monkey for 3 years. In [57], parylene-C and a polyimide, Pyralin PI-2555 (DuPont, Wilmington, DE) was found to be biocompatible when implanted subdurally in a cat for 16 weeks. Moreover, parylene-C was found to be chemically stable under physiological conditions for at least 6 months in [58][59]. PDMS is also regarded to be biocompatible in various studies [60][59] and is used in biomedical devices for decades. Polyimide is biocompatible in brain tissue[61]. Also, polyimide has good to excellent biocompatibility as defined by ISO 10933 depending on the type of polyimide used[62].

### 2.1.2 Mechanical Properties

The values of Young's modulus for parylene-C, polyimide and SU-8 are within the same order as tabulated in Table 2.1. PDMS on the other hand is more flexible. In addition, the tensile strength of the various materials are also tabulated in Table 2.1.

To determine the mechanical properties of parylene-C deposited at 35 mT using a Labcoter 2 Parylene Deposition System (Specialty Coating Systems, Indianapolis, IN), a tensile test is performed to obtain the elastic limit for the material. A load versus extension curve is obtained for a parylene-C film of width 1 cm and thickness 6.5  $\mu\text{m}$  using an Instron 5943 testing system. The film is cut using a plastic mold made from a laser cutter and peeled from the Si substrate. The width of the film is measured using a ruler and the thickness of the film is measured using a P-15 profilometer (KLA Tencor, Milpitas, CA). The load versus extension curve allows a stress-strain relationship for the film of parylene-C to be obtained and the elastic limit to be determined as seen in Figure 2-2. Based on the test data, the parylene-C film has an elastic limit of 59 MPa, indicated by point A and a yield strength of 68 MPa, indicated by point B. The initial slope of the curve corresponds to a Young's modulus value of 4.2 GPa. These values are in agreement with values reported in the literature.

### 2.1.3 Electrical Properties

Since the polymers are used as electrically insulating layers, the resistivity of the polymers should be as high as possible and the dielectric constant should be as low as possible to reduce resistive and capacitive coupling of noise. The electrical properties of the various polymers are summarized in Table 2.2. The dielectric constants of the various polymers are similar and the volume resistivities are high. Hence, all of these polymers are electrically suitable to be encapsulation materials.

Table 2.1: Mechanical properties of various polymers

Material	Young's modulus	Tensile strength (MPa)	Notes	References
Parylene-C	2.4 to 4.75 GPa	59		[63][64][65][66][67]
SU-8	2.0 to 4.1 GPa	49.4 to 74.1	Depends on processing conditions e.g. whether a hard bake step is performed	[68][69][70][71]
PDMS	0.1 to 3 MPa	3.9 to 10.8	Depends on processing conditions and relative amount of crosslinker	[72][73]
Polyimide	3.0 to 8.4 GPa	343	Depends on type of polyimide and processing conditions	[62][61]

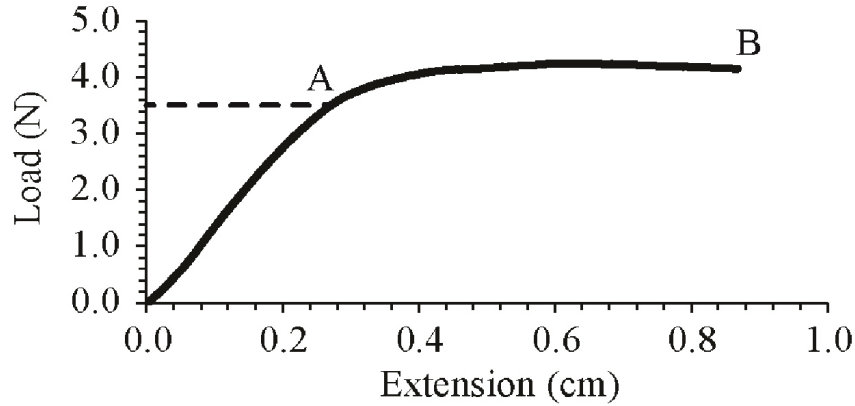


Figure 2-2: Experimental load versus extension for a 6.5  $\mu\text{m}$  thick, 10 mm wide sample of parylene-C.

Table 2.2: Electrical properties of various polymers

Material	Resistivity ( $\Omega \text{ cm}$ )	Dielectric constant	References
Parylene-C	$9 \times 10^{16}$	2.95	[74]
SU-8	$(1.8 \text{ to } 2.8) \times 10^{16}$	3.2 to 4.1	[71]
PDMS	$1 \times 10^{14}$	2.5 to 3	[75] [76]
Polyimide	$1.5 \times 10^{17}$	2.7 to 3.1	[77]

### 2.1.4 Processability

Another important consideration is the method of deposition and ease of processing of the material. Parylene-C is deposited using Chemical Vapor Deposition (CVD) and can be etched using O<sub>2</sub> plasmas[78], making it a very versatile material. It is also very inert [79] and does not swell appreciably in many solvents[80], which makes it a good material for fabrication. SU-8, PDMS and polyimide are deposited by spin-coating, which is a less conformal process compared to CVD. For the use of these materials as barriers, a conformal process is desirable so as to ensure complete coverage of the material across the entire device. This is especially important for devices with non-planar features. SU-8 and certain polyimides are photosensitive and hence can be easily patterned using photolithography. Fabrication on PDMS is difficult because it swells in different solvents resulting in cracking of thin films deposited on it [81].

These materials can be etched in O<sub>2</sub> plasmas, which can be generated in many equipment in most cleanrooms; for example in the barrel plasma etcher, in a parallel plate RIE system or in an ICP RIE system. The different systems allow for control of the type of etching required. For example, using a barrel etcher or an ICP RIE system without bias power will result in an isotropic etch whereas using a parallel plate RIE will result in a anisotropic etch.

A summary of the properties of SU-8, parylene-C, polyimide and PDMS are found in Table 2.3.

Given the processability, proven biocompatibility, electrical and mechanical properties of parylene-C, in this thesis, neural probes are fabricated predominantly using parylene-C as the material.

### 2.1.5 Chemical properties of parylene-C

The structure of parylene-C is shown in Figure 2-3(c). It belongs to the class of polymers known as parylenes that share a similar structure consisting of a benzene ring and two methylene bridges. For parylene-C, one of the hydrogen atoms in the benzene ring is substituted with Cl. Parylene-C is usually deposited using the stan-

Table 2.3: Summary of properties of various polymers

Property	Biocompatibility	Processability	References
Parylene-C	Good	Good, Deposition by CVD, etching processes well-characterized	[57][78] [80] [56] [58][59]
SU-8	Result of studies are mixed	Good, photosensitive to UV, spin-coated	[54]
PDMS	Good	Moderate, spin-coated, swelling in solvents causes cracking in other films	[81] [60][59]
Polyimide	Good	Moderate, spin-coated requires high temperature curing	[57] [61] [62]

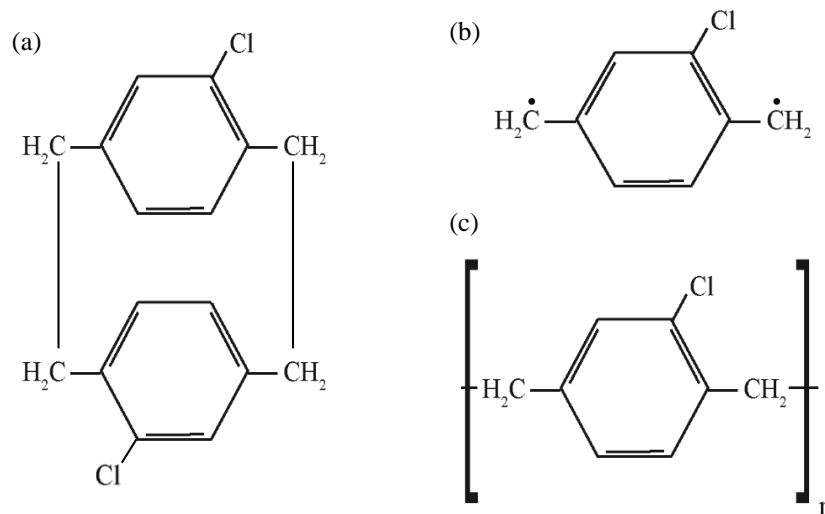


Figure 2-3: (a) Chemical structure of dimer used to deposit parylene-C. (b) Chemical structure of monomer used to deposit parylene-C. (c) Chemical structure of parylene-C

standard Gorham process[82]. The process involves three separate chambers (vaporizer, pyrolyzer and deposition chamber) that have different temperatures but are connected in space. The process begins with sublimation of the dimer (Figure 2-3(a)) in the vaporizer once a base pressure is reached (the base pressure is typically in the order of mT) by raising the temperature of the vaporizer. The dimer gas is then fed into a pyrolyzer where the dimer gas is split into the monomer at a high temperature (Figure 2-3(b)). To ensure minimal contamination of the deposited parylene-C with the dimer, it is essential that the pyrolyzer reaches a stable, and high temperature (typically 690°C) prior to the sublimation of the dimer so that all the dimer gas is split into the corresponding monomer gas. A parylene-C film with a high amount of dimer contaminant appears cloudy as opposed to pure parylene-C, which appears clear. The monomer is fed into the deposition chamber where the polymer is formed on the substrate and the chamber walls at room temperature. The deposition rate of parylene-C decreases with temperature of the substrate[83]. A baffle rod distributes the parylene-C evenly and controls the rate of deposition by controlling the flow rate of the monomer gas. This process continues until all the dimer is used up, which is determined when there is no increase in pressure when the temperature of the vaporizer continues to increase. By controlling the weight of the dimer fed into the machine, the thickness of the parylene-C can be controlled.

The most common adhesion promoter between parylene-C and silicon or silicon oxide is 3-(Trimethoxysilyl)propyl methacrylate (A174). A174 is a silane as shown in Figure 2-4(a). The A174 is prepared by first mixing the chemical with isopropyl alcohol (IPA) and deionized (DI) water (A174:IPA:DI water = 1:100:100 by volume) and leaving the mixture overnight. This converts the A174 to the structure shown in Figure 2-4(a) step 2. One component of A174 (The 'R' group indicated in Figure 2-4(a) reacts with the parylene-C whereas the -OH groups first form hydrogen bonds with the surface -OH groups on silicon or silicon oxide before forming covalent bonds as shown in Figure 2-4(a) steps 3-4. Hence, the A174 solution chemically adheres parylene-C to silicon or silicon oxide.

However, the use of A174 results in too strong of an adhesion between parylene-C

and silicon, which makes the devices unpeelable since the devices will break prior to initiation of peeling. On the other hand, since there needs to be significant processing to fabricate the parylene-C devices, the adhesion cannot be too poor since low adhesion can result in delamination during processing. Hence, in this thesis, another method of improving the adhesion force between silicon and parylene-C is investigated. By using HMDS, the hydrophobicity of the surface of Si can be controlled by substitution of the hydroxyl groups to methyl groups as shown in Figure 2-4(b) steps 1-2. Hence, the use of HMDS is investigated as a means of modulating adhesion between parylene-C and Si by controlling the coverage of -OH groups versus -CH<sub>3</sub> groups on the wafer. Since the adhesion between parylene-C and the Si surface will still be due to Van Der Waal's forces, which are relatively weak, the adhesion will be modulated within a range that allows for peelability.

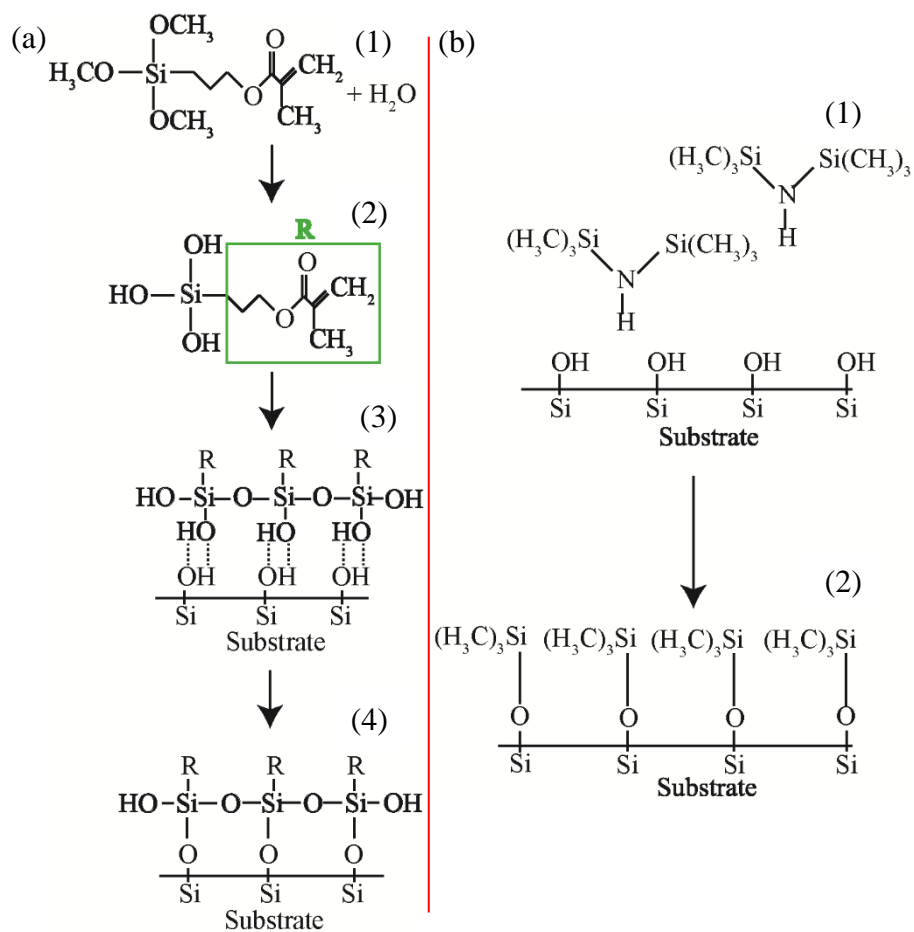


Figure 2-4: (a) Reaction between A174 and silicon or silicon oxide. (1) A174 and  $\text{H}_2\text{O}$  reaction. (2) Product of reaction between A174 and  $\text{H}_2\text{O}$ . (3) Hydrogen bond formation between silane and surface of Si. (4) Formation of covalent bonding between adsorbed A174 and the surface of Si. (b) Reaction between HMDS and silicon or silicon oxide surface. (1) unreacted HMDS and silicon surface. (2) Surface after reaction between HMDS and silicon surface.

## 2.2 Fabrication of peelable structures

Since the adhesion between the substrate and parylene-C is the critical parameter for fabrication of peelable structures, an investigation is performed on the modulation of adhesion between parylene-C and Si by modifying the HMDS treatment time. It is hypothesized that by changing the HMDS vapor prime time, the surface coverage of HMDS on Si will be modulated within a certain range before being saturated. By leveraging on the change in the surface coverage of HMDS, the adhesion between parylene-C and Si can be modulated through the change in surface coverage of HMDS.

In order to test this, contact angle measurements are used to determine the effect of HMDS on the surface properties of Si and derive the surface energy of the surface-modified Si. The peel force per unit width for parylene-C deposited on the various HMDS treated Si leads to a determination of the relationship between surface energy and peel force per unit width for parylene-C.

For the tests, HMDS (Shin-Etsu MicroSi, Phoenix, AZ) is applied either by vapor prime or by spin coating. HMDS application by vapor prime is carried out using a HMDS Vapor Prime Oven (Yield Engineering Systems, Livermore, CA) at 150°C. The wafers are first dehydrated in the HMDS Vapor Prime Oven at 150°C for 5 minutes. Following that, HMDS is vaporized in the HMDS Vapor Prime Oven for the desired vapor prime time. For the case of spin-coating of HMDS, the wafers are first dehydrated using the HMDS Vapor Prime Oven at 150°C for 5 min. Spin-coating of HMDS is then carried out by manually spreading HMDS across the wafer using a dropper and soaking the HMDS for approximately 10 s before spinning the wafer at 3000 rpm for 60 s using a wafer spinner (Solitec, Milpitas, CA). Typically, A174 (Specialty Coating Systems, Indianapolis, IN) is applied either by vapor prime or by immersing the substrate in a solution containing A174 [84]. In this chapter, A174 is applied by immersing the substrate in a IPA:DI Water:A174 solution (1:100:100 ratio by volume) and the treated substrate is air dried.

Small (25 mm-diameter) Si wafers were used as the substrate for the experiments to allow for a larger number of samples to be loaded per parylene-C deposition run.

The wafers are first cleaned with acetone followed by IPA and dried with nitrogen gas. They are then heated at 120°C for 10 minutes. Following that, the wafer surfaces are given one of the treatments listed below:

1. Spun at 3000 rpm with HMDS,
2. Vapor primed with HMDS for 1 min, 2 min, 5 min or 10 min,
3. Not treated further; and
4. Immersed in A174 solution.

For the peel force measurements, 10  $\mu\text{m}$  of parylene-C is deposited on each substrate at 35 mT and room temperature using a Labcoter 2. The samples used for substrate contact angle measurements are not coated with parylene-C. The sample sizes for each peel test is listed in Table 2.4.

In addition, three neural probe structures are prepared to determine the peel force per unit width *in situ*. 2  $\mu\text{m}$  of parylene-C is first deposited using a Labcoter 2 on a 100 mm Si wafer primed with HMDS vapor for 1 minute. Following that, 510 nm of Pt is deposited using a 6J Sputtering System (Perkin-Elmer, Waltham, MA). The Pt is patterned using a MA6 contact aligner (Karl Süss, Garching, Germany) and etched using an ion mill (Commonwealth Scientific, Wokingham, UK). Following this, 2  $\mu\text{m}$  of parylene-C is deposited using a Labcoter 2. The parylene-C is then patterned using

Table 2.4: Measured peel force per unit width in mN/cm for four different surface treatments of Si over 3 parylene-C deposition runs

Treatment	Run 1	Run 2	Run 3	Run 4
Dehydration Only	1	1	1	5
HMDS Spin Coat	1	1	1	5
1 min vapor prime	1	1	1	5
2 min vapor prime	1	1	1	5
5 min vapor prime	-	-	-	5
10 min vapor prime	-	-	-	5
A174 solution	2	-	-	-

a MA6 contact aligner (Karl Süss, Garching, Germany) and etched using a Phantom Reactive Ion Etch (RIE) System (Trion Technology, Tempe, AZ).

### 2.2.1 Contact angle measurements

The contact angle measurements on Si wafers treated with the various HMDS treatments using a goniometer (Ramé-Hart, Succasunna, NJ) as shown in Figure 2-5. Using a micropipette, 5  $\mu\text{L}$  of DI water is placed on the surface to be characterized (either treated Si or parylene-C) and the contact angle is measured on a computer with DROPimage edge detection software (Ramé-Hart, Succasunna, NJ). Three drops of DI water are placed at different points on the wafer and the average of the contact angles were taken. This process is repeated for ethylene glycol. A representative image generated by the edge detection software is shown in Figure 2-5(a) inset.

Figure 2-5(a) shows the contact angle results obtained for the various HMDS primed substrates and untreated substrates. It is clear from Figure 2-5(a) that there is an increase in the contact angle of the DI water and ethylene glycol with the substrate as HMDS prime time increases. The measured contact angle of the DI water and ethylene glycol with the substrate that is spun coated with HMDS is  $62.7^\circ$  and  $43.8^\circ$  respectively. Based on the data, the largest variation in contact angle is over the first 2 minutes of HMDS prime time. The DI water contact angle varies from  $46.3^\circ$  to  $74.9^\circ$  indicating increased hydrophobicity, which is consistent with a change from a surface dominated by -OH groups to a surface dominated by -CH<sub>3</sub> groups [85].

### 2.2.2 Work of adhesion from contact angle measurements

Using thermodynamic considerations, the surface energy of a film is related to the work of adhesion between the substrate and film  $W_{A,SF}$  by the Dupré equation [86]:

$$W_{A,SF} = \gamma_{SG} + \gamma_{FG} - \gamma_{SF} \quad (2.1)$$

where  $\gamma_{FG}$  is the surface energy of the film in a gas,  $\gamma_{SG}$  is the surface energy of the substrate in a gas and  $\gamma_{SF}$  is the interfacial surface energy between the substrate and

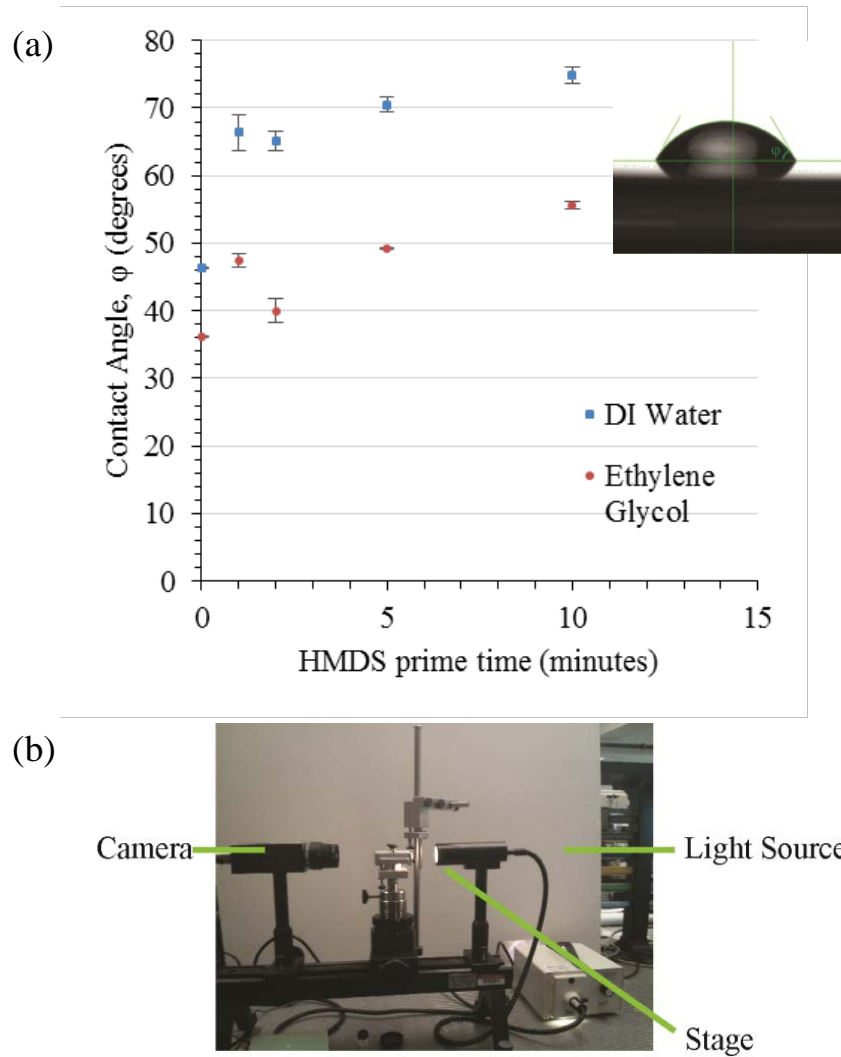


Figure 2-5: (a) Contact angle of DI water and ethylene glycol. Inset: representative result from one measurement using the Goniometer. (b) Setup for contact angle test using the goniometer.

the film.

These surface energies are determined using contact angles between liquids and surfaces. This is done by placing small volumes of different liquids on each surface and measuring the contact angles  $\phi_i$  of the droplets with the surfaces.

For liquids on a substrate, Young's equation [87] relates the interfacial energies of the liquid to that of the solid substrate:

$$\gamma_{SG} = \gamma_{SL} + \gamma_{LG} \cos \phi \quad (2.2)$$

where  $\gamma_{LG}$  is the surface energy of the liquid in air and  $\gamma_{SL}$  is the interfacial surface energy between the substrate and the liquid.

Each of the surface energies can be split into its dispersive and polar components. For example,

$$\gamma_{LG} = \gamma_{LG}^D + \gamma_{LG}^P \quad (2.3)$$

The dispersive component of surface energy arises due to Van Der Waals forces, which are due to temporary fluctuations in the electron clouds of atoms that create temporary dipoles. On the other hand, the polar component of surface energy arises due to permanent dipoles present in the substance.

By combining the proposal by Owens and Wendt [88] that  $W_{A,SL}$ , the work of adhesion between a solid and a liquid is the geometric mean of the respective surface energy components of the solid and the liquid, the proposal by Fowkes [89] that the dispersive (indicated by superscript D) and polar (indicated by superscript P) components of the interfacial energies are additive and (2.1) leads to:

$$W_{A,SL} = \gamma_{LG}(1 + \cos\phi) = 2\sqrt{\gamma_{SG}^D\gamma_{LG}^D} + 2\sqrt{\gamma_{SG}^P\gamma_{LG}^P} \quad (2.4)$$

Hence, if the contact angle test is performed using two liquids with known  $\gamma_{LG}^P$  and  $\gamma_{LG}^D$  on a solid's surface, the polar and dispersive surface energies of the solid is obtained by solving (2.4) for each of the two liquids simultaneously. Deionized (DI) water and ethylene glycol are used for the contact angle test as the surface energies

of these liquids have been characterized in air [1]. The dispersive component, polar component and total surface energy of these liquids are tabulated in Table 2.5.

### 2.2.2.1 Work of adhesion between solids and films

The work of adhesion between a solid and a film is important in many cases such as in the prediction of adhesive strength between parylene-C and Si. The work of adhesion between solids and films can also be represented using (2.4) [90]. Hence, the work of adhesion between parylene-C and Si is:

$$W_{A,PxSi} = 2\sqrt{\gamma_{Px,G}^D \gamma_{Si,G}^D} + 2\sqrt{\gamma_{Px,G}^P \gamma_{Si,G}^P} \quad (2.5)$$

where  $W_{A,PxSi}$  is the work of adhesion between parylene-C and Si,  $\gamma_{Px,G}^D$  is the dispersive surface energy of parylene-C,  $\gamma_{Si,G}^D$  is the dispersive surface energy of Si,  $\gamma_{Px,G}^P$  is the polar surface energy of parylene-C and  $\gamma_{Si,G}^P$  is the polar surface energy of Si.

As discussed, the various components of the interface energy that are needed to determine  $W_{A,PxSi}$  using (2.5) are found by performing the contact angle test with two liquids for both the substrate (HMDS treated Si) and the film of interest (parylene-C).

### 2.2.2.2 Derivation of surface energies of parylene-C, HMDS treated Si and A174 treated Si

The measured contact angles of DI water and ethylene glycol on parylene-C are 90.8° and 63.9° respectively. Solving (2.4) gives the values of dispersive surface energy, polar surface energy, and total surface energy of parylene-C to be 25 mJ/m<sup>2</sup>, 3.1 mJ/m<sup>2</sup> and 28.1 mJ/m<sup>2</sup> respectively. The derived values are consistent with the dispersive

Table 2.5: Surface energy components of DI water and ethylene glycol [1]

Liquid	Total Surface Energy (mJ/m <sup>2</sup> )	Dispersive Surface Energy (mJ/m <sup>2</sup> )	Polar Surface Energy (mJ/m <sup>2</sup> )
DI Water	72.8	21.8	51.0
Ethylene Glycol	48.0	29.0	19.0

nature of as-deposited parylene-C ( $\gamma_{P_x,G}^D \gg \gamma_{P_x,G}^P$ ). Hence, from (2.5) the work of adhesion between parylene-C and the substrate is mainly determined by the dispersive surface energy of the substrate. This means that parylene-C tends to adhere well to substrates with a high dispersive surface energy. Nevertheless, for the analysis used in this chapter, all components of the work of adhesion are considered.

Similar to parylene-C, the measured contact angle data is used to solve for the dispersive and polar surface energies of HMDS treated Si using (2.4). The work of adhesion between parylene-C and Si is calculated by substituting the measured surface energies of parylene-C and Si into (2.5). The variation in the surface energies and work of adhesion with HMDS prime time is shown in Figure 2-6.

A clear increase is observed in dispersive surface energy for surfaces vapor primed with HMDS from 0 min to 2 min. The linear variation in surface energy with HMDS prime time between 0 min to 2 min provides a process window for parylene-C/Si adhesion control.

The contact angles measured on two 25 mm Si substrates treated with A174 are  $58.6^\circ$  and  $48.9^\circ$  with DI water and  $41.9^\circ$  and  $36.8^\circ$  with ethylene glycol. Based on these measured contact angles, the dispersive, polar and total surface energies of A174 treated Si substrates are  $8.3 \text{ mJ/m}^2$ ,  $39.1 \text{ mJ/m}^2$  and  $47.4 \text{ mJ/m}^2$ , respectively. Using the obtained values of the various surface energy components of as-deposited parylene-C, the calculated work of adhesion between parylene-C and A174-treated Si substrates is  $50.7 \text{ mJ/m}^2$ .

### 2.2.3 Peel test analysis

Figure 2-7 illustrates the peeling of a film from a substrate. The peeling force  $P$  is the force required to overcome the adhesion between the film being peeled and the substrate, which is quantified by a thermodynamic work of adhesion  $W_A$ . It is assumed that the application of the peeling force is always at the peeling front and that the angle  $\theta$  between the substrate and the peeling force is constant throughout the peeling process. Since peeling is a dynamic process, statics do not apply. Hence, peeling is modeled using energy methods as described in [91]. If  $\Delta x$  of film is peeled

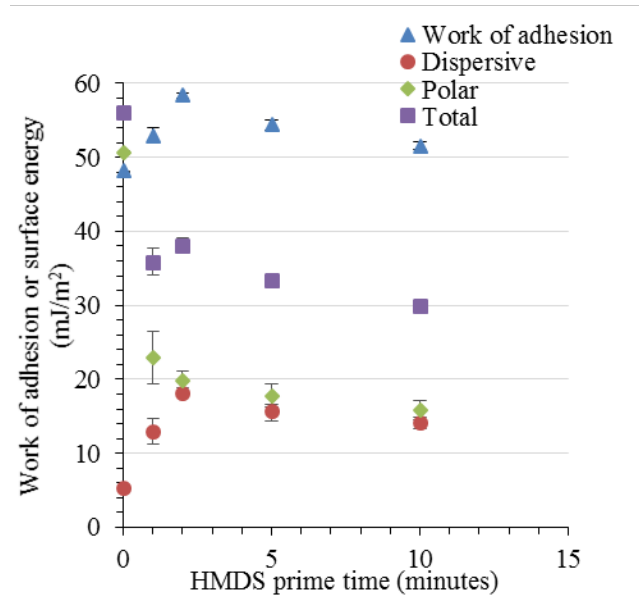


Figure 2-6: Work of adhesion for parylene-C on Si, and the polar and dispersive energies derived from measured contact angles versus HMDS vapor prime time

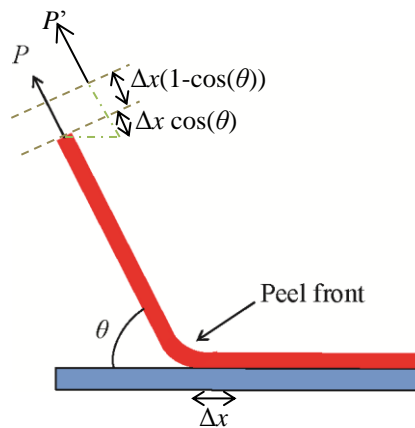


Figure 2-7: Schematic cross-section of a film being peeled from a substrate. The final position of the applied force after  $\Delta x$  of film is peeled is  $P'$ .

as illustrated in Figure 2-7, by conservation of energy, the work done by the force  $P$  is equal to the change in surface energy of the system or,

$$\frac{P^2\Delta x}{Et w} - \frac{P^2\Delta x}{2Et w} + P(1 - \cos\theta)\Delta x = R w \Delta x \quad (2.6)$$

where  $R$  is the average adhesion force per unit structure width,  $E$  is the Young's modulus of the film,  $w$  is the width of the film,  $t$  is the thickness of the film and  $0 < \theta \leq 180^\circ$ . On the left-hand side, the first term is due to the elastic strain of the newly released film, the second term is the recoverable strain energy of the newly released film and the third term is the work done due to the movement of the point of applied force during peeling as illustrated in Figure 2-7. The right-hand side of (2.6) is the change in surface energy of the system, which is given by the product of the peeled area and the peeling energy per unit area,  $R$ .  $R$  is the actual peel energy per unit area, which is measured from a peel test and is different from  $W_A$ , which is defined from thermodynamic considerations.  $W_A$ , which is also commonly called the reversible work of adhesion, is more idealistic and only considers the reversible bonds between the two materials at the interface.  $R$ , on the other hand, is also commonly known as adhesive fracture energy and is usually much larger than  $W_A$  as it includes irreversible processes such as plastic deformation[92]. Nevertheless, it is possible to use  $W_A$  to predict  $R$  since they are proportional to each other[92][93].

Simplifying (2.6) gives

$$\left(\frac{P}{w}\right)^2 \frac{1}{2Et} + \frac{P}{w}(1 - \cos\theta) - R = 0 \quad (2.7)$$

For many cases, including the experiments done in this thesis, the first term is negligible because the stress is usually much lower than  $E$ [94]. Hence, the peeling force per unit width is:

$$\frac{P}{w} = \frac{R}{(1 - \cos\theta)} \quad (2.8)$$

The action of peeling also stresses the structure being peeled, which can lead to plastic deformation of the structure. To avoid plastic deformation, the elastic limit

of the film is used to define the maximum axial force allowed in the structure, since the force is transmitted throughout the film. Assuming the film is peeled normal to the surface, i.e.  $\theta = 90^\circ$ , the peeling force is  $P = Rw$ . If the limit of the stress of the peeled material is given by  $\sigma_{limit}$ , the maximum allowable average peeling energy per unit area for a given structure thickness  $t$  is

$$R_{max} = \sigma_{limit}t \quad (2.9)$$

This relation assumes that the stress due to bending at the peel front is negligible, which is valid for thin compliant structures ( $< 10 \mu\text{m}$ ). For a composite beam, the validity of this assumption depends on the effective Young's modulus of the stack of materials.

The thickness of the film is subject to other constraints. In the neural probe application, for example, it is important to achieve mechanical compliance for biocompatibility reasons, which biases the design toward thinner films and limits the maximum thickness. Control of the adhesion force would allow the thinnest film to be designed to meet the application needs. To determine the minimum allowable structure thickness, we use a linear correlation between the average peeling energy per unit area and the work of adhesion [93]

$$R = mW_A - c \quad (2.10)$$

The negative offset ( $-c$ ) in the equation is attributed in [93] to the often observed phenomenon that the peeling energy is zero when  $W_A$  is not. This is attributed in [93] to the fact that during peeling, thermodynamic equilibrium is not achieved.  $c$  is also attributed to limits of measurement of  $R$ . Throughout this chapter,  $R$  is in N/m,  $W_A$  is in J/m<sup>2</sup>,  $m$  is a dimensionless quantity and  $c$  is in N/m.

Combining (2.10) with (2.9) leads to the structure design constraint:

$$t_{min} = \frac{mW_A - c}{\sigma_{limit}} \quad (2.11)$$

$\sigma_{limit}$  is obtained from tensile tests,  $W_A$  is obtained from the contact angle tests presented in this chapter, and  $m$  and  $c$  are empirical constants.  $m$  is dependent on particular surface treatments and  $c$  is an artifact of measurement.

## 2.2.4 Peel force measurement

To prepare the samples for the peel force measurement, a razor blade was used to cut the parylene-C films to the desired width using a mold that was formed by a laser cutter. The width of the films was 1 cm as indicated by  $w$  in the inset of Figure 2-8(b). The film at one end of the Si wafer was peeled using a pair of tweezers to separate approximately 2 cm of film from the substrate. The samples were mounted on an Instron 5943 tension tester (Instron, Norwood, MA), the free edge of the peeled film was clamped as shown in Figure 2-8(a) and the load versus extension is measured with the rate of extension set at 1 mm/min. A typical graph of load versus extension is shown in Figure 2-8(c). The initial portion of the graph represents the initial stretching of the film. The flat portion of the graph represents the period when the film is being peeled and it is the measurement in this region that is extracted as the peeling force  $P$  and used to determine the average peeling energy per unit area  $R$ . As shown in the peel test setup in Figure 2-8(a), the angle  $\theta$  between the line of action of the peeling force  $P$  and the substrate is  $180^\circ$ . This is due to equipment constraints; For an angle other than  $180^\circ$ , it is necessary to have a setup that moves the substrate both horizontally and vertically.

The peel test data collected over five samples in a single parylene-C deposition run is shown in Figure 2-9.

Figure 2-10 shows the relationship between the measured peel force and the calculated surface energies from Section 2.2.1. A strong positive correlation is observed between the peel force and the dispersive energy, which is expected based on Owens and Wendt's theory [88] since the bulk of the parylene-C surface energy is dispersive in nature.

A linear regression is performed on the surface energy per unit area for parylene-C on HMDS-treated Si substrates as a function of surface energy and work of adhesion

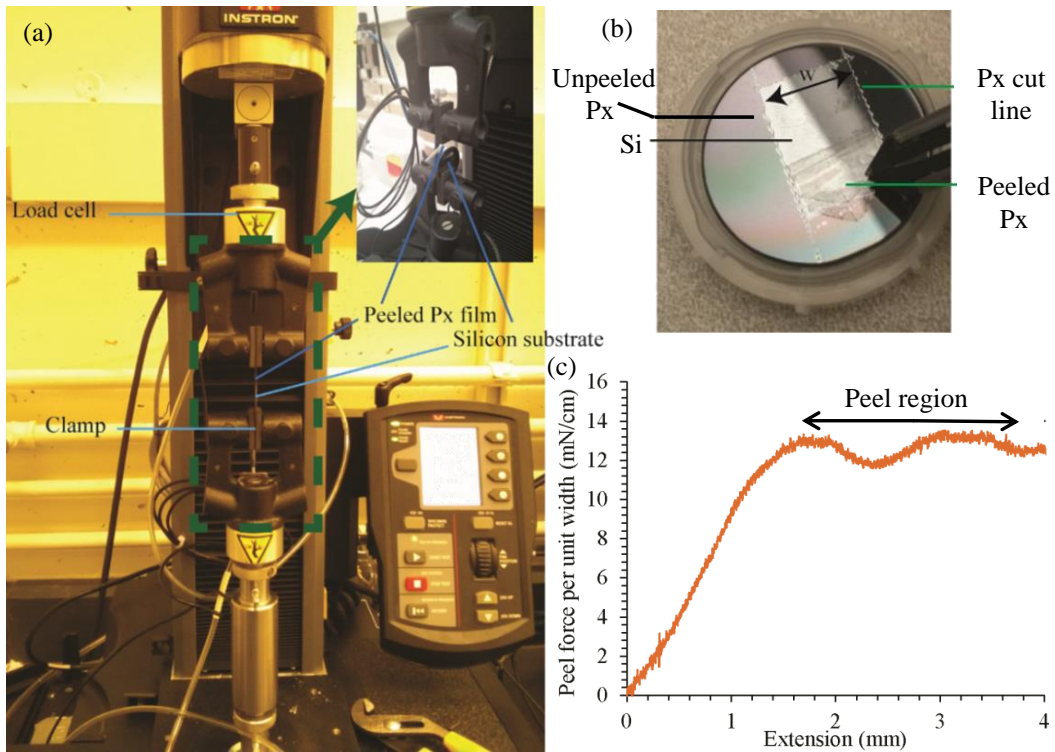


Figure 2-8: (a) Setup for peel test. Inset: Zoomed in image of clamp region of instron. (b) Sample used for peel test after completion of peeling test. Width of peeled film is indicated by  $w$ . (c) Representative peel force measurement result. The peel region is indicated on the graph.

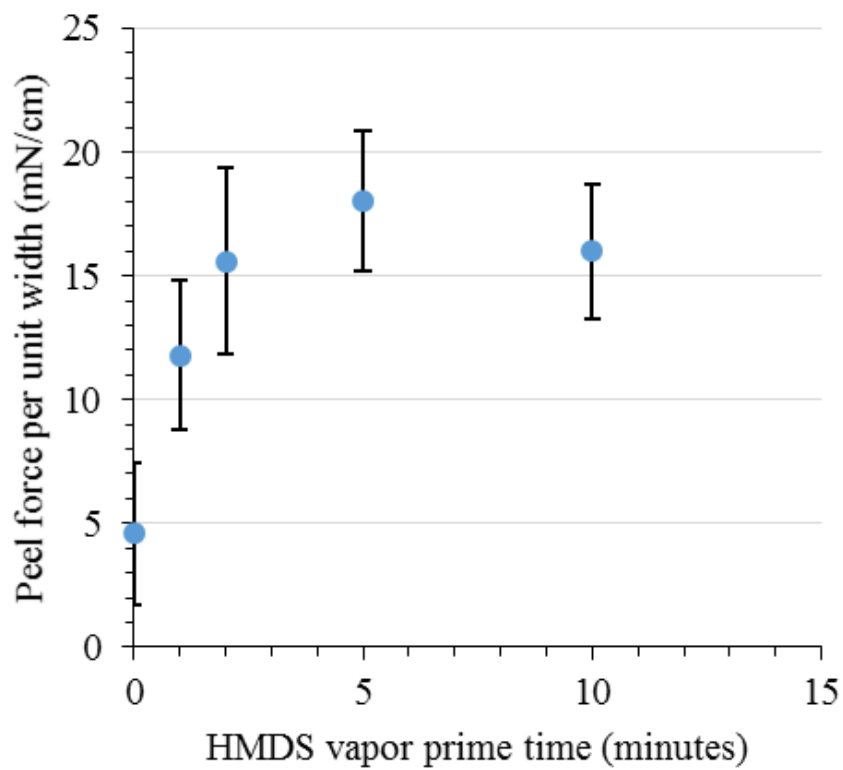


Figure 2-9: Peel force per unit width versus HMDS vapor prime time in minutes. Error bars are one standard deviation from the mean.

in Figure 2-10. The regression relation between the surface energy per unit area,  $R$  and the work of adhesion  $W_{A,PxSi}$  as shown in Figure 2-10 is:

$$R = 200W_{A,PxSi} - 8.1 \quad (2.12)$$

Using this equation, the expected peel force per unit width for A174 treated-Si surfaces is approximately 20 mN/cm for a 90° peel angle. However, the adhesion force is far greater than expected given that the samples of Si treated with A174 tear when being peeled. Therefore, this suggests that the bonds formed between A174-treated Si and parylene-C are covalent in nature and differ from the bonds formed between parylene-C and HMDS treated Si.

In addition, to get a sense of the variation across different runs, the peel test data collected in four parylene-C deposition runs is given in Table 2.6 for various surface treatments. From the computed standard deviation between groups and the standard deviation within groups, it is seen that the variation in peel force per unit width across different parylene-C deposition runs is mostly larger than the variation in peel force per unit width across different samples in the same parylene-C deposition run. The variation seen within a single run and across separate runs is considerable but comparable to that seen in other similar tests [95]. This means that considerable margins must be taken into consideration when designing a peelable process.

Table 2.6: Mean peel force per unit width in mN/cm for four different surface treatments of Si over four parylene-C deposition runs.  $SS_B$  is the standard deviation between groups,  $SS_W$  is the standard deviation within groups and  $SS_T$  is the total standard deviation.

Treatment	Run 1 ( $n = 1$ )	Run 2 ( $n = 1$ )	Run 3 ( $n = 1$ )	Run 4 ( $n = 5$ )	Mean	$SS_B$	$SS_W$	$SS_T$
Dehydration Only	12	2	5	5	6	4	3	7
1 min vapor prime	22	6	9	12	12	7	3	10
2 min vapor prime	12	13	13	16	15	3	4	7
HMDS Spin Coat	18	4	5	9	9	6	3	9

The considerable variation could be attributed to differences in parylene-C deposition. The nature of the process is such that base pressure of the machine is set to be below a certain value (15 mT for the runs used in this chapter) but there is no control on the exact value of pressure when the initial layers of parylene-C is deposited. Although the bulk of the parylene-C is deposited at the set operating pressure since the machine regulates the vaporizer temperature, the initial parylene-C is deposited below the operating pressure as the vaporizer temperature is ramping up. Since adhesion depends on the quality of the initial layer of the parylene-C deposited, this could explain the significant variation in measured peel force per unit width. Other possible sources of variation are the time between dehydration bake and HMDS spin coat; and the time between the various treatments and parylene-C deposition. The transfer of the substrate between the various machines is a manual process that can result in large variations in the wait time.

Using the results from the tests, an estimate of the minimum thickness of parylene-C required for a given surface treatment can be obtained. For example, for the 2 minute case, using the regression relation (2.12) presented in Figure 2-10 and  $W_A=58$  mJ/m<sup>2</sup> from Figure 2-6, the surface energy per unit area is 35 mN/cm. Hence, the peel force per unit width is also 35 mN/cm if the peel angle is 90° from (2.7). Based on  $\sigma_{limit} = 59$  MPa from the tensile test measurement presented in Figure 2-2, the minimum thickness of parylene-C for this case is 60 nm. Although analysis using the measured material properties would give a conservative estimate, in practice, significant margins should be given because of the variability in peeling angles and the adhesion force per unit width.

Based on this analysis, for the parylene-C devices with thickness of 2 μm, using a 2 minute HMDS vapor prime treatment would give a margin of approximately 30 times. The strongest adhesion possible without breaking the composite film should be chosen to improve process yield.

The *in situ* peel force is measured using an Instron machine as shown in Figure 2-11. The peeling of probe structures is initiated prior to clamping the sample in the Instron machine. Prior to the initiation of the measurement, the probe structure is

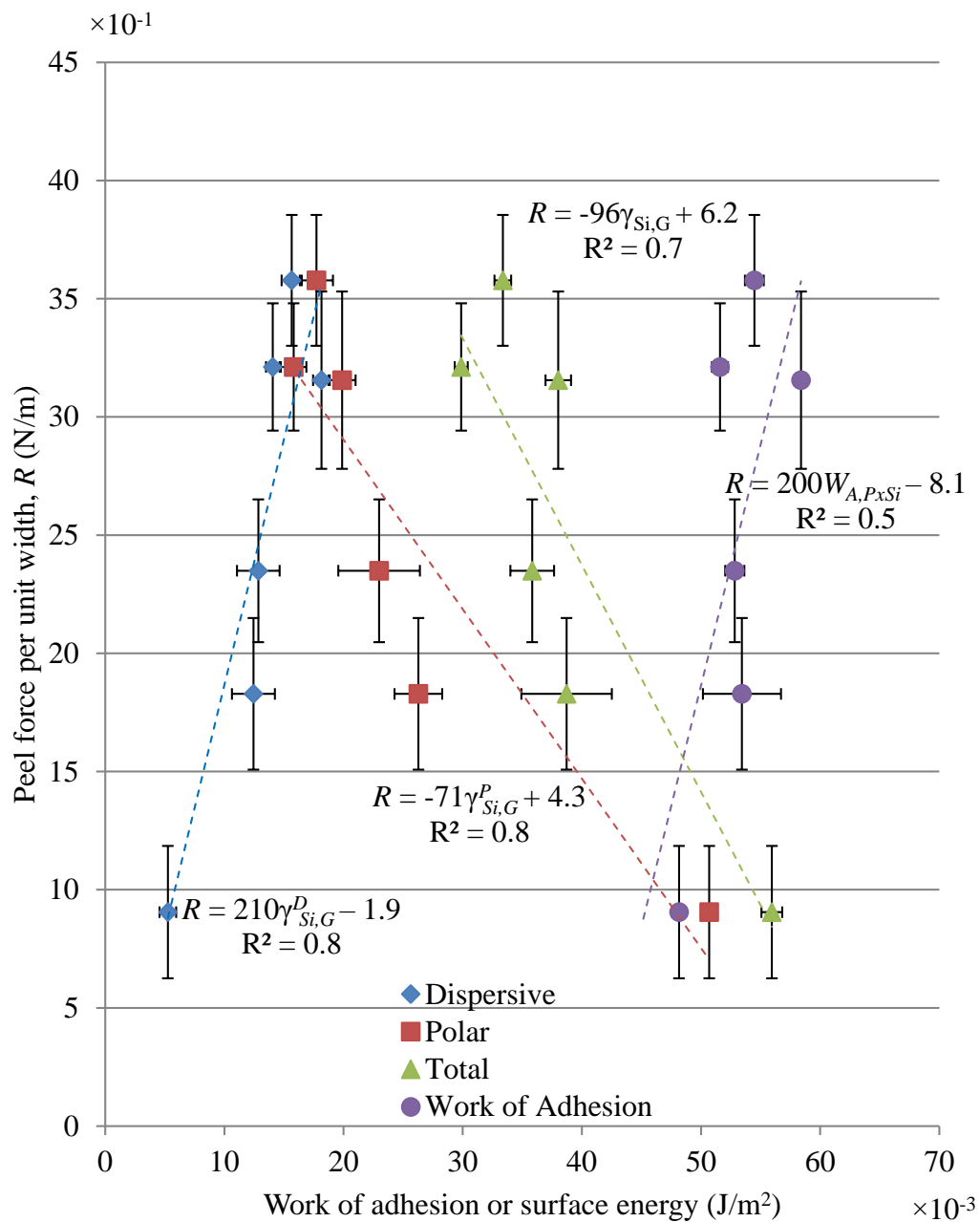


Figure 2-10: Peel force per unit width versus surface energy and work of adhesion for parylene-C film on HMDS-treated Si substrate. Error bars represent 1 standard deviation from the mean.

peeled until a region with constant width and angle is reached as shown in Figure 2-11(b). The *in situ* peel force per unit width measured on the neural probe structures is shown in Table 2.7. The Si is treated with HMDS for 2 minutes for these chips. The measured peel force is approximately 1 standard deviation away from the peel force per unit width derived from the peel test across different runs as seen in Table 2.6. This suggests that for parylene-C, the results from the peel tests apply to structures made using conventional patterning and etching processes.

Table 2.7: *In situ* peel force per unit width in mN/cm for 3 neural probe structures

	Peel force per unit width (mN/cm)
Sample 1	20
Sample 2	26
Sample 3	24
Mean	23
Standard Deviation	3

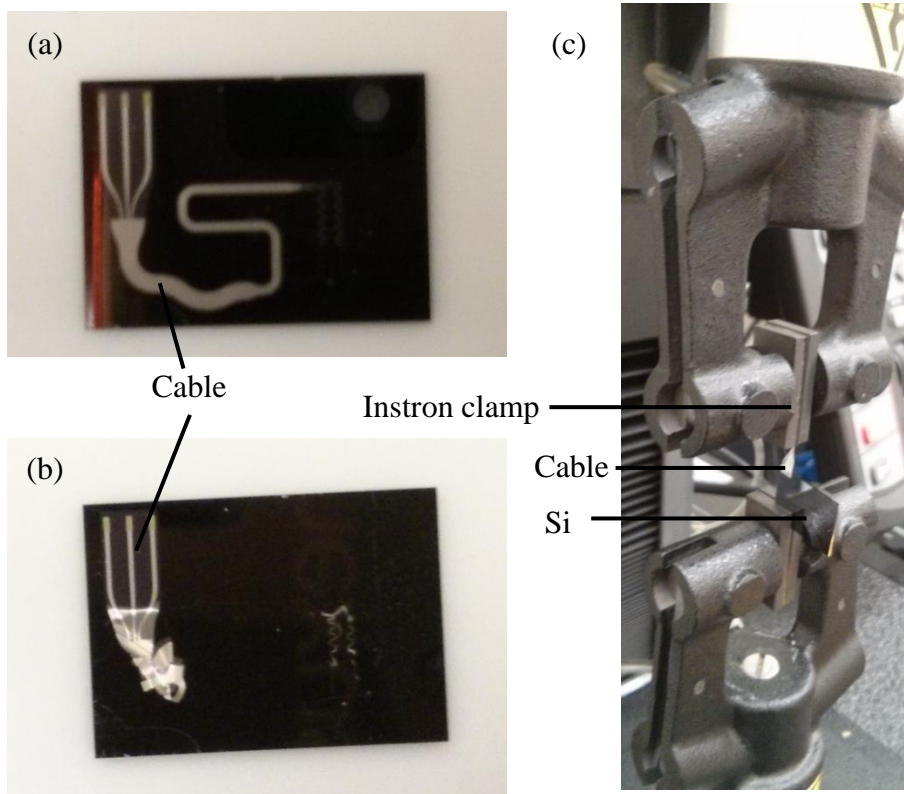


Figure 2-11: (a) Device prior to peeling. (b) Device after initiation of peeling. (c) Device mounted onto Instron machine for peel test measurement.

## 2.3 Processing of Electrodes

Apart from the insulation, in neural probes, the electrode also clearly plays a key role since it determines the region where a signal can be acquired and the signal to noise ratio. In particular, the electrode design, electrode material and electrode processing are critical. Since the electrode material has to be biocompatible, the electrode material is typically an inert material.

For recording electrodes, the impedance of the electrode is of importance. Having a low impedance is important to ensure low thermal noise and high capacitive coupling of the signal of interest (spikes from neurons) through the electrode. If the capacitance of the electrode is low relative to the capacitance between the interconnect and the tissue, the signal to noise ratio will be low because of the significant coupling of other signals through the insulator that effectively act as noise sources. The impedance of an electrode can be modelled using the electrical circuit shown in Figure 2-12(b).  $R_{CT}$  is a resistance that arises from chemical redox reactions that result in charge transfer from the electrode to the electrolyte and can be derived using the Stern-Geary equation for low overpotentials [96]:

$$R_{CT} = \frac{RT}{J_0 z F} \quad (2.13)$$

where  $J_0$  is the equilibrium exchange current density that can be derived from the kinetics of the redox reactions or experimentally,  $z$  is the metal valence,  $R$  is the universal gas constant,  $T$  is the temperature in Kelvin,  $F$  is the Faraday constant and  $RT/F$  is the thermal voltage  $U_T$ . Nevertheless, for recording electrodes used in this thesis that are made of Pt, the contribution of  $R_{CT}$  is small compared with  $C_{dl}$  and hence can be ignored.

$C_{dl}$  represents the double layer capacitance formed when a charged electrode is immersed in an electrolyte. The double layer capacitance can be modelled using the Gouy-Chapman-Stern model to be formed from the Helmholtz and diffuse regions as shown in Figure 2-12(a). This model assumes that when a charged electrode is immersed in an electrolyte, a layer of fixed thickness consisting of particles of opposite

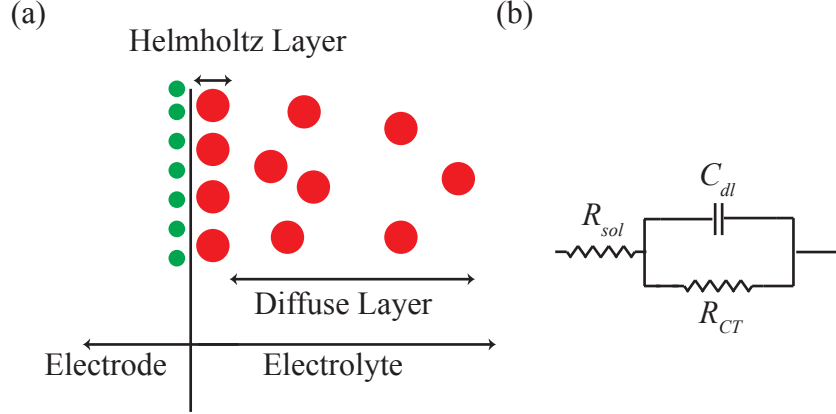


Figure 2-12: (a) Cartoon illustrating formation of a double-layer capacitance when an electrode is immersed in an electrolyte. Red and green dots represent oppositely charged particles. (b) Electrical model of an electrode.

charge form on the surface of the electrode (Helmholtz region). Furthermore, a diffuse layer forms due to the balance of electrostatic attraction of the species towards the electrode and diffusion of the species away from the electrode. The capacitance due to the Helmholtz region,  $C_H$ , is fixed for a given electrode and electrolyte but the capacitance due to the diffuse layer,  $C_G$ , varies depending on various factors such as potential, temperature and concentration since it depends on the balance between electrostatic attraction and diffusion.  $C_{dl}$  is the series combination of the capacitance due to both of these regions[96]:

$$C_{dl} = \frac{1}{C_H} + \frac{1}{C_G} = \frac{d_{OHP}}{\epsilon_0 \epsilon_r} + \frac{L_D}{\epsilon_0 \epsilon_r \cosh\left(\frac{z\phi_0}{2U_t}\right)} \quad (2.14)$$

where  $L_D$  is the Debye length given by

$$L_D = \sqrt{\frac{\epsilon_0 \epsilon_r U_t}{2n^0 z^2 q}} \quad (2.15)$$

where  $U_t$  is the thermal voltage,  $n^0$  is the bulk number concentration of ions in solution,  $z$  is the charge of the ion in the solution,  $q$  is the charge of an electron,  $\epsilon_0$  is the permittivity of free space,  $\epsilon_r$  is the relative permittivity,  $\phi_0$  is the applied voltage and  $d_{OHP}$  is the thickness of the Helmholtz region also known as the outer Helmholtz

plane. To account for the diffusion of charge, a Warburg impedance element is also often added in series with  $R_{CT}$  in the model of an electrode[96]. The model presented in Figure 2-12(b) is one of the simplest models, which does not take the diffusion of charge[97]. For the Pt electrodes used in this chapter, the  $R_{CT}$  component is negligible at the frequencies of interest ( $\sim 1$  kHz) and hence, both the Warburg impedance element and  $R_{CT}$  can be neglected.

The requirements of an electrode are dependent on the application. For single unit recordings, spatial specificity is important and can be achieved using an electrode with a small geometric or 2D area. However, this approach results in a smaller capacitance if all other design and process parameters are unchanged. Hence, to improve capacitance, the electrochemical surface area can be increased by increasing the roughness of the electrodes.

A comparison of various electrode materials[2] is reproduced in Table 2.8 that uses another model of an electrode:

$$C_w = \frac{B}{f^\beta} \quad (2.16)$$

where  $C_w$  is the Warburg capacitance,  $B$  and  $\beta$  are material dependent and  $f$  is the frequency of the applied current. The larger the value of  $B$ , the better is the electrode material. Many materials in [48] are not biocompatible, for example, copper and silver. Also, many of these metals like iridium and rhodium are rare, expensive and not commonly found in many cleanrooms. Furthermore, in [98], it is found that platinum has a lower impedance than gold for various electrode areas. Hence, based on these considerations, Pt is used as the electrode material for the recording electrodes used in this thesis. There is in general, a large variation of measured values of  $B$  and  $\beta$  as illustrated in the different values of stainless steel electrodes found in Table 2.8. The large Warburg capacitance of platinum black motivates use of techniques to roughen the electrodes such as electrodeposition. However, electrodes made using this method suffer from poor long-term adhesion[99].

For stimulation electrodes, charge injection is an important consideration. Safe injection limits are determined by two considerations: electrochemical limits and

Table 2.8: Warburg capacitance per unit area( $\mu\text{F}/\text{cm}^2$ ) of metals in contact with 0.9% saline (Reproduced from [2])

Metal type	Warburg Capacitance ( $\mu\text{F}/\text{cm}^2$ )
Platinum black heavy (PtB) (estimated)	$149,700f^{-0.366}$
Platinum-iridium black (PtIrB)	$8619f^{-0.299}$
Platinum black medium (PtB)	$4950f^{-0.366}$
Platinum-iridium (PtIr)	$2696f^{-0.79}$
Copper (Cu)	$3705f^{-0.518}$
Rhodium (Rh)	$112f^{-0.210}$
Silver (Ag)	$103f^{-0.259}$
Stainless steel (1) (SS)	$161f^{-0.525}$
Platinum (Pt)	$21.6f^{-0.143}$
Stainless steel (2) (SS)	$17.2f^{-0.266}$
MP35N (Ni Co Cr Mo)	$8.4f^{-0.127}$
Palladium (Pd)	$7.3f^{-0.113}$
Aluminum (Al)	$2.94f^{-0.126}$

tissue damage due to the applied current. Electrochemical limits are determined by the reactions that occur as the electrical potential of the electrode is increased. The charge that can be stored or injected within the electrical potential window where no irreversible reactions occur is then the reversible charge storage capacity or the reversible charge injection limit of the electrode. For Pt and  $\text{IrO}_2$ , this potential window is typically taken to be  $-0.6$  V to  $0.8$  V with respect to  $\text{Ag}|\text{AgCl}$  and is termed the water window. The  $\text{Ag}|\text{AgCl}$  electrode is a common reference electrode consisting of Ag in contact with AgCl that gives rise to a reversible redox reaction. The system maintains a potential of approximately  $0.230$  V at room temperature versus the standard hydrogen electrode (which is taken to be  $0$  V in electrochemistry) even at relatively high currents.

The difference between the charge storage and charge injection is determined by the charge utilization[100]. The charge storage capacity is measured at very slow rates using cyclic voltammetry so that all the reactions can be considered. Charge injection, on the other hand, is also determined by the stimulation protocol, which usually occurs at a rate that makes much of the charge inaccessible. The high current

density is also postulated to cause damage simply because of the passing of current through the tissue [48][101][102][103]. By summarizing data in [102], the authors of [101] found that an approximate limit where damage is observed is represented by:

$$\log D = k_{limit} - \log Q \quad (2.17)$$

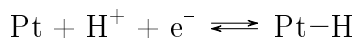
where  $D$  is the charge density in  $\mu\text{C}/\text{cm}^2/\text{phase}$  and  $Q$  is charge in  $\mu\text{C}/\text{phase}$  and  $k_{limit}$  is suggested to be 1.5 in [101] and 1.85 in [103]. If the parameters of the stimulation are such that  $k$  exceeds  $k_{limit}$ , damage is predicted. This indicates that damage is due to both amount of charge transferred and charge density. Substituting  $D = Q/A = It/A$ [101],

$$It = \sqrt{A \times 10^k} \quad (2.18)$$

where  $I$  is the current,  $t$  is the duration of each phase of a biphasic pulse, and  $A$  is the geometric surface area of the electrode. (2.18) can be used to determine the minimum area required given a charge required for stimulation.

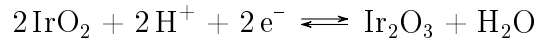
In addition, for microelectrodes with small surface areas (200-2000  $\mu\text{m}^2$ ) that are typically used in penetrating probes for spatially selective stimulation, damage occurs far below that predicted by (2.17) and that a charge per phase threshold of 4 nC/phase was observed for tissue damage [103].

Pt is also a commonly used stimulation electrode. Apart from charge transfer due to the double layer capacitance, Pt also has a pseudocapacity of 210  $\mu\text{C}/\text{cm}^2$  [48], which allows for larger charge transfer. Pseudocapacitance arises from chemical reactions at the electrode such that the products of the reaction remain bonded to the electrode surface, which makes the reaction reversible. This is unlike regular capacitance where the charged species does not participate in any chemical reaction. In the case of Pt electrodes, pseudocapacitance arises from hydrogen plating:



The H atoms remain bonded to the Pt, which makes the reaction reversible. If a higher charge density is desired, the roughness of the Pt electrodes can be increased or, more commonly, iridium oxide is used[104]. Depending on the stimulating conditions and

method of processing, charge injection capacities ranging from 1 to 9 mC/cm<sup>2</sup> [104] are possible. The faradaic reaction that allows for charge transfer in IrO<sub>2</sub> films is:



### 2.3.1 Processing of Pt electrodes for flexible neural probes

The most common way of etching parylene-C is oxygen plasma. In order to fabricate Pt electrodes on parylene-C based probes, the Pt is typically exposed by etching parylene-C on the electrode. This step also exposes the Pt to oxygen plasma, which may affect the surface properties of the electrode. Since the surface conducting property of Pt is essential, test structures are fabricated using the process steps described in Figure 2-13 to test the effects of oxygen plasma on the Pt electrodes. In order to eliminate conductive effects of the substrate during electrochemical measurements, the test structures were fabricated on a soda lime glass substrate instead of silicon.

The glass wafer is first dipped in A174 solution (1:100:100 A174:IPA:DI water by volume) for 30 min and air dried to improve adhesion of parylene-C to glass. A 2.2 μm thick layer of parylene-C is then deposited using a Labcoter 2 as shown in Figure 2-13(a). Following that, 127 nm of Pt is sputter deposited using a Perkin-Elmer 2400-6J system. The deposition occurs over patterned AZ5214E inversion resist. The resist is then lifted off in acetone with the application of ultrasonic vibration for approximately 2 h, leaving behind the patterned Pt as shown in Figure 2-13(b). Following an O<sub>2</sub> plasma descum step, a second 2.2 μm layer of parylene-C is then deposited. A 20 nm-thick Cr mask is sputter deposited using a Perkin Elmer 2400-8L and patterned using Transene Chromium Etchant 1020 as shown in as shown in Figure 2-13(c). The parylene-C is then etched for 40 min using a 50 W O<sub>2</sub>-RIE process in a Trion Phantom II RIE machine. Following the etch, the resist is stripped in acetone, an oxygen plasma descum is performed and the remaining Cr is removed using Transene Chromium Etchant 1020 as shown in as shown in Figure 2-13(d). The process of etching using O<sub>2</sub>-RIE leaves behind a PtO<sub>2</sub> film as shown in Figure 2-13(d). A protective resist is then spun on the wafer before it is diced. Following dicing, the

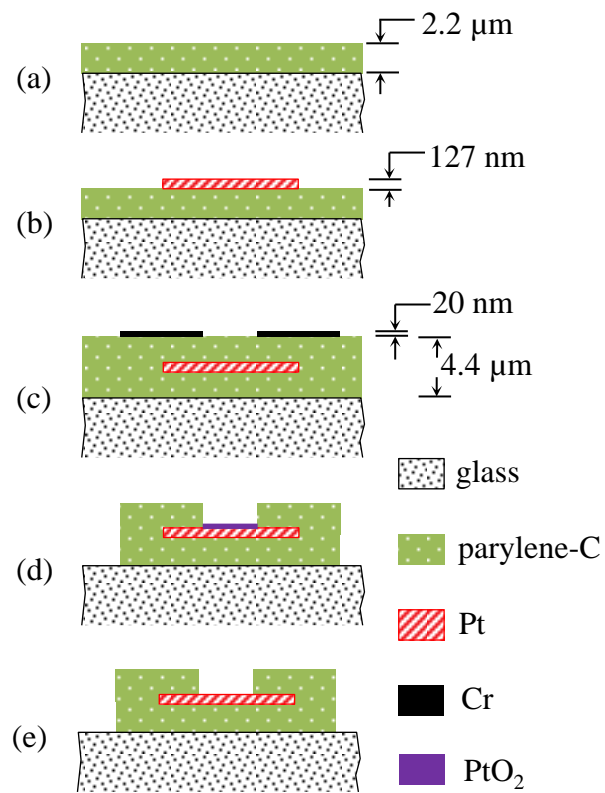


Figure 2-13: Process flow to fabricate test devices to investigate effect of processing on Pt electrodes.

resist is removed and the chip is annealed at 300°C in a 10 mT N<sub>2</sub> environment for 3 h. Annealing at 300°C is shown to improve the encapsulation properties of parylene-C-platinum sandwich structures [105]. A 1 min 50 W Ar<sup>+</sup> ion milling treatment using the Trion Phantom II RIE machine is performed on select devices before annealing to remove surface oxidation formed during the O<sub>2</sub> RIE as shown in Figure 2-13(e).

### 2.3.1.1 Surface chemistry test by XPS

X-ray photoelectron spectroscopy (XPS) is used to investigate the effect of the O<sub>2</sub>-RIE process on the surface chemistry of the electrodes. XPS is performed using an ESCALAB 250 XI Thermo Scientific XPS using a monochromated Al K- $\alpha$  source on the counter electrodes of chips that are treated with Ar<sup>+</sup> ion milling and on the counter electrodes of chips that did not have the additional Ar<sup>+</sup> step. The size of the counter electrode used is 5.2 mm by 11.6 mm, which is sufficiently large to perform XPS on. A charge compensating flood gun was activated in order to mitigate the effects of charging due to the insulating substrate.

Figure 2-14a shows the Pt 4f XPS performed on an electrode that is not treated with Ar<sup>+</sup> ion milling and Figure 2-14b shows the Pt 4f XPS performed on an electrode that is exposed to the Ar<sup>+</sup> treatment. The Pt 4f peaks are used to identify the various oxidation states of Pt. Based on the NIST XPS database [106], the Pt 4f peaks of pure Pt are 71.0 eV and 74.3 eV. In PtO<sub>2</sub>, the Pt 4f peaks are chemically shifted to 74.6 eV and 77.9 eV. The XPS of the Pt 4f electrode that has not been treated with Ar<sup>+</sup> show peaks corresponding to both PtO<sub>2</sub> and Pt, indicating that some, but not all, of the Pt within the sampling depth of the XPS is oxidized. Hence, it is likely that this surface layer of PtO<sub>2</sub> is less than the 3-10 nm sampling depth of XPS. For the sample that is etched with Ar<sup>+</sup>, the XPS indicates that only Pt metal remains. This indicates that the Ar<sup>+</sup> ion milling is a suitable method to remove the oxidized surface Pt.

In order to support the hypothesis that the formation of PtO<sub>2</sub> is due to the O<sub>2</sub> RIE, XPS is also performed on pieces of silicon with 2.2  $\mu$ m of parylene-C deposited followed by 127 nm of Pt. Some of the pieces are then exposed to 20 mins of O<sub>2</sub> RIE,

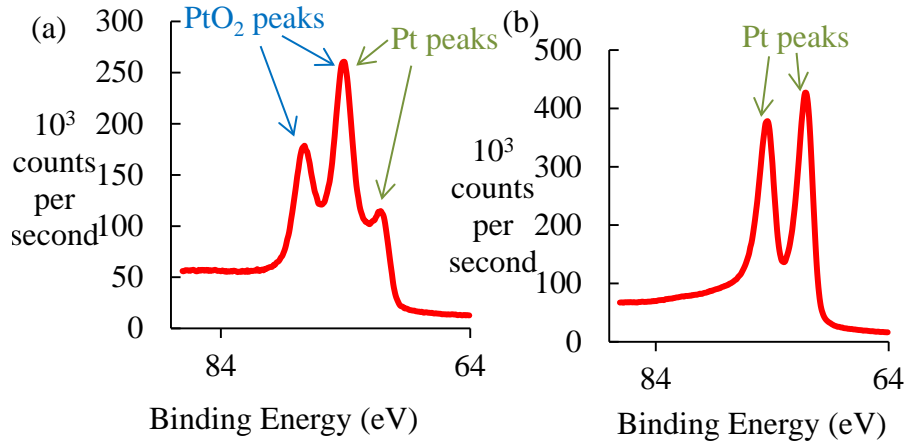


Figure 2-14: XPS results on Pt electrodes after O<sub>2</sub> RIE deinsulation process performed to remove parylene-C covering it (a) without Ar<sup>+</sup> etch and (b) with Ar<sup>+</sup> etch.

which is the estimated time that the Pt electrodes are exposed to during the parylene-C etch. The XPS performed on pieces that are exposed to O<sub>2</sub> RIE are similar to that of Figure 2-15a whereas XPS performed on pieces that were not exposed to O<sub>2</sub> RIE are similar to that of Figure 2-15b indicating that the layer of PtO<sub>2</sub> is formed due to the O<sub>2</sub> RIE.

### 2.3.1.2 Surface chemistry test by EIS

In order to test the effect of the oxide removal on the electrochemical properties of the electrode, electrochemical impedance spectroscopy (EIS) is performed on two 80 μm by 80 μm electrodes that are treated with Ar<sup>+</sup> ion milling and on two 80 μm by 80 μm electrodes that were not treated with Ar<sup>+</sup>. Anisotropic conductive film (ACF) is used to bond the pads on the fabricated devices onto a flat-flexible cable (FFC) using a Laurier M9A device bonder. Epoxy is then applied to the pad region of the chip in order to ensure insulation of that area. After the epoxy cured, the FFC is then attached to a PCB using a ZIF clip. The samples are inserted into room temperature phosphate buffered saline (PBS) in physiological concentration. Around 30 min after insertion in PBS, EIS is performed using 30 mV excitation voltage over a frequency range of 100 mHz to 100 kHz; this range includes the frequencies that are relevant to neural recordings (up to 1 kHz).

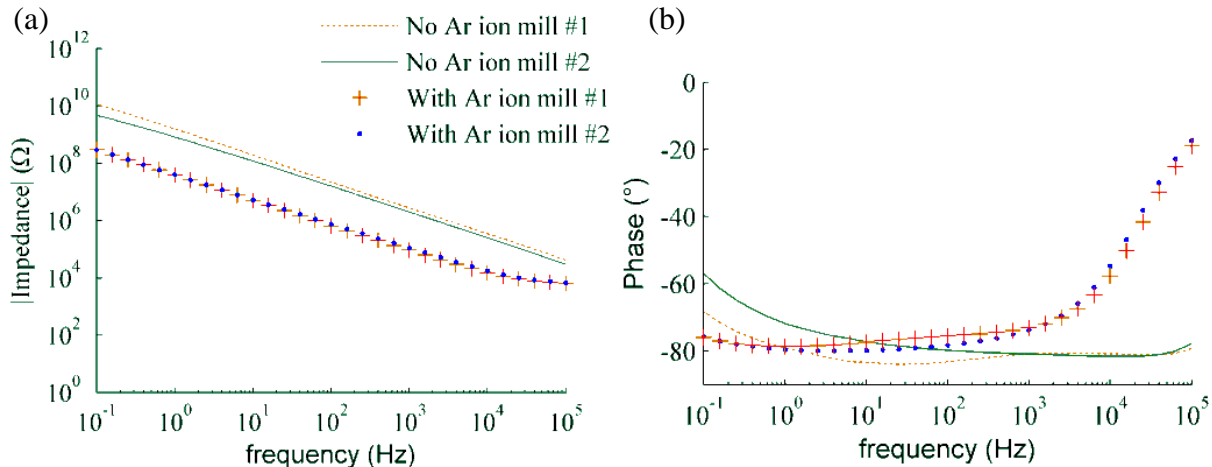


Figure 2-15: EIS result on 80  $\mu\text{m}$  by 80  $\mu\text{m}$  electrodes with and without  $\text{Ar}^+$  etch. (a) Magnitude of measured impedance and (b) phase of measured impedance. Sample numbers are indicated in the legend. EIS is performed by Mats Forssell.

Figure 2-15 shows Bode plots for the EIS performed on four samples. Two samples are treated with  $\text{Ar}^+$  ion milling and two samples are not. The samples without  $\text{Ar}^+$  ion milling have significantly larger impedance, over the entire range of frequency measured, compared to the samples that are etched. The impedance after ion milling is roughly an order of magnitude smaller. All the samples have mostly pseudo-capacitive behavior over the majority of the frequency range, as evidenced by the constant phase around  $-80^\circ$ . For a  $6400 \mu\text{m}^2$  Pt electrode, the double-layer capacitance is expected to dominate the impedance in this frequency range. In the higher frequency range, the contribution of the saline resistance starts being noticeable for the sample that underwent ion milling (with the phase increasing to  $0^\circ$ ); this effect is not a result of the etching, but simply a consequence of the lower overall electrode impedance.

Using a common value for the double-layer capacitance of Pt of  $0.5 \text{ F/m}^2$  derived using the Gouy-Chapman-Stern model (2.14)[96], the expected value for the capacitance of this electrode is  $C_{dl}, \approx 3.2 \text{ nF}$ . This translates into an impedance magnitude at 1 kHz of  $Z_{1k} \approx 50 \text{ k}\Omega$ . The measured impedance magnitude at 1 kHz for the electrodes without etching is  $Z_{1k} \approx 2.3 \text{ M}\Omega$ , around 50 times the expected value.

The sample that had undergone  $\text{Ar}^+$  ion milling has  $Z_{1k} \approx 100 \text{ k}\Omega$ . This is close to the calculated value that neglects all other contributions to the impedance. The impedance of the non-etched sample corresponds to a capacitance of  $C \approx 70 \text{ pF}$ . This would be equivalent to the capacitance created by a 3 nm layer of  $\text{PtO}_2$ . This value is consistent with the XPS observation of both Pt and  $\text{PtO}_2$  in the sampling depth of samples without additional  $\text{Ar}^+$  treatment.

The surface morphology of an electrode is also measured using a Park XE-70 AFM over a  $6 \text{ }\mu\text{m}$  by  $20 \text{ }\mu\text{m}$  scan region. The AFM surface profile in Figure 2-16(a) shows that the surface of the electrode is roughened considerably by the  $\text{O}_2$  RIE. The measured surface roughness  $R_a$  from the AFM measurement on a sample that has not undergone  $\text{Ar}^+$  ion milling is 12.3 nm. After  $\text{Ar}^+$  ion milling, the measured  $R_a$  is 13.1 nm. Most of the difference in impedance seen in the EIS in Section 2.3.1.2 is due to the removal of surface  $\text{PtO}_2$  as the  $\text{Ar}^+$  ion milling increases the surface roughness by less than 10%.

A surface roughness value of 3.4 nm is obtained with the AFM measurement of Pt as-deposited on parylene-C coated silicon as shown in Figure 2-17. The very low roughness of the starting Pt surface indicates that the increased roughening occurs due to the  $\text{O}_2$  RIE step.

### 2.3.2 Processing of $\text{IrO}_2$ electrodes for flexible neural probes

$\text{IrO}_2$  is deposited by sputtering at 100 W using a custom built reactive sputtering system at different pressures while keeping the ratio of Ar:O constant at 3.33 based on process parameters in [107] where 40 sccm Ar and 12 sccm  $\text{O}_2$  flow is found to be optimum. At high pressures (14.5 mT), the film deposited is non-uniform as shown in Figure 2-18(a). This thickness non-uniformity is likely due to the non-uniform gas distribution in the system. Using a profilometer scan, the thickness of the film varies from 100 nm at the wafer edges to  $1 \text{ }\mu\text{m}$  at the center. In contrast, a lower pressure of 6.95 mT results in a more uniform film as shown in Figure 2-18(b), with the trade-off of a lower deposition rate. For this wafer, the thickness varies from 100 nm at the wafer edges to 200 nm at the center.

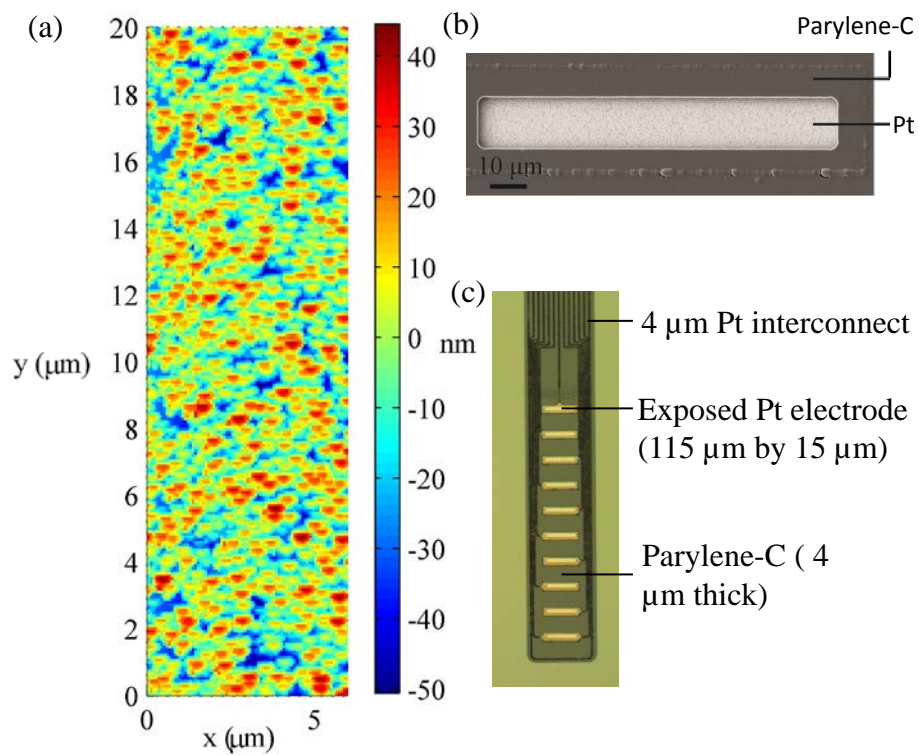


Figure 2-16: (a) Surface morphology of a Pt electrode using AFM over a 6 μm by 20 μm scan region, (b) SEM of a Pt electrode, (c) Optical microscope showing exposed Pt electrodes.

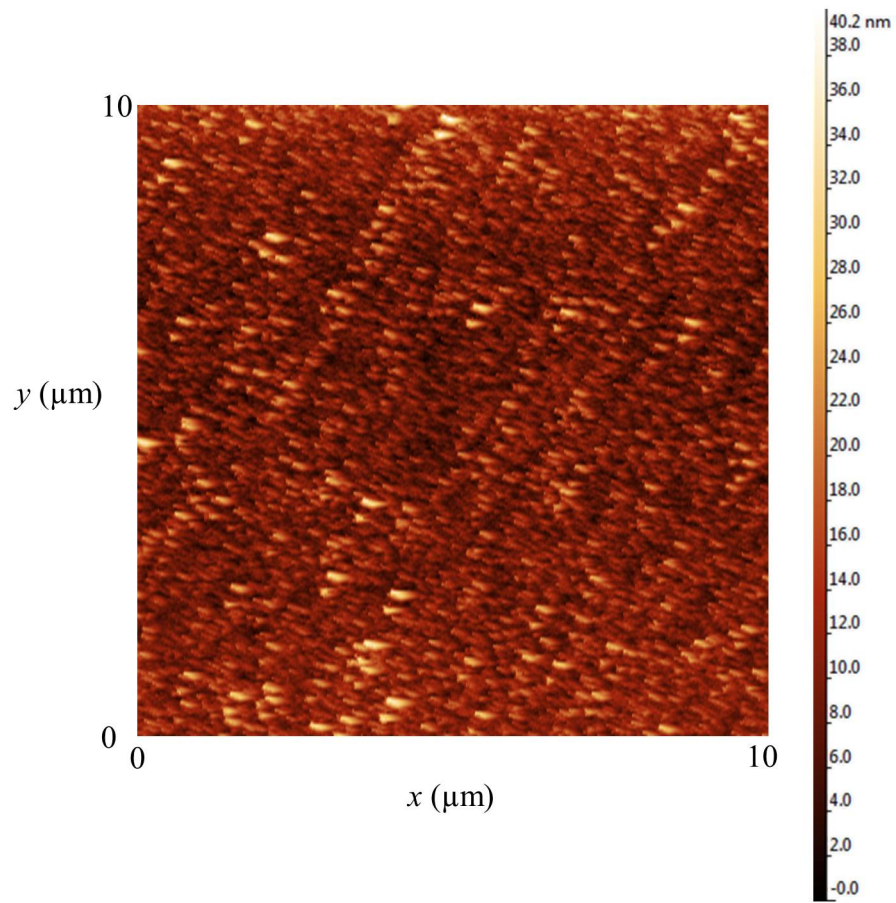


Figure 2-17: Surface morphology of Pt coated on parylene-C using AFM over a  $10\ \mu\text{m}$  by  $10\ \mu\text{m}$  scan region

In addition, the stoichiometry of the films is characterized using EDX as shown in Figure 2-19. The measured O:Ir ratio is 1.76 at the sides and 1.64 at the center for the film deposited at 100 W DC, 14.5 mT. For the film deposited at 100 W RF at 6.95 mT, the measured O:Ir is 2.1.

Using the developed IrO<sub>2</sub> process parameters, test structures are fabricated on a test device. The fabrication of the test devices emulates the steps of the fabrication of protruding electrodes on Si, with the top conductive layer being 250 nm of IrO<sub>2</sub>. A fabricated test electrode is shown in Figure 2-20.

Following fabrication of the test electrode, the IrO<sub>2</sub> is activated by performing repeated cyclic voltammetry (CV) scans from  $-0.6$  V to  $0.8$  V at  $0.1$  V/s, which improves the charge storage capacity of the film. The effect of the IrO<sub>2</sub> activation by CV activation on the cathodic charge storage capacity is shown in Figure 2-21. The number of CV activation cycles before a stable CV is obtained is also similar to the typical value of 193 cycles in [104]. The obtained CSC after the CV is stable is approximately  $64$  mC/cm<sup>2</sup> for  $25$  by  $25$   $\mu\text{m}^2$  electrodes,  $20$  mC/cm<sup>2</sup> for  $50$  by  $50$   $\mu\text{m}^2$  electrodes,  $8$  mC/cm<sup>2</sup> for  $100$  by  $100$   $\mu\text{m}^2$  electrodes and  $3.5$  mC/cm<sup>2</sup> for  $200$  by  $200$   $\mu\text{m}^2$  electrodes. The values are slightly lower than the reported values of  $78$  mC/cm<sup>2</sup> for  $50$   $\mu\text{m}$  diameter electrodes[104] for electrodes with a similar thickness of IrO<sub>2</sub> ( $240$  nm). From the figure, it is seen that the larger electrodes require a longer time to activate.

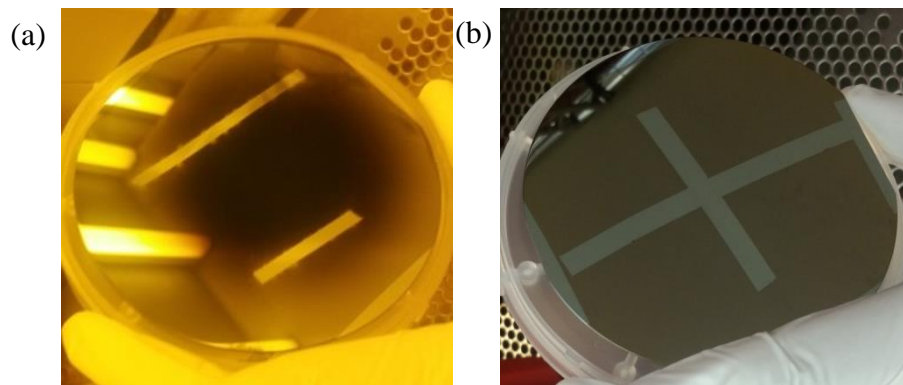


Figure 2-18: Observed non-uniformity in deposited film with pressure during deposition. Thicknesses were measured using a profilometer. (a) Wafer with  $\text{IrO}_2$  deposited at 14.5 mT. (b) Wafer with  $\text{IrO}_2$  deposited at 6.95 mT.

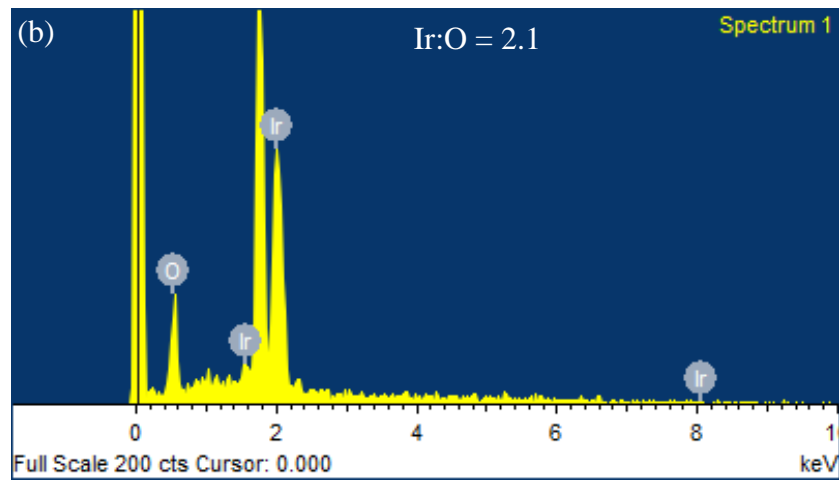
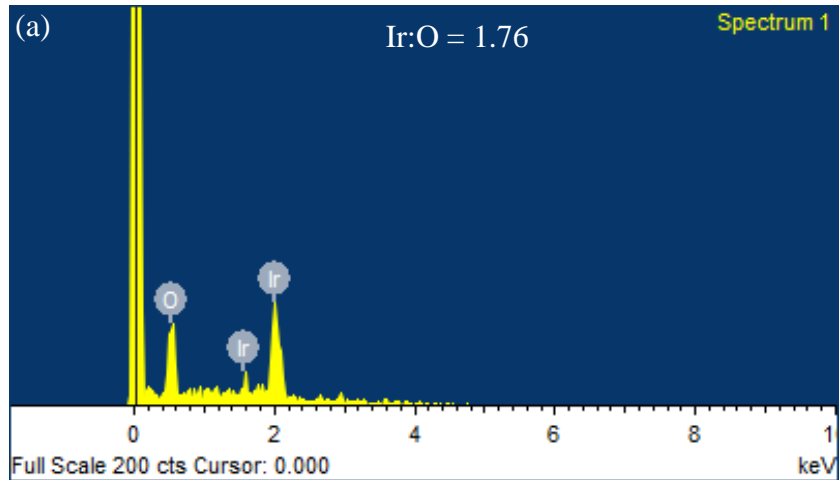


Figure 2-19: EDX performed on (a) film deposited at 14.5 mT, 100 W DC and (b) film deposited at 6.95 mT, 100 W RF to determine stoichiometry of oxygen to iridium in deposited film.

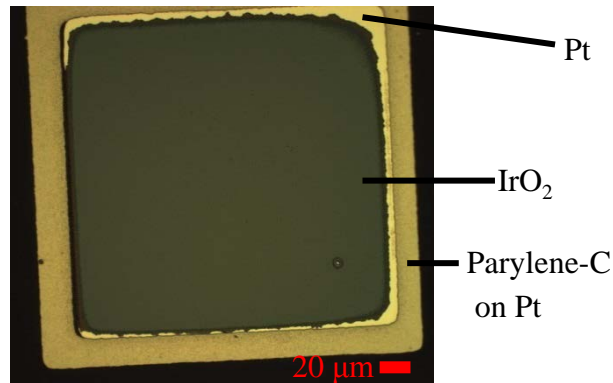


Figure 2-20: 200  $\mu\text{m}$  by 200  $\mu\text{m}$  test electrode fabricated on glass to test charge injection capacity.

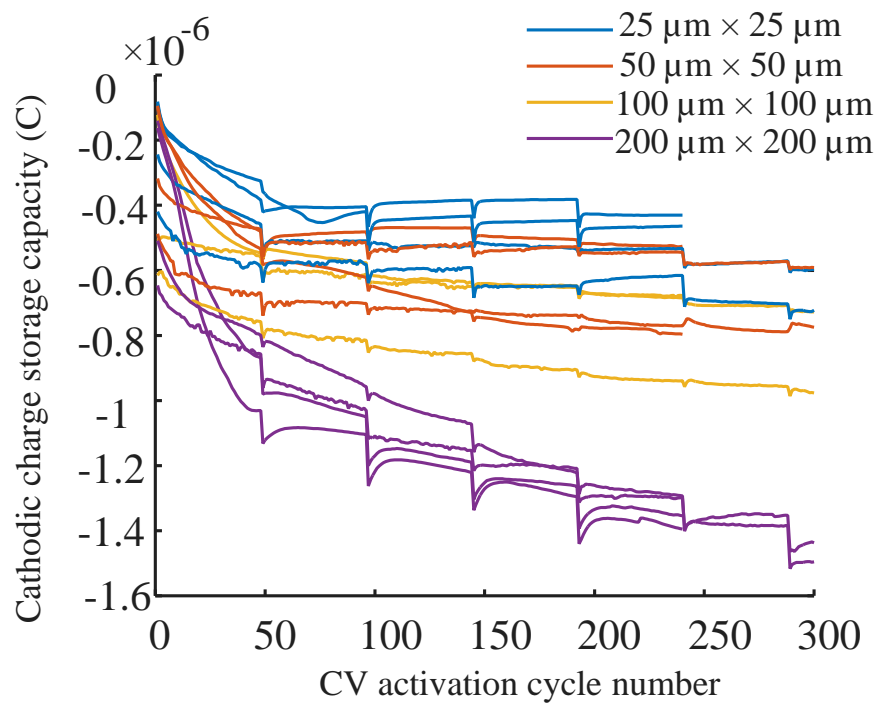


Figure 2-21: Evolution of the charge storage capacity of the  $\text{IrO}_2$  electrodes during the CV activation. The periodic dips in the activation are artifacts of the CV measurement and do not indicate a change in the charge storage capacity. CV test is performed by Mats Forssell.

## 2.4 Summary

In this chapter, details about fabrication of the various components of a neural probe is presented. Parylene-C is chosen as the insulating material given its high resistivity, biocompatibility and flexibility. Pt is chosen as the recording electrode material based on cost and relatively high double-layer capacitance for recording electrodes. IrO<sub>2</sub> is chosen as the stimulating electrode material based on high charge transfer capacity. The O<sub>2</sub> RIE processing on Pt electrodes is also found to oxidize the surface of Pt electrodes but this oxidation can be removed using Ar<sup>+</sup> ion etching.

In addition, a peelable process is presented in this chapter. The adhesion of parylene-C to Si is evaluated using various HMDS treatments in order to fabricate these structures successfully. In the next chapter, a transfer process is presented. The transfer process is a more expensive and complicated process. However, it improves upon the peelable process by allowing for a wider range of processes such as thermal annealing, which increases the adhesion between parylene-C and Si and makes the peeling process unfeasible.

# Chapter 3

## A transfer process to fabricate probes strongly-adhered to silicon substrates

### 3.1 Introduction

Peelable processes, such as the process discussed in Chapter 2, provide a means of introducing unconventional materials because the release step, i.e., peeling, does not require harsh chemicals that can damage the material. However, the nature of peeling requires that careful control of adhesion is required. This imposes restrictions on the process flow. For example, thermal annealing of parylene-C on Si beyond the melting point of parylene-C increases the adhesion between parylene-C to Si.

In this chapter, a transfer process is used to integrate biodissolvable carboxymethyl-cellulose-glucose (CMC-glucose) needles with parylene-C probes fabricated using conventional MEMS processes. The fabrication of parylene-C probes on Si is discussed in Section 3.2. This is achieved by first transferring the parylene-C probes onto a sacrificial wax (BGL7080) that is dissovable in isopropyl alcohol as discussed in Section 3.3. Isopropyl alcohol is compatible with CMC-glucose as discussed in Section 3.6. Transfer onto other sacrificial materials is discussed in Section 3.5.

Following transfer of parylene-C probes onto BGL7080, two methods of integrating biodissolvable needles with the probe is attempted. The first method involves molding the needle directly onto the transferred probe as discussed in Section 3.4. The second

method involves bonding premolded needles onto the transferred probe as discussed in Section 3.8. As discussed in Section 3.7 and Section 3.8, the stress induced by directly molding the needles on the probe degrades the insulation performance of the parylene-C probes. Bonding premolded needles onto the transferred parylene-C probes alleviates this issue.

### **3.1.1 Embedding ultra-compliant probes in a biodissolvable needle**

Ultra-compliant neural probes lower the mechanical mismatch between brain tissue and the probe while stiffness of a probe is necessary for successful insertion of a probe. Embedding the probe directly in a needle [108][67][41] is among several approaches for fabricating ultra-compliant neural probes discussed in Chapter 2. However, that approach requires application of a peeling process to release the probe-needle assembly from its handle wafer. As seen from Chapter 2, the adhesion between parylene-C and Si varies significantly which can result in low yield. Too low of an adhesion results in failures while patterning the features and too high of an adhesion results in failures while peeling. Furthermore, the peeling process is restrictive as it imposes a thermal budget: the use of thermal annealing in vacuum at 300°C to improve encapsulation properties of parylene-C results in increased adhesion to the substrate that undermines the peeling process [109]. Imposing a temperature limit, in particular, is detrimental for processing since thermal annealing of parylene-C in vacuum at temperatures up to 300°C significantly improves its electrical and mechanical encapsulation properties [105]. Current processes typically circumvent this adhesion problem by the use of a release layer where 5 µm of deposited SiO<sub>2</sub> sacrificial oxide is released in buffered hydrofluoric acid for 3 h [110] or by releasing the structure prior to the heating step where the heating step is used to thermoform parylene-C to create 3D structures [111]. However, it is typically difficult to handle released structures manually if they are below 25 µm in thickness, which has in practice constrained the lower limit of the mechanical compliance of the neural probe processed

using such methods. Embedding an ultra-compliant neural probe in a stiff biodissolvable needle before release is one way of solving this problem, provided that a suitable release material that is compatible with the dissolvable nature of the needle is identified. The biodissolvable needle material considered in this work is a blend of carboxymethyl cellulose (CMC) and glucose (15% glucose by weight); however, the outlined approach should be valid for other biodissolvable blends of CMC and sugars since they are expected to have similarly adhesion and thermal properties. Owing to the dissolvable property of the needle, the needle material is difficult to integrate with typical process flows which involve cleaning with water and the use of various acids and developers that are water based.

### **3.1.2 Bonding ultra-compliant probes on a biodissolvable needle**

Embedding ultra-compliant probes in biodissolvable needles involves molding of the biodissolvable needle onto the probe. This process involves the evaporation of solvent from the needle material, which can introduce stress onto the probe. Given the relative thickness of the needle relative to the probe, the stress can be significant enough to damage the probe. In order to alleviate this, another process is developed involving the bonding of prefabricated needles onto the ultra-compliant probe. A release process is required for release of the assembly, however, the processing of the probe is separate from the processing of the needle. This also allows for improved yield.

A process step to transfer the probe from its silicon handle wafer onto a second handle substrate with adhesive is a way of introducing release materials and unconventional substrates and materials that would have otherwise not been compatible with the probe process flow of embedding the probe in a needle. Transfer printing has been demonstrated to be an effective way of increasing process versatility [112] but typically involves structures that are weakly adhered to the substrate since it requires breaking the interfacial bonds between the substrate and the structure. For exam-

ple, the transfer of nanowires has been demonstrated to thermal release tapes and to Post-it<sup>®</sup> Notes among other unconventional substrates [113]. The typical transfer processes rely on differential adhesion between a carrier and the donor substrate and the carrier and the receiver substrate. Differential adhesion can be achieved, for example, by using polydimethylsiloxane (PDMS) as the carrier and using different peel velocities when peeling away from the receiver and the donor substrates [114]. The viscoelastic properties of PDMS result in a rate varying adhesion force. Another way of achieving differential adhesion is to rely on the difference in bonding strength between the donor substrate and the structure to be transferred and the receiver substrate and the structure to be transferred [115].

This chapter describes a transfer process step that eliminates the peeling process and allows the potential use of a wide range of sacrificial release materials[116]. The transfer step increases the versatility of the overall fabrication approach since it allows the integration of insertion needle and sacrificial release materials that otherwise would not have been compatible with the high-temperature annealing. Several sacrificial release materials, including photoresist, polydimethylsiloxane, mounting adhesive, and liquid wax, are investigated and characterized for suitability in the transfer process. The materials are employed in a sacrificial release layer that is subsequently chemically etched, eliminating the need for mechanical removal (i.e., peeling) of parylene-C from the donor substrate. Considering compatibility with the biodissolvable needle attachment, a liquid wax is identified to be an effective material because of its strong adhesion to relevant surfaces, its ability to be spin coated, and its dissolvability in isopropyl alcohol. The main difference between the transfer process developed in this chapter and the aforementioned transfer processes is that the structures in this chapter prior to fabrication are strongly adhered to the donor substrate. In particular, applying the peeling process to the structures used in this chapter results in breakage of the probes.

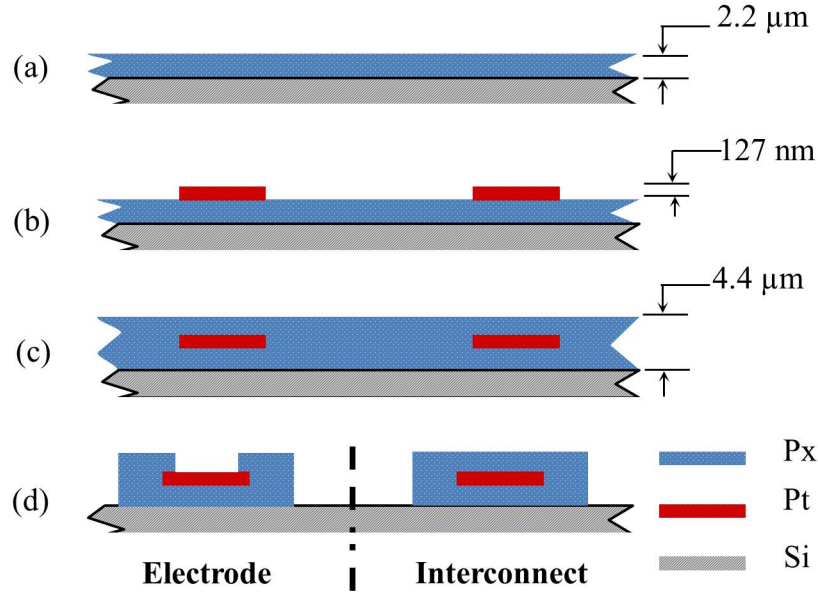


Figure 3-1: Neural probe fabrication process. (a) Deposition of parylene-C (Px) on a Si wafer. (b) Pt is patterned using lift-off. (c) A second layer of Px is deposited (d) Parylene-C RIE.

### 3.2 Fabrication of Parylene-C probes on Si substrate

The basic fabrication process of parylene-C probes with  $115\ \mu\text{m}$  by  $15\ \mu\text{m}$  electrodes and  $\sim 2\ \text{cm}$  long cables integrated into the design of the probe is illustrated in Figure 3-1. The cable is an integral part of the probe itself and is fabricated on the silicon and transferred onto the adhesive spun on the glass substrate. This particular electrode size is selected to realize a probe for recording and stimulation from peripheral nerves, such as the sciatic nerve of a cat. The electrode size has been demonstrated to successfully acquire single-unit activity in silicon probes in the substantia nigra region of the brain [117]. Briefly, a  $2.2\ \mu\text{m}$ -thick layer of parylene-C is deposited by chemical vapor deposition onto a  $250\ \mu\text{m}$  thick,  $10\ \text{cm}$  diameter Si substrate that has been treated with adhesion promoter as shown in Figure 3-1(a). The Si substrate used is thinner compared to typical  $525\ \mu\text{m}$ -thick wafers in order to reduce the silicon etch time required during the transfer processes described in Section 3.3. A  $127\ \text{nm}$ -thick film of Pt is patterned using lift-off as shown in Figure 3-1(b). No adhesion layer is used between Pt and parylene-C because Pt has better adhesion than conventional

adhesion layers (Ti/Cr)[118]. Following this, a second 2.2  $\mu\text{m}$ -thick layer of parylene-C is deposited as shown in Figure 3-1c. A nominally 20 nm-thick layer of Cr is then deposited as a hard mask and patterned. The parylene-C is then etched and any remaining resist and Cr mask is removed. The resultant structure is shown in Figure 3-1d. The wafer is then diced into chips.

Figure 3-2 shows optical images of a fabricated probe on Si. A 1 min  $\text{Ar}^+$  mill is performed to remove  $\text{PtO}_2$  formed on the electrodes during the etching of parylene-C using  $\text{O}_2$  RIE. The presence of the  $\text{PtO}_2$  is detrimental to electrode performance [119]. The dice are then heated to  $300^\circ\text{C}$  in a custom built vacuum heater with a flow of  $\text{N}_2$  to achieve a pressure of 10 mT in order to improve the encapsulation properties of parylene-C [105]. The annealing also increases the adhesion between parylene-C and Si [109].

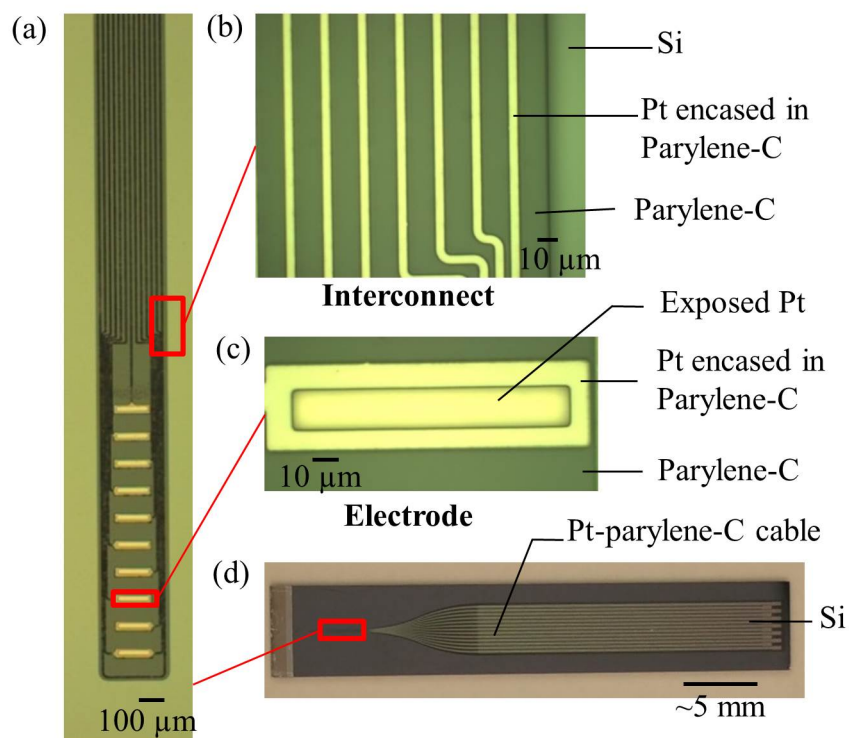


Figure 3-2: (a) Optical microscope image of the needle region of a fabricated probe. (b) Zoomed-in optical image of the interconnect region. (c) Zoomed-in optical image of the electrode region. (d) A fabricated chip

### 3.3 Transfer of Strongly Adhered Structures

In order to overcome the increased adhesion between parylene-C and Si, a variation of the transfer process is developed where the parylene-C and Pt device is first transferred onto an adhesive that also acts as a sacrificial layer. The transfer process is described in Figure 3-3. An adhesive is spin coated onto a glass wafer as shown in Figure 3-3a. The spin speed and any thermal or vacuum treatments post-spinning are adhesive dependent and will be described, along with the bonding process details, in Section 3.5. The diced chip is flipped and pressed onto the adhesive coated glass as shown in Figure 3-3b using a M9A flip-chip device bonder (Besi, The Netherlands). For some of the adhesives, heat is applied during the bonding process in order to make the adhesive flow. The applied pressure and time is selected such that the adhesive completely encases the device. For adhesives that require reflow, the temperature is set to above the glass transition temperature of the adhesive. The Si is then etched using 100 W SF<sub>6</sub> RIE for 90 min followed by 80 cycles of XeF<sub>2</sub> in a Xactix Xetch System (SPTS, Newport, UK) at 2.8 Torr to completely etch the Si as shown in Figure 3-3c. The two-step etch process is used because the SF<sub>6</sub> RIE etches the Si faster but can physically etch the parylene-C whereas the XeF<sub>2</sub> etch is completely chemical in nature and hence does not damage the parylene-C. The two-step process avoids any exposure of the parylene-C to the SF<sub>6</sub> RIE. An optional undercut can be produced by dipping the assembly in a wet etchant for a short time as shown in Figure 3-3d.

The probe can be released fully using an appropriate wet etchant at this point or can be integrated with a molding process to incorporate the probes in biodissolvable needles before being released depending on the application. For example, releasing the structures fully at this point will be useful to fabricate ECoG arrays [120] and incorporating probes in biodissolvable needles will be useful to fabricate implantable neural probes. For the application involving the assembly of a biodissolvable needle onto a probe, the undercut can aid in ensuring that the probe remains adhered to the needle. In this chapter, the assembly is achieved through a needle molding pro-

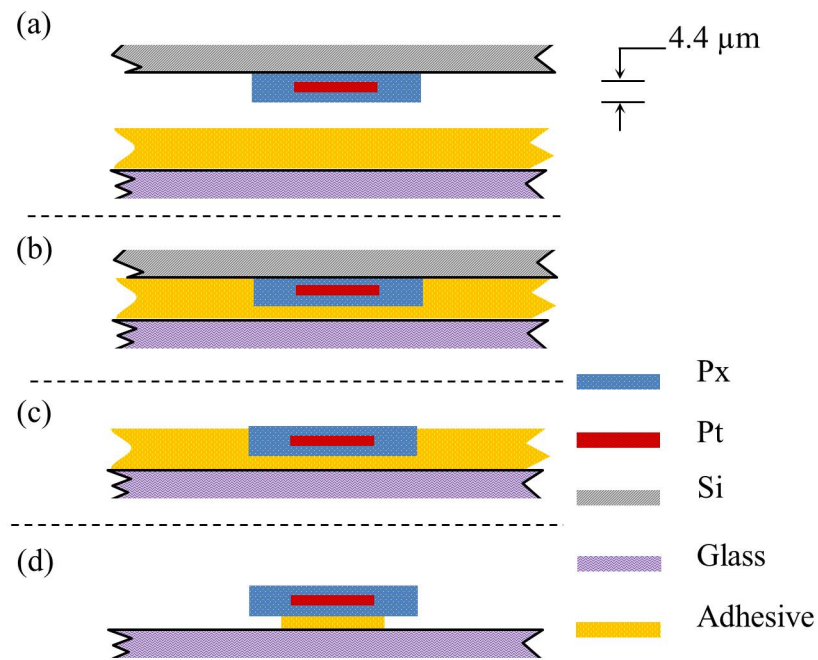


Figure 3-3: Transfer process. (a) Adhesive is spin coated on glass receiving substrate. (b) After pressing the substrates together, the combined donor Si substrate and receiving substrate are heated. Pressure is applied. (c) Donor Si substrate is removed by RIE followed by XeF<sub>2</sub>. (d) Adhesive is partially etched to produce an undercut is performed for some processes.

cess that is performed on the transferred probes. Incorporating the molding process introduces material limitations because aqueous solutions are not compatible with the needle. Thus, this application of the transfer process demonstrates the ability to circumvent material compatibility issues in processing by effectively isolating the new materials introduced after the transfer from incompatible release steps. The molding steps will be described in more detail in Section 3.4.

### 3.4 Molding

One way of integrating the CMC-glucose needle to an ultra-compliant probe is to mold the needle onto the probe. The CMC-glucose molded structure includes a handling tab so that the ultra-compliant probes can be more easily manipulated by hand during the insertion procedure [41]. The molding process is developed by Rakesh Khilwani of Prof. Burak Ozdoganlar's Group.

The molding procedure is performed after removing the Si and completing the transfer process, and is illustrated in Figure 3-4. A top mold with the shape of the needle is made out of a UV curable polyurethane-based material NOA-63 (Norland Products, Cranbury, NJ), as described in [41]. Briefly, the resin is poured onto a machined poly(methyl methacrylate) (PMMA) inverted mold that is fabricated by micromilling. The resin is then sandwiched between a glass slide and the PMMA mold and pressed to squeeze out the excess resin. The sandwich assembly is cured under UV light (365 nm) for 6 min. As a result of this sandwich molding process, the cured resin has through structures identical to that of the final needle geometry.

Subsequently, using the M9A device bonder, the polyurethane-based mold is aligned to the transferred probe, and the mold and the probe are pressed together under 17 N load ( Figure 3-4a). 500 mg of 15% (wt/wt %) solution of 85 CMC:15 glucose is then dispensed onto the assembled mold and a spin-casting process is used to form the insertion needles [41][121]. The filled mold is centrifuged at speed of 3000 rpm for 16 h at 15°C (Thermo Scientific, Heraeus Multifuge X3R) to densify and dry the CMC-glucose mixture. Excess CMC-glucose is removed by adding trace

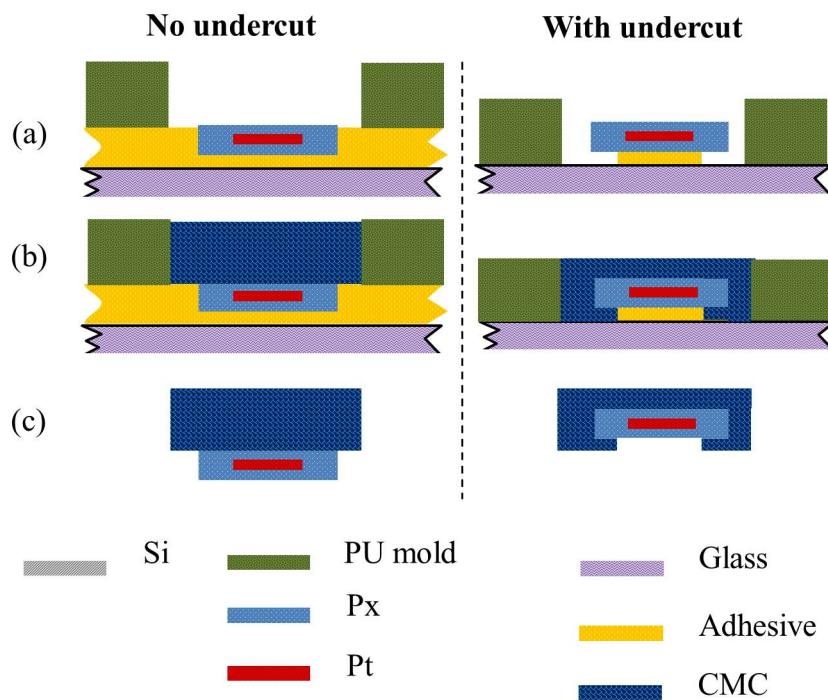


Figure 3-4: Molding process flow. (a) A top mold is mounted onto the transferred device. (b) CMC-glucose solution is applied and the device is centrifuged. (c) The molded device is released in isopropyl alcohol.

amounts of water using a brush and using a sharp blade until the needle and the handling tab are exposed. The additional moisture introduced in the previous step is removed using the centrifuge under the same conditions for 30 min. The device is then placed in an appropriate solvent in order to release the probes embedded in CMC-glucose.

### 3.5 Adhesives for the transfer process

As in the case of transfer of structures weakly adhered to the substrate[114] which rely on viscoelastic properties of the adhesive, the choice of adhesive is key for the transfer process for the case of devices strongly adhered on Si. Four different adhesives are investigated in this chapter (PDMS, photoresist and two thermoplastic adhesives). This covers a wide range of adhesives that can be spin-coated. Test loops, as can be seen in Figure 3-5(b), are incorporated into the design to test for interconnect functionality. This is used as an indication of success of the transfer process.

Photoresist (AZP4620), Sylgard 184 PDMS (Dow Corning, Auburn, MI), BGL7080 liquid wax (AI Technologies, Princeton Junction, NJ) and Crystal Bond 509 mounting adhesive (SPI Supplies, West Chester, PA) are investigated as suitable adhesives for use on the receiving substrate. The transfer process involves adhesives that can conform to the shape of the structure in a fluid phase and set to become a solid for subsequent processing. However, there are a number of different mechanisms for this phase change. AZP4620 can be solidified by removal of solvent during a soft bake step in order to set the photoresist as is typically performed during photolithography. AZP4620 also reflows at high temperatures [122], as used, for example in the fabrication of microlens arrays when the reflowed resist forms plano-convex structures [123]. On the other hand, a mixture of PDMS precursors change from a liquid phase to a solid phase as it cures thermally to form PDMS. Crystal Bond 509, a mixture of phthalic anhydride and ethylene glycol is purchased in solid form [124]. BGL7080 is a film forming wax that is purchased dissolved in isopropyl alcohol (IPA) [124]. Both Crystal Bond 509 and BGL7080 are thermoplastic polymers. Hence, they can

be reversibly converted into a fluidic phase by raising their temperatures beyond their respective glass transition temperatures. Details of the four transfer approaches are given to inspire future potential spin-off activities. Ultimately, for the application of integrating biodissolvable CMC-glucose needles with parylene-C/Pt probes, the BGL7080 liquid wax approach satisfied all process flow requirements.

### 3.5.1 PDMS (Sylgard 184)

PDMS is a polymer that is popular with transfer processes because of its viscoelastic properties [114] and for microfluidics because it is easily molded [125]. The relationship between spin speed and PDMS has been characterized in [126]. Sylgard 184 base and precursor is combined in a 10:1 ratio using a paint mixer (Badger Air-Brush, Franklin Park, IL). The mixture is then degassed for 30 min in vacuum and spun on a glass slide at 3000 rpm for 1 min creating a 26  $\mu\text{m}$  thick film. The Si chip is then pressed at 40 N onto the PDMS coated glass slide using the M9A device bonder. The bonded chips are then left at room temperature for 48 h to allow the PDMS to cure as recommended by the manufacturer. Although bonding of cured PDMS onto glass using  $\text{O}_2$  plasma to activate the PDMS has been widely demonstrated [127], the PDMS is left uncured while the device is being pressed onto it in order to take advantage of the larger adhesion of uncured PDMS to glass and Si [128] and the fluidic nature of uncured PDMS that allows the PDMS to fill any crevices.

After the PDMS is cured, the Si substrate is removed using a  $\text{SF}_6$  RIE followed by a  $\text{XeF}_2$  etch as described in Section 3.3. Using this method leads to successful transfer of the parylene-C/Pt neural probe onto the PDMS coated glass as seen in Figure 3-5(a) and Figure 3-5(b). Following the molding process, immersing the bonded device into Dynasolve 220 (Dynaloy, Indianapolis, IN), a reactive solvent that dissolves PDMS, for 48 h releases the device. Microscope images of a released probe embedded in a CMC-glucose needle processed using this method is shown in Figure 3-5(c). Although the process results in fabricated probes, it is found using dissolution studies and FTIR that the use of Dynasolve 220 resulted in chemical changes to the CMC-glucose that affected its dissolution rate. The result of this study is described in Section 3.6.

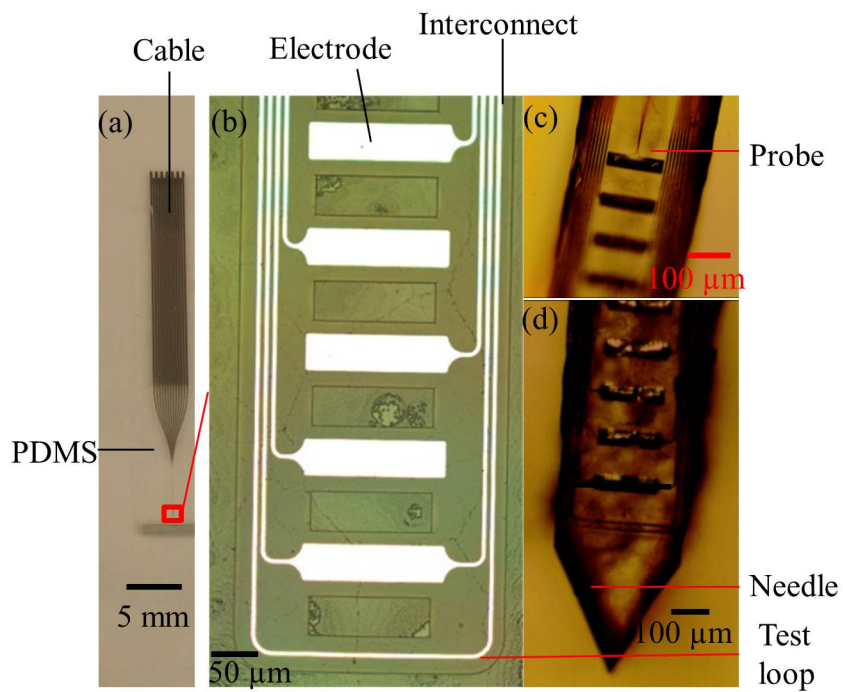


Figure 3-5: (a) Optical image of a probe transferred onto PDMS coated glass. (b) Microscope image of needle portion of probe transferred onto PDMS coated glass. (c-d) Images of dissolvable needles molded over probes and released using Dynasolve 220.

### 3.5.2 Photoresist (AZ4620)

Photoresists are typically synthesized with adhesion and ease of removal in mind and so are alternative candidates for the receiver substrate adhesive. AZP4620 is selected because it can be spun into thick films more than 10  $\mu\text{m}$  and is easily stripped using acetone. The spin curve of AZP4620 has been characterized by the manufacturer [129].

One way of inducing a phase change is to remove the propylene glycol methyl ether acetate (PGMEA) solvent by baking. This process is carried out by first spin coating the resist at 2000 rpm on a glass slide for 1 min, giving a film thickness of about 10  $\mu\text{m}$ , and then pressing the chip onto the resist coated glass. However, this results in bubble formation when the sandwiched device is placed in vacuum or when the sandwiched device is heated at 90°C. Performing a 90°C bake in a convection oven for 1 h after spinning the resist at 2000 rpm on the other hand results in the photoresist losing its tackiness and providing insufficient adhesion to survive the process.

Another way of introducing a phase change is to reflow the resist by increasing the temperature of the resist beyond its reflow temperature during the bonding process. This process is carried out by first spin coating the resist at 2000 rpm on a glass slide for 1 min giving a film thickness of 10  $\mu\text{m}$ . In order to prevent bubble formation, a bake at 130°C for 30 min, i.e., at the temperature at which the reflow is performed, removes most of the solvent. Baking at 90°C for 1 h instead of 130°C is insufficient to prevent bubble formation during the reflow process as shown in Figure 3-6b where significant bubble formation occurs. This is likely due to residual solvent present even after the baking process [130].

Although there will still be some residual solvent after baking at 130°C, it is expected that no additional solvent will be released during the reflow step at the same temperature. Following the baking process, the Si chip is then pressed onto the resist coated glass slide with a force of 50 N for 30 min with both the Si and the resist-coated glass slide heated to 130°C using the M9A device bonder. Using this method eliminates the problem of bubbles in the photoresist as shown in Figure

3-6c. However, the adhesion of the photoresist to parylene-Pt cables is found to be insufficient. The parylene-Pt cables delaminated from the photoresist during the XeF<sub>2</sub> silicon etch as seen in Figure 3-6c.

### 3.5.3 Crystal Bond 509

Crystal Bond 509 is a popular thermoplastic polymer that is used as an adhesive for backgrinding and potting because it adheres strongly to other materials and does not leave any residue after dissolution in acetone [131]. As a thermoplastic polymer, it also does not release volatile products during the reflow process, making it a suitable adhesive for the transfer process. Crystal Bond 509 is purchased in solid form and is typically applied by heating it above its flow point then cooling the mounted device to solidify the adhesive.

There is a range of reported flow points of Crystal Bond 509, e.g., 107°C [132], 121°C [133] and 135°C [134]. Differential scanning calorimetry (DSC) is performed in order to characterize the glass transition point of Crystal Bond 509 using a Q20 DSC (TA Instruments, New Castle, DE). A pestle and mortar is used to crush the solid adhesive into small pieces. 8.1 mg of crushed Crystal Bond 509 is placed in a Tzero aluminum pan (TA Instruments). A Tzero lid is crimped onto the Tzero aluminum pan using a Tzero sample press. A Tzero lid is crimped onto an empty Tzero aluminum pan as a reference. Fitting the transition region in the DSC plot using the vendor's Universal Analysis software indicates a value of 116°C for the glass transition temperature, which is within the range of reported flow points (Figure 3-7).

The dependence of thickness on the spin speed is also characterized. Crushed crystal bond 509 is dissolved in acetone at two different concentrations (20% and 40% by weight). The mixture is agitated using a paint mixer until the adhesive is completely dissolved. The solution is then spun on glass slides using a spinner (Solitec, Milpitas, CA) at different spin speeds for 60 s. No spread step is performed. The thickness of the films is obtained by removing part of the films on the glass slide using acetone and measuring the step height using a P-15 profilometer (KLA Tencor, Milpitas CA). For each concentration and spin speed condition, the thickness of the

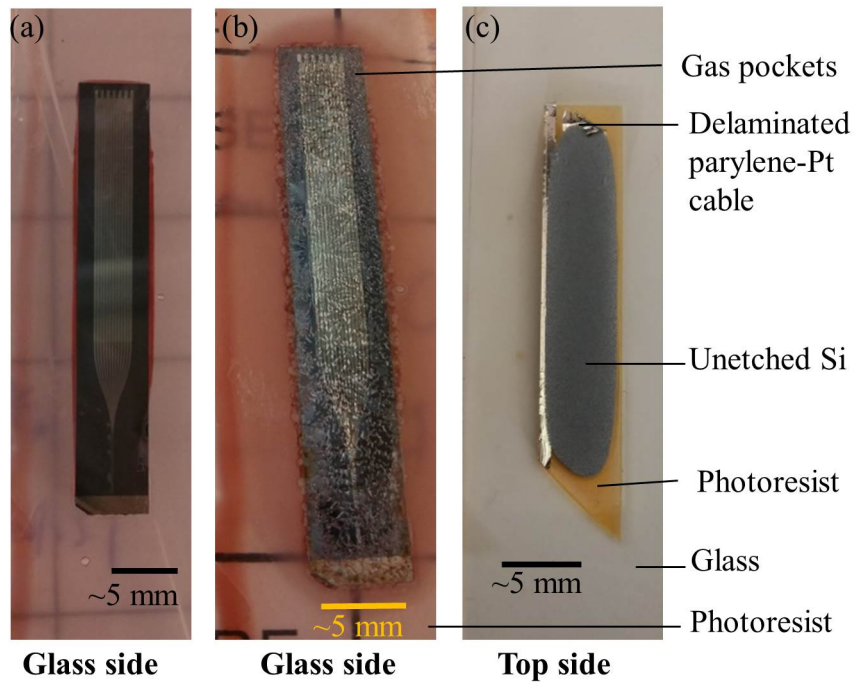


Figure 3-6: Optical images of (a) Si chip with fabricated probe mounted on glass using AZ4620 photoresist as an adhesive. (b) Despite an extended softbake, gas pockets are formed during the reflow process. (c) Prebaking the resist before mounting eliminates formation of gas pockets. However, adhesion is insufficient as seen by the observed delamination while etching Si. Glass side refers to the image being taken with the glass on top (viewing through the glass) and top side refers to the image being taken with the glass at the bottom.

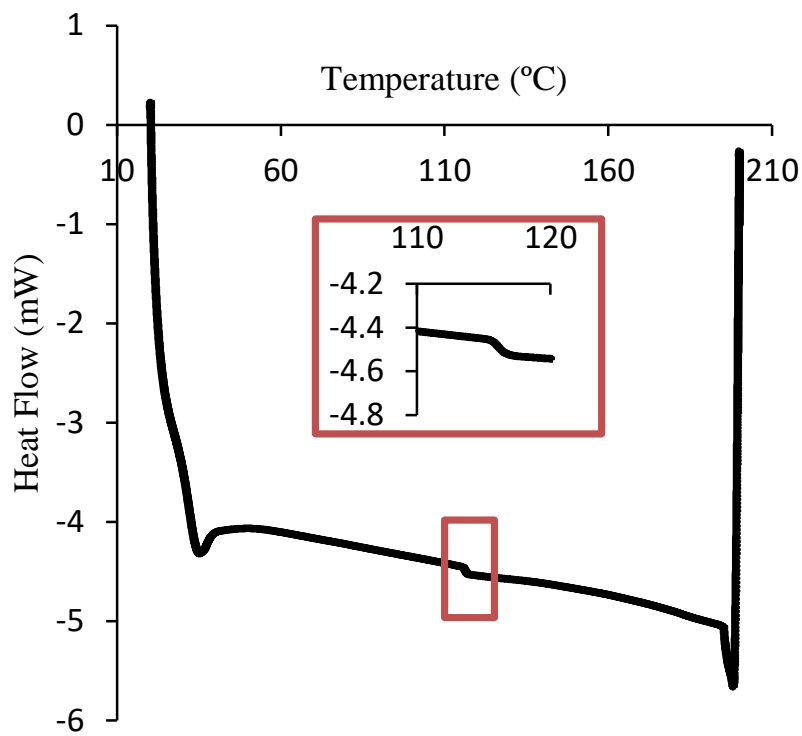


Figure 3-7: DSC of Crystal Bond 509. The measured glass transition temperature from the sample is 116°C.

film is measured on three separate glass slides. The obtained spin curves along with the standard deviations for the thicknesses of each condition are plotted in Figure 3-8. An empirical relation between film thickness and spin speed is [135]:

$$t = k\omega^\alpha \quad (3.1)$$

where  $t$  is the film thickness,  $\omega$  is the spin speed, and  $k$  and  $\alpha$  are experimentally determined constants.  $\alpha$  is unitless. A least-squares fit gives  $\alpha = -0.728$  and  $k = 1165 \text{ } \mu\text{m}/\text{rpm}^{-0.728}$  for the case when the concentration of Crystal Bond 509 in acetone is 40% by weight and  $\alpha = -0.531$  and  $k = 65.4 \text{ } \mu\text{m}/\text{rpm}^{-0.531}$  for the case when the concentration is 20%.

The transfer process begins with 40% Crystal Bond 509 spun on a glass slide at 500 rpm and heated in a 90°C oven for 30 min to evaporate the solvent. The Si chip and receiver substrate is then heated to 125°C and pressed together at 40 N for 20 min using the M9A device bonder. After the bonded structures are cooled to room temperature, the Si is etched as described in Section 3.3. A probe that is transferred onto Crystal Bond 509 is shown in Figure 3-9(a). A 10  $\mu\text{m}$  undercut below the parylene-C is performed by immersing the transferred structure into acetone for 1 min resulting in the structure shown in Figure 3-9. Performing the molding process on the undercut structures and releasing in acetone for 3 h successfully resulted in probes embedded in CMC-glucose as shown in Figure 3-9d. Successful transfer is determined by the connectivity of an electrical test loop in the probe. Although working devices are fabricated, some devices cracked because of curling of the polyurethane mold during the release process that is described in Section 3.4. The curling of the mold is likely due to the swelling of the polyurethane mold in acetone[136].

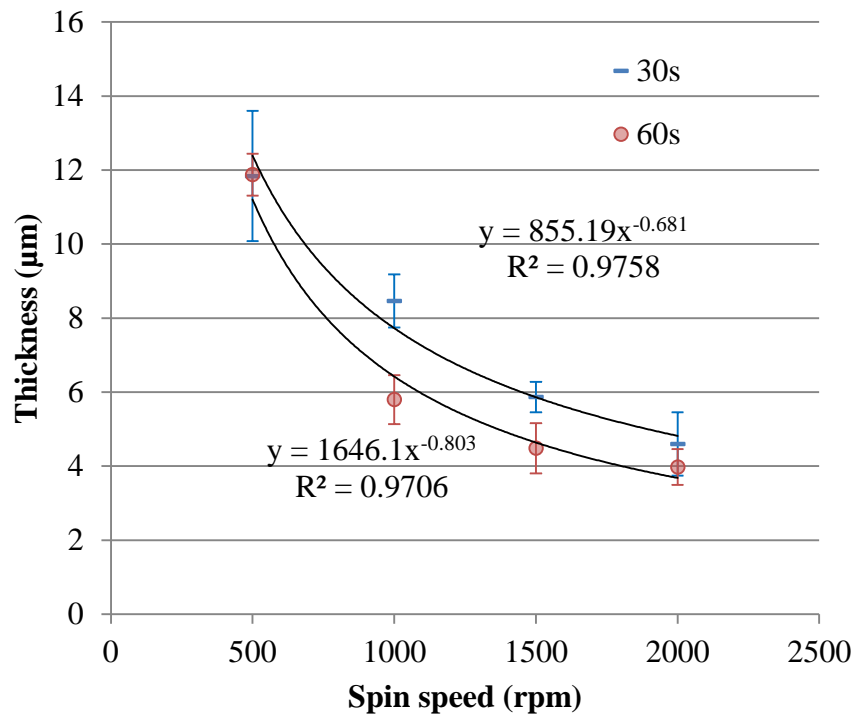


Figure 3-8: Thickness versus spin speed for Crystal Bond 509 dissolved in acetone at 20% and 40% by weight. Spin time is 60 s. Error bars represent the standard deviation of the measured thicknesses.

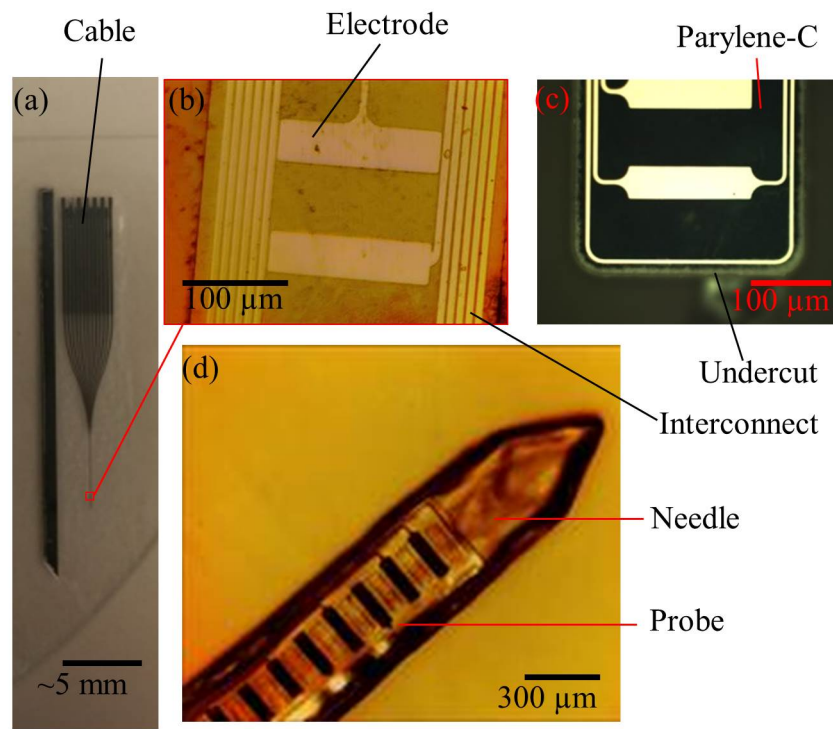


Figure 3-9: Probe transferred using Crystal Bond 509. (a) Optical image of a probe transferred onto the receiver substrate. (b) Microscope image of a transferred probe. (c) Microscope image after performing the undercut using acetone. (d) A molded and released probe embedded in CMC-glucose.

### 3.5.4 BGL7080

BGL7080 is a back-grinding liquid wax that is purchased dissolved in IPA (30% nominal concentration by weight) [137]. It is a suitable material for use as a transfer adhesive because it is easily removed by IPA and can be reflowed without releasing any volatile solvents. BGL7080 can be removed using IPA without causing deformation or bending of the polyurethane-based mold. The glass transition of BGL7080 is characterized using DSC in a similar way as Crystal Bond 509 described in Section 3.5.3. The BGL7080 is first heated in an oven for 90°C for 1 h in order to remove the IPA in the BGL7080. 6.1 mg of solidified BGL7080 is placed in the Tzero pan. The measured glass transition of BGL7080 is approximately 98°C, as shown in Figure 3-10.

The dependence of thickness on the spin speed of BGL7080 is characterized using two different spin times (30 s and 60 s) and plotted in Figure 3-11. No spread step is performed. Using (3.1) to fit the measured values of thickness for different spin speed gives  $\alpha = -0.8$  and  $k = 1646 \text{ }\mu\text{m}/\text{rpm}^{-0.8}$  for 60 s spin time; and  $\alpha = -0.68$  and  $k = 855 \text{ }\mu\text{m}/\text{rpm}^{-0.68}$  for 30 s spin time.

The steps for the transfer of parylene-C based devices using BGL7080 are similar to that using Crystal Bond 509. After spinning the BGL7080 on the glass slides, the slides are heated at 90°C for 15 min to remove the IPA solvent before being kept in 100 mT vacuum overnight to remove any further remaining solvent. The slide and the Si chip are then heated and pressed at 115°C and 40 N using the M9A device bonder for 30 min. After the bonded chips are cooled, the Si is removed using SF<sub>6</sub> RIE and XeF<sub>2</sub> etch as described in Section 3.3. A glass piece with the transferred probe after Si removal is shown in Figure 3-12a. The molding process is then performed on the probe using the steps described in Section 3.4. Needles with attached probes are released successfully in IPA for approximately 3 h as shown in Figure 3-12b and Figure 3-12c. To verify that BGL7080 is removed from the electrodes, the electrodes of probes that are transferred onto BGL7080 and released in IPA solvent are observed using a Quanta 200 SEM (FEI, Hillsboro, OR) scanning electron microscopy. No significant

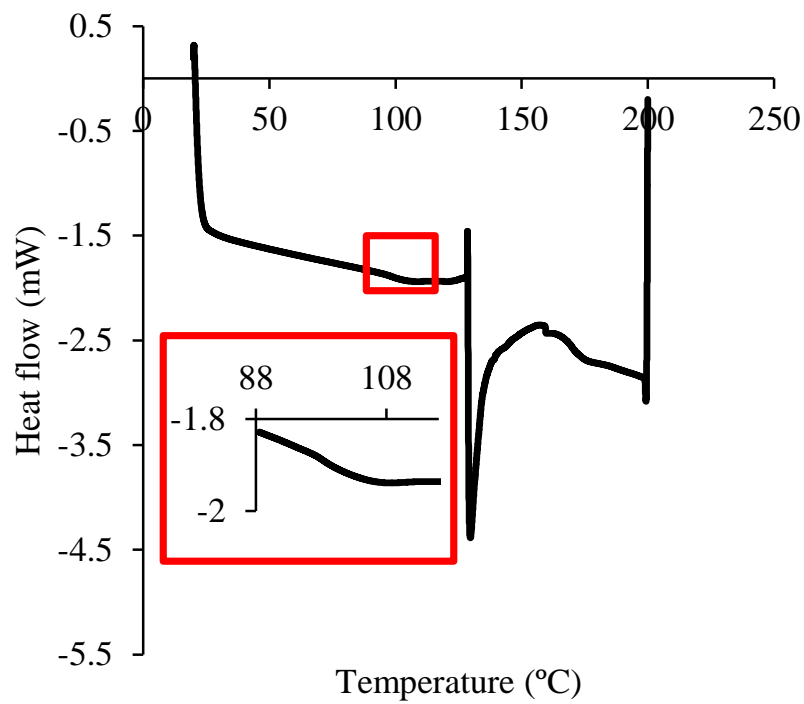


Figure 3-10: DSC of BGL7080. The measured glass transition temperature is approximately 98°C. A melting point of approximately 129°C is also detected.

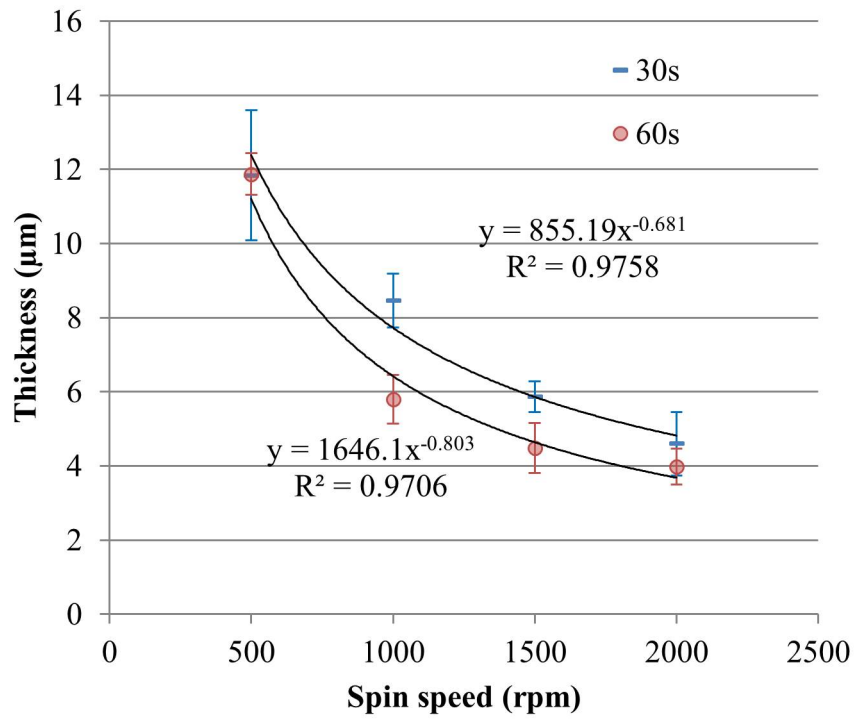


Figure 3-11: BGL7080 spin curves for two spin times (30 s and 60 s). Each test case is performed with three samples. Error bars represent the standard deviation of the measured thickness.

change in morphology of the electrodes or additional residue is observed after transfer and release. Analysis of the electrode surface using x-ray photoelectron spectroscopy after transfer and release does not show any significant change as compared to the electrode surface before transfer. As will be described in Section 3.7, the derived value of the double layer capacitance from the impedance after transfer and release is within range of platinum in PBS (Phosphate Buffered Saline) [138]. The residue in the electrodes seen in Figure 3-12 is CMC-glucose that has seeped onto the electrode surface during the molding process and is seen to dissolve when left in PBS.

In addition, large probes with multiple shanks are transferred as shown in Figure 3-13. The large area of these probes warrants modifications to the bonding parameters. Since the maximum force that can be applied by the M9A device bonder is 90 N, the bonding time is increased to 2 h and 4 h for the two shank probe and four shank probe respectively. This time is determined by observing the probes optically until the BGL7080 is seen to completely bond with the probe in all regions. The successful transfer of these large probes demonstrates the versatility of the process even for large devices. However, the molding step is not performed on these probes because it is not used at the moment for any applications.

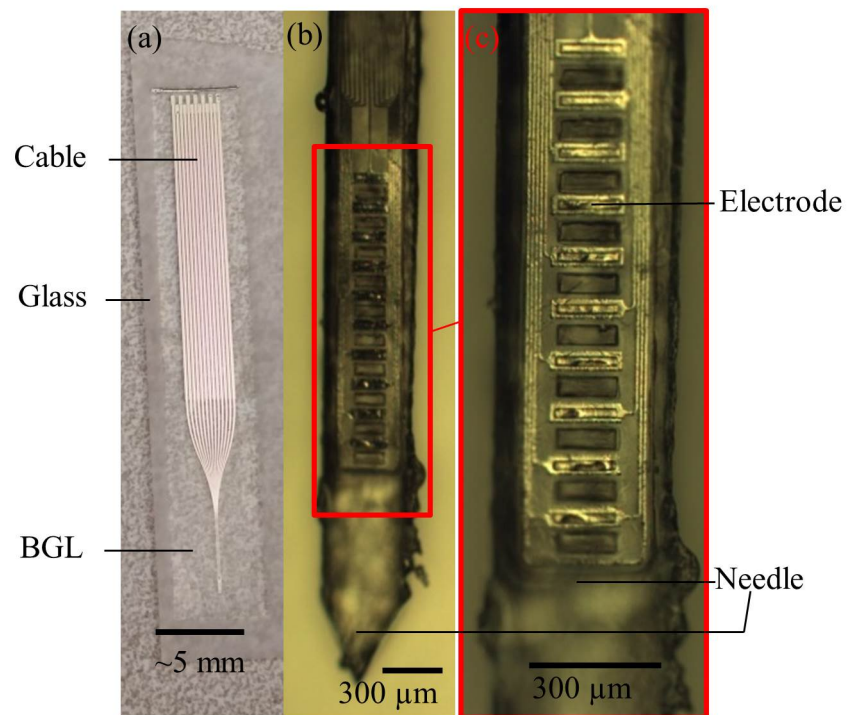


Figure 3-12: Probe transferred using BGL7080 as an adhesive. (a) Optical image of a probe transferred onto BGL7080 coated glass. (b) Microscope image of a molded and released probe embedded in a CMC-glucose needle. (c) Zoomed-in microscope image of a molded and released probe. Some residual amount of CMC-glucose remaining from the molding process is seen on the electrode surface.

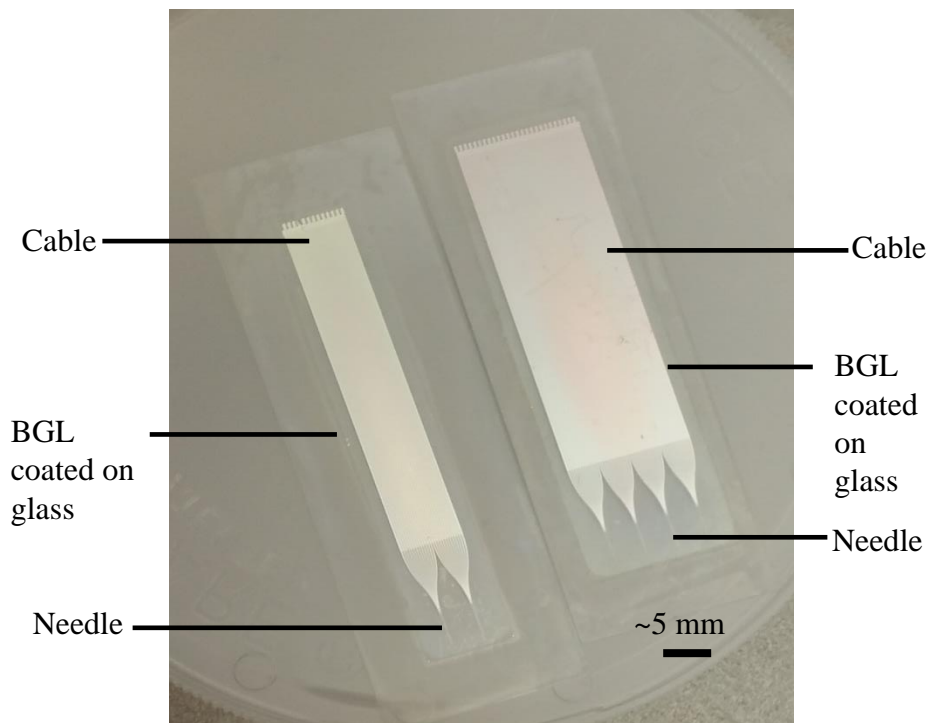


Figure 3-13: Optical images of transferred two and four shank probes using BGL7080 as an adhesive. The successful transfer of large devices demonstrates the versatility of this process.

## 3.6 Compatibility of process with CMC-glucose

Carboxymethyl cellulose (CMC) [139] and glucose are both biocompatible and biodissolvable materials. It is important to ensure that the chemical properties of CMC and glucose are maintained throughout the process.

The primary chemical that CMC-glucose is exposed to when undergoing the process described in Section 3.4 is the solvent used to release the probes. The choice of solvent depends on the adhesive used. In this chapter, the relevant solvents are acetone, IPA and Dynasolve 220. An insertion study is performed to investigate the effects of the solvent on the needles. 300  $\mu\text{m}$  by 100  $\mu\text{m}$  by 5 mm-long (nominal) needles are molded using CMC-glucose by Rakesh Khilwani and separately immersed in acetone, Dynasolve 220 and IPA for 48 h. One needle is not treated with any solvent and used as the control. The needles are then inserted into a 1% agarose gel. The evolution of the dissolution of the needles in agar is then observed. The width of the center of the needle at 30 s time intervals relative to its width when it is first inserted is plotted in Figure 3-14. Images of the needles at these time intervals are shown in Figure 3-15. The evolution of the width of the needle is similar for acetone treated needles and IPA treated needles but differs significantly for Dynasolve 220 treated needles. Dynasolve 220 significantly affects the dissolution properties of CMC-glucose whereas acetone or IPA does not affect the dissolution properties of CMC-glucose.

In order to gain a better understanding of the mechanism for this change in dissolution behavior, Attenuated Total Reflectance Fourier Transform Infrared (ATR-FTIR) spectroscopy with a Frontier FTIR system (Perkin-Elmer, Waltham, MA) is performed to assess chemical changes to the CMC-glucose after exposure to the various solvents. Pieces of CMC-glucose are separately immersed in acetone, Dynasolve 220 and IPA for 48 h. One piece is not treated with any solvent. The results of the FTIR are shown in Figure 3-16.

The FTIR spectra of the untreated sample, sample treated with acetone and sample treated with IPA has peaks at 3280  $\text{cm}^{-1}$ , 2920  $\text{cm}^{-1}$ , 1590  $\text{cm}^{-1}$ , 1410  $\text{cm}^{-1}$ ,

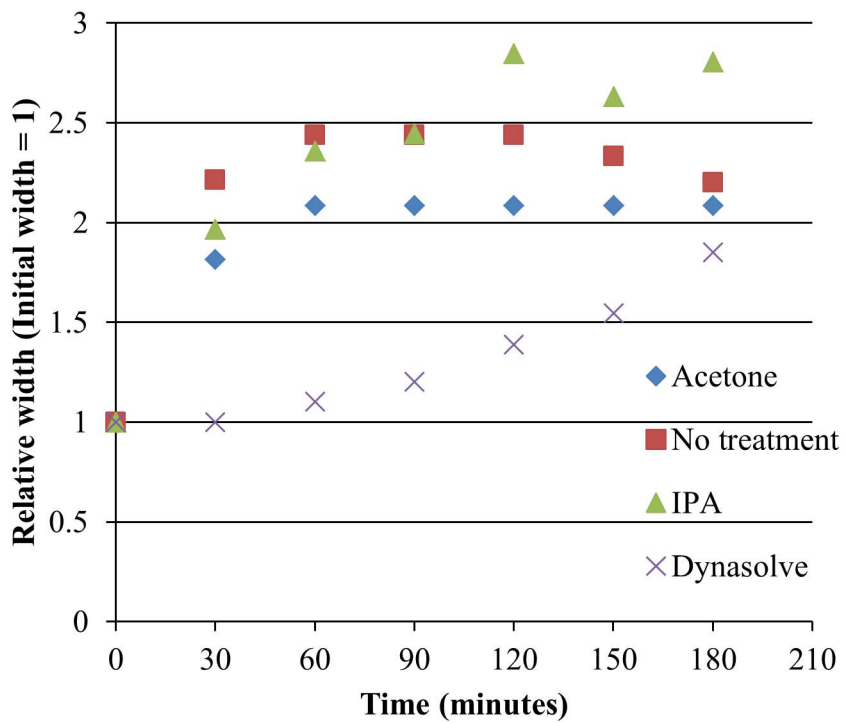


Figure 3-14: Width of the CMC-glucose extent at 30 s time intervals relative to initial width after insertion into agar. The width is measured at the midpoint along the shank.

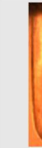
<b>Time (s)</b>	0	30	60	90	120	150	180
Acetone							
No treatment							
Dynasolve							
IPA							

Figure 3-15: Snapshots at 30 s time intervals of needles treated for 48 h with various solvents inserted into agar.

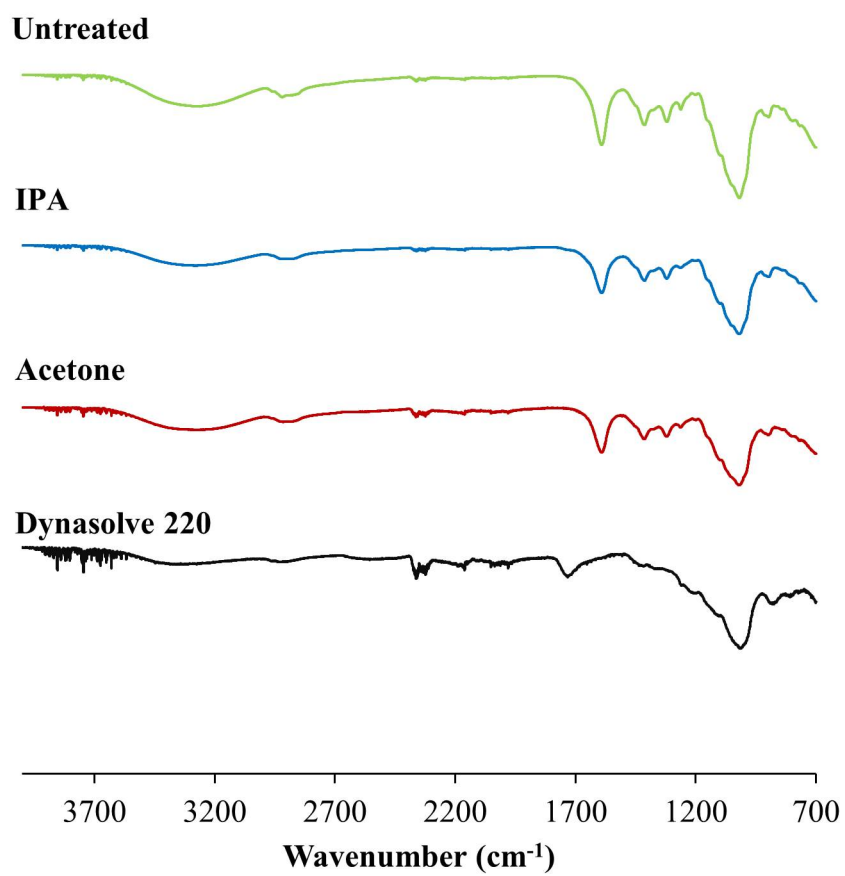


Figure 3-16: FTIR spectra of untreated CMC, and of CMC immersed in IPA, acetone, and Dynasolve 220 for 48 h.

1320  $\text{cm}^{-1}$  and 1020  $\text{cm}^{-1}$  indicating that there is no evidence of any chemical change of the CMC-glucose or absorption of solvents occurring due to immersion of CMC-glucose in acetone or IPA. The broad peak at 3280  $\text{cm}^{-1}$  is attributed to the -OH stretching, the peak at 2920  $\text{cm}^{-1}$  is attributed to asymmetric  $\text{CH}_2$  stretching, 1590  $\text{cm}^{-1}$  due to  $\text{COO}^-$  asymmetric stretching, 1410  $\text{cm}^{-1}$  due to  $\text{COO}^-$  symmetric stretching, 1320  $\text{cm}^{-1}$  due to C-CH and O-CH stretching and the peak at 1020  $\text{cm}^{-1}$  is attributed to -CO stretching ( $\text{RCH}_2\text{OH}$ ) [139][140][141][142]. Compared to untreated CMC-glucose, the FTIR of the Dynasolve 220 treated sample has an additional peak at 1730  $\text{cm}^{-1}$  that corresponds to an ester bond [143] but does not have observable peaks at 1590  $\text{cm}^{-1}$ , 1410  $\text{cm}^{-1}$ , 1320  $\text{cm}^{-1}$  and 1260  $\text{cm}^{-1}$ , indicating that the CO-groups have reacted to form an ester bond. The FTIR results suggest that transfer using Dynasolve 220 as the wet etchant is not suitable as it is possible for the biocompatibility of CMC-glucose to be affected by Dynasolve 220.

### 3.7 Impedance experiment results

Molded probes fabricated using BGL7080 as an adhesive and having undergone post-fabrication annealing at 300°C for 3 h in 10 mT  $\text{N}_2$  environment are tested in PBS (10X Solution, Fisher BioReagents, Waltham, MA) that is diluted to a 1X solution. The probe impedance spectrum is measured for 12 h against a Pt coil counter electrode (MW-1033, BASi) with an Ag/AgCl reference (MF-2052, BASi). The impedance is measured using a PGSTAT302N potentiostat (Metrohm-Autolab, The Netherlands) by applying a 30 mV sinusoidal excitation over a period of around 13 h.

As shown in Figure 3-18, the impedance measured between the electrode and PBS ( $Z^{\text{measured}}$ ) is the parallel combination of the actual electrode impedance ( $Z^{\text{electrode}}$ ) and of the impedance between the wiring and PBS ( $Z^{\text{wiring}}$ ), i.e.,

$$Z^{\text{measured}} = \frac{Z^{\text{electrode}} Z^{\text{wiring}}}{Z^{\text{electrode}} + Z^{\text{wiring}}} \quad (3.2)$$

In Figure 3-17, the impedance of an electrode and a self-test loop is compared

at 1 kHz. The impedance at 1 kHz is used as a predictor of recording capability of neurological signals. Hence, for electrodes, the impedance at 1 kHz is used to characterize the electrode. The exposed electrode area is  $1725 \mu\text{m}^2$  and is connected to the pad using approximately  $20,000 \mu\text{m}^2$  of insulated area along the probe shaft. The insulated self-test loop comprises a  $4 \mu\text{m}$ -wide Pt trace that is routed around the periphery of the probe at a distance  $10 \mu\text{m}$  inset from the edge. It does not have an exposed electrode and has approximately twice the insulated wiring area as the wiring of the electrode.

As seen from Figure 3-17,  $Z^{wiring}$  can be estimated from the measurement of the self-test loop impedance ( $Z^{loop}$ ) assuming the impedance is proportional to the metal area since the length of the wiring to the electrode is approximately half of the total length of the interconnect in the loop, i.e.,

$$Z^{wiring} = 2Z^{loop} \quad (3.3)$$

We can then estimate the value of the actual electrode impedance using the equation

$$Z^{electrode} = \frac{Z^{measured} Z^{wiring}}{Z^{wiring} - Z^{measured}} \quad (3.4)$$

The measured impedance of the electrodes ( $Z^{measured}$ ) and self-test loop ( $Z^{loop}$ ) at 1 kHz are approximately  $143 \text{ k}\Omega$  and  $148 \text{ k}\Omega$  respectively at  $t = 0$  indicating that at  $t = 0$ ,  $Z^{wiring}$  is approximately  $296 \text{ k}\Omega$  and  $Z^{electrode}$  is approximately  $277 \text{ k}\Omega$ , indicating that spike recording is possible using these electrodes. The low value of the wiring impedance indicates that the probe insulation may not be performing adequately. A leaky insulation will result in high noise during neural recording.

In order to verify that the probe insulation is still functional after transfer processing but before molding, *in vitro* impedance experiments are performed on probes which that did not undergo the molding process: after transfer to glass using BGL7080 as described in Section 3.5.4, the probes are released in IPA and manually placed onto a glass slide and inserted into 1X PBS. The impedance is measured in identical conditions to those described for the molded probes. Four samples are tested, but one

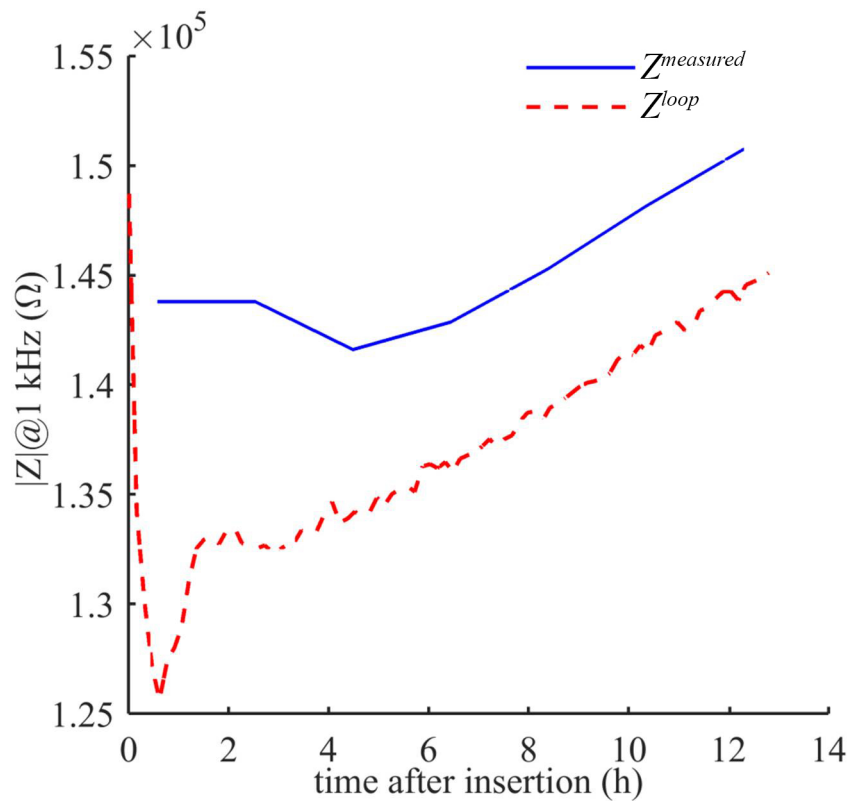


Figure 3-17: Impedance magnitude of  $Z^{measured}$  and  $Z^{loop}$  at 1 kHz of a molded probe versus time. Test is performed by Mats Forssell.

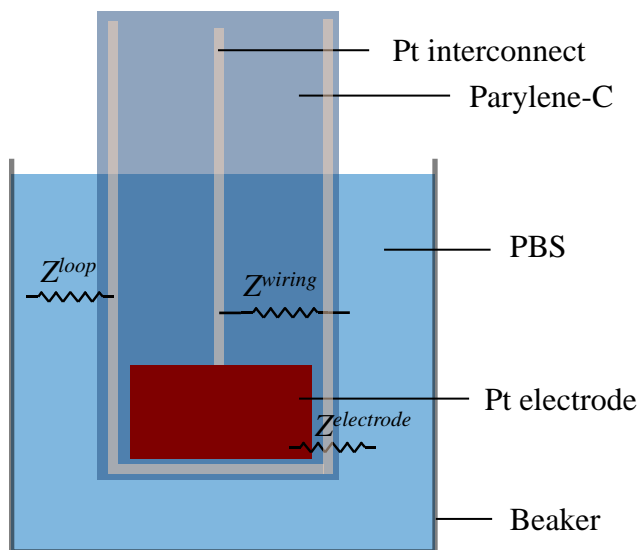


Figure 3-18: Diagram showing the various impedances ( $Z^{loop}$ ,  $Z^{wire}$ ,  $Z^{electrode}$ ) that are measured or derived.

sample is excluded from analysis due to manufacturing defects. Plots of the geometric average of the remaining  $n = 3$  measured electrode impedances ( $Z^{measured}$ ) and self-test loop impedances ( $Z^{loop}$ ) are plotted in Figure 3-19. At 1 kHz the self-test loop impedance is four times larger than the electrode impedance indicating that the insulation performance is significantly better than that of the molded probes. This suggests that pinholes are not the likely explanation for the low impedance of the trace of molded probes. It is likely that mechanical stresses incurred during molding appear to affect the insulation. An alternative method of bonding pre-made needles to the probes to improve the insulation is discussed in Section 3.8. By applying (3.3) and (3.4), the estimated real electrode impedance ( $Z^{electrode}$ ) at  $t = 0$  and 1 kHz for the three samples are 59 k $\Omega$ , 320 k $\Omega$ , and 290 k $\Omega$ .  $Z$  is not computed for one of the tests because  $Z^{measured} > Z^{wiring}$  for that test, likely due to defects on the insulation wiring during fabrication for that sample.

We use  $Z^{electrode}$  to estimate the double-layer capacitance of the platinum electrode. The values found are 1.6 pF/ $\mu\text{m}^2$  for one of the tests and 0.3 pF/ $\mu\text{m}^2$  for two of the tests. The variation in double-layer capacitance can be due to fabrication variance across wafers since the samples are fabricated on different wafers.

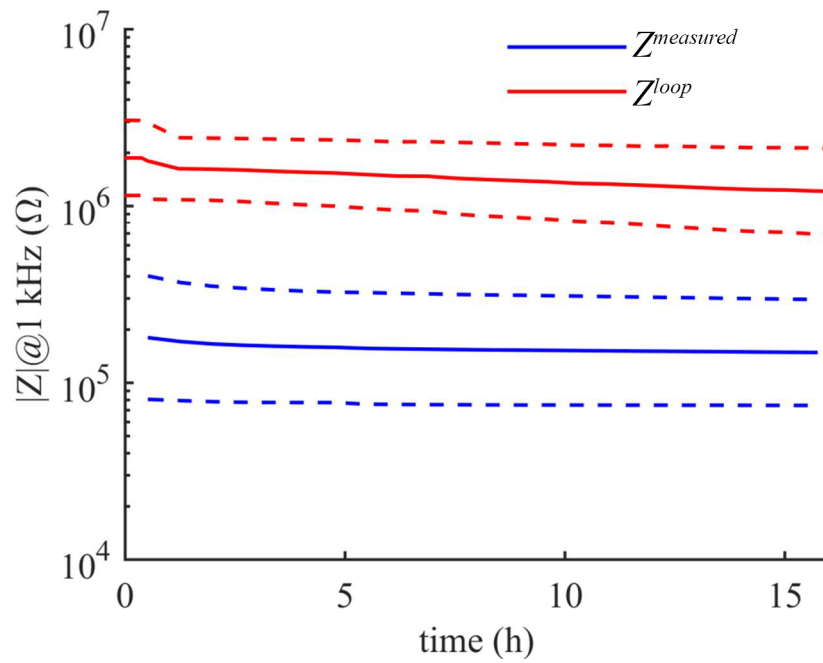


Figure 3-19: Impedance magnitude of  $Z^{measured}$  and  $Z^{loop}$  at 1 kHz of transferred probes without CMC molding versus time. The geometric average of  $n = 3$  tests is plotted with solid lines. The impedance one geometric standard deviation apart from the geometric average is represented in dashed lines. Test is performed by Mats Forssell.

## 3.8 Bonding of needles to probes transferred on to BGL7080

To test whether the molding of CMC on the probes is a cause of the lowered impedance, the impedance of insulation test structures (10  $\mu\text{m}$  wide wires of Pt encapsulated in parylene-C on a glass substrate as described in Chapter 4) is measured without exposure to CMC; with CMC placed on the chip and dried in air; and with CMC placed on the chip and dried in a centrifuge which mimics the molding step described in Section 3.4. The placement of CMC on the chip and drying the chip in the centrifuge is performed by Rakesh Khilwani. The impedance at 0.1 Hz over time is plotted in Figure 3-20. Low frequency impedance is used to characterize insulation performance as it is more sensitive as compared with impedance measured at higher frequencies to insulation degradation. It is seen that the drying of CMC, whether in air or in a centrifuge, results in a significant drop in impedance of the test structure which implies that the drying of CMC degrades the insulation performance of parylene-C/Pt/parylene-C sandwich structures.

To alleviate this, the process is modified so that molding of the needles is done separately. A thin layer of gelatin is molded on the CMC needle to aid adhesion. The molded needles are then bonded to the probe using a M9A Device Bonder at 80°C to reflow the gelatin. For this process, the adhesion between the parylene-C and gelatin is critical. Initial bonding between the CMC needles coated with gelatin and parylene-C probes show very weak adhesion between parylene-C and gelatin which resulted in very low yields. To improve the adhesion between parylene-C and gelatin, the parylene-C is treated with O<sub>2</sub> plasma prior to bonding which makes the surface of the parylene-C hydrophilic. Treating parylene-C at 200 W O<sub>2</sub> plasma in an IPC barrel etcher for 1 minute makes the parylene-C hydrophilic as indicated by the contact angle of DI water on parylene-C deposited on Si as shown in Figure 3-21. The contact angle maintains hydrophilic quality even after 1 week. By performing this pre-treatment, the bonding between the needles and the probes is found to be sufficiently strong for the needle-to-probe bonding process.

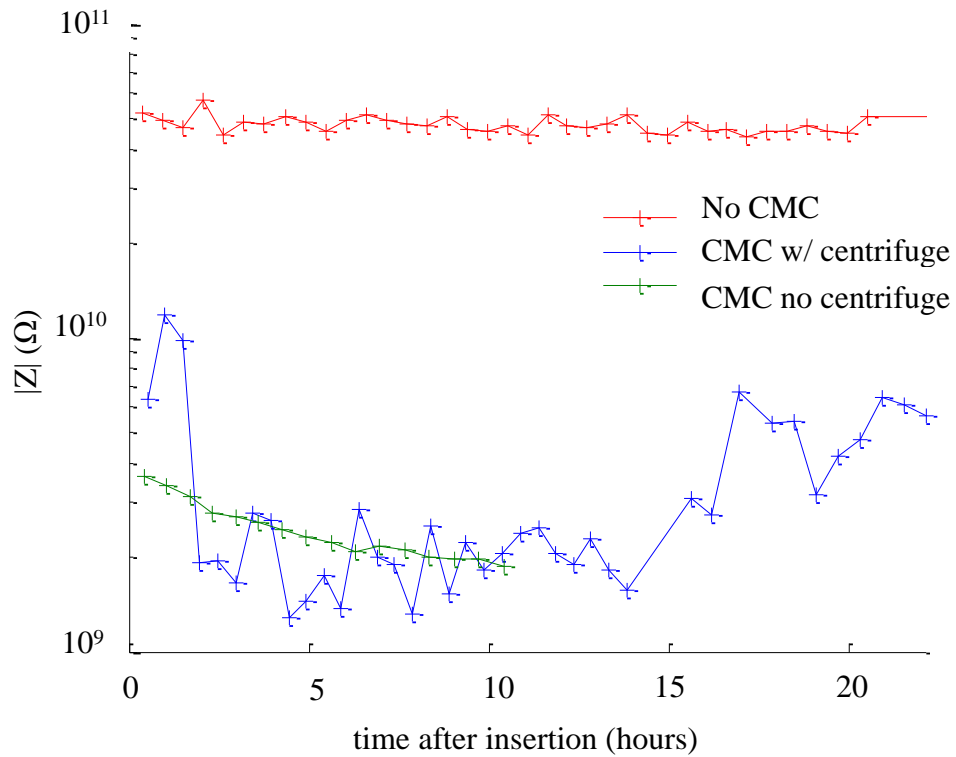


Figure 3-20: Impedance of completely insulated test structures at 0.1 Hz in PBS under different conditions. The drying of CMC in air or in a centrifuge degrades the insulation of the test structure as seen by the lower impedance compared with a sample not exposed to CMC.



As-deposited parylene-C



2 minutes after 200W O<sub>2</sub> plasma for 1 minute

Figure 3-21: Contact angle of DI water on as deposited parylene-C and parylene-C treated with O<sub>2</sub> plasma

To verify that this method of bonding needles to the probe improves the encapsulation properties of parylene-C compared with molding the needles over the probe, EIS is performed on the completely insulated self-test loop for probes with molded CMC, probes with no CMC and probes with the CMC needle bonded as shown in Figure 3-22. The impedance of the self-test loop is higher for the probe with CMC needle bonded versus the probe with the CMC needle molded on it, indicating that the insulation quality of the probe with bonded CMC needles is better than that of the probe with the CMC needle spun on it.

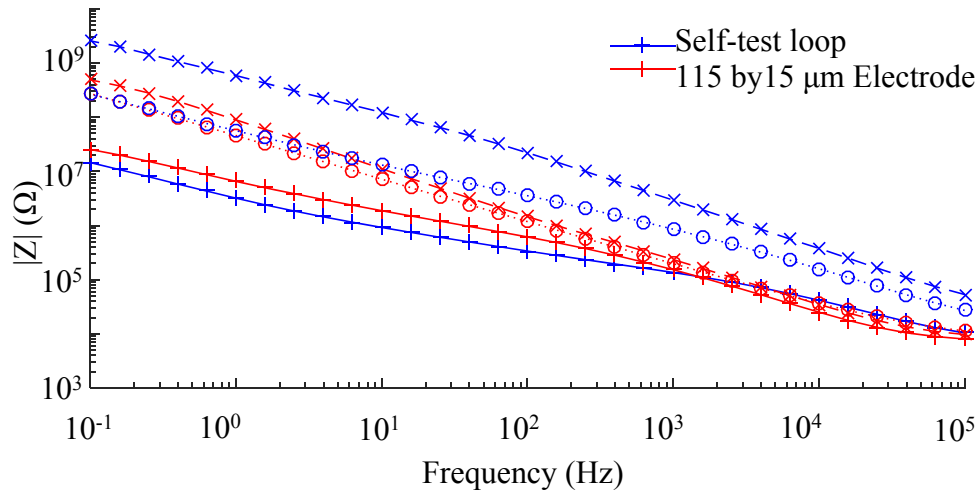


Figure 3-22: Initial *in vitro* impedance of recording probe in three different assembly configurations: 1) molded CMC needle (full line), 2) low stress bonded attached CMC needle (dashed line), and 3) no CMC needle (dotted lines). The self-test loop does not have exposed metal and its impedance is indicative of insulation quality. Test is performed by Mats Forssell.

### 3.9 Summary

Transfer of ultra-compliant parylene probes strongly adhered to their original substrate has been demonstrated using various transfer adhesives and extends beyond typical transfer processes that require weak probe-substrate adhesion. This transfer method increases the versatility of the process flow and can thus be used to integrate a wider range of materials and processes. The process involves bonding the ultra-compliant structures to an adhesive spin-coated on glass and etching the original Si substrate completely. The process improves on the handling of the probes which is critical when probes are thin and allows for integration of an annealing step to improve parylene-C to parylene-C adhesion. The process also exposes the backside of the probe which potentially allows for fabrication of double sided probes.

Four different adhesives are evaluated for the transfer process with the BGL7080 liquid wax providing the best results for the application of embedding parylene-C based probes on molded CMC-glucose needles due to its ability to reflow without release of volatile materials and its dissolution in IPA, which does not affect the

CMC-glucose needle. Release of volatile materials such as when AZ4620 is used as an adhesive can result in bubbles during subsequent processing. The ability to dissolve in IPA makes the release process compatible with polyurethane molds and CMC-glucose structures.

In addition, probe-needle bonding is a means to reduce stress induced on the probes, and is an improvement over needle molding onto the probe.



## Chapter 4

# Atomic layer deposited ceramic nanolaminates for sealing

Given that neural probes operate in bodily fluids that contain saline and water among many other chemicals, the viability of the probes often depends on the ability of the polymer to maintain its characteristics and successfully encapsulate the probe. As shown in Figure 4-1, bulk water penetration, poor adhesion and corrosion can result in exposure of the interconnect to the surrounding body fluid. The exposed interconnect effectively acts as an electrode that will affect the selectivity of the probe. Hence, resistance to corrosion, water penetration capabilities and adhesion of the various materials in the probe tend to be important physical characteristics for the insulating material. Since the insulating material that is used predominantly in this thesis is parylene-C, Section 4.1 discusses the adhesion between parylene-C and various materials and investigates different methods of improving the adhesive properties of parylene-C.

Although the polymers used for insulation discussed in Section 2.1 are biocompatible and have suitable electrical and mechanical properties, they have lower resistance to water penetration through the bulk of the material compared to other encapsulation materials like glass and ceramics. In a study by [144], the capability of different encapsulation schemes are investigated using a Mg test, where the time taken for corrosion to appear in encapsulated Mg is used to determine barrier failure. It is

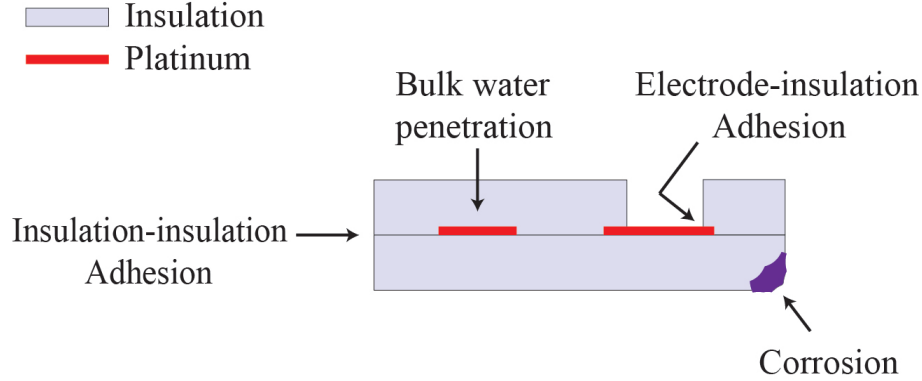


Figure 4-1: Different means of insulation failure

determined that any 1  $\mu\text{m}$ -thick layer of SU-8, PDMS or parylene-C is poor barrier material with the encapsulation surviving for less than a day under physiological conditions. Comparatively, ceramics tend to have better barrier properties in terms of water vapor transmission [145][146]. On the other hand, materials with good water penetration capabilities like glass and ceramics tend to be stiffer. Hence, using a hybrid approach of combining ceramic layers with polymer layers is one approach in improving water vapor transmission while maintaining flexibility of the device. A study on the combination of ceramic layers with polymer layers is presented in Sections 4.2 and 4.3.

It is important to control the properties of the ceramic used such as the conductivity and resistance to corrosion of the ceramic. The use of atomic layer deposition (ALD), which uses self-limiting reactions to deposit materials one atomic layer at a time, allows creation of hybrid materials (nanolaminates) by alternating between different materials for each layer that is deposited. The properties of nanolaminates can be engineered to have suitable properties as will be discussed in Section 4.2. Similar to ALD is MLD (molecular layer deposition) where materials are deposited one molecule at a time. This allows for inorganic-organic hybrids such as alucone other metalcones[147] which are metal alkoxides based on the metal precursor (such as trimethylaluminum for alucone) and ethylene glycol. Although alucone is shown to be a poor barrier that is unstable in water and is brittle, combining the material with  $\text{Al}_2\text{O}_3$  to form a  $\text{Al}_2\text{O}_3$ -alucone nanolaminate has been shown to create a hybrid

material that allows for higher mechanical strain and better gas barrier properties as compared with  $\text{Al}_2\text{O}_3$ [148].

In this chapter, various surface treatments of the first parylene-C layer prior to the deposition of the second parylene-C layer are used to improve the adhesion between parylene-C layers. The ability to encapsulate the neural probes is tested using electrochemical impedance spectroscopy (EIS) and the surface properties of the neural probes is tested using X-ray photoelectron spectroscopy. Using  $\text{O}_2$  plasma provides the best treatment of when compared with  $\text{Ar}^+$  ion milling, A174 and fluorination. In addition, a hybrid encapsulation scheme is used. A nanolaminate of  $\text{TiO}_2$  and  $\text{Al}_2\text{O}_3$  provides sufficiently high electrical resistivity and resistance to corrosion in saline as compared with  $\text{TiO}_2$  alone and  $\text{Al}_2\text{O}_3$  but does not adhere well to parylene-C. A hybrid encapsulation scheme is used that has a layer of  $\text{TiO}_2$  used as an adhesion layer between the nanolaminate and parylene-C. This encapsulation scheme provides the best performance as determined by EIS when the samples are aged at  $60^\circ\text{C}$  for 500 hours.

## 4.1 Improving adhesion of parylene-C for flexible neural probes

One disadvantage of using the various polymers discussed in Section 2.1 including parylene-C is the low adhesion to many surfaces because of low surface energy and chemical inertness. The adhesion between parylene-C and other materials is recognized as an area of concern and attempts have been made to address this issue in a number of studies[95].

### 4.1.0.1 Adhesion between parylene-C and other materials

Besides adhesion between parylene-C, adhesion between parylene-C and the electrode material, which is typically a metal, also needs to be considered. In a study using atomistic simulations[149], it is expected that the adhesion between parylene-C and

Pt, parylene-C and  $\text{TiO}_2$ , and parylene-C and Ti are strong but the adhesion between parylene-C and Au is weak. This is corroborated experimentally by [95] where strong adhesion between parylene-C and Pt is measured but weak adhesion between parylene-C and Au is measured. In a study to determine suitable adhesion layers between parylene-C and Au, [118] compared Ti, Cr and Pt and found that Pt provides the best adhesion of the three. The practice of using Pt as an adhesion layer between parylene-C and Au is also adopted in [39]. For the devices that are fabricated for this thesis, it is observed that there is strong adhesion between parylene-C and Pt; and parylene-C and  $\text{TiO}_2$  but weak adhesion between parylene-C and  $\text{Al}_2\text{O}_3$  based on observed delamination during fabrication. This corroborates with the results found in literature.

#### **4.1.0.2 Annealing to improve parylene-C to parylene-C adhesion**

Methods of improving adhesion between two separately deposited layers of parylene-C include heating the material above its glass transition temperature [150][151][152] or its melting point [105] and heating while applying pressure [153]. There is no universally accepted best practice for annealing treatment of parylene-C to improve adhesion and techniques to improve adhesion differ from lab to lab, possibly because of differences in equipment availability. For example, in [153] annealing at  $230^\circ\text{C}$  for 30 min with 800 N of force over a 4 inch wafer at 0.15 mT vacuum is found to be optimum whereas in [105],  $300^\circ\text{C}$ , 3 hours in a nitrogen atmosphere is used. In [150] the optimal bonding parameters are  $160^\circ\text{C}$  in air while applying pressure of 1.5 MPa and in [154] the optimal bonding temperatures are 4.9 MPa,  $160^\circ\text{C}$  for 30 min.

However, annealing also affects other properties of parylene-C if the conditions are not controlled. Oxidative degradation of parylene-C is observed in air at temperatures higher than  $180^\circ\text{C}$  in [154] and at temperatures higher than  $170^\circ\text{C}$  in [150] which limits the maximum temperature allowable in air. In addition, in [155], it is found that heating parylene-C above its melting point significantly increases adhesion between parylene-C and Si. This means that heating parylene-C beyond its melting point makes peelable processes unfeasible. Hence, in order to integrate the annealing step

into a process flow, it is necessary to introduce additional steps such as that discussed in Chapter 3[116]. A study is performed to investigate different methods of improving parylene-C to parylene-C adhesion in Section 4.1.2.

### 4.1.1 Quantification of encapsulation capability by EIS

In this thesis, electrochemical impedance spectroscopy (EIS) is used as a means to determine encapsulation quality. EIS can be performed using the two-electrode or three-electrode configuration. In the two electrode configuration, as depicted in Figure 4-2(a), the device under test is the working electrode and a counter electrode is immersed in saline solution. The device under test varies depending on the test being conducted. For example, if the property of an electrode is designed, the device under test will have an exposed electrode region. If the quality of insulation is being tested, then the device under test will be an insulated structure with no electrode opening as depicted in Figure 4-2(a). The other electrode in a two electrode configuration is a very large counter electrode that has a much lower impedance as compared with the working electrode because of the large exposed area of the electrode. The impedance spectrum is measured between the two by applying a sinusoidal voltage, measuring the current and sweeping across different frequencies. For the case of a three-electrode setup, a known reference voltage (supplied for example, by a Ag|AgCl system) is used as the third electrode. In the three electrode setup, the reference electrode sets the potential whereas the counter electrode acts as the current sink. In this thesis, a two electrode setup is used for the majority of the tests because of the large number of tests conducted that makes a three electrode setup unfeasible.

The model of a device under test is shown in shown in Figure 4-2(b) and is adapted from the model proposed by [144][156]. The spreading resistance of the solution is given by  $R_{sol}$ , the encapsulation is modelled as a capacitor  $C_{enc}$ , and the electrode is modelled with a series resistance  $R_{elec}$  that represents the interconnect resistance and any additional spreading resistance due to the geometry of the electrode,  $C_{dl}$  represents the double layer capacitance and  $R_{CT}$  represents the charge transfer resistance of an electrode. In the case of degradation, delamination or water penetration, the

metal areas exposed to the surrounding saline are represented as an expansion of the electrode.

For the case of an inert electrode material like Pt,  $R_{CT}$  tends to be large and the double layer capacitance  $C_{dl}$  dominates. When delamination occurs or if a pore is formed, the area of exposed metal increases, which results in increased  $C_{dl}$ . When degradation occurs, the encapsulation is effectively thinned and  $C_{enc}$  is increased. Both of these factors result in reduced impedance measured. For the case of test structures without electrodes, ideally, only  $C_{enc}$  is present. However, as the test structure degrades, the interconnect begins to be exposed by pores or other mechanisms and acts as an electrode giving a  $R_{CT}$  and  $C_{dl}$  component. As this 'electrode' expands in area,  $C_{dl}$  increases and  $R_{CT}$  reduces, reducing the impedance. In the case of insulation degradation, a low frequency such as 0.1 Hz is typically used because the impedances at low frequencies is more sensitive to insulation degradation.

In order to investigate the effects of various treatments, test structures are designed consisting of insulated traces of Pt wires 10  $\mu\text{m}$  wide and 1.5 cm long. The completely insulated traces provide a means of testing insulation using the model proposed in 4-2(b). The Pt counter electrode (5 mm<sup>2</sup> by 12 mm<sup>2</sup>) is incorporated into the design to simplify testing. The electrodes are fabricated so that electrochemical impedance spectroscopy (EIS) can be used to quantify the insulation characteristics of the probes.

Work done in this chapter is part of the project: 'Ultra-Compliant Transverse Intrafascicular Electrode Arrays for Electro-Pharmaceutics' under the DARPA ElectRx program. The proposal of the various encapsulation schemes, fabrication, process design, all XPS tests, analysis of XPS tests, mechanical analysis and crosstalk analysis are performed by the author of this thesis. All EIS tests in this chapter are performed by Mats Forssell.

### 4.1.2 Parylene-C to parylene-C adhesion

The adhesion between two separate layers of parylene-C is important to ensure sufficient insulation, but this adhesion tends to be poor. Plasma treatment is a possible candidate in improving the adhesion between two separately deposited layers of

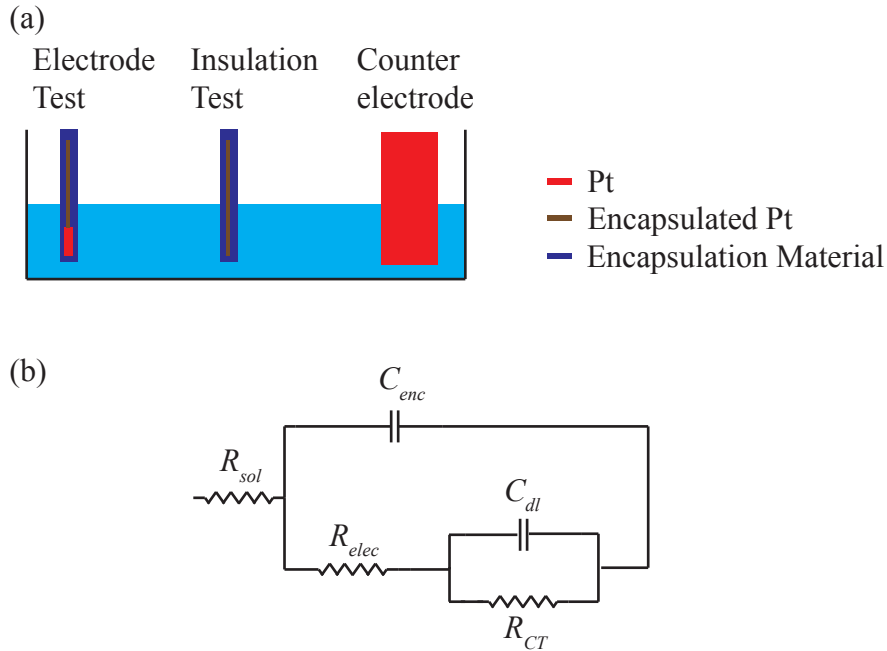


Figure 4-2: Electrochemical Impedance Spectroscopy. (a) Test setup for electrodes and insulation tests. (b) Model for encapsulation with degradation or electrode on an encapsulated wire.

parylene-C given its ability to dramatically change surface properties such as roughness and surface energy of the polymers[157][158]. In order to investigate suitable methods for improving parylene-C to parylene-C adhesion, test structures are fabricated so that the effects of various plasma treatments, chemical treatments and annealing treatments are investigated as methods to improve adhesion between the two parylene-C layers.

#### 4.1.2.1 Process flow for test structure fabrication

Test structures are fabricated on 4 inch soda lime glass wafers to eliminate any effects of substrate conduction on the test structures. The test structures are fabricated as described in Figure 4-3. A 2.2  $\mu\text{m}$  or 4.5  $\mu\text{m}$  of parylene-C is deposited on the wafers that are treated with adhesion promoter. 127 nm of Pt is sputter deposited and patterned using lift-off as shown in Figure 4-3(a). Different surface treatments are applied to different wafers at this point. Another 2.2  $\mu\text{m}$  or 4.5  $\mu\text{m}$  of parylene-C is then deposited and is followed by a 20 nm or 33 nm Cr deposition. The Cr is patterned

using a wet etch as seen in Figure 4-3(b). The parylene-C is then etched for 40 minutes (2 layers of 2.2  $\mu\text{m}$ ) or 80 minutes (2 layers of 4.5  $\mu\text{m}$ ). The remaining resist and Cr is then removed. Details of the fabrication steps can be found in Appendix A.

Optical images of devices fabricated at different points of the process are shown in Figure 4-4. In Figure 4-4(a) and (b), the images are taken after lift-off is performed, corresponding to Figure 4-3(a). Devices that are completely fabricated prior to dicing are shown in Figure 4-4(c) and (d). A photograph of a device after dicing is shown in Figure 4-4(e). A fabricated test electrode is shown in Figure 4-4(f).

The following treatments are investigated:

1. 1 min, 100 W, barrel etch using  $\text{O}_2$  plasma as a descum step after photoresist development of the first parylene-C surface just prior to deposition of the second parylene-C layer;
2. Creating a superhydrophobic surface on the first layer of parylene-C[159] using a combination of 5 min of  $\text{O}_2$  RIE followed by 1 min  $\text{SF}_6$  RIE. The result of this is the fluorination of the surface of parylene-C;
3. A 1 min  $\text{Ar}^+$  ion mill after photoresist development of the parylene-C surface just before the deposition of the second parylene-C layer. This process, like the barrel etch, acts as a descum step. However, this process isolates the chemical effect of the  $\text{O}_2$  on parylene-C because  $\text{Ar}^+$  is inert;
4. Treating the surface of the first parylene-C layer with A-174, a adhesion promoter typically used to improve adhesion between parylene-C and Si prior to deposition of the second parylene-C layer; and
5. Annealing the device as a last step to  $300^\circ\text{C}$ , beyond the melting point of parylene-C ( $290^\circ\text{C}$ ) at 10 mT  $\text{N}_2$  for 3 hours followed by a gradual cooling step of about 2-3 hours.

The treatments cover a range of different surface treatments ranging from a superhydrophobic surface (using the fluorination technique listed as item (2) and a

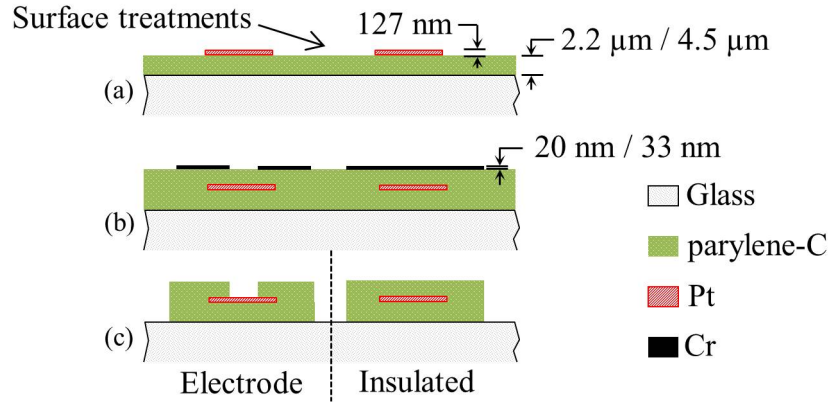


Figure 4-3: Process flow to fabricate test devices to investigate different methods of improving encapsulation properties of parylene-C

hydrophilic surface using the oxygenation technique listed as item (1). Other techniques used to improve parylene-C to parylene-C adhesion in literature such as heating parylene-C to beyond its melting point[105] are also explored i.e. item (5).

#### 4.1.2.2 Determination of surface modification efficacy of plasma treatments by XPS

The effects of the various surface treatments namely fluorination to create a hydrophobic surface and oxygen plasma is compared with untreated parylene-C using XPS to determine the efficacy of the various treatments in modifying the surface chemistry of the samples. XPS works by using the photoelectric effect. The sample of interest is exposed to X-ray radiation from an X-ray source which results in emission of photoelectrons. The kinetic energy of the photoelectrons is related to the binding energy as

$$E_k = h\nu - BE - \phi \quad (4.1)$$

where  $E_k$  is the kinetic energy of the emitted photoelectron,  $h\nu$  is the energy of the X-ray photon (such as an Al K- $\alpha$  source with mean of energy of 1486.7 eV), BE is the binding energy and  $\phi$  is the work function for conducting samples or a term that captures surface potential uncertainties [160]. By measuring the kinetic energies of the emitted photoelectrons and compensating for  $\phi$ , the BE can then be determined.

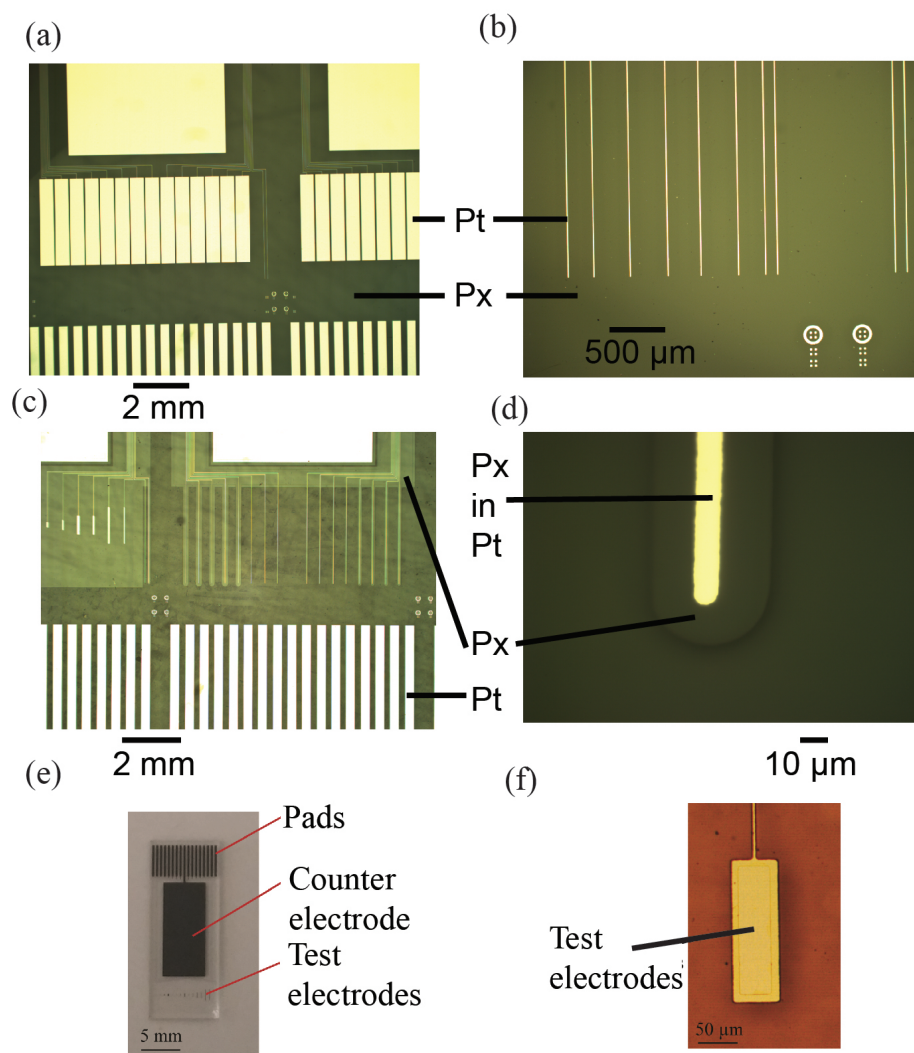


Figure 4-4: Optical images of fabricated test structure chips. (a) After Pt lift-off. (b) Zoomed-in image of test structures after lift-off. (c) After patterning of parylene-C. (d) Zoomed-in image of test structure after patterning of parylene-C. (e) Image of a fabricated test structure chip showing the location of the pads, counter electrode and test electrodes. (f) Image of another test structure with an exposed electrode.

Various surface properties of the material such as the elemental composition and chemical states of the elements are determined by measuring intensity of photoelectrons (in counts per second) at different energy levels. The resulting plot of intensity versus energy is the XPS spectrum. The measured spectrum of binding energies does not show discrete lines but rather peaks. This is due to the lines being broadened because of various effects such as lifetime broadening arising from a finite lifetime of a state that results in a Lorentzian line-shape; and doppler broadening arising from thermal motion that results in a Gaussian line-shape[161]. Hence, in order to identify the various elements, a fit is performed using a Lorentzian-Gaussian function that consists of the convolution of a Gaussian and a Lorentzian. XPS is used because it is extremely surface sensitive since the inelastic mean free path of an electron ( $\lambda$ ) in a solid is on the order of 1-3.5 nm for Al K- $\alpha$  radiation, which gives a sampling depth ( $3\lambda$ ) of approximately 3-10 nm [162]. A limitation of XPS is that it cannot be used to detect H since H has only one electron that participates in chemical bonding.

In this thesis, all XPS is done using an ESCALAB 250 XI Thermo Scientific XPS with a monochromated Al K- $\alpha$  source. For all samples, a survey scan is first performed with 1 eV energy steps and taking an average over two scans. Once elements have been identified in the survey scan, a detailed scan is performed across the relevant energy ranges for the various elements with 0.1 eV energy steps and taking an average over five scans. The detailed scan can reveal more information about the element. Due to the different energy step sizes for the survey scan and the detailed scan, the dwell time and absolute counts for the detailed scan and survey scan will differ considerably. Furthermore, the auto height adjustment used to optimize the count number prior to every scan will significantly affect the absolute value of counts for every scan. In practice, the peaks are used for element identification and hence, the relative counts rather than the absolute counts are more significant.

Samples are prepared by depositing 4.5  $\mu\text{m}$  of parylene-C on a blank Si wafer that is then cleaved into small approximately 2 cm by 2 cm pieces. One of the pieces (referred to as fluorinated parylene-C) is treated with 5 min of O<sub>2</sub> RIE at 50 W 50 mT with 14.2 sccm O<sub>2</sub> gas flow using the Trion RIE machine followed by 1 min of SF<sub>6</sub>

RIE 100 W 100 mT 20 sccm as described in Section 4.1.2 Treatment (2). Another piece (referred to as oxygenated parylene-C) is treated with 1 min of O<sub>2</sub> plasma using an IPC barrel etcher with 1 Torr pressure and 100 W as described in Section 4.1.2 Treatment (1).

#### **4.1.2.3 XPS results on untreated parylene-C**

The result of XPS performed on 4.5 μm of parylene-C on a cleaved Si wafer as-deposited is shown in Figure 4-5. Based on the result of the quantitative analysis of parylene-C tabulated in Table 4.1, the atomic ratio Cl:C is approximately 1:7.5. This is close to the expected value of 1:8 based on the chemical structure of parylene-C.

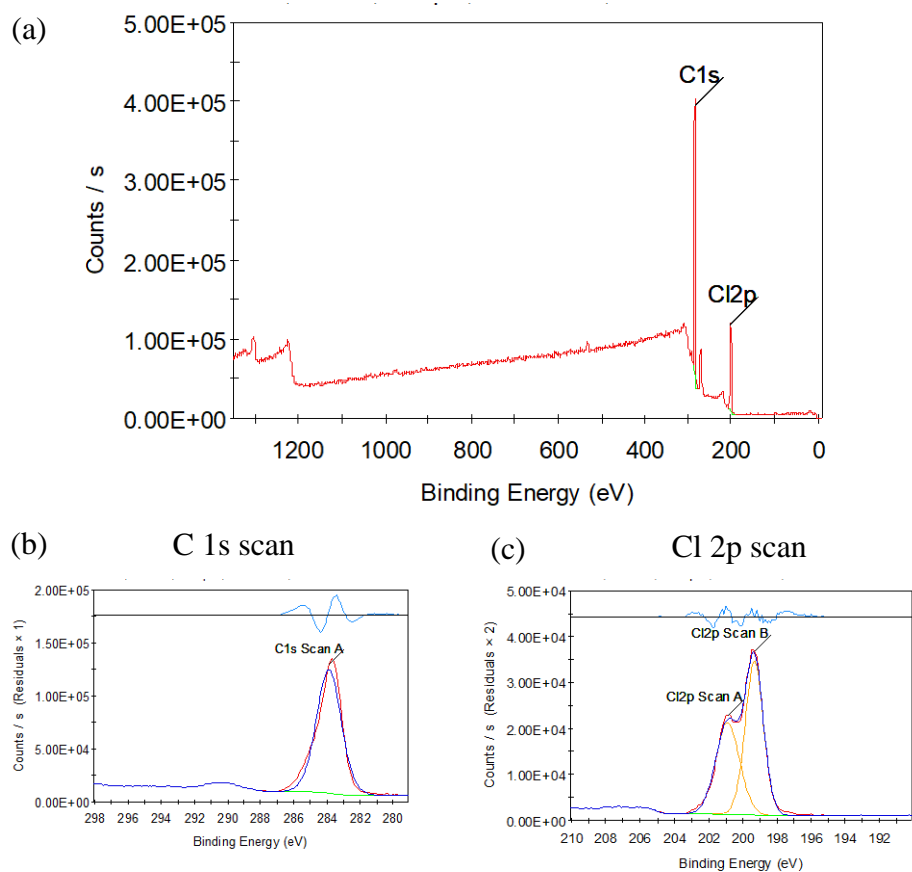


Figure 4-5: XPS of as-deposited parylene-C. (a) Survey scan of sample. (b) Detailed C 1s scan. (c) Detailed Cl 2p scan. The green lines are the fitted background spectrum. The orange lines are the fitted individual peaks. The dark blue lines are the fitted summed peaks. The red lines are the measured spectra. The light blue lines are a graphical plot, in arbitrary units, showing the variation in the difference between the fit and the measured values across binding energies.

#### 4.1.2.4 XPS results on fluorinated parylene-C

The result of XPS performed on fluorinated parylene-C is shown in Figure 4-6. Based on the result of the quantitative analysis of fluorinated parylene-C tabulated in Table 4.2, the ratio O:Cl:C:F is approximately 1:1.1:20.2:20.2. Since the ratio Cl+F:C is approximately 1:1, this suggests that the mechanism for fluorination is likely substitution of H and Cl with F as the structure of the untreated parylene-C monomer consists of 8 C atoms, 7 H atoms and 1 Cl atom. The low fraction of Cl:C in fluorinated parylene-C relative to untreated parylene-C supports this hypothesis. The remaining O present could be from oxygen embedded from the O<sub>2</sub> RIE carried out before the SF<sub>6</sub> RIE and the remaining Cl suggests that either some of the Cl in parylene-C remains unsubstituted or the fluorination occurs only in the top few nm and that the penetration depth of the photoelectrons exceed that thickness.

Table 4.1: Quantitative Analysis of XPS performed on parylene-C

Peak	FWHM (eV)	Area (counts/s-eV)	Sensitivity Factor	Atomic %
C 1s	1.74	220446.72	1	88.2
Cl 2p Scan A	1.62	35357.33	2.741	5.2
Cl 2p Scan B	1.24	45463.7	2.741	6.6

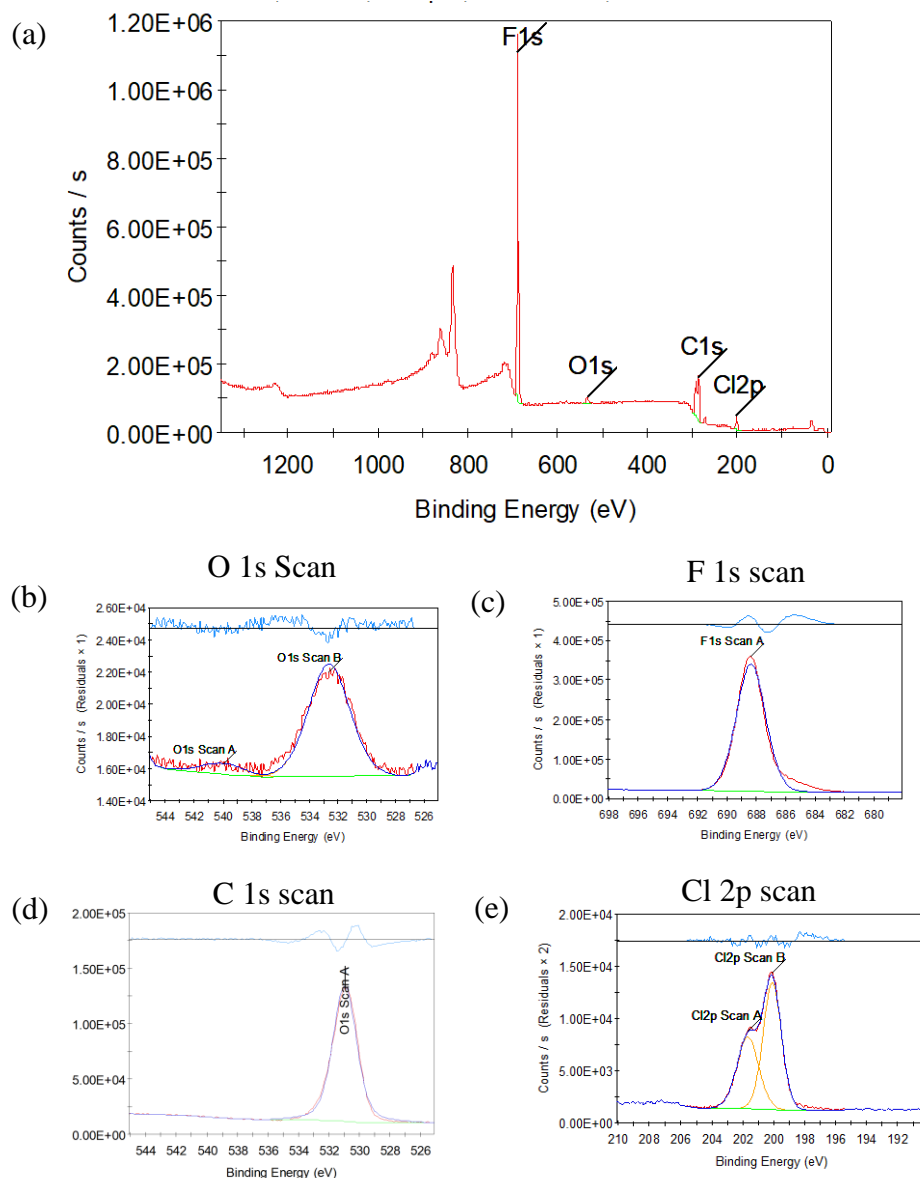


Figure 4-6: XPS of fluorinated parylene-C. (a) Survey scan of sample. (b) Detailed O 1s scan. (c) Detailed F 1s scan. (d) Detailed C 1s scan. (e) Detailed Cl 2p scan. The green lines are the fitted background spectrum. The orange lines are the fitted individual peaks. The dark blue lines are the fitted summed peaks. The red lines are the measured spectra. The light blue lines are a graphical plot, in arbitrary units, showing the variation in the difference between the fit and the measured values across binding energies.

Table 4.2: Quantitative Analysis of XPS performed on fluorinated parylene-C

Peak	FWHM (eV)	Area (CPS.eV)	Sensitivity Factor	Atomic %
Cl 2p Scan A	1.64	12259.14	2.741	1.1
Cl 2p Scan B	1.37	18065.78	2.741	1.6
O 1s Scan A	3.37	2443.93	2.881	0.2
O 1s Scan B	3.37	25506.04	2.881	2.1
C 1s Scan A	1.37	51512.68	1	12.5
C 1s Scan B	1.5	47782.13	1	11.6
C 1s Scan C	1.79	33427.67	1	8.1
C 1s Scan D	3.3	54481.44	1	13.2
C 1s Scan E	1.41	8835.43	1	2.1
F 1s	2.3	806669.78	4.118	47.5

#### 4.1.2.5 XPS results on oxygenated parylene-C

The result of XPS performed on oxygenated parylene-C is shown in Figure 4-7. Based on the result of the quantitative analysis of oxygenated parylene-C tabulated in Table 4.3, the ratio of Cl:O:C is 1:2.8:7.9. Since the ratio of Cl:C is close to 1:8, it is likely that the Cl is not substituted by the oxygenation. On the other hand, it appears that the the reaction occurs by substitution of H with O. Since the Cl:O ratio is close to 3, it is possible that the H atoms that are substituted are the H atoms attached to the aromatic ring.

Based on the results of the XPS, the plasma treatments have successfully modified the surface of the parylene-C. If the aromatic H are indeed substituted with O or F, it is expected that oxygenation of parylene-C would result in a more reactive layer compared to untreated parylene-C whereas fluorination of parylene-C would result in a less reactive layer because of the effect of the respective species on the electron

Table 4.3: Quantitative Analysis of XPS performed on oxygenated parylene-C

Peak	FWHM (eV)	Area (counts/s-eV)	Sensitivity Factor	Atomic %
C 1s	1.68	146689.38	1	67.5
O 1s	1.62	150308.64	2.881	24.0
Cl 2p3	1.24	32980.77	1.78	8.5

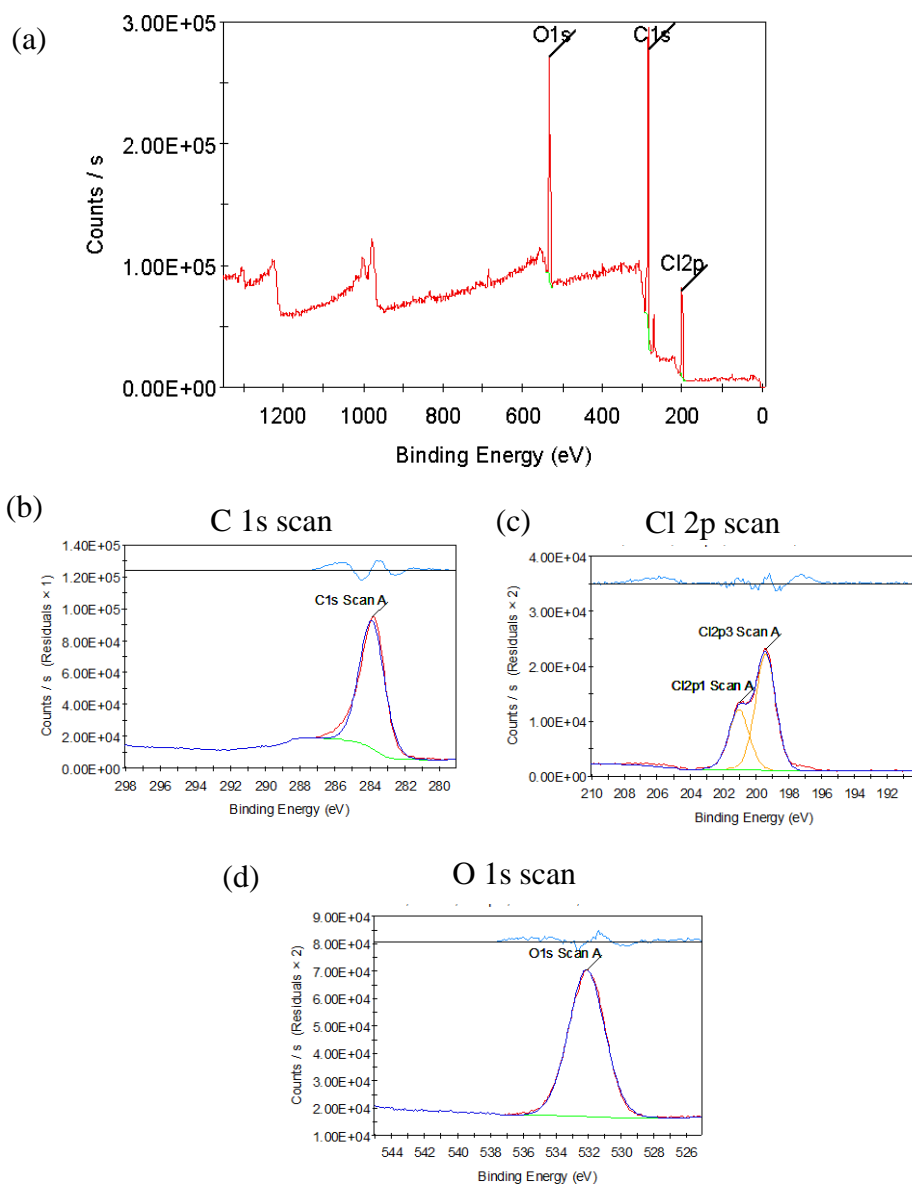


Figure 4-7: XPS of oxygenated parylene-C. (a) Survey scan of sample. (b) Detailed C 1s scan. (c) Detailed Cl 2p scan. (d) Detailed O 1s scan. The green lines are the fitted background spectrum. The orange lines are the fitted individual peaks. The dark blue lines are the fitted summed peaks. The red lines are the measured spectra. The light blue lines are a graphical plot, in arbitrary units, showing the variation in the difference between the fit and the measured values across binding energies.

density of the benzene ring.

#### **4.1.2.6 Results of EIS performed on samples with various surface treatments.**

The typical impedance at 0.1 Hz for various test structures is plotted against time in Figure 4-8. The results of the tests on structures containing alumina (PA-n, PA-a, PA-i) that are in Figure 4-8 will be discussed in Section 4.2.1.5. As discussed in Section 4.1.1, higher, more stable impedance indicates better electrical insulation. The ion mill treatment (P-i) significantly reduces the impedance of the test structure at 0.1 Hz over the 2000 hours measured. Within the time frame measured, parylene-C with regular oxygen plasma descum treatment (P-n) results in high impedance of the test structures and performed the best as compared with parylene-C treated with A174 (P-a), fluorinated parylene-C (P-f) and parylene-C treated with ion milling (P-i).

There does not appear to be any significant correlation of insulation performance with hydrophobicity (P-f is the most hydrophobic, P-n is the most hydrophilic but P-i performs worse than P-f). This suggests that the mechanism for improvement in adhesion for the P-n case is the increased chemical reactivity introduced by the oxygen plasma step as suggested by the XPS results and not simply due to changes in surface energy of the parylene-C.

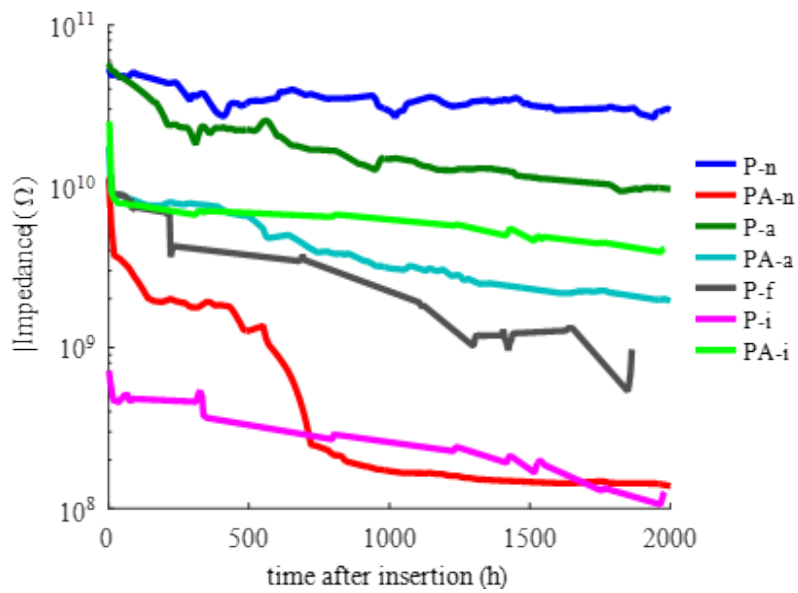


Figure 4-8: Magnitude of impedance measured at 0.1 Hz over time in hours to determine encapsulation properties using various treatments. P-n, P-a, P-f, P-i indicates parylene-C only encapsulation with various treatments (regular oxygen plasma descum treatment, A174 treatment, fluorination treatment and ion mill treatment respectively). PA-n, PA-a, PA-i indicate similar surface treatments with a parylene-C-alumina hybrid encapsulation scheme. Measurement is performed by Mats Forssell.

#### 4.1.2.7 Results of EIS performed on samples with annealing

The effect of annealing is also evaluated on fabricated test structures as seen in Figure 4-9. The design of the test structure is shown in Figure 4-4(d), but with the 50  $\mu\text{m}$  width insulation on each side of the Pt. The higher impedance at 0.1 Hz of the annealed test structures indicates better insulation performance when compared to the unannealed samples. The annealing is performed at 300°C for 3 hours in a  $\text{N}_2$  atmosphere.

Hence, the results suggest that a oxygen descum with annealing with the 300°C annealing treatment produces the best parylene-C to parylene-C adhesion out of all the tests.

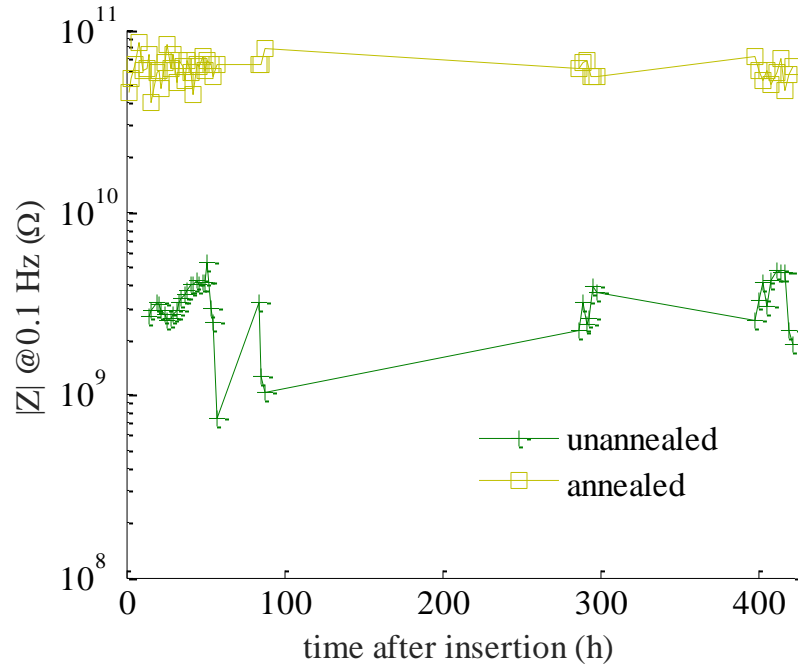


Figure 4-9: Test results comparing annealed and unannealed chips for test structures with 2.2  $\mu\text{m}$  thick, 50  $\mu\text{m}$  wide insulation.

## 4.2 ALD ceramics for flexible neural probes

As mentioned in Section 2.1.4, the method of deposition is an important consideration when depositing a thin film to ensure that there is sufficient coverage over the entire structure of the device. ALD is one process that is used to deposit a conformal layer of film. It achieves an extremely conformal and precisely deposited film by utilizing two self-limiting reactions. By alternating between the two self-limiting reactions, films are deposited one atomic layer at a time as shown in Figure 4-10. For example,  $\text{Al}_2\text{O}_3$  can be deposited using trimethylaluminum (TMA) as the first precursor and  $\text{H}_2\text{O}$  or plasma  $\text{O}_2$  as the other precursor with  $\text{CH}_4$  as the byproduct. In reality, a number of different reactions can occur [163]. For example, TMA reacts with the hydroxyl group ( $-\text{OH}$ ) giving  $\text{CH}_4$  as a byproduct:



where  $||$  represents the surface of the substrate. However, it is also possible for a simultaneous reaction with two hydroxyl groups:



There are a large number of oxides, nitrides, metals and other compounds that can be deposited using ALD[164]. If coverage of very high aspect ratio structures is desired, the step coverage of the process can be controlled by the delay time between the two reactions[164].

The combination of ceramic and polymer layers (in particular  $\text{Al}_2\text{O}_3$  has been used in rigid Si MEAs in a study from the University of Utah [146] but the results of the studies are mixed. The study reported the use of 52 nm of ALD alumina and 6  $\mu\text{m}$  thick parylene-C as a suitable encapsulation material for Utah probes, achieving much better encapsulation properties compared with parylene-C alone. However, another later study from the same group [165] affirmed that the alumina did not provide much improvement (parylene-C only samples survived much longer for most of the test structure designs) because of its ease in being etched in saline and that previous results are largely due to corrosion of electrodes. In [144], it is found that the same 50 nm of alumina followed by 6  $\mu\text{m}$  thick parylene-C encapsulation scheme only provides 5 - 11 days of encapsulation at physiological conditions using an Mg test. Many of the discrepancies arise in how insulation failure is defined. In [165], failure is defined as a leakage current exceeding 1 nA at 5V bias whereas the test in [144] uses Mg which is a chemical method of testing. Furthermore, the test structures differ significantly and in [165], it is shown that the choice of test structures can result in conflicting results. Hence, it is often difficult to compare results obtained from different groups.

The nature of ALD deposition allows for other hybrid materials to be created by alternating between more than two elements. For example, instead of alternating between TMA and  $\text{H}_2\text{O}$  as depicted in Figure 4-10, cycling between TMA,  $\text{H}_2\text{O}$ , Tetrakis(dimethylamido) titanium(IV) (TDMA-Ti),  $\text{H}_2\text{O}$  repeatedly would give

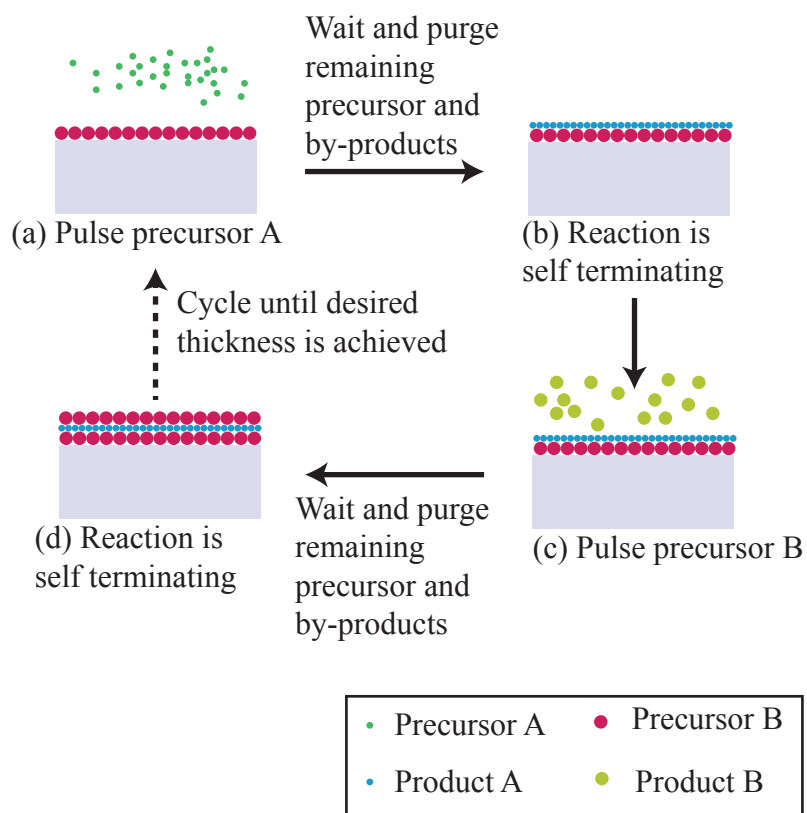


Figure 4-10: Description of ALD process.

a  $\text{Al}_2\text{O}_3\text{-TiO}_2\text{-Al}_2\text{O}_3\text{-TiO}_2\text{...}$  hybrid nanolaminate material. By modifying the sequence and number of steps in each cycle, it is possible to change the thicknesses of each monolayer and hence tune the physical properties of the hybrid material. The nanolaminate material can have different properties compared with its constituent materials when the layer thicknesses are less than the length scale that determines that property[164]. Nanolaminates have also been used to fabricate Bragg mirrors and charge dissipative coatings for RF MEMS switches by relying on the ability to easily tune the property of the material [164].

A significant number of studies with regards to barriers with are in the area of OLEDs because exposure to atmospheric moisture and oxygen results in oxidation of the materials in the OLED[166][167][145][151][168]. One major difference between OLEDs and neural probes is that OLEDs are either fabricated on glass or 100  $\mu\text{m}$  thick plastic substrates which are much stiffer compared to the envisioned flexible neural probes. Another major difference between the application of OLEDs and neural probes is that for OLEDs, the barrier layers only need to encapsulate the entire device without any need for patterning. For neural probes, it is usually necessary to pattern the encapsulation which means that penetration through interfaces play a larger role.

Since the  $\text{Al}_2\text{O}_3\text{-TiO}_2$  nanolaminates [151] have been shown to have promising WVTR properties in rigid substrates,  $\text{Al}_2\text{O}_3\text{-TiO}_2$  nanolaminates are engineered to be incorporated into flexible neural probes. The choice of this nanolaminate is also motivated by biocompatibility.  $\text{TiO}_2$  is found to be biocompatible in neuroprosthetic systems [169]. In [170], ALD alumina is found to be biocompatible.

#### **4.2.1 Test structures to investigate ALD ceramics**

In order to choose the appropriate ceramic to use as a water barrier, an initial test is performed using Pt encased in the various ceramics alone. Three ceramics are namely:

1.  $\text{Al}_2\text{O}_3$ ,
2.  $\text{TiO}_2$ , and

3. a nanolaminate of  $\text{Al}_2\text{O}_3$  and  $\text{TiO}_2$

are investigated.

The choice of ceramics used in this study is motivated by results in the literature. Given the available literature on using  $\text{Al}_2\text{O}_3$  as an encapsulation material in Si based probes[146], 47 nm of  $\text{Al}_2\text{O}_3$  is investigated to find out if the encapsulation properties can be used in flexible probes as well. In addition, 42 nm of  $\text{TiO}_2$  is investigated as it is reported to have better resistance to water corrosion as compared with  $\text{Al}_2\text{O}_3$  [171]. A nanolaminate of  $\text{TiO}_2$  and  $\text{Al}_2\text{O}_3$  is also used as 50 nm of it is reported to have better WVTR as compared with 50 nm of  $\text{Al}_2\text{O}_3$  and 50 nm of  $\text{TiO}_2$  alone[151] when deposited on 200  $\mu\text{m}$  polyethylene naphthalate which is a polyester with good barrier properties. A description on nanolaminates is provided in Section 4.3.

#### 4.2.1.1 Etching of ALD ceramics

The etching of many ALD ceramics are not well studied because the majority of studies use a blanket film of ALD and do not require any etching. However, for the purposes of neural probes in this thesis, it is necessary to perform etching of the ALD ceramics since lift-off processing is more suited for deposition techniques which are directional. Hence, different techniques are investigated to etch the various ceramics.

The choice of techniques range from using a wet-etchant to various dry etching techniques and are chosen because some of these techniques are known to etch either  $\text{Al}_2\text{O}_3$ ,  $\text{TiO}_2$  or both [172]. Ion milling is also attempted because it physically etches various materials. There has been no known attempt in the literature to etch the nanolaminate. Buffered HF Improved (BHF) (Transene, Danvers, MA) is a mixture of HF and typically  $\text{NH}_4\text{F}$  which acts as a buffer so that the etch rate becomes more controlled. In addition, BHF penetrates photoresist less as compared with HF and hence is less likely to cause problems with delamination of photoresist[173].

Etch rates are obtained from films deposited on 1 inch Si test coupons, protecting part of the coupon with resist, and measuring the step height using a profilometer after 30 s of etching. Based on the test results tabulated in Table 4.4, BHF is a suitable etchant for  $\text{Al}_2\text{O}_3$ ,  $\text{SF}_6$  RIE is a suitable method to etch  $\text{TiO}_2$  and the  $\text{Cl}_2$

ICP-RIE is a suitable method of etching the nanolaminate. BHF is not used to etch the nanolaminate because of the observation of residues formed after the etch as shown in Figure 4-11(a-c). Using  $\text{Cl}_2$  ICP-RIE results in a much cleaner etch as shown in Figure 4-11(d).

#### 4.2.1.2 Fabrication of test structures with ALD ceramics only

To investigate these ceramics as barrier materials, test structures are fabricated on 4 inch soda lime glass (University Wafer) to eliminate any effects of substrate conduction on the test structures. The test structures are fabricated as described in Figure 4-12. The respective ceramic to be investigated (47 nm of  $\text{Al}_2\text{O}_3$ , 42 nm of  $\text{TiO}_2$  or a 78 nm nanolaminate of  $\text{Al}_2\text{O}_3$  and  $\text{TiO}_2$ ) is deposited using a Fiji ALD (Cambridge Nanotech, Waltham, MA) machine at  $150^\circ\text{C}$ . Deposition of  $\text{Al}_2\text{O}_3$  uses 500 ALD cycles with trimethyl aluminum (TMA) and  $\text{H}_2\text{O}$  used as precursors. Deposition of  $\text{TiO}_2$  uses 1100 ALD cycles with Tetrakis(dimethylamido)titanium(IV) (TDMA-Ti) and  $\text{H}_2\text{O}$  used as precursors. For the nanolaminate, 550 cycles is performed with each cycle consisting of a TMA step,  $\text{O}_2$  plasma step, TDMA-Ti step, and a  $\text{O}_2$  plasma step.

A lift-off process is then performed to pattern a Ti-Pt-Ti stack. After patterning reversal photoresist (AZ5214E) using a MA6 exposure tool (Karl-Suss, Garching, Germany), 10 nm of Ti, 127 nm of Pt and 10 nm of Ti (50 W at 5 mT, 20 sccm Ar flow, 34 s) is deposited by sputtering using the 2400-6J deposition system. A second layer of the same ceramic is deposited. A positive resist (AZ4210, MicroChemicals GmbH, Ulm, Germany) is patterned and the ceramic is etched using  $\text{SF}_6$  RIE with

Table 4.4: Measured etch rates of different ALD ceramics

	$\text{TiO}_2$	$\text{Al}_2\text{O}_3$	$\text{TiO}_2 / \text{Al}_2\text{O}_3$ NL
Buffered HF	Not etched	40 nm/min	40 nm/min
Trion RIE $\text{SF}_6$ plasma	10 nm/min	Not etched	Not etched
Versaline ICP-RIE $\text{Cl}_2$ plasma	40 nm/min	50 nm/min	30 nm/min
Ion mill	5 nm/min	5 nm/min	4 nm/min

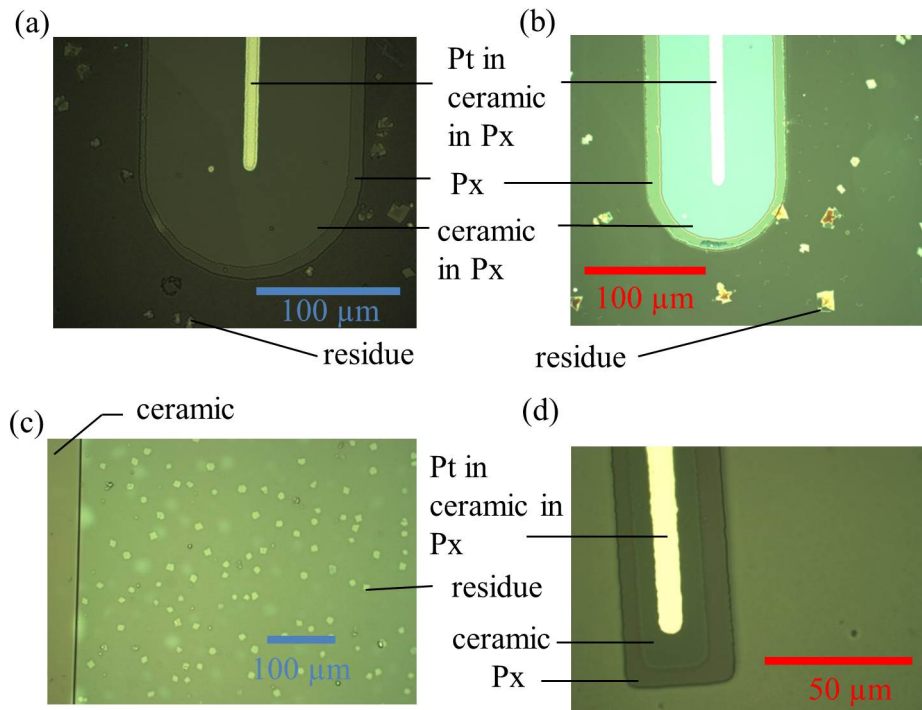


Figure 4-11: Microscope images showing residue left after BHF etch of the nanolaminate. (a) Optical image showing residue in a chip that has completed fabrication (parlylene-C layer is also patterned). (b) Differential Interference Contrast (DIC) image showing residue in a chip that has completed fabrication. (c) Optical image showing residue just after the nanolaminate etch. (d) Optical image showing test structure processed using  $\text{Cl}_2$  ICP-RIE.

a Phantom II RIE for  $\text{TiO}_2$ , BHF wet etch (Transene, Danvers, MA) for  $\text{Al}_2\text{O}_3$  and  $\text{Cl}_2$  based ICP-RIE using the Versaline (Plasma-Therm, Saint Petersburg, FL) for the nanolaminate. Following this, the remaining photoresist is removed using acetone.  $\text{O}_2$  plasma cleaning is performed using a barrel etcher (International Plasma Corporation, Hayward, CA) after every development and photoresist stripping step. Details of the fabrication steps can be found in Appendix A.

Fabricated devices at different stages of fabrication are shown in Figure 4-13 for  $\text{TiO}_2$  and in Figure 4-14 for the nanolaminate test structures.

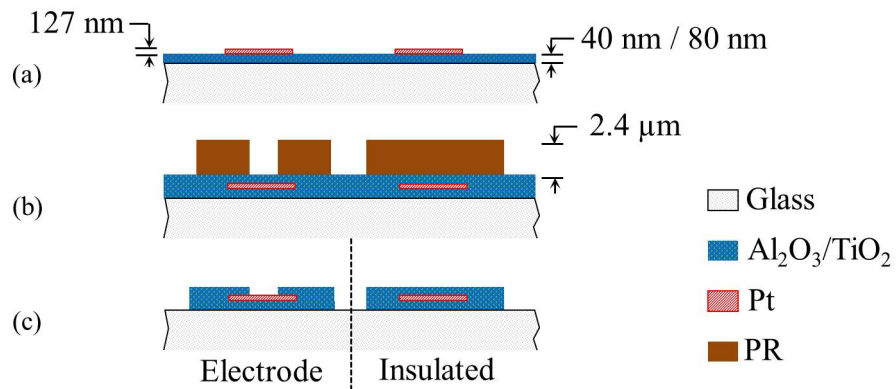


Figure 4-12: Process flow to fabricate test devices to investigate different methods of improving encapsulation properties of ceramics

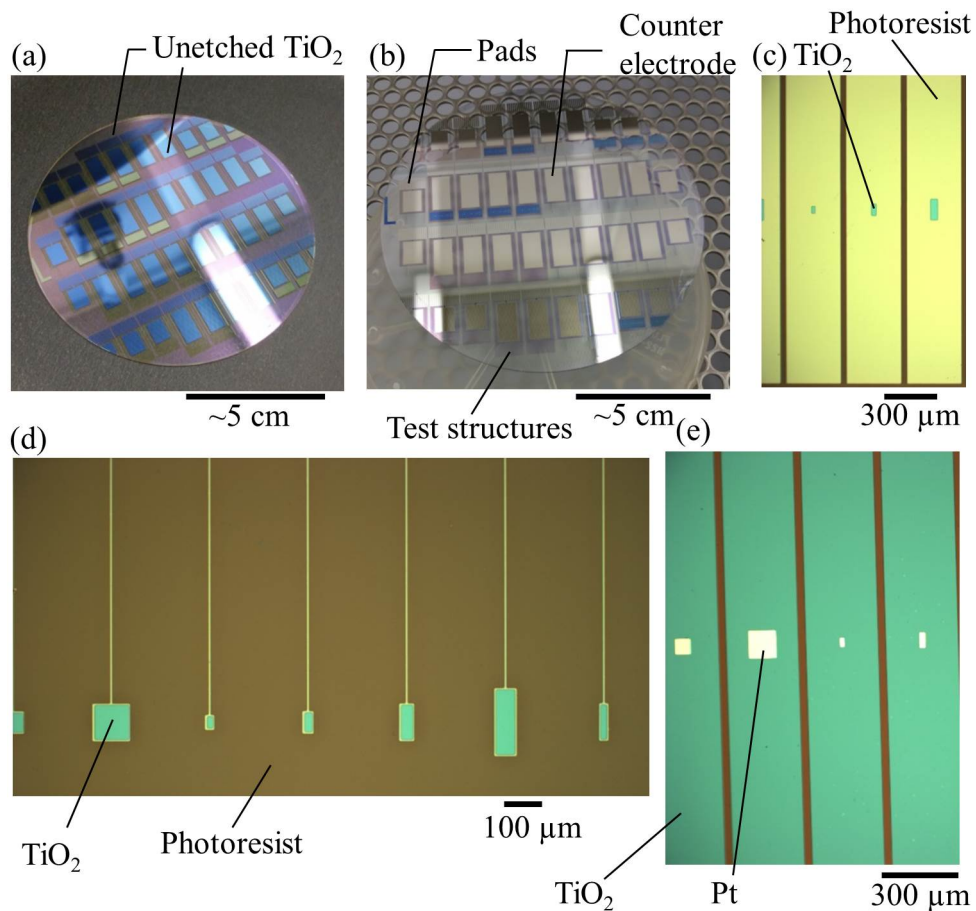


Figure 4-13: Optical images of test structures to test  $\text{TiO}_2$  at different points of processing. (a) Glass wafer after second layer of  $\text{TiO}_2$  deposition. (b) Glass wafer after  $\text{TiO}_2$  etch and resist removal. (c) Test structure after photoresist patterning of  $\text{TiO}_2$ . (d) Other test structures after photoresist patterning of  $\text{TiO}_2$ . (e) Test structures such as those in (c) after  $\text{TiO}_2$  etch and resist removal.

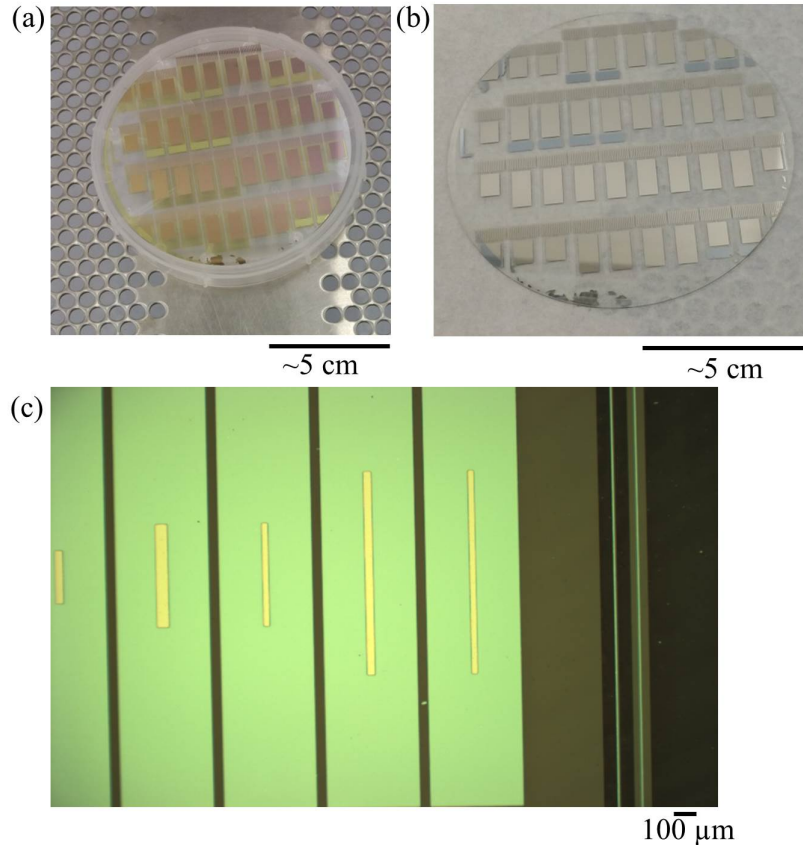


Figure 4-14: Optical images at different points of processing for the nanolaminate test structures. (a) After 1 minute of etching in BHF (b) After etching of the nanolaminate is completed and photoresist is stripped. (c) Microscope image of fabricated test electrodes and encapsulated test structures after completion of fabrication.

#### 4.2.1.3 Result of EIS tests on ALD ceramics

The EIS at 0.1 Hz is performed at 60°C to accelerate the ageing process. The result of the EIS is shown in Figure 4-15. Although the use of 60°C to accelerate the ageing process allows for faster identification of failures, in order to compare between the different materials, it is necessary to assume that the rate of ageing with respect to temperature is the same which might not be true. Nevertheless, the results give an understanding of the failure modes.

Compared to parylene-C only test structures (P-n), alumina only test structures (A-n) have lower impedances throughout the entire study. This can be attributed to the corrosion of alumina in water[151]. Another possible cause of the lower impedance of A-n versus P-n is that the alumina is thinner and has a higher dielectric constant compared with parylene-C. The titania only (T-n) test structure has a much lower impedance because of the relatively high conductivity of the material which results in an effective weak short between the different channels on the same chip. Comparatively, the nanolaminate test structure (N-n) maintains a higher impedance compared to P-n and A-n test structures likely because of its improved resistance to corrosion[151].

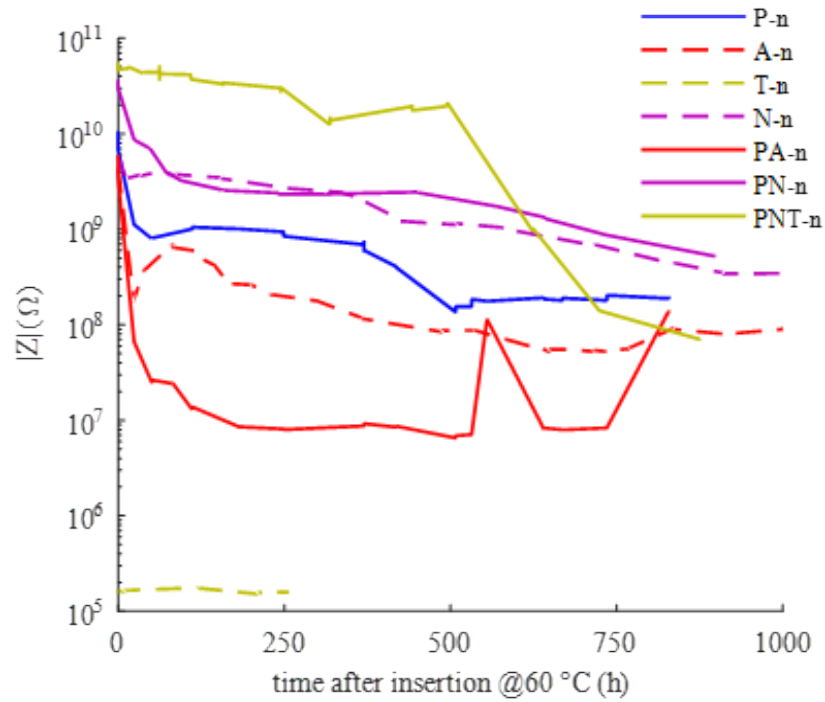


Figure 4-15: Magnitude of impedance versus time at 0.1 Hz versus of time of samples aged at 60°C. The increased temperature accelerates the time to failure. P-n refers to the sample with parylene-C insulation only. A-n refers to the sample with ALD alumina insulation only. T-n refers to the sample with titania insulation only. N-n refers to the sample with TiO<sub>2</sub>/Al<sub>2</sub>O<sub>3</sub> nanolaminate (NL) insulation only. PA-n refers to the sample with parylene-C/alumina hybrid encapsulation only. PN-n refers to the sample with parylene-C/nanolaminate hybrid encapsulation only. PNT-n refers to parylene-C/nanolaminate/TiO<sub>2</sub> triple encapsulation. Measurement is performed by Mats Forssell.

#### 4.2.1.4 Test structures to investigate a hybrid encapsulation strategy using ALD ceramics combined with parylene-C

In order to combine the advantages of flexibility of polymers and the encapsulation properties of ceramics, a hybrid encapsulation scheme is used. Three different hybrid encapsulations are attempted:

1. Parylene-C (2.2  $\mu\text{m}$ ) followed by 48 nm of alumina (PA),
2. Parylene-C (2.2  $\mu\text{m}$ ) followed by 78 nm of the nanolaminate (PN), and
3. Parylene-C (2.2  $\mu\text{m}$ ) followed by 5 nm of  $\text{TiO}_2$  followed by 78 nm of the nanolaminate (PNT)

The first hybrid encapsulation scheme is attempted based on the result by [146] which showed promising results when combining parylene-C and alumina. However, based on results when fabricated in-house, the performance of alumina is poor and is described in Section 4.2.1 which is corroborated with results from other groups [151].

In addition, for the case of the hybrid encapsulation scheme with alumina and parylene-C, different surface treatments are attempted (typical oxygen plasma descum (PA-n), A174 treatment (PA-a), and ion mill to replace oxygen plasma treatment (PA-i)).

The use of  $\text{TiO}_2$  alone is found to be unsuitable because of the low resistivity of  $\text{TiO}_2$  (35.7  $\Omega\text{-cm}$ ) that can result in shorts between interconnects (2 k $\Omega$  resistance between 1 cm long interconnects spaced 5  $\mu\text{m}$  apart). A continuous film is necessary if high interconnect density is desired. Hence, a hybrid encapsulation combining parylene-C and the nanolaminate is attempted. The poor adhesion of parylene-C on the nanolaminate is observed during fabrication resulting in a low yield. This resulted in development of a triple encapsulation scheme combining  $\text{TiO}_2$  as a adhesion layer between parylene-C and the nanolaminate.

The process to fabricate test structures with the hybrid encapsulation scheme is shown in Figure 4-16 for the PA and PN test structures and in Figure 4-17 for the PNT case. The fabrication step begins with deposition of 2.2  $\mu\text{m}$  of parylene-C. This

is followed by deposition of 48 nm of alumina (PA); 78 nm of the nanolaminate (PN); or 5 nm of TiO<sub>2</sub> followed by 78 nm of the nanolaminate (PNT) using the process described in Section 4.2. 10 nm of Ti, 127 nm of Pt and 10 nm of Ti is deposited by sputtering and patterned by lift-off. A second layer of the same ceramic is deposited (but 78 nm of the nanolaminate followed by 5 nm of TiO<sub>2</sub> for the triple encapsulation case). The ceramic is then patterned and etched using SF<sub>6</sub> RIE with a Phantom II RIE for TiO<sub>2</sub>, BHF wet etch (Transcene) for Al<sub>2</sub>O<sub>3</sub> and Cl<sub>2</sub> based ICP-RIE using the Versaline for the nanolaminate. The remaining resist is removed using acetone. After a O<sub>2</sub> plasma descum step (O<sub>2</sub> RIE is used for versaline processes because the resist exposed to Cl<sub>2</sub> is difficult to remove with O<sub>2</sub> plasma in the barrel etcher), a second layer of parylene-C is deposited (2.2 μm) followed by a 20 nm layer of Cr. The Cr is then patterned and wet etched. The parylene-C is then etched and any remaining photoresist and Cr is stripped. Details of the fabrication steps can be found in Appendix A.

Fabricated test structures are shown in Figure 4-18.

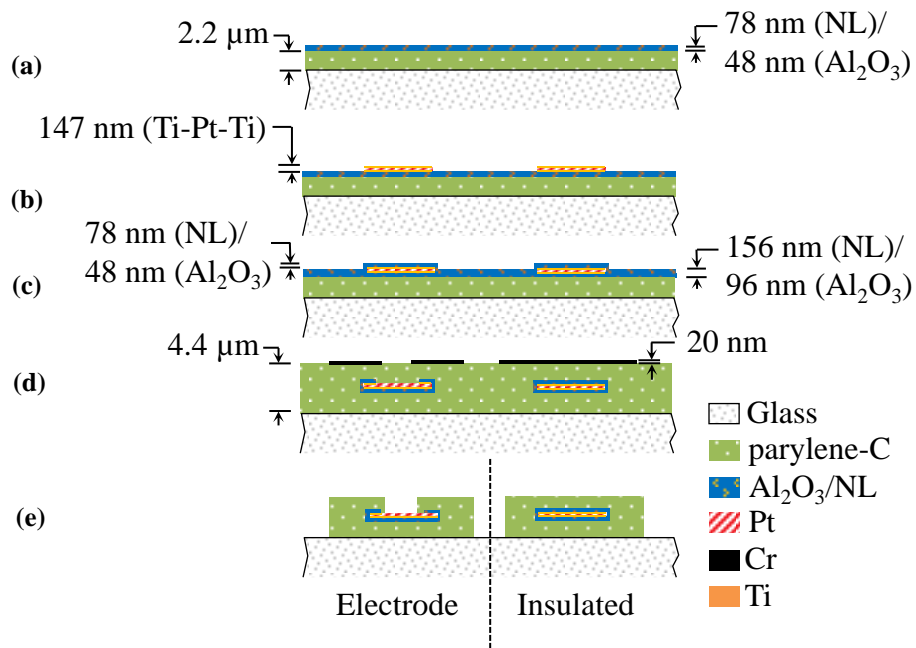


Figure 4-16: Process flow to fabricate test devices with parylene-C and alumina (PA) and with parylene-C and nanolaminate (PN). (a) Parylene-C and a ceramic is deposited. (b) Ti-Pt-Ti is deposited and patterned. (c) A second layer of ceramic is deposited. (d) The ceramic is patterned and a second layer of parylene-C is deposited. Cr is deposited and patterned for use as a hard mask. (e) parylene-C is etched and any remaining Cr is removed.

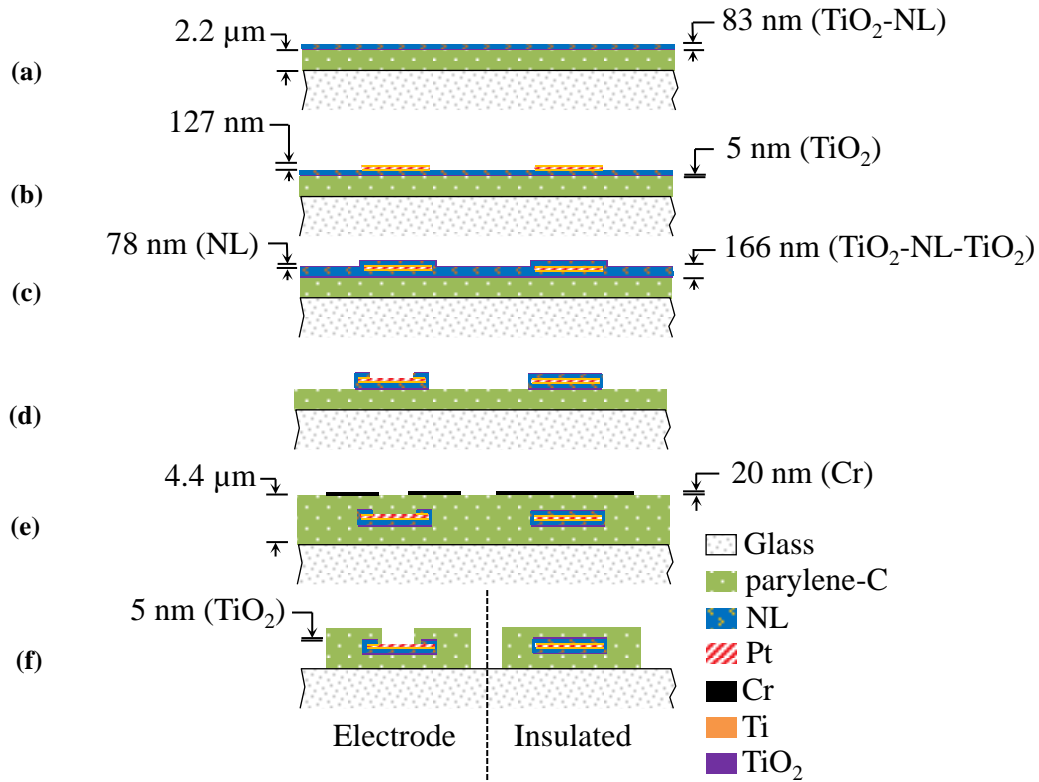


Figure 4-17: Process flow to fabricate test devices with parylene-C,  $\text{TiO}_2$  as an adhesion layer and nanolaminate (PNT). (a) Parylene-C is deposited followed by  $\text{TiO}_2$  and NL. (b) Ti-Pt-Ti is deposited and patterned. (c) A second layer of NL is deposited followed by  $\text{TiO}_2$ . (d)  $\text{TiO}_2$  and NL layers are patterned. (e) A second layer of parylene-C is deposited followed by Cr. Cr is patterned and used as a hard mask. (f) Parylene-C is patterned and any remaining Cr is removed.

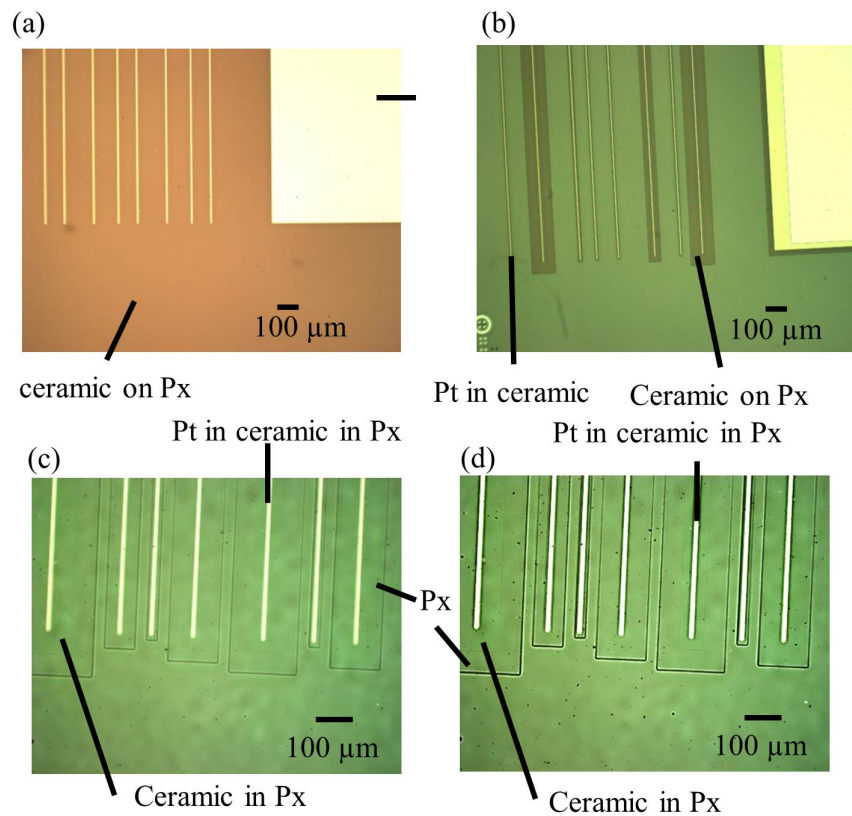


Figure 4-18: Optical images at different points of processing of hybrid encapsulation test structures. (a) After first Pt layer lift-off. (b) After patterning of ceramic layer. (c) After parylene-C outline patterning. The image is taken with a protective photoresist layer is on the structures after dicing. (d) A sharpened version of (c) with increased contrast so that the encased ceramic is more visible.

#### 4.2.1.5 Result of tests on hybrid parylene-C ALD ceramics insulation scheme

EIS at room temperature is performed on hybrid encapsulation schemes with parylene-C and alumina using different surface treatments. The results of the EIS are shown in Figure 4-8. With O<sub>2</sub> plasma descum treatment (PA-n), the magnitude of impedance at 0.1 Hz drops rapidly, likely because of poor adhesion between parylene-C and alumina. For both the cases where an ion mill treatment to replace O<sub>2</sub> plasma descum (PA-i) and A174 (PA-a) is used, the insulation remains more stable although it also decreases, indicating better adhesion but degradation because of other factors such as corrosion of the parylene-C layers.

EIS of samples aged at 60°C is also performed on the multilayered hybrid encapsulation schemes as shown in Figure 4-15, the parylene-C coated nanolaminate bilayer test structures (PN-n) have an initially high impedance that degrade to values approaching that of nanolaminate only test structures. This is likely due to the poor adhesion between parylene-C and nanolaminate. This delamination is also observed optically where parylene-C is seen to come off the test structures. For the case of parylene-C and alumina hybrid encapsulation scheme (PA-n), the impedance drops rapidly, even going below the A-n test test structures possibly due to a combination of poor adhesion between alumina and parylene-C and degradation of the alumina layer.

Of the hybrid encapsulation schemes, a combination of parylene-C with nanolaminate and titania as the adhesion layer between parylene-C and titania (PNT-n) provide the best encapsulation for the first 500 hours before decaying rapidly. The excellent insulation performance provided at the beginning is likely because of the good adhesion between parylene-C and titania and the resistance to corrosion of alumina and titania. When the parylene-C is compromised in certain regions, the layer of conductive titania is exposed to the solution that shorts a larger effective region in the structure to the potential of the solution and can result in rapid degradation in impedance.

## 4.2.2 Determination of stoichiometry of TiO<sub>2</sub> by XPS

Given the dependence of stoichiometry on resistivity for TiO<sub>2</sub> [174], XPS (ThermoFischer, ESCA) is performed to characterize the stoichiometry of TiO<sub>2</sub> and a four point probe measurement is used to characterize the resistivity of the film. 41 nm of TiO<sub>2</sub> is deposited on glass wafers and Si wafers. Resistivity is measured using a standard 4 point probe setup on the glass wafers. The Si wafers are cleaved and loaded into the XPS machine for analysis. The results of the XPS is shown in Figure 4-19. All the peaks can be accounted to be from either Ti or O. Quantitative analysis is then performed on the XPS results to determine the stoichiometry between O and Ti. The area under each peak after subtracting the fitted background x-ray radiation using the ESCA Lab software. The atomic percentages are then computed using:

$$\text{Atomic \%} = \frac{(\text{Area of Element of Interest}/\text{Sensitivity of Element of Interest})}{\sum_{\text{all elements}} (\text{Area of Element}/\text{Sensitivity of Element})} \quad (4.4)$$

where the sensitivity accounts for different factors contributing to different number of photoelectrons detected for various elements. The sensitivity factors are empirically determined by the manufacturers of the machine.

Based on the analysis, the ratio of O:Ti is approximately 2.05 to 1, close to the expected ratio of O:Ti obtained by [174] when the ALD film is deposited at 150°C.

The measured resistivity using a four-point probe measurement is 35.7 Ω-cm with a standard deviation of 18.2 Ω-cm over 3 samples.

Table 4.5: Quantitative Analysis of XPS performed on TiO<sub>2</sub>

Peak	FWHM (eV)	Area (counts/s-eV)	Sensitivity Factor	Atomic %
O 1s	3.5	314346.1	2.881	67.2
Ti 2p	5.01	344234.15	6.471	32.8

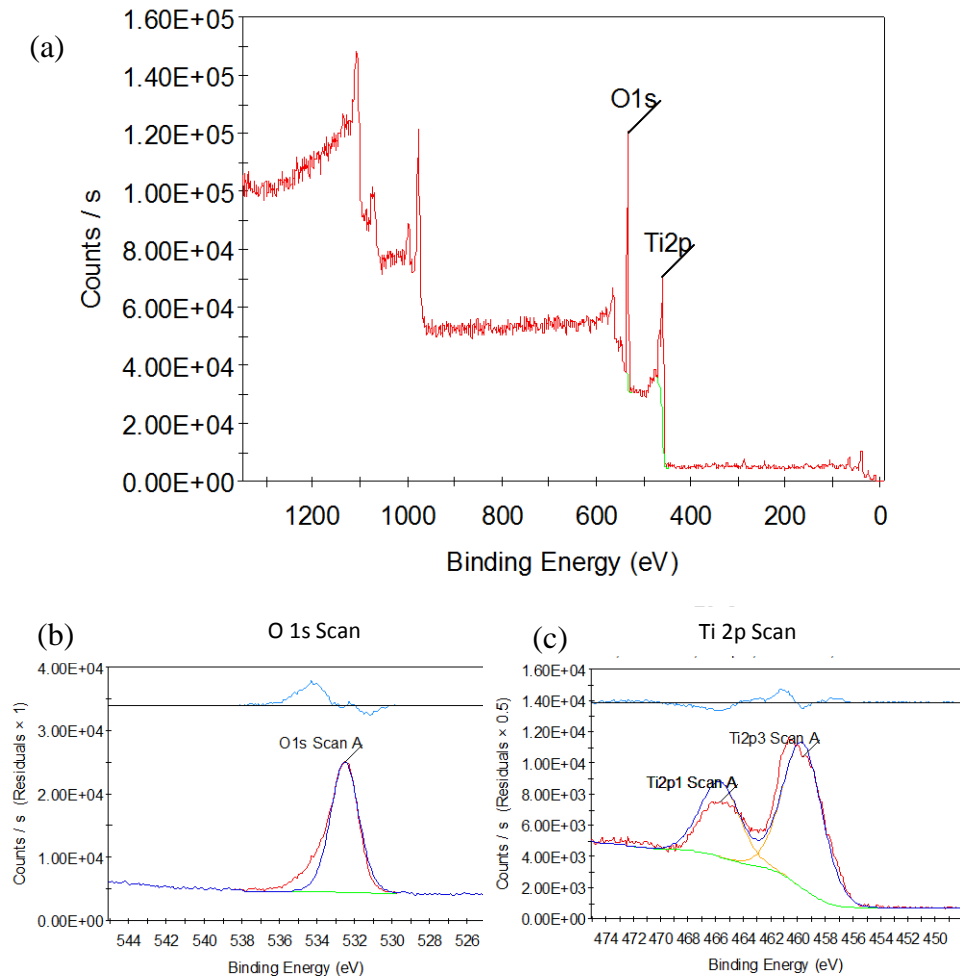


Figure 4-19: XPS Spectra of TiO<sub>2</sub>. (a) Survey spectra of TiO<sub>2</sub> sample. (b) Detailed scan around O 1s region. (c) Detailed scan around Ti 2p region. Red line is measured spectra. Green line is fitted background spectra. Orange line is fitted spectra of each peak. Dark blue line is combined fitted spectra. The light blue lines are a graphical plot, in arbitrary units, showing the variation in the difference between the fit and the measured values across binding energies.

## 4.3 Nanolaminates for flexible neural probes

### 4.3.1 Al<sub>2</sub>O<sub>3</sub>-TiO<sub>2</sub> nanolaminates as a barrier material

#### 4.3.1.1 Determination of chemical composition of nanolaminates by XPS

The composition of the nanolaminate is investigated by XPS. The results of the XPS is shown in Figure 4-20 and the quantitative analysis of the XPS is tabulated in Table 4.6.

From the results of the quantitative analysis performed as tabulated in Table 4.6, the ratio of Ti:Al:O is approximately 1:2.3:4.5. The relative amount of oxygen is lower than is expected if both oxides formed are stoichiometric TiO<sub>2</sub> and Al<sub>2</sub>O<sub>3</sub>. The higher relative amount of Al versus Ti can be at least partially explained from the deposition rates. The deposition rate of TiO<sub>2</sub> is approximately 0.4 Å/cycle as compared with 1 Å/cycle for Al<sub>2</sub>O<sub>3</sub>. Hence, the expected ratio of Ti:Al based on this argument is approximately 1:2.5 which is close to the measured value of 1:2.3.

Table 4.6: Quantitative Analysis of XPS performed on the nanolaminate.

Peak	FWHM (eV)	Area (counts/s-eV)	Sensitivity Factor	Atomic %
O 1s	1.82	261492.81	2.881	57.6
Ti 2p3 Scan A	2.03	46261.65	4.415	6.6
Ti 2p3 Scan B	1.6	43209.71	4.415	6.2
Al 2p	1.55	261492.81	0.56	29.6

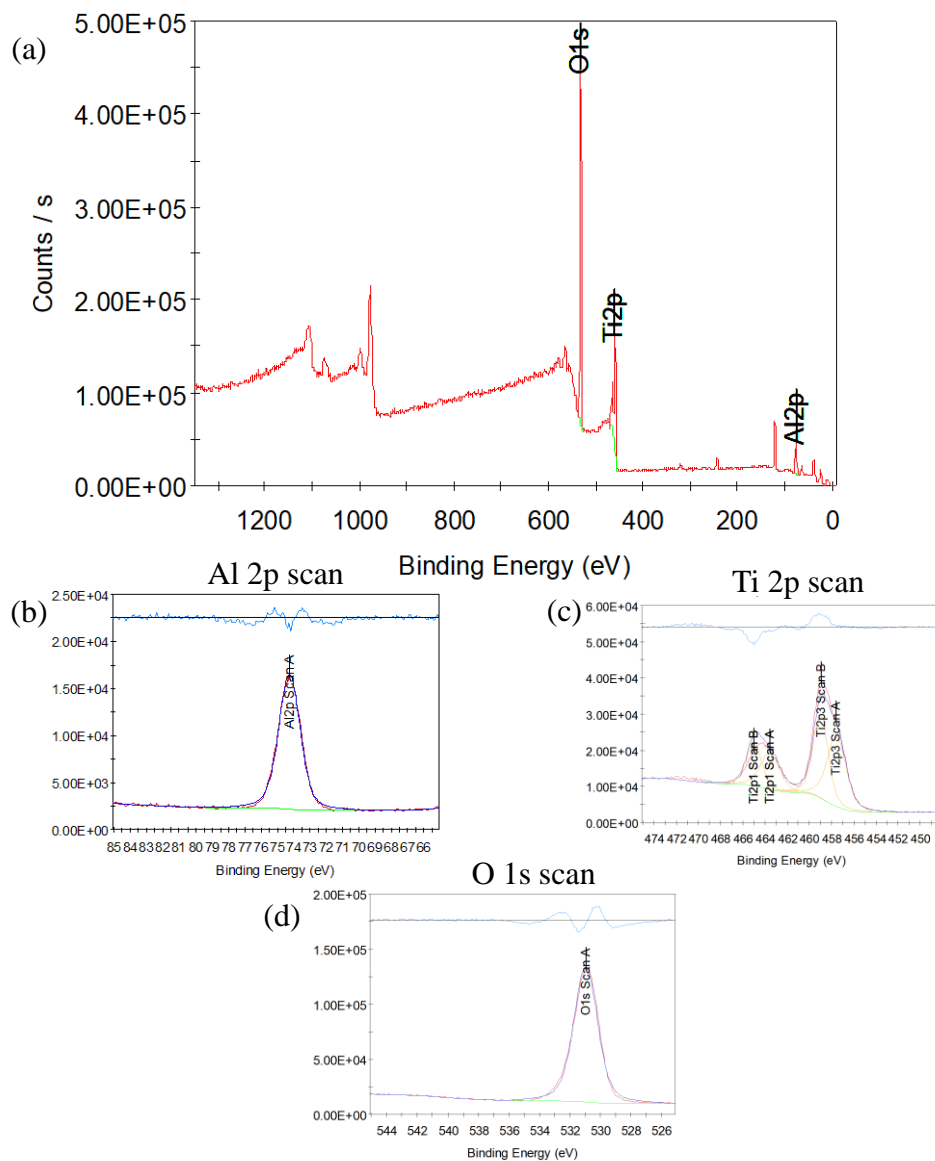


Figure 4-20: XPS spectra of the nanolaminate. (a) Survey spectra of the nanolaminate sample. (b) Detailed scan around O 1s region. (c) Detailed scan around Ti 2p region. Red line is measured spectra. Green line is fitted background spectra. Orange line is fitted spectra of each peak. Blue line is combined fitted spectra. The dark blue lines are combined fitted spectra. The light blue lines are a graphical plot, in arbitrary units, showing the variation in the difference between the fit and the measured values across binding energies.

## 4.4 Three layer hybrid encapsulation scheme

The use of a relatively high conductive material ( $\text{TiO}_2$ ) and rigid material (the nanolaminate and  $\text{TiO}_2$ ) for flexible neural probes means that electrical and mechanical considerations need to be considered in the design of the probe. In particular, electrical crosstalk between interconnects and the mechanical stress in the different layers during bending is considered.

### 4.4.1 Analysis of Crosstalk

For the encapsulation scheme proposed in Figure 4-21(a), the high capacitance of the nanolaminate and the low resistance of the titania provides a possible path where crosstalk is possible. A lumped parameter model is proposed in Figure 4-21(c) which models the parylene-C and the nanolaminate layers as capacitances and the titania as a resistance. The choice of this lumped parameter model is based on the material properties and design of the probe. The nanolaminate layer is very resistive but is thin and has a high relative permittivity, making a capacitor a suitable model for it. Similarly, the parylene-C is very resistive making a capacitor a suitable model. The low resistance of the titania layer makes a resistor a suitable model for it. The values of the lumped parameters are obtained using the conventional equations for capacitances and resistances:

$$R = \frac{l}{\sigma A} \quad (4.5)$$

$$C = \epsilon_r \epsilon_0 \frac{A}{d} \quad (4.6)$$

The parameters used for the analysis and simulation are:  $\sigma_{\text{TiO}_2} = 0.001 \text{ S/m}$ , the relative permittivity of  $\text{TiO}_2$ ,  $\epsilon_{r,\text{TiO}_2} = 100$ , the electrical conductivity of the nanolaminate,  $\sigma_{r,NL} = 14.6$ , the electrical conductivity of parylene-C,  $\sigma_{px} = 1.8 \times 10^{-17} \text{ S/m}$  and the relative permittivity of parylene-C,  $\epsilon_{r,Px} = 3.15$ . The driven node is driven at  $1 V_{AC}$ .

Using symmetry, the lumped parameter model in Figure 4-21(c) can be simplified

to Figure 4-21(d). The transfer function is

$$\frac{V_{out}}{V_{in}} = \frac{\frac{sR_T}{4C_{Px}} + \frac{1}{2C_{Px}^2}}{\frac{sR_T}{4}\left(\frac{1}{C_{Px}} + \frac{1}{C_{NL}}\right) + \frac{1}{4C_{Px}^2} + \frac{1}{2C_{Px}C_{NL}}} \quad (4.7)$$

There is one zero and one pole in the transfer function. The zero occurs at

$$s = -\frac{2}{R_T C_{Px}} \quad (4.8)$$

and the pole occurs at

$$s = -\frac{\frac{C_{NL}}{C_{Px}} + 2}{R_T(C_{Px} + C_{NL})} \approx -\frac{1}{R_T C_{Px}} \quad (4.9)$$

assuming  $C_{NL} \gg C_{Px}$ . By substituting the values used, the calculated zero is at 2.85 kHz and the calculated pole is at 1.43 kHz. The SPICE circuit simulation using the lumped parameter model in Figure 4-22 matches this behavior.

To verify that the lumped parameter model is a sufficient representation of the distributed nature of the device, a COMSOL Multiphysics finite element simulation is performed using the setup shown in Figure 4-21(b). With the output node floating, the simulation results (Figure 4-23) closely matches with the predicted result based on the lumped parameter model that is shown in Figure 4-22. This shows that although the actual capacitances and resistances in the device are distributed, the lumped parameter model presented is a suitable model.

Based on this model, there is significant crosstalk around the 1 kHz region which is around the frequencies of interest given the high voltages seen at the output node in that region. However, the model is a worst case model. In reality, there is an electrode at the output node and a distributed resistance along the interconnect since the resistance of the Pt is finite. Moreover, the neurons do not drive the driven node like an ideal voltage source. The driving source is typically modelled as a Norton source with a high membrane resistance. When using the more realistic driving and load models as shown in Figure 4-21(f) ( $R_M = 100 \text{ M}\Omega$ ,  $R_s = 10 \text{ k}\Omega$ ,  $R_L = 10 \text{ k}\Omega$ ),

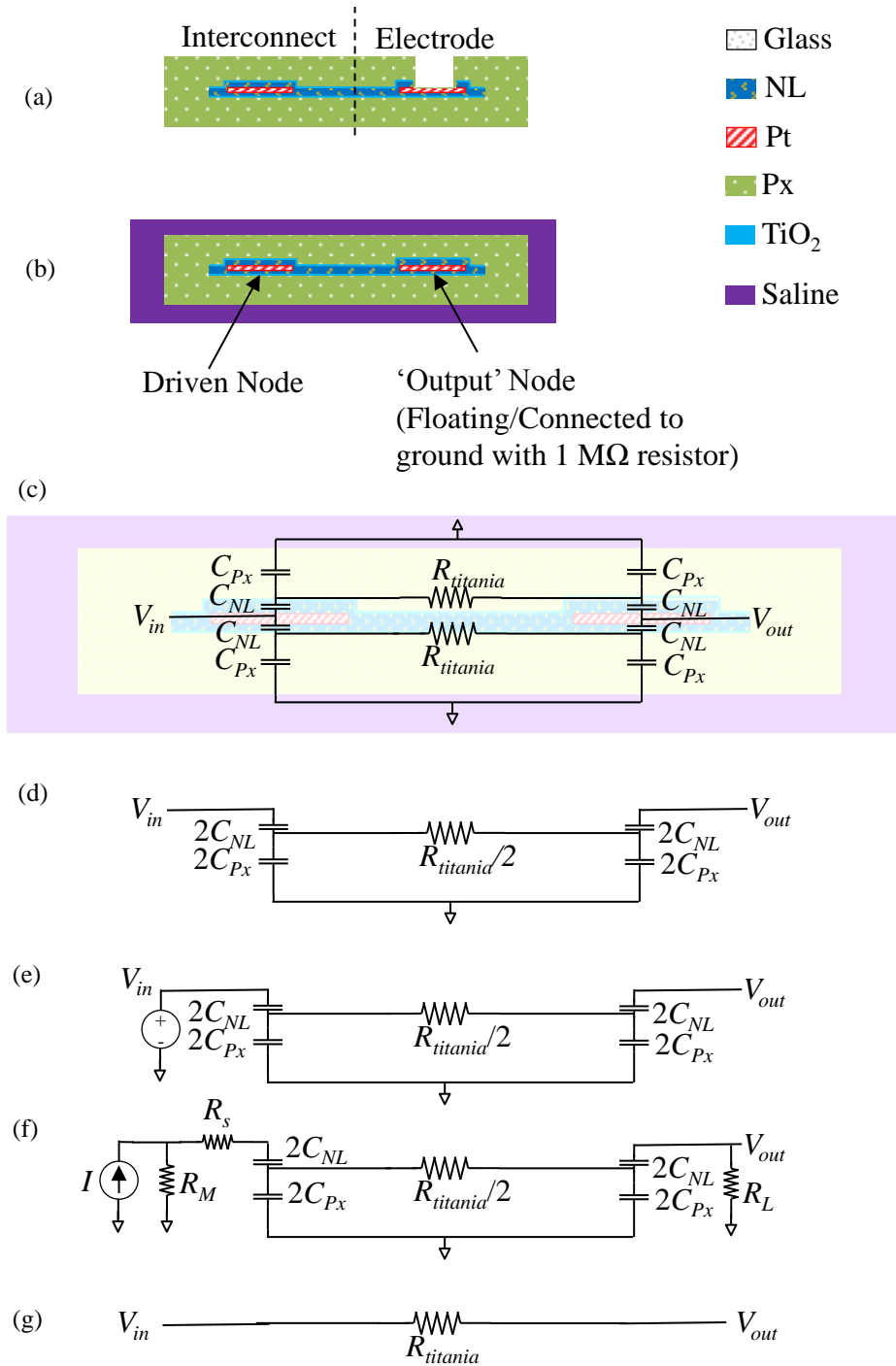


Figure 4-21: Cartoons and schematics of the proposed encapsulation schemes. (a) Interconnect scheme with electrode. (b) Simulation setup in COMSOL. (c) Proposed lumped parameter model. (d) Reduced circuit from (c) based on symmetry. (e) Setup for crosstalk analysis. (f) Setup for more realistic model of the input and output circuits. (g) Lumped parameter model of titania only scheme.

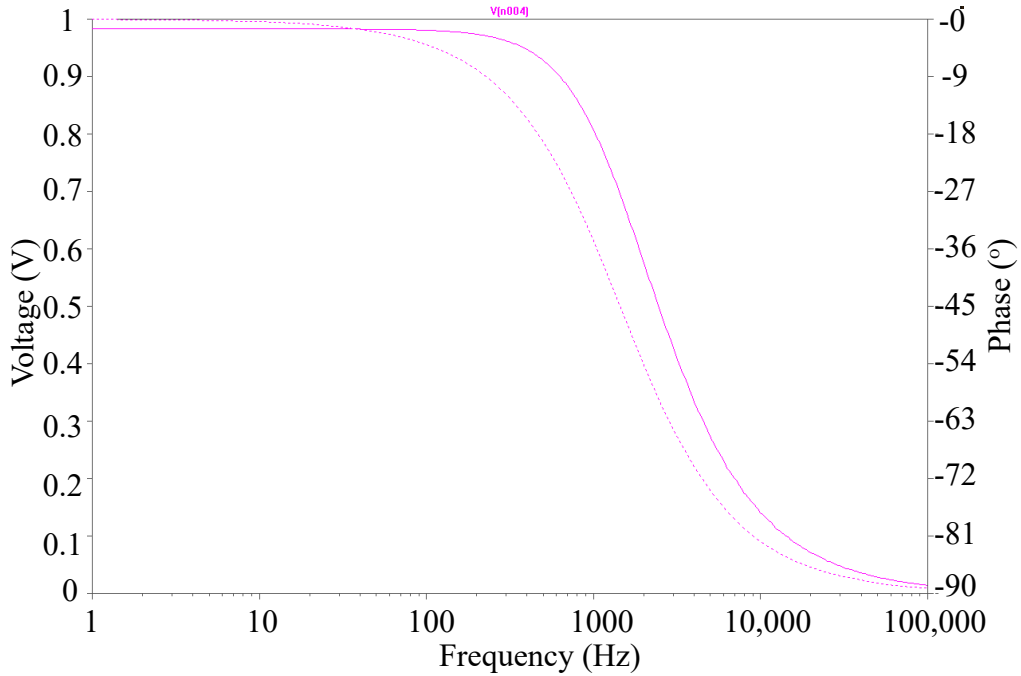


Figure 4-22: Simulation results from SPICE simulation based on lumped parameter model. Lighter dashed line is the phase. Solid line is the magnitude in voltage.

the voltage at the output node is less than  $11 \mu\text{V}/\text{V}$  for the frequencies of interest. This indicates that with the proposed triple layer encapsulation, crosstalk is not likely to be significant.

If titania is used alone without NL, a resistive connection occurs between  $V_{in}$  and  $V_{out}$  because of the high conductivity of titania as shown in Figure 4-21(g). Unlike the triple encapsulation scheme that is discussed and shown in Figure 4-21(d), this direct resistive connection results in significant crosstalk across all frequencies.

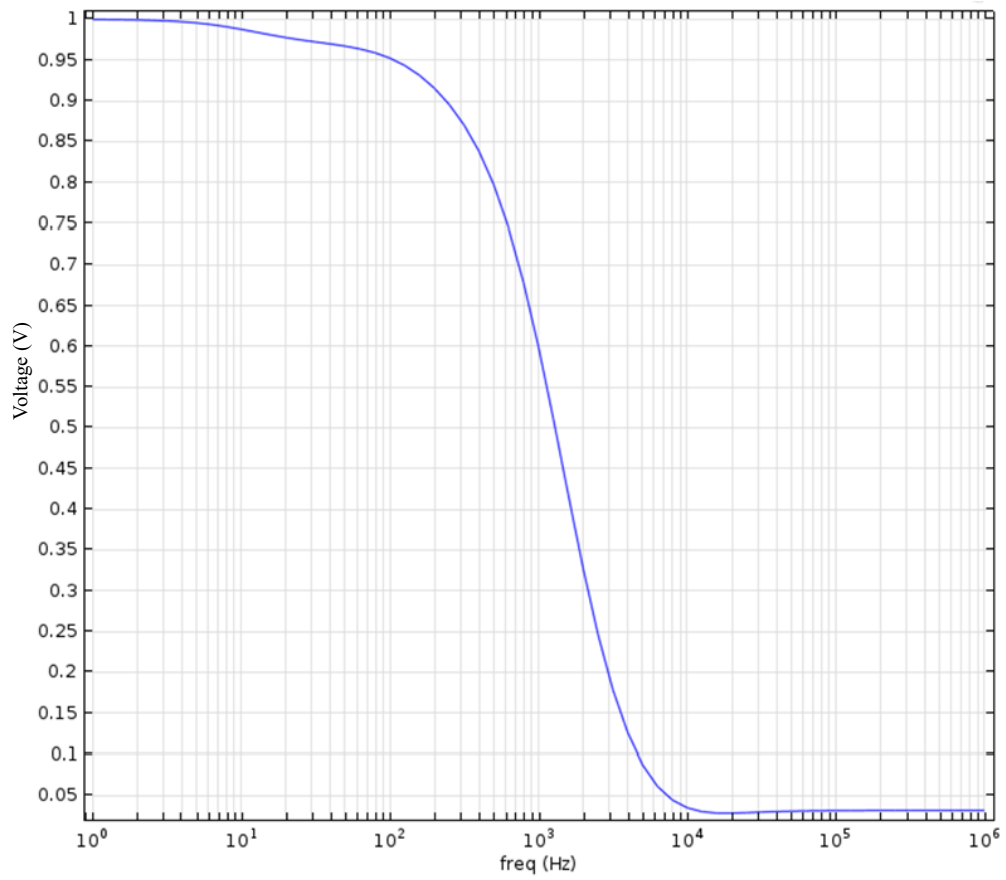


Figure 4-23: Simulation results from COMSOL Multiphysics finite element analysis.

#### 4.4.2 Analysis of mechanical properties of hybrid encapsulation

An analysis is also performed to determine the ability of the encapsulation layer to survive mechanical bending since it is meant for use in applications where flexibility is required. To analyze the bending capability of the hybrid encapsulation scheme, an analysis of the mechanical stress in each layer is performed.

The equation used is derived from equations for pure bending

$$\sigma_{max,material} = \frac{E_{material}y_{max,material}\rho}{(EI)_{total}} \quad (4.10)$$

where  $\sigma_{max,material}$  is the maximum stress in the material,  $E_{material}$  is the Young's modulus of the material,  $(EI)_{total}$  is the flexural rigidity of the entire beam,  $y_{max}$  is the maximum distance of the material from the neutral axis of the beam which is in this case in the centre of the beam and  $\rho$  is the radius of curvature of the beam. The area of interconnects is assumed to take up half of the area and hence, the effective Young's modulus of the platinum region is taken to be the average of Pt and parylene-C based on a mixture model.

The Young's modulus and yield strength of the materials are tabulated in Table 4.7. The Young's modulus of  $TiO_2$ ,  $Al_2O_3$  and the nanolaminate are obtained from a study by [175] where the Young's modulus of various  $TiO_2$ - $Al_2O_3$  nanolaminates,  $TiO_2$  and  $Al_2O_3$  are measured using a nanoindentor. The values obtained largely agree with another study performed by [176] using MEMS shaft-loading and bulge tests. The Young's modulus of Pt and yield strengths of the various materials are obtained from [177][178][179][180]. The yield strength of the nanolaminates is computed using the rule of mixtures[181]:

$$\sigma_{y,NL} = f_T\sigma_{y,TiO_2} + (1 - f_T)\sigma_{y,Al_2O_3}, \quad (4.11)$$

where  $\sigma_{y,NL}$  is the yield strength of the nanolaminate,  $f_T$  is the fraction of  $TiO_2$  in the nanolaminate,  $\sigma_{y,TiO_2}$  is the yield strength of  $TiO_2$  and  $\sigma_{y,Al_2O_3}$  is the yield strength

of  $\text{Al}_2\text{O}_3$ .  $f_T$  is taken to be  $1/3.3 = 0.303$  based on the XPS results in Table 4.6.

This rule of mixtures is the simplest rule to estimate yield strength of composites and there are a number of modified rule of mixtures [181]. However, given that the yield strengths of  $\text{TiO}_2$  and  $\text{Al}_2\text{O}_3$  are close, it is unlikely that there will be significant changes in the derived yield strength of nanolaminates even when these modified versions are used.

Based on the analysis shown in Figure 4-24, Pt and the the nanolaminate/ $\text{TiO}_2$  ceramics are likely to break down at around 100  $\mu\text{m}$  radius of curvature. For the application of penetrating electrodes, this is unlikely to be of concern. However, for other applications such as cuff-electrodes, the radius of curvature can be smaller depending on the size of the nerve. Hence, if a smaller radius of curvature is required, the thicknesses of these layers should be reduced.

The quantities tabulated in Table 4.7 also allows for an analytical analysis of the increase in stiffness of the probe due to the ceramic encapsulation scheme. To predict axial stiffness, the ratio of the axial rigidities  $EA$  can be computed as follows:

$$\frac{(EA)_{wNL}}{(EA)_{noNL}} = \frac{A_{wNL}}{A_{noNL}} \frac{f_t E_t + f_{NL} E_{NL} + f_{Pt} E_{Pt} + f_{Px} E_{Px}}{f_{Px} E_{Px} + f_{Pt} E_{Pt}} \quad (4.12)$$

where  $(EA)_{wNL}$  is the axial rigidity with nanolaminate,  $(EA)_{noNL}$  is the axial rigidity with no nanolaminate,  $f_t$  is the volume fraction of titania,  $f_{Pt}$  is the volume fraction of Pt,  $f_{Px}$  is the volume fraction of parylene-C,  $f_{NL}$  is the volume fraction of nanolaminate.  $E_t$ ,  $E_{Pt}$ ,  $E_{NL}$  and  $E_{Px}$  are the Young's moduli of  $\text{TiO}_2$ , Pt, NL and Px respectively. For a typical probe fabricated, the thickness of each layer of parylene-C

Table 4.7: Mechanical properties of various ceramic layers

Material	Young's Modulus (GPa)	Elastic Limit/Yield Strength (MPa)
$\text{TiO}_2$	136	333
Nanolaminate	140	309
Parylene-C	4	3200
$\text{Al}_2\text{O}_3$	143	300
Pt	168	125

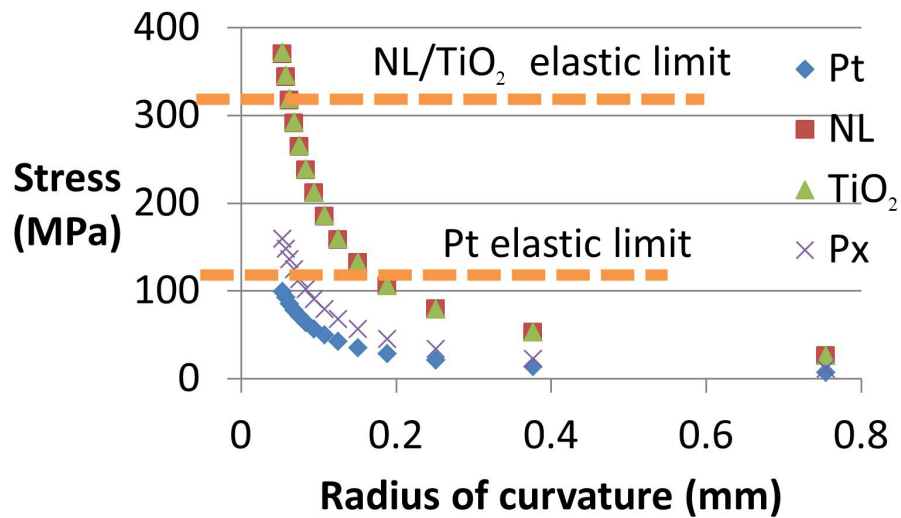


Figure 4-24: Stress in MPa versus radius of curvature (mm) based on theoretical calculations. Various elastic limits are also plotted to indicate point of failure.

is 2.2  $\mu\text{m}$ , the thickness of Pt is 125 nm, the thickness of each layer of NL is 80 nm and the the thickness of each layer of  $\text{TiO}_2$  is 5 nm. Assuming that 50% of the probe is covered with Pt, the calculated ratio of axial rigidities indicates that the stiffness of the probes increases by 85%.

To predict bending stiffness, the ratio for flexural rigidity,  $\frac{(EI)_{wNL}}{(EI)_{noNL}}$  is obtained. Given the proximity of the nanolaminate coatings to the neutral axis, the flexural rigidity is dominated by the parylene-C for both cases. For the same thicknesses, the calculated increase in flexural rigidity is 1%.

## 4.5 Summary

Different methods to improve parylene-C to parylene-C adhesion is investigated and tested by EIS. The effect of the various plasma treatments is investigated by XPS. It is found that out of the treatments presented, oxygen plasma improves parylene-C to parylene-C adhesion the most. It is also found that there is no observable correlation between adhesion improvement and hydrophobicity, indicating that the improvement

in adhesion is not likely to be due simply to Van Der Waals forces.

ALD ceramics are also tested by EIS to determine efficacy of treatment. The composition of the nanolaminate is determined by XPS. It is found that alumina corrodes too quickly in water and titania has too low of a resistivity for successful encapsulation.  $\text{TiO}_2/\text{Al}_2\text{O}_3$  nanolaminate is found to have high enough resistivity and is resistant to corrosion in water. However, the adhesion between the nanolaminate and parylene-C is poor.

Hence, a three-layer encapsulation scheme is proposed with  $\text{TiO}_2$  acting as the adhesion layer. The electrical crosstalk arising from the conductive  $\text{TiO}_2$  is analyzed and suggests that crosstalk is insignificant with the  $\text{TiO}_2$  thickness used (5 nm). Analytical simulations show that devices insulated with this scheme can be bent down to a radius of curvature of 100  $\mu\text{m}$  without fracture, indicating that flexibility is not compromised by this encapsulation scheme.

# Chapter 5

## Protruding electrodes

An important consideration as described in Chapter 1 is the distance separating the electrodes from the neurons since this will affect the signal-to-noise ratio. The deposit-and-etch group of subtractive processes that is widely used to remove the dielectric from the top of the electrode in flexible neural probes[182][38][183][22] and is also used for the process described in Chapter 2 result in recessed electrodes. For stiff Si probes with specialized process flows that result in protruding electrodes such as the Utah array[23], the design space is usually limited and electrode counts low (in the case of the Utah array, it is only possible to have one electrode per shank). In contrast, recessed electrodes result in an increased distance between the region of interest and the recording electrode. A method to incorporate protruding electrodes in order to reduce this distance while maintaining the versatility of the deposit-and-etch group of processes is developed.

Improving electrode density is often important to acquire single-unit recordings from more neurons. Increasing the interconnect density is often essential in order to improve electrode density without increasing the size of the probe which is important to reduce tissue damage. One way of improving interconnect density is to incorporate vias that allow interconnects to span across multiple layers of metal.

Since there are similar challenges in the fabrication of vias and protruding electrodes, both will be discussed in this chapter.

## 5.1 Vias and interconnects

### 5.1.1 Existing processes for fabrication of vias

The manufacture of vias is well established in CMOS technology. These methods involve the etching of the dielectric followed by deposition of a barrier layer and a metal fill. The success of the via technology usually hinges on the ability to deposit the metal conformally so that no voids are created and the subsequent planarization of the metal[184]. To do this, methods such as CVD of tungsten[184], organometallic chemical vapor deposition of Cu(OMCVD)[185], electroless plating of Cu[186], electroplating of Cu, reflow of Cu after sputtering[184], are employed. The choice of process is largely determined by reliability and cost of the process.

Vias are also common in printed circuit boards (PCBs) and other board-level architectures. In PCBs, vias are usually created using mechanical drills or CO<sub>2</sub> lasers and plated with metal[187]. ACF (anisotropic conductive film) adhesives are also commonly used for connecting neural probe pads to flat flexible cables and PCBs largely because they do not require very precise alignment [188][40][22]. In [182], ACF adhesives are used to electrically bond and stack devices together, essentially creating a form of vias which help in achieving higher electrode density.

In neural probes, vias are also fabricated in Si-based probes with flexible regions [39] and in stiff Si based probes[22] using etch and metal-fill based processes.

In this thesis, vias are incorporated into compliant probes that do not have any stiff Si regions. This introduces new challenges compared with the aforementioned processes. Using a flexible substrate would introduce new challenges because any large abrupt changes in stiffness at the interface between the dielectric and the metal fill would cause would create large amounts of stress which would result in failure.

## 5.2 A metal-fill based process to fabricate vias

The fabrication of vias basically requires a connection between two layers of metal. The first approach attempted is a metal-fill approach similar to that used in CMOS

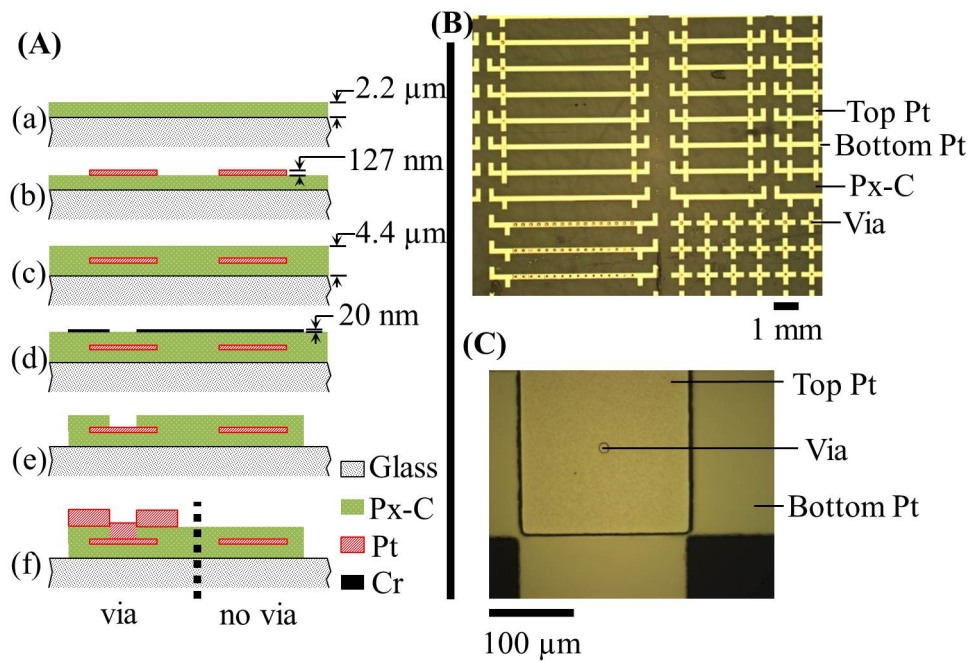


Figure 5-1: A. Condensed process flow to fabricate vias using an etch and metal-fill kind of process. A description of each step depicted in the process flow is found in the text. B. An optical image of test structures fabricated using described process flow. C. Zoomed-in image of a fabricated via.

processes where the dielectric at the regions where a connection is desired is etched and a metal is used to fill the gap. A test wafer is fabricated to develop and investigate this type of process. The process flow is illustrated in Figure 5-1A. A 2.2  $\mu\text{m}$  layer of parylene-C is first deposited using a CVD process as shown in Figure 5-1a. A 126 nm layer of Pt is then deposited by sputtering and patterned by lift-off as shown in Figure 5-1b. Following that, a second layer of 2.2  $\mu\text{m}$  layer of parylene-C is deposited as shown in Figure 5-1c. A 20 nm Cr hard mask is then deposited and patterned as shown in Figure 5-1d. At the vias, the top layer of parylene-C is then etched using  $\text{O}_2$  reactive ion etching (RIE) as shown in Figure 5-1e. Following an  $\text{Ar}^+$  RIE etch to remove  $\text{PtO}_2$  formed on the Pt during the etch and etching of the remaining Cr hard mask using a wet etchant, a second 2.5  $\mu\text{m}$  layer of Pt is deposited and patterned by lift-off as shown in Figure 5-1f. Details of this process flow is found in Appendix A.

Optical images of fabricated vias are shown in Figure 5-1B and Figure 5-1C. Results of the four-point probe tests performed on the vias using the test structures is tabulated in Table 5.1 and show via resistance values of 1.2  $\Omega$  to 11.2  $\Omega$  which is negligible compared to interconnect resistance in neural probes (typically k $\Omega$ s). Although contacts are successfully made using this method, the measured resistances are not inversely proportional to the area of the vias as would be expected from theory. Hence, SEM is performed on the vias as shown in Figure 5-2 which shows sign of delamination at the edges of the vias. EDX is also performed which confirmed that there is a void present at the edge of the vias. Only Pt is detected on the via and on the sides of the via.

The presence of delamination explains the inconsistent values of resistance for

Table 5.1: Measured resistances of different vias

Via Size ( $\mu\text{m}$ by $\mu\text{m}$ )	Resistance ( $\Omega$ )
40 by 40	8.9
60 by 60	7.9
80 by 80	11.2
100 by 100	1.2

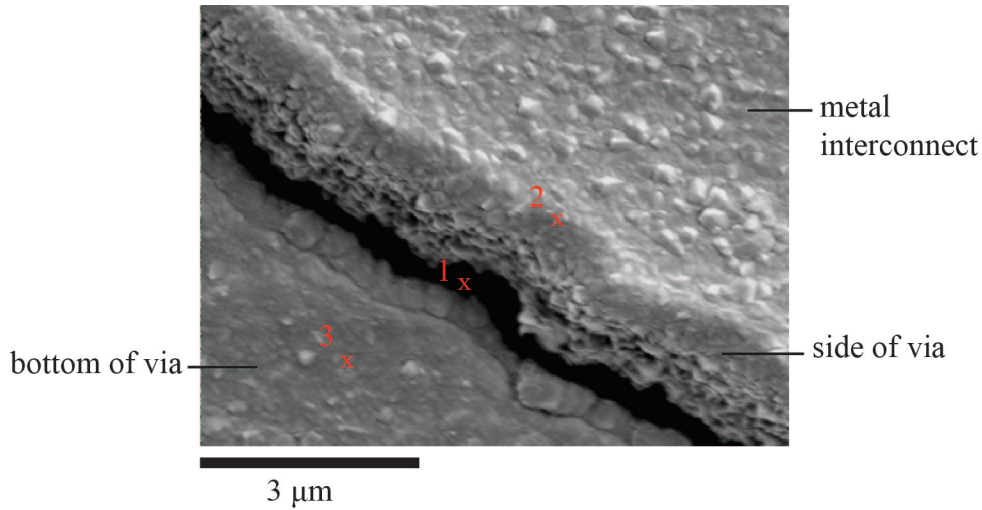


Figure 5-2: SEM of a fabricated via showing signs of delamination at the edges. EDX is performed at points 1,2 and 3 labelled on the figure. No material is detected at point 1. Only Pt is detected at points 2 and 3.

the different via sizes and also affects the long-term reliability of the vias. For this process, the second layer of Pt is required to be in the same order of thickness as the top dielectric layer because the method of deposition (sputtering) is not as conformal as other processes such as chemical vapor deposition (CVD) or atomic layer deposition (ALD), where the material is deposited in the vapor phase. The thick layer of Pt makes the integrity of the structure very sensitive to residual stress in this Pt layer. The intrinsic stress of a 577 nm-thick layer of Pt is 282 MPa measured using a FLX-2320 (KLA-TENCOR, Milpitas, CA). Furthermore, the thickness of the Pt has to scale with the thickness of the top dielectric layer. For thick dielectrics, this can make the process prohibitively expensive and unreliable because of the process' sensitivity to stress in the thick Pt film. The thickness of dielectric affects the insulation properties of the probe and hence, it is ideal to be able to control the thickness of the probe independently. In addition, this method is undesirable in the case of flexible devices because the sharp transitions result in stress concentration that leads to mechanical failure of the device. Sloping sidewalls of the parylene-C via, described in Section 5.3.2, solve these issues.

### 5.2.1 Fabrication of Vias

Using the grayscale lithography and transfer process described in Section 5.3.2, vias are fabricated using Dr. Jinsheng Gao's existing masks, which consists of grayscale patterns made up of 8 by 8 squares of length 1  $\mu\text{m}$  each fabricated from Compu-graphics. 2.3  $\mu\text{m}$  of parylene-C is first deposited on a 10 cm Si wafer. Following that, 2.4  $\mu\text{m}$  of AZ4210 is spun on the wafer at 3000 rpm for 30 s and baked for 1 min on a 100°C hotplate. The wafer is then exposed using a Karl-Suss MA6 (Garching, Germany) in proximity exposure mode with a gap of 150  $\mu\text{m}$  for 320 s. Following that, the wafer is developed for 1 min in 1:2.7 AZ developer:DI water. The wafer is then etched in the Trion RIE machine using 50 W  $\text{O}_2$  at 50 mT for 15 min. After cleaning the wafer in acetone and IPA followed by a  $\text{O}_2$  barrel etcher clean at 100 W for 1 minute, 126 nm of Pt is deposited on 2.3  $\mu\text{m}$  of Px that is patterned and etched. The optical image of a fabricated slope is shown in Figure 5-3a and the profile using contact profilometry is shown in Figure 5-3b.

Successful fabrication of vias are determined by a two-point measurement. Electrical contact is achieved across the sloped sidewalls but not across steep sidewalls which are also present in the mask, demonstrating successful fabrication of vias. Structures with both stepped and sloped sidewalls are visible in Figure 5-3a. Using an SEM to examine the morphology of the slope shows successful fabrication of a gradual slope as seen in Figure 5-4a. A zoomed-in SEM of the slope shows the morphology of the bumps, which are in the order of the dimensions of the individual pixels (1  $\mu\text{m}$  by 1  $\mu\text{m}$ ) and give rise to the roughness observed in the contact profilometer scan in Figure 5-3.

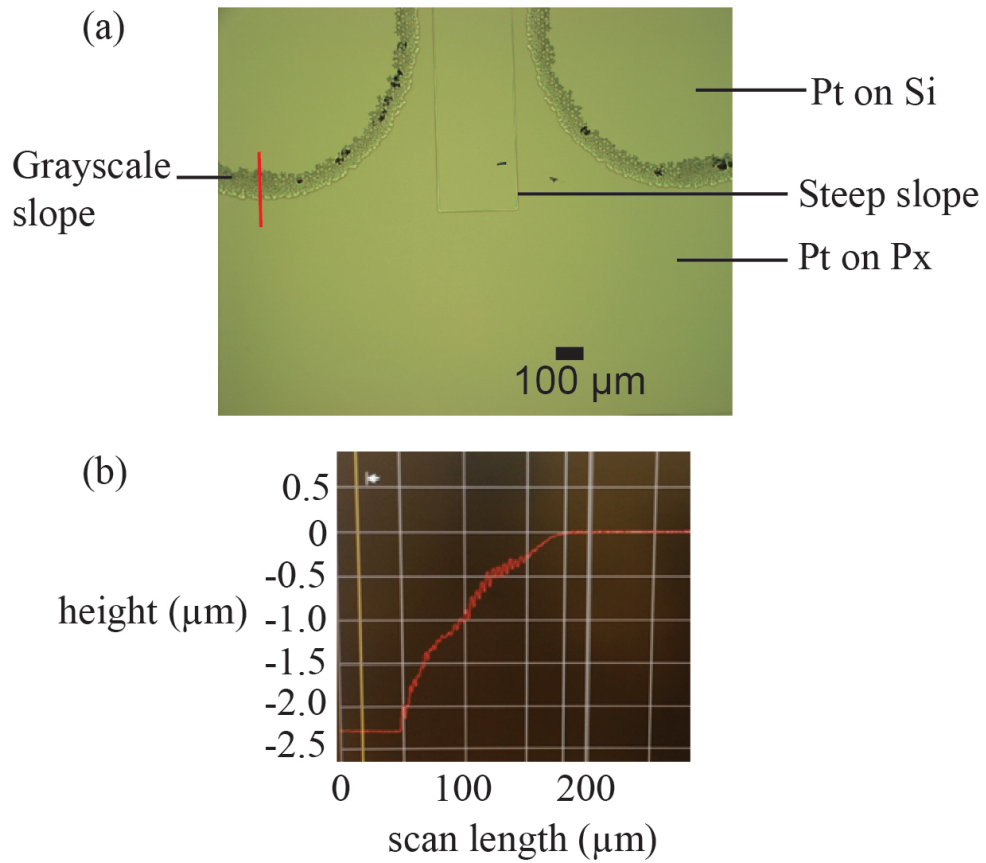


Figure 5-3: Optical image and profilometer measurement of sloped sidewall fabricated using grayscale lithography.

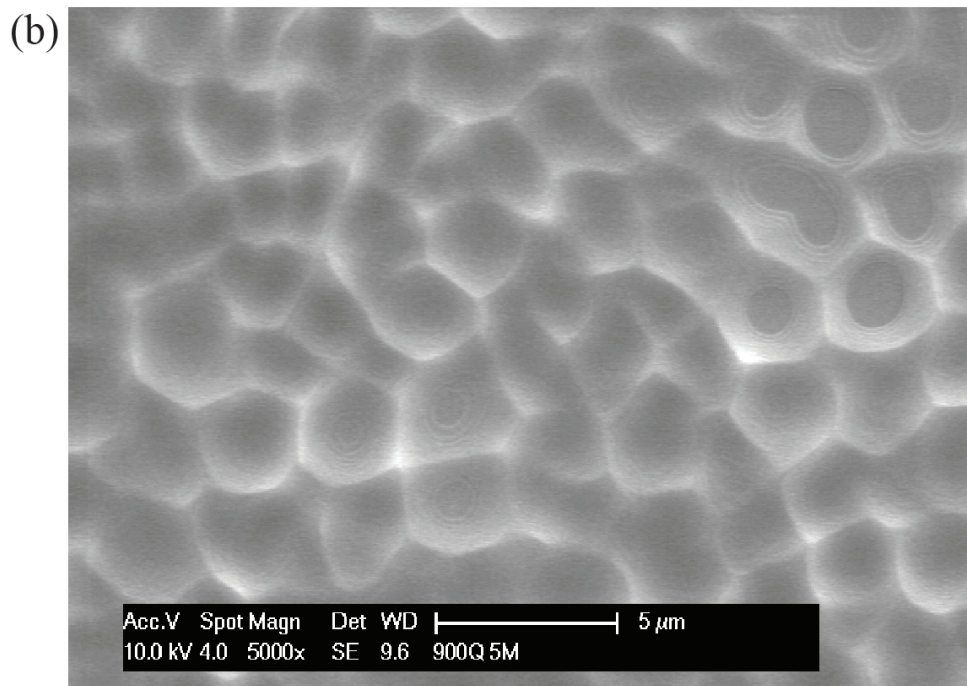
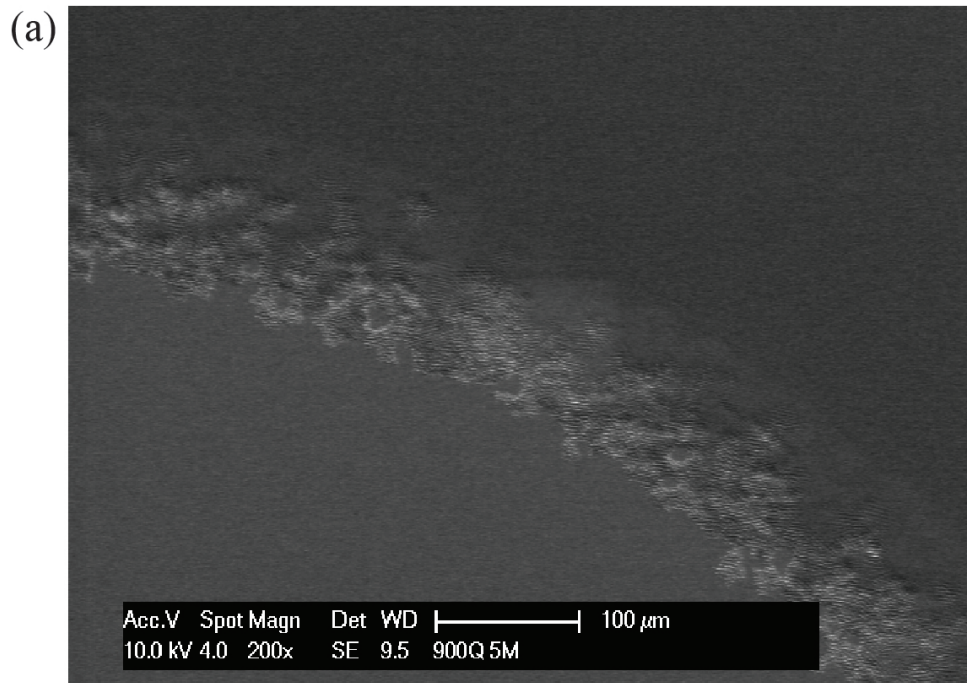


Figure 5-4: SEM of side of a via fabricated using grayscale lithography. (a) Zoomed-out SEM showing extent of slope. (b) Zoomed-in SEM showing microstructures formed by grayscale lithography.

## 5.3 Protruding Electrodes

### 5.3.1 Existing processes for fabrication of protruding electrodes

Existing protruding electrodes are typically fabricated on rigid substrates[23][189][190][25][191]. The main applications for these protruding electrodes are typically for recording and stimulation from cultures and ex-vivo preparations[189][190] or as a means of insertion[23][25].

The protruding electrodes in [189] are fabricated by isotropically etching glass substrates with an appropriate mask to create sharp tips on the rigid substrates. It is proposed in [189] that the sharp pyramidal protruding electrodes improve recording quality by penetrating through a layer of dead cells that are present in cultures and ex-vivo preparations. In [190], the protrusions are fabricated using an electrodeposition step to create a rounded mushroom-like protrusion and it is shown that the significant improvement in recording quality arises from cultured cells engulfing these protrusions. These studies show that there is a significant advantage of using protruding electrodes for *in-vitro* applications on rigid substrates.

In the case of stiff probes meant for *in-vivo* preparations such as the Utah array[23] and Microprobes electrodes[25], the probes are needle-like and are a mechanism to insert the probe and allow the electrodes to reach the target recording or stimulation site. The Utah arrays[23] are fabricated from a block of Si from a combination of dicing and etching steps in order to create the needles. Microprobes electrodes[25] are fabricated by deinsulating an insulator-coated wire at the tip. The process design of these probes result in electrodes that are flush with the surface of the needles. However, the electrode height is a result of the processing technique to create sharp needles rather than a deliberate means of improving signal recording. Hence, many design parameters such as the length of the needles are determined by other factors such as insertion depth. These technologies tend to result in very small design spaces since the design is essentially fixed by the process flow.

In this thesis, protrusions are fabricated under electrodes that would have been typically recessed on flexible substrates, combining the benefits of mechanical compliance, versatility of design and proximity of the electrodes to the sites of interest. The techniques used to create these protrusions, which aim to overcome problems similar to the fabrication of vias, are also demonstrated in a via fabrication process.

### 5.3.2 Sloped sidewalls of parylene-C to fabricate vias or protruding electrodes

The requirement for a thick metal fill for vias comes from the fact that the sidewall of the vias are steep making the requirement of step coverage difficult to meet without a conformal process to deposit Pt. A profilometer scan showing the sidewalls of a 9  $\mu\text{m}$ -thick probe created by etching parylene-C deposited on Si using RIE is shown in Figure 5-5. Although conformal processes to deposit Pt exist [192], they are expensive and slow as compared to physical processes like sputtering and evaporation. One way of relaxing the condition for a conformal process while maintaining step coverage is to make the sidewalls less steep. This motivates the development of a process to create sloped sidewalls.

In the case of fabrication of vias or protruding electrodes on parylene-C based structures, the proposed method of fabrication using sloped structures is described in

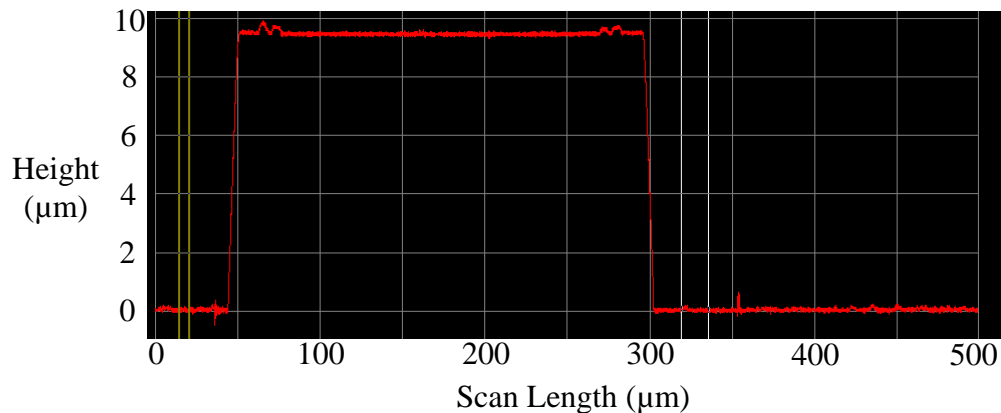


Figure 5-5: Profilometer scan of a parylene-C probe.

Figure 5-6. The steps described in Figure 5-6(a-c) are used to fabricate a parylene-C/Pt/parylene-C sandwich and are similar as the corresponding steps described in Section 5.2 with the exception that the electrode region is not exposed. The first Pt layer is removed directly under the protruding electrode to improve structural integrity by increasing parylene-parylene interface area under the protruding electrode site. Following that, sloped sidewalls in photoresist are fabricated as shown in Figure 5-6(d) and explained further below. The slope is then transferred to the parylene-C using a controlled etch step and a second layer of Pt is patterned and deposited using a lift-off process as shown in Figure 5-6(e).

The two critical steps in this process are (a) to create sloped profiles in the photoresist and (b) to transfer the obtained profiles onto the dielectric material using a calibrated etch step.

In the literature, creation of 2.5D profiles with photoresist is used to fabricate microlens[122][193] and MEMS structures[194][195]. There are a number of methods to create sloped profiles including reflow of resist and relying on surface properties to create lens-like structures[122], modifying exposure and development parameters to modify the slope of the resist and grayscale lithography[193]. The reflow of resist can only be used to create a very limited design space of curved lens-like structures. Modifying exposure and development parameters is briefly attempted but can only be used to fabricate a very limited range of slopes. Hence, in order to improve the versatility of the process, grayscale lithography is used. The development of the grayscale lithography process for this application is described in Section 5.3.3.

Following creation of 2.5D profiles in the resist, it is then necessary to transfer the pattern onto the material of interest (parylene-C in this case). There are different methods of transferring patterns including molding[193] and etching[195]. Since parylene-C is deposited in the vapor phase which makes methods like molding difficult, etching is the method used to transfer the photoresist pattern onto parylene-C. The analysis and implementation of this process is discussed in Sections 5.3.4 and 5.3.5.

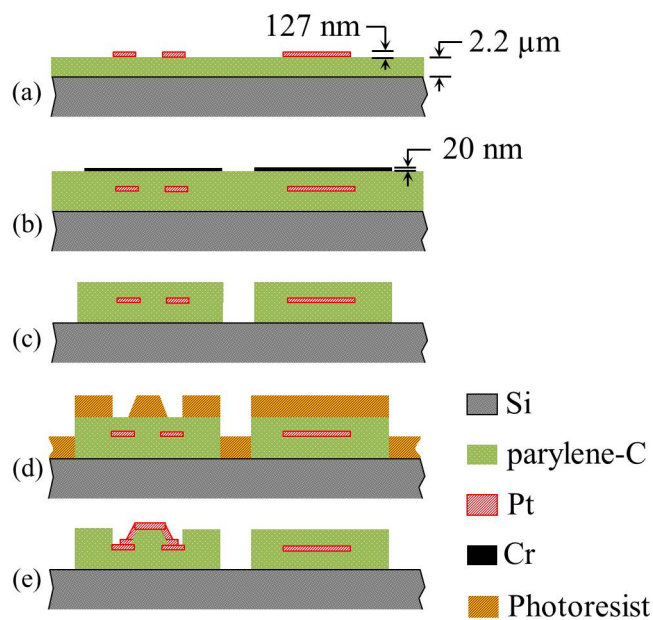


Figure 5-6: Process flow to fabricate neural probes with sloped sidewalls. (a) Deposition of parylene-C. (b) Patterning and deposition of Pt by lift-off. (c) Deposition of second layer of parylene-C. (d) Grayscale lithography to fabricate sloped sidewalls in photoresist. (e) Transfer of slope sidewall pattern from photoresist to parylene-C followed by patterning and deposition of second layer of Pt by lift-off.

### 5.3.3 Grayscale lithography

Grayscale profiles in lithography is obtained using direct write (maskless) approaches and by using specially designed masks to vary the exposure dose at different locations of the wafer. Grayscale lithography relies on the fact that photoresists do not have infinite contrast, where the contrast  $\gamma$ , is defined by:

$$\gamma = \frac{1}{\log_{10} \frac{D_{100}}{D_0}}, \quad (5.1)$$

where for a positive resist,  $D_{100}$  is the dose where 100% of the resist remains and  $D_0$  is the dose where 0% of the resist remains. For a negative resist, this definition is inverted. Unlike conventional photolithography, where a high contrast is desired, in grayscale lithography, a sufficiently low contrast is desired so that sufficient levels of grayscale is achieved. Since contrast is a function of the photoresist and processing conditions such as temperature, development time and developer type, appropriate modifications to the process is done to achieve a low contrast. Modification of the contrast can also affect the profile of the obtained resist. For example, if a grayscale pattern consisting of a gradual slope is fabricated, the slope will increase as the contrast increases. An investigation on the effect of various parameters like development time on the contrast of AZ4210 resist is performed in [195].

#### 5.3.3.1 Appropriate parameters for development of a process to achieve contrast in AZ4620

In this thesis, the same principles of using dilute developer and having an extended development time to achieve low contrast is investigated for another resist (AZ4620). Development of the process for this thicker resist is required because of the thicker parylene-C layers for certain devices. In order to determine the appropriate parameters to achieve sufficiently low contrast, test structures are fabricated as shown in Figure 5-7(b). The test mask contains 120  $\mu\text{m}$  squares filled with grayscale patterns that are used in the designs. These grayscale patterns consist of four 1 by 1  $\mu\text{m}$  squares. If one of the four squares is covered with Cr, the transmission ratio is 25%.

The four 120  $\mu\text{m}$  squares in the test structures have transmission ratios of 25%, 50%, 75% and 100%.

The test structures are fabricated on a Si wafer with a 4.5  $\mu\text{m}$ -thick layer of parylene-C coated on it. AZ4620 is spun at 3500 rpm and soft baked for 2 min on a 100°C hotplate. It is found that exposure with a 150  $\mu\text{m}$  gap between the wafer and the mask for 280 s with 5  $\text{mW}/\text{cm}^2$  intensity at 320 nm wavelength with the MA6 (Karl-Suss) and developing with dilute AZ developer (AZ developer: water = 1:2.7) for 50 min achieved sufficient contrast for a 7.4  $\mu\text{m}$  AZ4620 resist. This is determined by a profilometer scan across the test structures to obtain the height of each of the fabricated test structures as shown in Figure 5-7(a). Using this set of parameters results in the photoresist height to dose profile shown in Figure 5-7(c).

### 5.3.3.2 Methods to control exposure dose at different locations on a wafer

Once an appropriately low contrast is achieved, the range of exposure dose is set within a range such that the resist thickness is controlled by the exposure dose. In the direct write approaches, this exposure dose is controlled pixel by pixel by varying the e-beam dose[196] or light intensity[193][197] at each location by scanning the e-beam or light source line by line. However, the direct write approaches are slow and expensive as they require writing pixel by pixel.

Another approach more suitable for large scale manufacturing is to use grayscale masks. Since photolithographic masks are typically binary in nature (regions with Cr typically used to block UV light completely and glass is used as a substrate to allow transmission of UV light in regions without Cr), one way of achieving grayscale features is by exposing the resist with multiple exposures with different masks[198][199]; Regions that are exposed multiple times will have a higher dose. However, this process is expensive as it requires multiple masks and alignment steps. A similar method of creating sloped features is to use the 'moving mask' technique where the mask is moved in-plane during exposure which will similarly create regions with different dose[200].

Another way of achieving grayscale features that is used in this thesis is by drawing

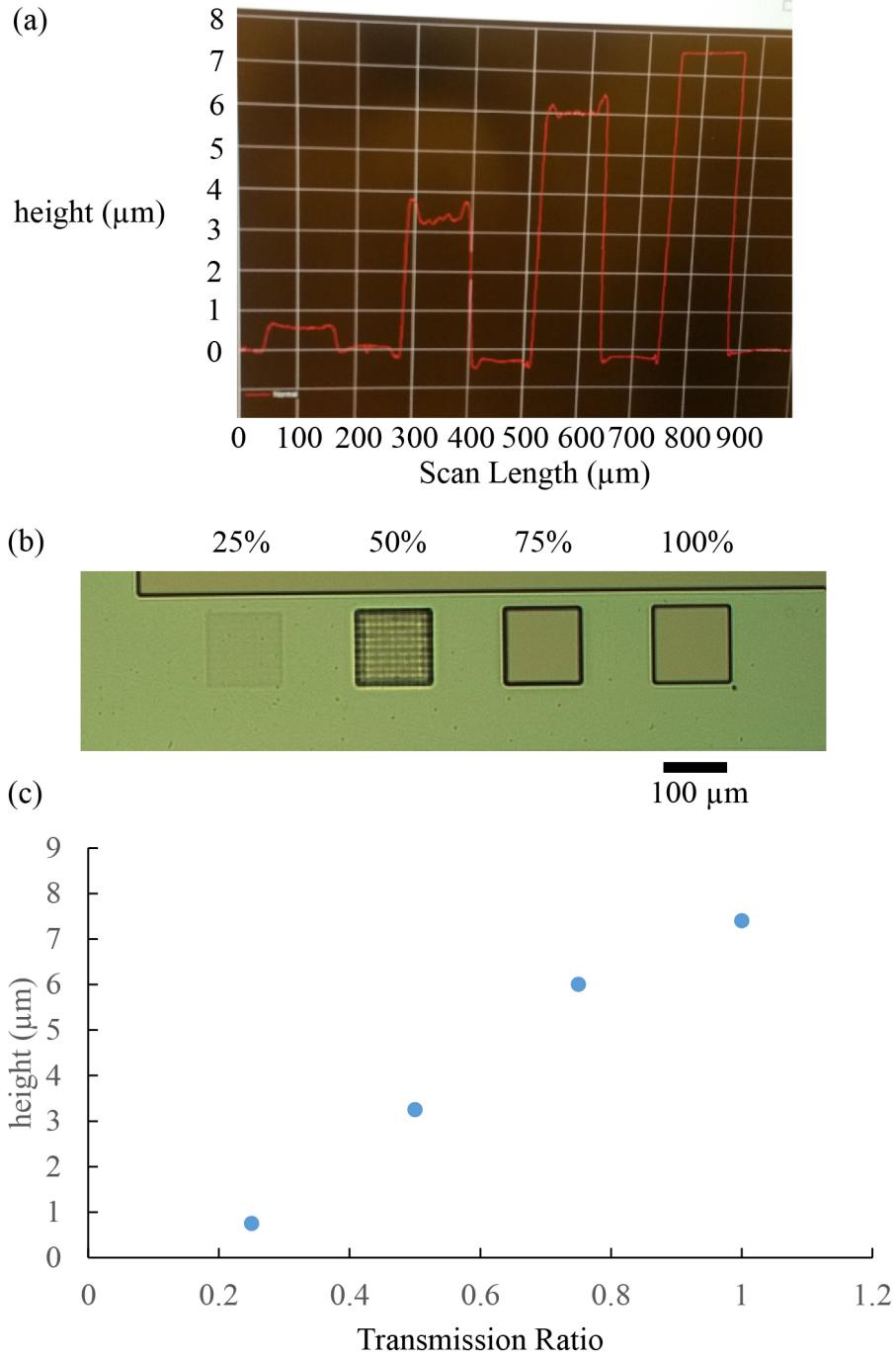


Figure 5-7: (a) Profilometer scan to show variation in height for four different doses used in the test structure. (b) Optical image of grayscale test structures after development. Percentages indicate transmission ratio used. (c) Graph of height of photoresist versus transmission ratio. Photoresist used is AZ4620.

features below the resolution limit of the exposure system to control the effective local exposure dose without actually fabricating the drawn features. This is similar to generating smooth looking images by using the halftone technique. Different mask designs are possible but the method largely relies on the use of modulation of the transmitted UV light by controlling the area of the opening across each unit cell [198][194][199]. If a tool to create features sufficiently below the resolution of the limit of the exposure system is not available or is too expensive, the minimum resolution is increased, for example, by exposing the wafer in proximity mode and increasing the distance between the mask and the wafer which effectively blurs the pattern [198]. Hence, the distance between the mask and the wafer is used to control the smoothness of the grayscale pattern. The relation between resolution limit and the distance between the mask and the photoresist during proximity exposure is given by[201]:

$$R = \sqrt{k\lambda g}, \quad (5.2)$$

where  $R$  is the minimum resolution of features in the photoresist in  $\mu\text{m}$ ,  $\lambda$  is the wavelength of light in  $\mu\text{m}$ ,  $g$  is the gap between the middle of the resist and the written features of the mask in  $\mu\text{m}$ , and  $k$  is a machine dependent constant that is usually close to 1. In this thesis, grayscale lithography is performed using soda lime glass masks that are made in the Carnegie Mellon University Nanofabrication facility (Nanofab) using the Heidelberg DWL 66FS Laser Lithography System which gives  $\sim 1 \mu\text{m}$  resolution for features on the mask. In the Nanofab, the tool for proximity exposure (Karl-Suss MA6) has  $\lambda = 0.32 \mu\text{m}$ . In this process, the gap between the mask and wafer,  $g$ , is chosen to be  $150 \mu\text{m}$ , which gives  $R \sim 7 \mu\text{m}$ . It may appear from (5.2) that the parameter  $g$  can be arbitrarily large. However,  $g$  also affects the slope of the non-grayscale features and thus determines the maximum slope possible with the process.

An initial test of use of grayscale lithography is performed using Dr. Jinsheng Gao's previously fabricated grayscale mask fabricated in Compugraphics which consists of a subpattern of 8 by 8 one  $\mu\text{m}$  squares[195]. By controlling the number of

squares that are blocking light, the amount of transmitted light is controlled using the following equation:

$$T = 1 - \frac{N_A}{N_T}, \quad (5.3)$$

where  $T$  is the fraction of light transmitted,  $N_A$  and  $N_T$  are the number of  $1 \mu\text{m}$  by  $1 \mu\text{m}$  squares that are blocking light and  $N_T$  is the total number of one by one  $\mu\text{m}$  squares in the subpattern.

Assuming the same minimum feature size on the mask, the use of a larger subpattern allows for higher vertical resolution (perpendicular to the wafer) because of more grayscale levels but limits the horizontal resolution (along the wafer) of the designs because of the large unit cells required to be tessellated [198]. For example, using Dr. Jinsheng Gao's test structure allows for creation of slopes in photoresist with horizontal length on the order of  $100 \mu\text{m}$  or more along the plane of the wafer because each subpattern has width  $\sim 8 \mu\text{m}$ . However, for the application of protruding electrodes, the slopes have to be much steeper because the size of the electrodes is in the order of  $10 \mu\text{m}$ . Hence, in the masks for protruding electrodes, the subpattern is modified to be smaller (one  $\mu\text{m}$  length squares arranged in a 2 by 2 subpattern) although this limits the number of grayscale levels (4 versus 64). However, if the proximity distance is kept at  $150 \mu\text{m}$ , the size of the subpattern is smaller than the resolution limit which would allow for smoothing of the pattern across subpatterns.

### 5.3.4 Analysis of pattern transfer for anisotropic etch processes

Once a sloped profile is achieved in the resist, an etch step is performed in order to transfer the slope pattern from the resist to the parylene-C. This pattern transfer by etching is analyzed starting with the relationship between the parylene-C etched and the respective etch times and etch rates. By assuming that the etch step is perfectly anisotropic, this relationship is written as[195]:

$$d_{Px}(x, y) = R_{Px}t - R_{Px}t_{PR}(x, y) = R_{Px}t - R_{Px} \frac{d_{PR}(x, y)}{R_{PR}}, \quad (5.4)$$

where  $t$  is the total etch time,  $d_{Px}$  is the actual depth of parylene-C etched,  $R_{Px}$  is the etch rate of parylene-C,  $R_{PR}$  is the etch rate of photoresist,  $d_{PR}$  is the depth of photoresist etched and  $t_{PR}$  is the time the photoresist is etched. In this analysis, the etch rates are assumed to be independent of location on the wafer.

For the creation of vias and protruding electrodes, the etch time is designed such that parylene-C in the regions without photoresist is *just* etched completely so that the platinum in the lower level is exposed. This means that the thickness of the parylene-C encasing the platinum is written as

$$T_{Px} = R_{Px}t. \quad (5.5)$$

The thickness of parylene-C is usually fixed by other device considerations and  $R_{Px}$  is determined by processing conditions. Hence, (5.5) is a design constraint that sets the total etch time for a given process. Applying this constraint to (5.4) gives

$$d_{Px}(x, y) = T_{Px} - Sd_{PR}(x, y) \quad (5.6)$$

where  $S = R_{Px}/R_{PR}$  is the selectivity of the etch.

If the thickness of the resist is also set to be

$$T_{PR} = T_{Px}/S \quad (5.7)$$

which makes  $T_{PR} = R_{PR}t$  so that the resist is also *just* etched completely,

$$d_{PR}(x, y) = h_{PR}(x, y) \quad (5.8)$$

where  $h_{PR}(x, y)$  is the height profile of the photoresist. In addition,

$$h_{Px}(x, y) = T_{Px}(x, y) - d_{Px}(x, y). \quad (5.9)$$

Hence, substitution of (5.8) and (5.9) into (5.6) yields:

$$T_{Px}(x, y) - h_{Px}(x, y) = S(T_{PR} - h_{PR}(x, y)) \quad (5.10)$$

which is simplified to

$$h_{Px}(x, y) = Sh_{PR}(x, y). \quad (5.11)$$

Hence, if the etch time and resist thickness are set appropriately using the constraints represented by (5.4) and (5.7), the final height and slope of the parylene-C structures are scaled by a factor  $S$  versus that of the grayscale patterns obtained in the photoresist during development.

The effect of the various deviations from the constraints is seen in Figure 5-8. In Figure 5-8(a), the ideal case is shown where the etch time and resist thickness are set appropriately.

In the case where the etch time is longer than required, which is usually necessary to account for non-uniformities across the wafer, the constraint (5.4) on parylene thickness and etch time becomes

$$T_{Px} + \epsilon_{Px} = R_{Px}t \quad (5.12)$$

where  $\epsilon_{Px}$  is the magnitude of the deviation in thickness of  $T_{Px}$  from  $R_{Px}t$ . However, all the photoresist is still etched and hence, the equality  $d_{PR}(x, y) = h_{PR}(x, y)$  does not change. Hence,

$$h_{Px}(x, y) = Sh_{PR}(x, y) - \epsilon_{Px}. \quad (5.13)$$

When  $h_{Px}(x, y) \leq 0$ , all the parylene-C is etched at that point. From (5.13), overetching does not change the slope of the obtained profile but introduces a downward shift to the profile. This is seen in Figure 5-8(b).

The effect of deviations of the resist thickness,  $T_{PR}$  from  $T_{Px}/S$  is seen by changing the constraint on resist thickness to

$$T_{PR} = T_{Px}/S \pm \epsilon_{PR}. \quad (5.14)$$

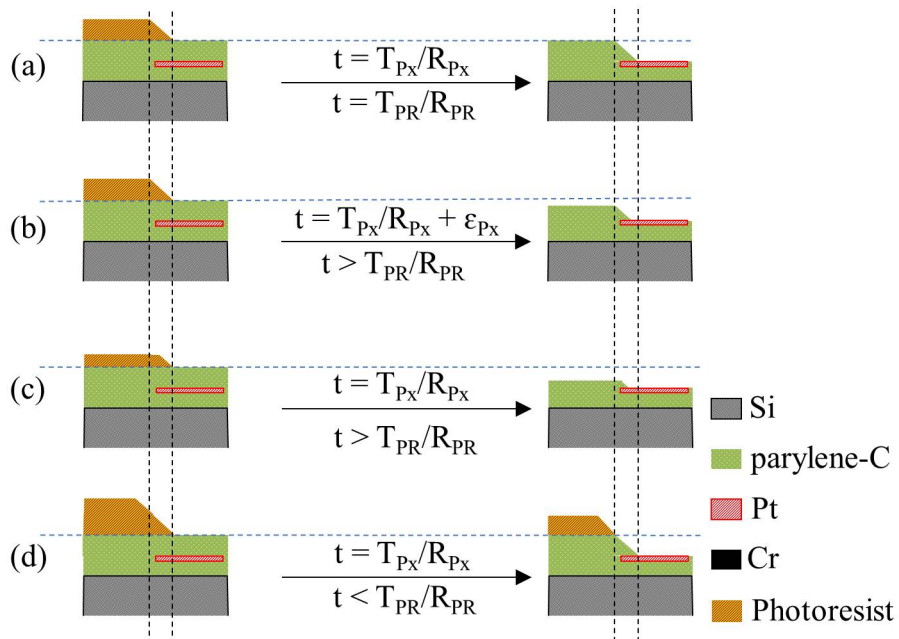


Figure 5-8: Effect of process variations on the pattern transfer process from photoresist to parylene-C. (a) In the ideal case where both photoresist and top layer parylene-C are just etched. (b) Case where parylene-C is overetched. (c) Case where photoresist is thinner than the ideal case. (d) Case where photoresist is thicker than the ideal case.

where  $\epsilon_{PR}$  is the magnitude of the deviation in thickness of the resist from  $T_{Px}/S$ . For the case  $T_{PR} = T_{Px}/S - \epsilon_{PR}$ , this gives:

$$h_{Px}(x, y) = Sh_{PR}(x, y) - S\epsilon_{PR}. \quad (5.15)$$

Having a resist thinner by  $\epsilon_{PR}$  results in a shift in the parylene profile downwards by  $S$  times  $\epsilon_{PR}$  as seen in Figure 5-8(c).

For the case  $T_{PR} = T_{Px}/S + \epsilon_{PR}$ , the equation  $d_{PR}(x, y) = h_{PR}(x, y)$  no longer applies since there will be remaining photoresist after the etch and is substituted with:

$$d_{PR}(x, y) + \epsilon_{PR} = h_{PR}(x, y) \quad (5.16)$$

for  $h_{PR}(x, y) < T_{Px}/S$ , and

$$d_{PR}(x, y) = T_{Px}/S \quad (5.17)$$

for  $h_{PR}(x, y) > T_{Px}/S$ .

For the case  $h_{PR}(x, y) < T_{Px}/S$ , this gives the same equation

$$h_{Px}(x, y) = Sh_{PR}(x, y). \quad (5.18)$$

For the case  $h_{PR}(x, y) > T_{Px}/S$ , the parylene remains unetched or

$$h_{Px}(x, y) = T_{Px}. \quad (5.19)$$

This is seen in Figure 5-8(d), where the final parylene-C profile is the same as the profile in the ideal case in the regions without remaining resist but in regions with remaining resist, the parylene-C remains unetched.

### 5.3.5 Implementation of pattern transfer

To design for the final slope of the features, it is necessary to first characterize  $S$ . Since  $O_2$  RIE is the most common method of etching parylene-C anisotropically, the

pattern transfer process is characterized using O<sub>2</sub> RIE as the method of etching to transfer the pattern from photoresist to parylene-C.

To characterize the etch rate of the various materials using O<sub>2</sub> RIE, parylene-C, AZ4210 and AZ4620 are deposited/spun on one inch Si test coupons. 4.5 μm of parylene-C is deposited using the standard Gorham process. AZ4210 and AZ4620 is spin coated on 1"-diameter Si test coupons at 3000 rpm and baked at 100°C on a hotplate to give a thickness of 2.4 μm and 8.8 μm measured using a P-15 Profilometer (KLA Tencor, Milpitas, CA). Following 5 min of etching in the Phantom II RIE (Trion Technology, Clearwater, FL) using O<sub>2</sub> RIE at 50W and 14 sccm, the thicknesses of the various resists and parylene-C are measured to obtain the etch rates that are tabulated in Table 5.2. As expected, since both parylene-C and photoresist are polymers, the etch rates for all the compounds are within the same order.

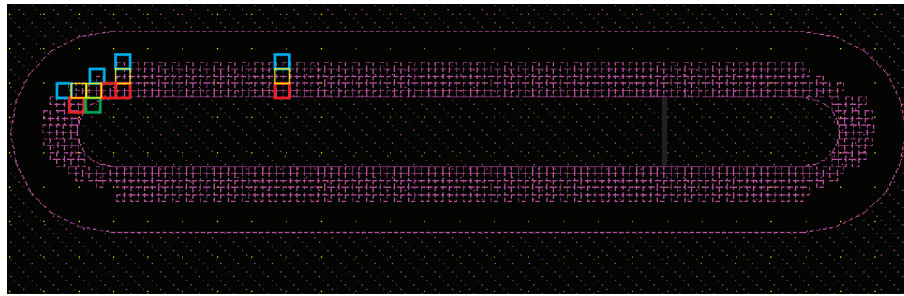
Two different resists are investigated in order to allow for a larger range of thicknesses of parylene-C. For typical spin speeds (2000 rpm to 4000 rpm) AZ4210 gives a resist thickness of approximately 2-4 μm and AZ4620 gives a resist thickness of approximately 6-10 μm. Hence, based on the selectivities obtained from the measured etch rates, AZ4210 allows for grayscale lithographic transfer to parylene-C layers of approximately 2.4-4.8 μm-thick whereas AZ4620 allows for 4.7-7.9 μm-thick layers.

### 5.3.6 Fabrication of Protruding Electrodes

Protruding electrodes are fabricated using the technology developed for vias. In this case, the slopes created using 2.5D lithography are used to create electrodes that protrude out of the substrate.

Table 5.2: Measured etch rate of various materials in O<sub>2</sub> plasma RIE and calculated selectivities based on the etch rates

Material	Measured etch rate (μm/min)	S = (R <sub>Px</sub> /R <sub>PR</sub> )
Parylene-C	0.15	1
AZ4620	0.19	0.79
AZ4210	0.13	1.2



- 3/4 squares covered
- 2/4 squares covered
- 1/4 squares covered
- Approximately 2/3 covered

15 μm

Figure 5-9: Layout of a protruding electrode. Grayscale tones are obtained by using a subpattern of 4 squares.

The layout for a protruding electrode is shown in Figure 5-9. A gradual slope is designed using grayscale lithography to ensure continuity between the lower Pt layer and the top of the protrusion at the sides of the protrusion using a series of subpatterns consisting of 4 squares. The arrangement of the different subpatterns is shown in Figure 5-9.

Since probes of two different parylene-C thicknesses are fabricated in this thesis, two separate process flows for grayscale lithography is developed. The initial steps for both probes are similar. Initially, the 250 to 300 μm-thick 10 cm Si wafer is treated with a mixture of A174, IPA and DI water (1:100:100 by volume) that has been left to cure overnight. Parylene-C (2.2 μm for 4.5 μm-thick probes, 4.5 μm for 9 μm-thick probes) is then deposited on the wafer. Following that, AZ5214E is spun at 4000 rpm and baked on a hotplate at 100°C for 1 minute to give a thickness of 1.4 μm. Following contact exposure for 40 s in the MA6 with the Pt-layer mask, the wafer is baked at 115°C for 2 min. The wafer is then developed in a mixture of AZ developer:DI water (2:1 by volume of AZ developer:water) for 1 minute. Following a 1 minute, 100 W descum in an O<sub>2</sub> barrel etcher at 1 Torr, 126 nm of Pt is deposited using the Perkin-Elmer 2400-6J sputtering system at 20 mT, 65 sccm Ar flow rate. The wafer is then soaked overnight in acetone and transferred into a new beaker of acetone where it

is ultrasonicated until the lift-off is complete. A 1 minute, 100 W descum in an O<sub>2</sub> barrel etcher at 1 Torr is then performed and a second layer of parylene-C (2.2 μm for 4.5 μm-thick probes, 4.5 μm for 9 μm-thick probes) is then deposited. Following a Cr hard mask deposition (20 nm for 4.5 μm-thick probes, 33 nm for 9 μm-thick probes) using a Perkin-Elmer 2400 8L sputtering system, AZ4210 is spun at 3000 rpm to give a 2.4 μm thick layer of resist. The wafer is baked in a 90°C oven for 20 min. Following exposure with a mask to define the outline of the probes in the MA6 for 120 s, the wafer is developed in AZ developer for 1 minute. Following a 1 minute, 100 W descum at 1 Torr, the exposed Cr is etched in Cr etchant (Trascene) for 30 s. The wafer is then etched using a Trion RIE system using O<sub>2</sub> plasma at 50 mT, 100 W, 14 sccm (40 min for 4.5 μm-thick probes, 80 min for 9 μm-thick probes). Following that, any remaining photoresist is removed using acetone and following a 1 minute, 100 W descum at 1 Torr, the remaining Cr is removed by immersing the wafer in Trascene Cr etchant for 60 s.

For 4.5 μm-thick probes, AZ4210 is used to perform the grayscale lithography steps and is spun at 3000 rpm and baked for 1 minute on a 100°C hotplate, giving a thickness of 2.4 μm. Using proximity exposure mode on the MA6 (Karl-Suss, Garching, Germany), the resist is exposed for 320 s with a 150 μm gap between the mask and photoresist followed by 50 min development in AZ developer solution (1 AZ developer:2.7 water). The wafer is then etched in a Trion RIE O<sub>2</sub> plasma at 50 W 14.2 sccm for 15 min which resulted in a slight overetch. This gives an etch rate of approximately 0.17 μm/min which is close to the 0.13 μm/min etch rate characterized in Table 5.2.

Optical images at different points of processing are seen shown in Figure 5-10. Figure 5-10(a) shows an image of a probe after lift-off. Figure 5-10(b) shows an image of a probe after a ceramic is patterned. A detailed description of different ceramics used is given in chapter 4. Figure 5-10(c) shows an image of a probe after the outline of the parylene-C is patterned and the electrode regions are defined by grayscale lithography. Figure 5-10(d) shows a final image of a probe with the second layer of Pt deposited and patterned to define the protruding electrode.

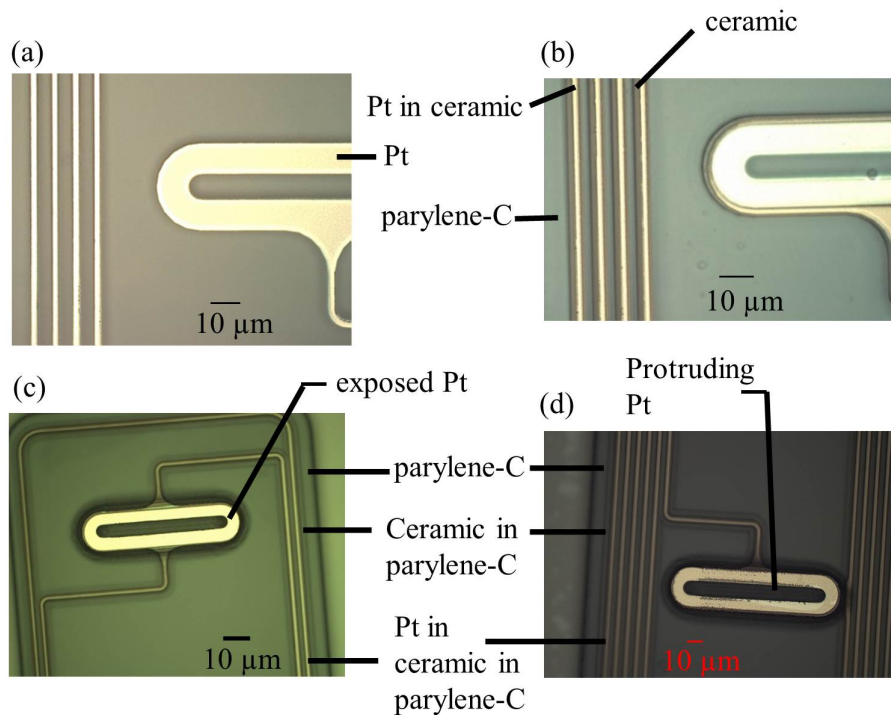


Figure 5-10: Optical images at different points of processing of protruding electrodes. (a) After first Pt layer lift-off. (b) After patterning of ceramic layer (a description of the use of ceramics is found in chapter 4). (c) After parylene-C outline patterning and grayscale patterning of parylene-C in electrode regions. (d) After second layer Pt deposition and lift-off.

A zoomed-out optical image of a fabricated probe with protruding electrodes is shown in Figure 5-11(a). An SEM of a protruding electrode that illustrates the morphology of the protrusion is shown in Figure 5-11(b). The protruding electrode is also characterized using a Newview 7300 optical profilometer (Zygo Corporation, Middlefield, CT) as shown in Figure 5-12(a). The 2D profile across the dotted line shown in Figure 5-12(a) is plotted in Figure 5-12(b). The optical interference nature of the Zygo measurement makes thickness values taken over transparent surfaces (like parylene-C) unreliable. Hence, this explains unreliable values of height obtained by the Zygo in areas such as the region 'parylene over Pt' indicated in Figure 5-12(a), where a deep recess is indicated by the Newview 7300 (The additional Pt in that region should result in a mesa and this is confirmed by contact profilometry). However, the protruding region is coated by Pt which is not transparent and hence is not expected to produce unreliable results with the Newview 7300. An Alicona Infinite Focus microscope is also used to characterize the morphology of the protruding electrode. The obtained 3D profile is shown in Figure 5-13(a) and the 2D profile along the red line plotted in Figure 5-13(a) is shown in Figure 5-13(b).

For 9  $\mu\text{m}$  probes, AZ4620 is used to perform the grayscale lithography steps and is spun at 3500 rpm for 30 s with a 6 s spread at 600 rpm and baked for 2 min on a 100°C hot plate, giving a thickness of 7.4  $\mu\text{m}$ . Using proximity exposure mode on the MA6 (Karl-Suss, Garching, Germany), the resist is exposed for 280 s with a 150  $\mu\text{m}$  gap between the mask and photoresist followed by a 50 min development step in diluted AZ developer solution (1 AZ developer:2.7 water). The wafer is then etched in a Trion RIE O<sub>2</sub> plasma at 50 W 14.2 sccm for 30 min which resulted in a slight overetch. This gives an etch rate of approximately 0.25  $\mu\text{m}/\text{min}$  which is close to the 0.19  $\mu\text{m}/\text{min}$  etch rate characterized in Table 5.2. The protruding electrode is characterized using a Newview 7300 optical profilometer as shown in Figure 5-14(a). The 2D profile across the dotted line shown in Figure 5-14(a) is plotted in Figure 5-14(b). The obtained 3D profile using the Alicona Infinite Focus microscope is shown in Figure 5-15(a) and various 2D profiles are extracted from the 3D profile in Figure 5-15(b) and Figure 5-15(c).

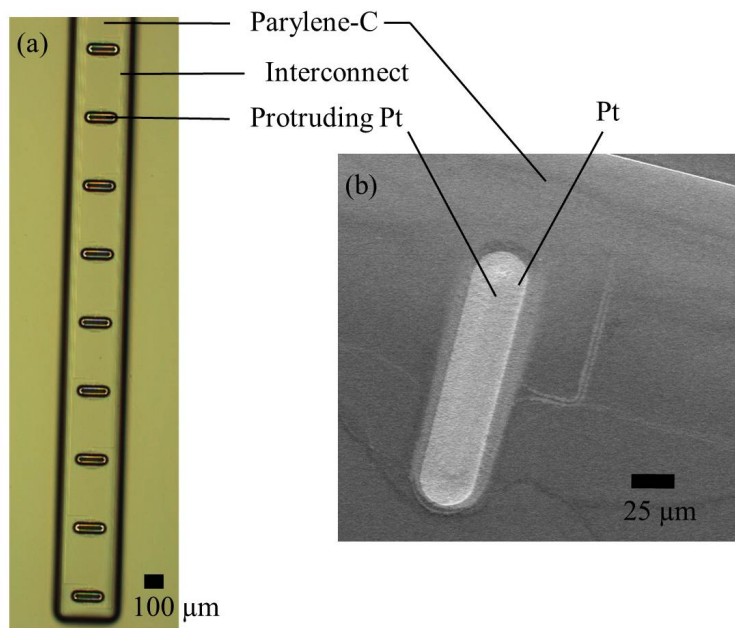


Figure 5-11: Images of protruding electrodes. (a) Optical image of 9 protruding electrodes in a penetrating neural probe. (b) SEM of a protruding electrode.

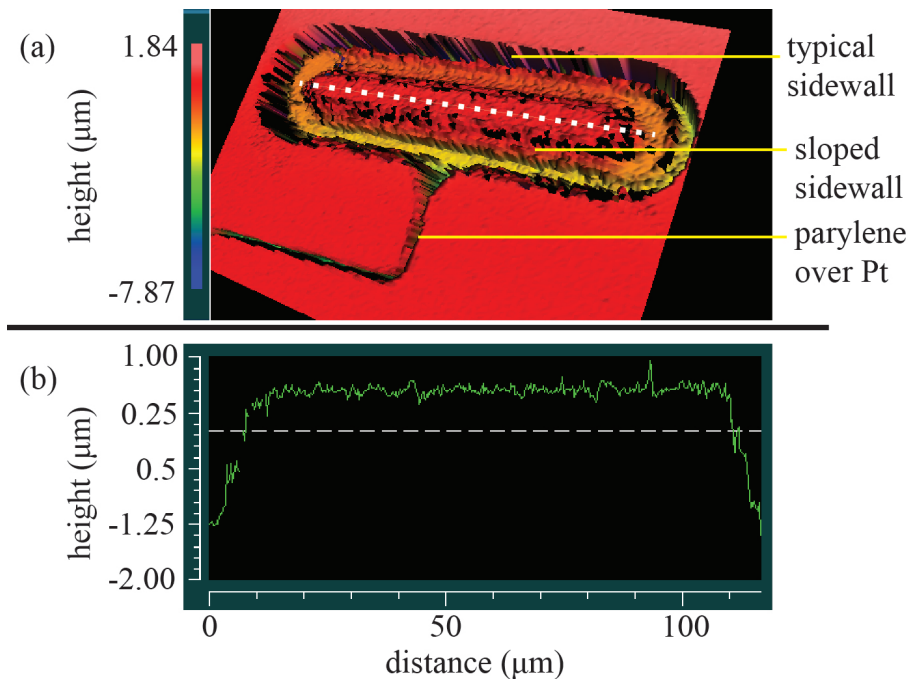


Figure 5-12: Zygo measurement of the profile of a protruding electrode in a 4.5 μm-thick probe. The contrast in slope between a typical and sloped sidewall is evident here. The slope obtained is approximately 0.15 μm/μm (a) 3D profile of a protruding electrode. (b) extracted 2D profile across dotted white line seen in (a).

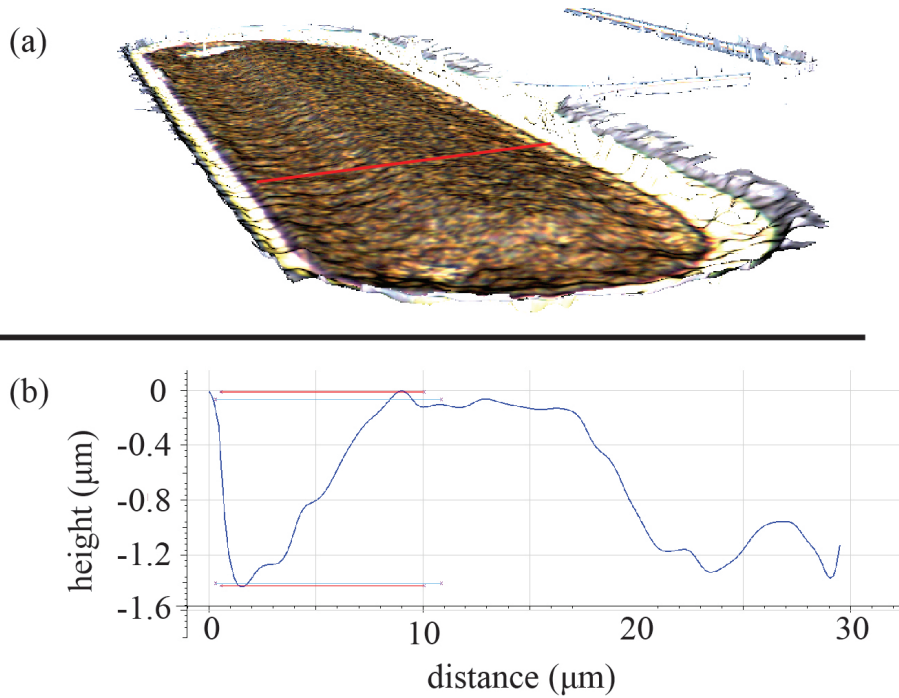


Figure 5-13: (a) 3D profile of a protruding electrode in a 4.5  $\mu\text{m}$ -thick probe obtained using the Alicona microscope. (b) extracted 2D profile across red line seen in (a).

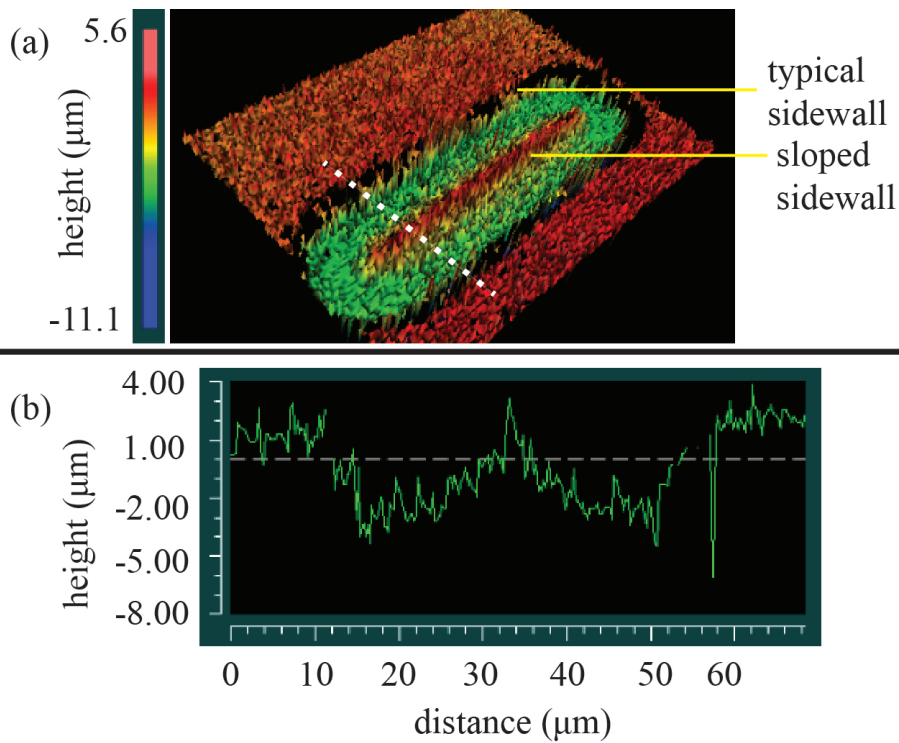


Figure 5-14: Zygo measurement of the profile of a protruding electrode in a 9  $\mu\text{m}$  probe. (a) 3D profile of a protruding electrode. (b) extracted 2D profile across dotted white line seen in (a).

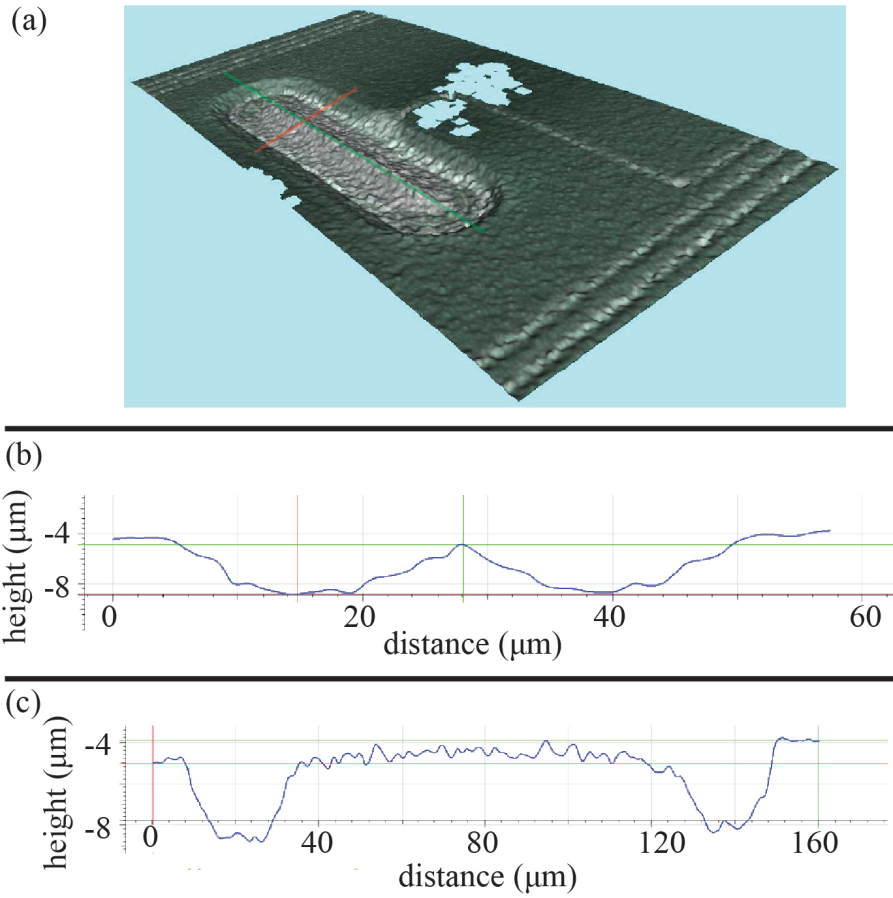


Figure 5-15: (a) 3D profile of a protruding electrode in a 9  $\mu\text{m}$  probe obtained using the Alicona microscope. (b) Extracted 2D profile across red line seen in (a). (c) Extracted 2D profile across green line seen in (a).

Electrical continuity is also confirmed for both electrodes fabricated in 4.5  $\mu\text{m}$ -thick probes and 9  $\mu\text{m}$ -thick probes by using a measuring the resistance between an electrode and a pad using a probe station.

### 5.3.7 Roughening of electrodes

In this section, the metric used to characterize roughness in this section is the arithmetical mean deviation of the assessed profile, which is given by

$$R_a = \frac{1}{n} \sum_{i=1}^n |y_i| \quad (5.20)$$

where  $n$  is the total number of points measured,  $y_i$  is the height of the profile at point  $i$  after subtracting the mean of the entire profile.

AFM is performed on a 3  $\mu\text{m}$  by 3  $\mu\text{m}$  area of a flat portion of the protruding electrode of the 4.5  $\mu\text{m}$ -thick probe. The result of the AFM is shown in Figure 5-16. The measured  $R_a$  is 107 nm compared to 13 nm for conventional recessed electrodes as measured in Chapter 2. The measured  $R_a$  of the flat portion of the protruding electrode after 300°C anneal is measured to be 103 nm. This method of electrode fabrication reduces the electrode impedance at 1 kHz from 70 k $\Omega$  to 21.6 k $\Omega$  for 115  $\mu\text{m}$  by 15  $\mu\text{m}$  electrodes, 293 k $\Omega$  to 160 k $\Omega$  for 15  $\mu\text{m}$  by 15  $\mu\text{m}$  electrodes and 128 k $\Omega$  to 82 k $\Omega$  for 65  $\mu\text{m}$  by 15  $\mu\text{m}$  electrodes as shown in Figure 5-17.

The cause of the increased roughness is investigated using AFM. The measured  $R_a$  for as-deposited parylene-C is 4 nm for as-deposited parylene-C, 7 nm for parylene-C etched for 2 min in O<sub>2</sub> RIE and 22 nm for parylene-C etched for 5 min as shown in Figure 5-18. The conditions for the O<sub>2</sub> RIE etch are the same as for the protruding electrodes (i.e., 50 W, 14.2 sccm in the Trion RIE machine). The measured  $R_a$  is much lower compared to that of protruding electrodes (107 nm). Hence, the approximately 3 min of overetch of parylene-C during the processing of protruding electrodes alone cannot account for the increased roughness completely.

Furthermore, coating the untreated and etched parylene-C with approximately 126 nm of Pt is seen to reduce the roughness of the parylene-C as seen in Figure 5-19.

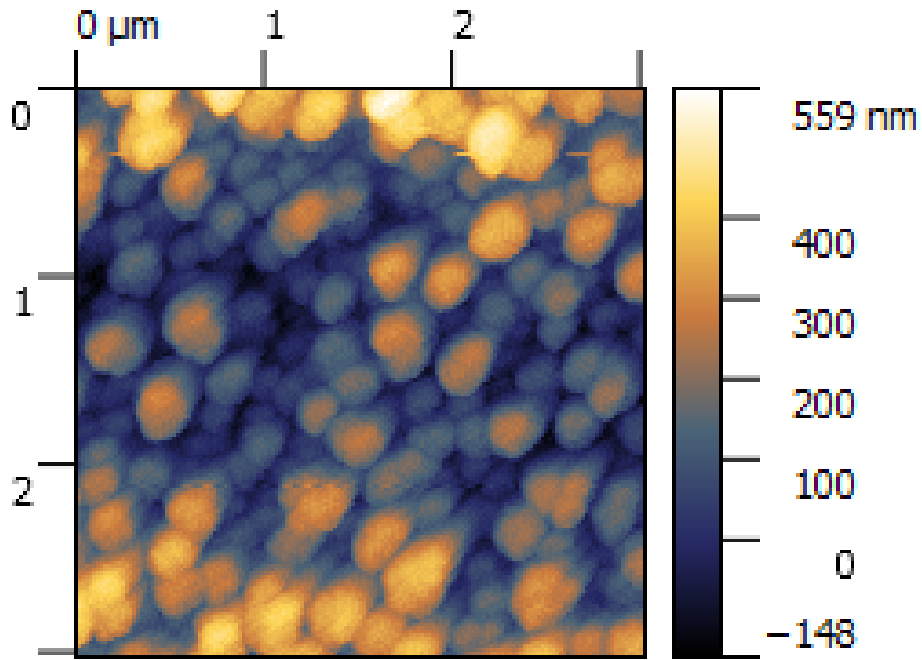


Figure 5-16: AFM of protruding electrode.

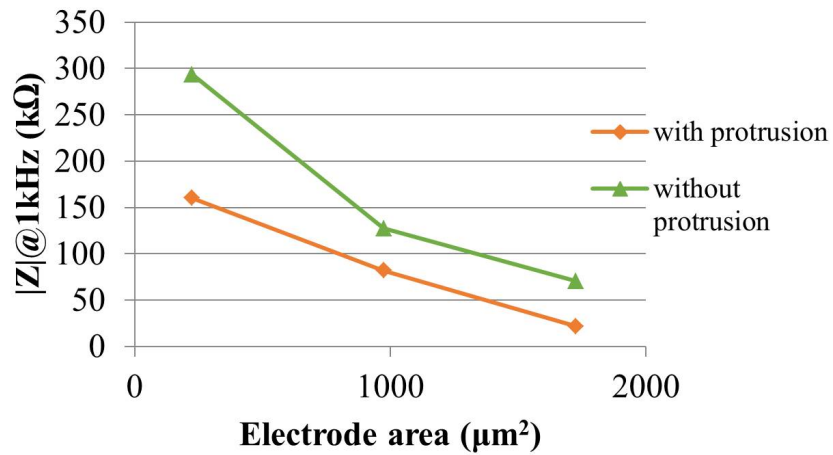


Figure 5-17: Comparison of the impedance of electrodes with and without protrusion.

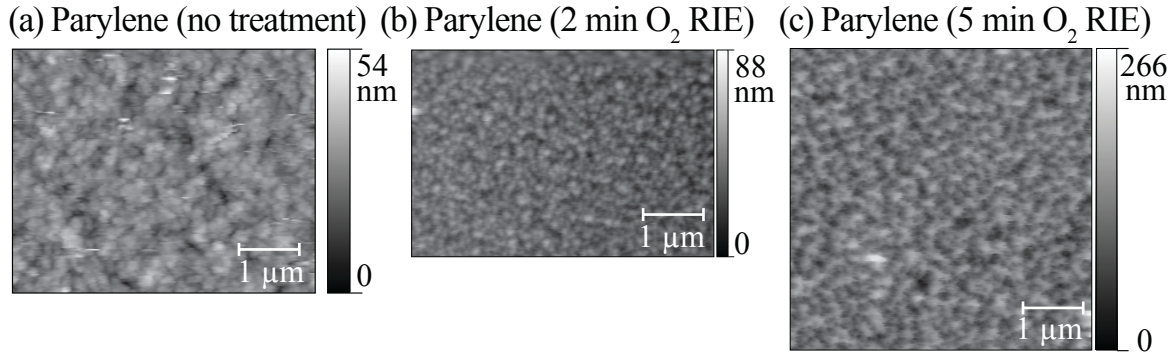


Figure 5-18: AFM of 4.5  $\mu\text{m}$ -thick parylene-C (a) with no treatment (b) after 2 min etch in O<sub>2</sub> RIE (c) after 5 min etch in O<sub>2</sub> RIE. Measured roughness,  $R_a$  is 4 nm for (a), 7 nm for (b) and 22 nm for (c).

The  $R_a$  is seen to be reduced from 4 nm to 3 nm when Pt is deposited on untreated parylene-C, from 7 nm to 5 nm when Pt is deposited on parylene-C that has been etched for 2 min in O<sub>2</sub> RIE and from 22 nm to 18 nm when Pt is deposited on parylene-C that has been etched for 5 min in O<sub>2</sub> RIE. It is also observed that the grain sizes of the Pt increases with the O<sub>2</sub> RIE time of the parylene-C.

During the fabrication of protruding electrodes, the photoresist is etched completely prior to parylene-C. By performing AFM on photoresist spun on parylene-C, it is seen that although as-deposited photoresist is smooth, the photoresist gets considerably roughened after O<sub>2</sub> RIE as shown in Figure 5-20. Since the photoresist is etched through (for 12 min) prior to the etching of parylene-C, this roughness will be transferred to the parylene-C. This explains the discrepancy between the roughness of etched parylene-C and the roughness of the protruding electrode. Other reasons for the discrepancy include differences in the microloading conditions since the tests were done on pieces of Si coated with parylene-C whereas for the fabrication of protruding electrodes, the surface of the wafer is patterned with photoresist with only very small regions of parylene-C exposed.

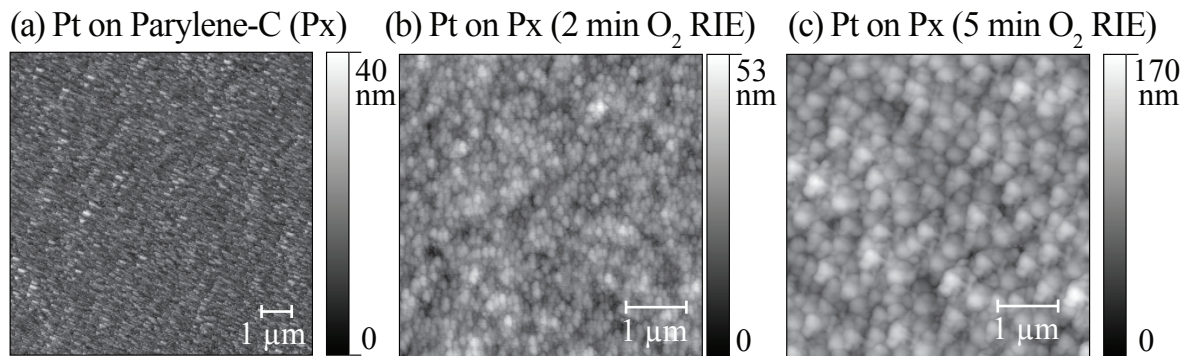


Figure 5-19: AFM of Pt on 4.5  $\mu\text{m}$ -thick parylene-C (a) with no treatment of parylene-C (b) with parylene-C etched for 2 min in O<sub>2</sub> RIE (c) with parylene-C etched for 5 min etch in O<sub>2</sub> RIE. Measured roughness,  $R_a$  is 3 nm for (a), 5 nm for (b) and 18 nm for (c).

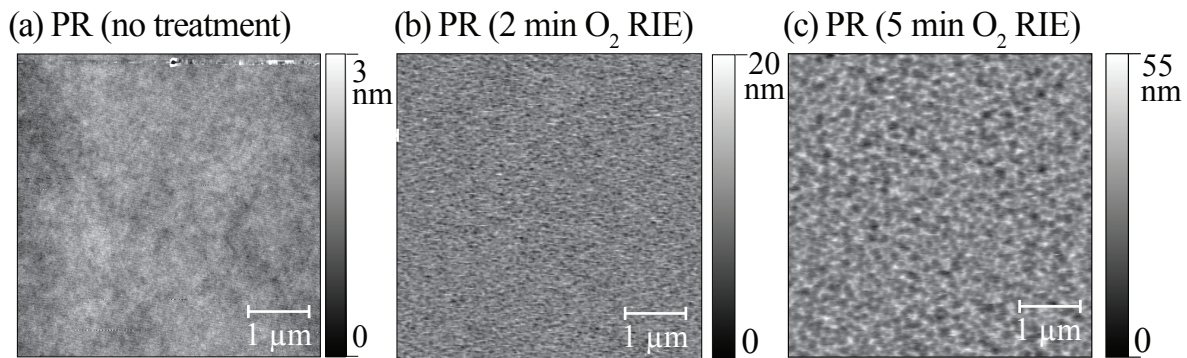


Figure 5-20: AFM of positive photoresist (AZ4210) spun on 4.5  $\mu\text{m}$ -thick parylene-C (a) with no treatment (b) after 2 min etch in O<sub>2</sub> RIE (c) after 5 min etch in O<sub>2</sub> RIE. Measured roughness,  $R_a$  is 0.3 nm for (a), 2 nm for (b) and 6 nm for (c).

## 5.4 Summary

The fabrication of protruding electrodes, which reduces the distance between the recording or stimulation site of interest and the electrode, is developed using grayscale lithography and pattern transfer from the photoresist to parylene-C. Grayscale lithography is achieved using grid-like patterns below the resolution limit of the photolithography system that can control the effective intensity of transmitted light in an area. Pattern transfer is analyzed and performed assuming an anisotropic etch where the ratio of etch rates determines the final slope of the structure. The use of grayscale lithography eliminates the need for thick layers of metal that causes reliability problems because of intrinsic stress and allows flexibility in the design of the electrode.

The same method is also demonstrated as a means to fabricate vias on a flexible neural probe substrate.

This method of fabricating protruding electrodes is found to reduce the impedance of the electrode as compared with recessed electrodes. This can be explained by the increased roughness of protruding electrodes.

# Chapter 6

## Design of probes and *in vivo* experiments for specific applications

The principles of electrical neural stimulation and sensing are generally similar across different applications. For sensing, a high signal-to-noise ratio is achieved when the electrodes are close to the recording site-of-interest, impedance of the electrodes is low and the impedance of the insulated regions in the probe is high. For stimulation, a large capacity for charge transfer without exceeding safe limits and proximity to the stimulation site-of-interest is critical. The design of electrodes for stimulation and sensing is discussed in Chapter 2.

Despite the similarities, the design of various probes are very application specific largely because of the very different anatomy where stimulation and sensing is desired; and the different methods required to deploy the probes. Furthermore, due to the tradeoffs in the design of probes (for example, penetrating probes are more specific than cuff electrodes for peripheral applications but cause more damage to tissue), the optimal design of probes differs across applications.

This chapter first describes the mechanical design of probes for implantable brain probes and peripheral probes. For the case of penetrating probes in the brain, an *in vivo* comparison between dissolvable probes and Si probes is provided. Preliminary work on the actuation of neural probes is then described.

## 6.1 Meanders to improve axial compliance in implantable probes

An implanted neural probe can be modeled as a lumped parameter system as shown in Figure 6-1. This model consists of a mechanical spring representing the stiffness of the electrical wiring between the brain and the skull ( $k_a$ ) and an effective stiffness of the spring in the brain ( $k_b$ ). Thus, in order to reduce micromotion of the probe in the brain, it is necessary to reduce  $k_a$ , the spring constant of the probe between the brain and the skull. In addition, it is also necessary to decouple the electrode from this micromotion to ensure recording stability[202]. This can be achieved by reducing  $k_b$ . The assumed fixed boundary condition of the end of the probe embedded in the brain can be enforced through the use of design modifications such as anchoring structures[203]. This, along with a low  $k_b$  improves recording stability.

Contributors to micromotion include respiration and vascular pulsation [204][205][206], and mechanical acceleration of the head [205][206]. Based on this, the approach to minimizing the impact of micromotion involves minimizing the spring constant  $k_a$  in the radial direction with fixed-guided boundary conditions. The second approach involves minimizing the spring constant of a probe under fixed-free conditions in the  $x$ ,  $y$  and  $z$  components. For the circular meanders analyzed in this section, it is found that both boundary conditions yield approximately the same results when the probe has more than three circular segments.

### 6.1.1 Analysis of circular meanders for probes

Using the model in Figure 6-2, a framework is developed to compare and analyze different probe connection structures. The primary metric used is the spring constant of the connection between the brain and the skull. Reference [207] considers the use of rectangular meandering probes and compared them with straight beams. In this section, a class of meandering neural probes built using circular sections is analyzed under the constraints typically required for neural probes. The analysis provides a

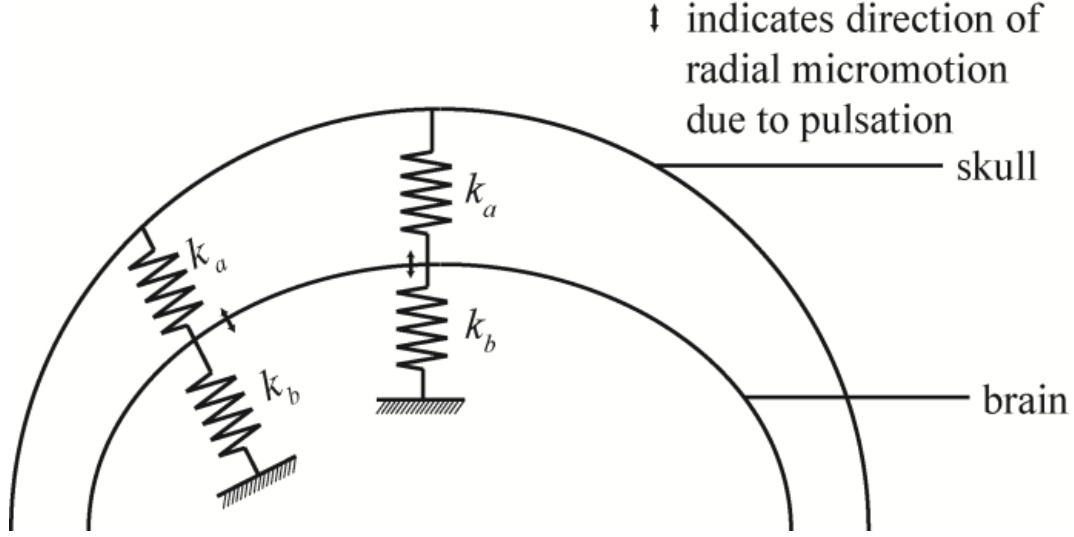


Figure 6-1: Schematic representing the mechanical model of a probe implanted in a brain.

structured means of designing probes using such circular sections. As compared to rectangular meanders, meanders based on conic sections allow for increased probe packing density and do not have sharp corners or localized stress concentrations.

By considering a different axis for each unit structure as shown in Figure 6-2, the method described in [208] that is used to determine the spring constant of rectangular is applied for the structures shown in Figure 6-2. Due to the circular shape of the unit structure, polar coordinates are used. For the case where only in-plane forces and moments are applied, the moment in the  $j$ th meander section is

$$M_{j,in} = (-1)^j F_y R (\sin \theta - \sin \theta_1) + F_x R (\cos \theta_1 - \cos \theta + 2j \cos \theta_1) + M_0 \quad (6.1)$$

where  $\theta_1$  is defined to be  $\frac{\pi - \theta_s}{2}$ . For the case when only an out-of-plane force,  $F_z$  is applied, the moment,  $M_{j,out}$  and torsion,  $T_{j,out}$ , in the  $j$ th meander section are

$$M_{j,out} = F_z R \sqrt{(\sin \theta - \sin \theta_1)^2 + (\cos \theta_1 - \cos \theta + 2j \cos \theta_1)^2} \cos \left( \frac{\theta - \theta_1}{2} \right) \quad (6.2)$$

$$T_{j,out} = F_z R \sqrt{(\sin \theta - \sin \theta_1)^2 + (\cos \theta_1 - \cos \theta + 2j \cos \theta_1)^2} \sin \left( \frac{\theta - \theta_1}{2} \right) \quad (6.3)$$

respectively where  $F_x$ ,  $F_y$ ,  $F_z$ ,  $M_0$  are forces and moments applied as shown in Fig-

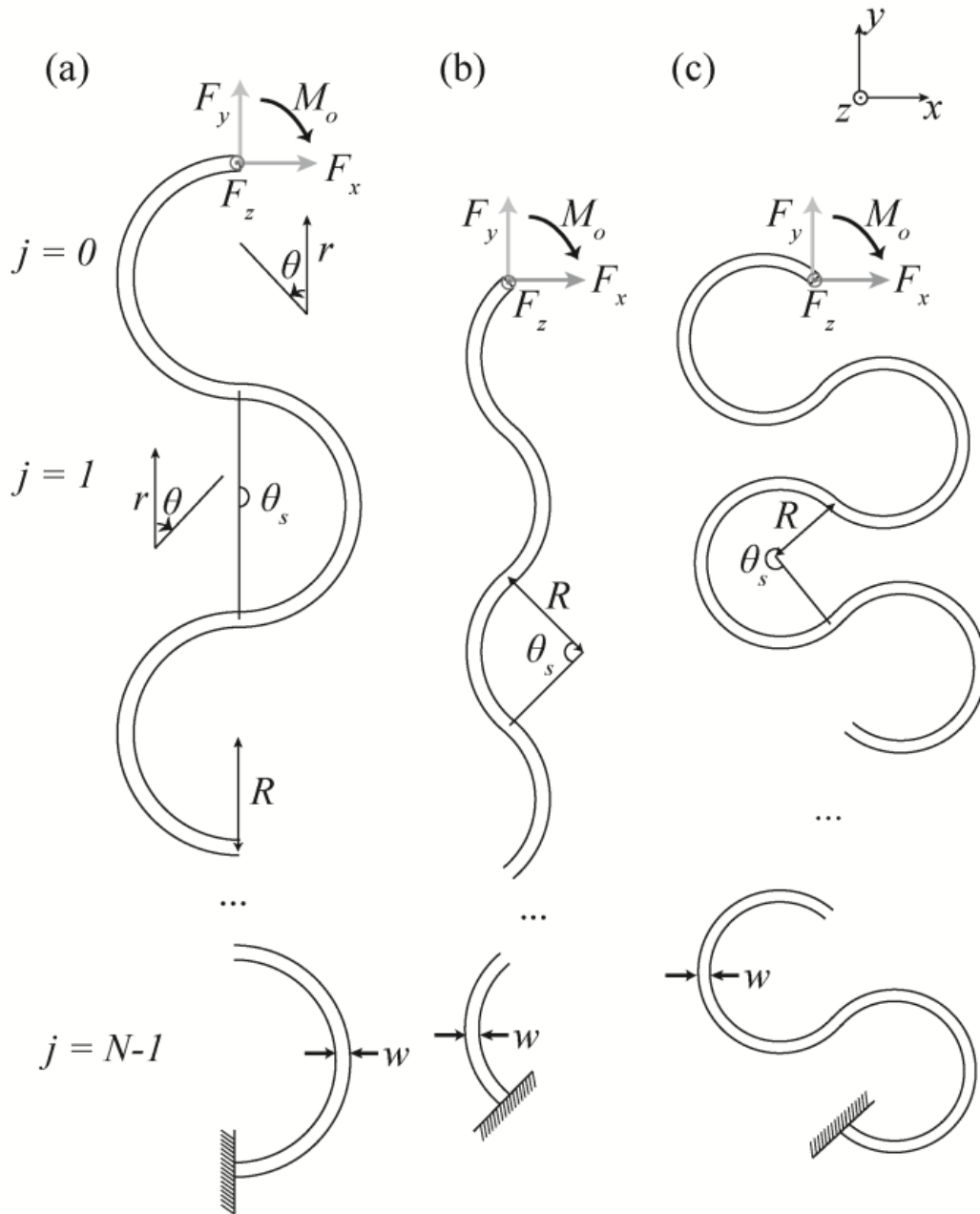


Figure 6-2: (a) Meanders formed using circular segments with (a)  $\theta_s = \pi$ , (b)  $\theta_s < \pi$  and (c)  $\theta_s > \pi$ .

Figure 6-2. Applying Castigliano's theorem yields

$$U_{in} = \sum_{j=0}^{N-1} \int \frac{M_{j,in}^2}{2EI_z} ds \quad (6.4)$$

$$\delta_x = \frac{\partial U_{in}}{\partial F_x} \quad (6.5)$$

$$\delta_y = \frac{\partial U_{in}}{\partial F_y} \quad (6.6)$$

$$\theta_r = \frac{\partial U_{in}}{\partial M_0} \quad (6.7)$$

$$U_{out} = \sum_{j=0}^{N-1} \int \frac{M_{j,out}^2}{2EI_x} ds + \sum_{j=0}^{N-1} \int \frac{T_{j,out}^2}{2GJ} ds \quad (6.8)$$

$$\delta_z = \frac{\partial U_{out}}{\partial F_z} \quad (6.9)$$

where  $\delta_x$ ,  $\delta_y$ ,  $\delta_z$ ,  $\theta_r$  are the displacement in  $x$ , displacement in  $y$ , displacement in  $z$  and rotation at the point of application of the forces and moment.  $U_{in}$  and  $U_{out}$  are the strain energy due to the in-plane forces and the strain energy due to the out-of-plane forces respectively.  $E$  is the Young's Modulus of the material,  $G$  is the shear modulus of the material,  $J$  is the torsional rigidity of the material,  $I_z$  is the bending moment of inertia about the  $z$  axis and  $I_x$  is the bending moment of inertia about the  $x$  axis. Throughout this section, the assumption of a planar fabricated structure is used. Thus, the cross section is rectangular,  $I_z = \frac{wt^3}{12}$  and  $I_x = \frac{wt^3}{12}$ , where  $w$  is defined to be the width of each structure and  $t$  is the cross-sectional thickness of the structure. Using polar coordinates,  $ds = R d\theta$ .

Two boundary conditions are of interest for this application, namely fixed-free and fixed-guided boundary conditions. In the case where the origin of the displacement arises due to brain pulses during respiration or vascular pulsation, a fixed-guided boundary condition would be more appropriate. For other cases such as motion induced due to locomotion, a fixed-free condition is more appropriate.

For the case of fixed-free boundary conditions

$$\delta_x = \frac{\partial U_{in}}{\partial F_x} \Big|_{\substack{M_0=0 \\ F_y=0}} = \frac{F_x N R^3}{6 E I_z} ((2 + 4N^2)(\pi - 2\theta_1) + (4N^2 - 1)(\pi - 2\theta_1) \cos(2\theta_1) - 3 \sin(2\theta_1)) \quad (6.10)$$

$$\delta_y = \frac{\partial U_{in}}{\partial F_y} \Big|_{\substack{M_0=0 \\ F_x=0}} = \frac{F_y N R^3}{E I_z} ((\pi - 2\theta_1)(\sin^2 \theta_1 + \frac{1}{2}) - \frac{3}{2} \sin(2\theta_1)) \quad (6.11)$$

$$\begin{aligned} \delta_z = \frac{\partial U_{out}}{\partial F_z} = \frac{F_z N R^3}{12} & \left( ((5 - 3N + 4N^2)\theta_s + (4N^2 - 3N - 1)\theta_s \cos(2\theta_1) + \right. \\ & 4(4N^2 + 3N - 7) \cos^3(\theta_1) \sin(\theta_1) + 3 \sin(4\theta_1)) / E I_x + \\ & \left. ((11 + 3N + 4N^2)\theta_s + (4N^2 + 3N - 7)\theta_s \cos(2\theta_1) - \right. \\ & \left. 4(4N^2 + 3N - 7) \cos^3(\theta_1) \sin(\theta_1) - 3 \sin(4\theta_1) - 24 \sin(2\theta_1)) / G J \right) \quad (6.12) \end{aligned}$$

The spring constants are obtained by using the relations  $k_x = \frac{F_x}{\delta_x}$ ,  $k_y = \frac{F_y}{\delta_y}$  and  $k_z = \frac{F_z}{\delta_z}$ . The graphs of  $\delta_x$ ,  $\delta_y$  and  $\delta_z$  are plotted in Figure 6-3. Over  $\theta_s$ , no stationary point exists for  $\delta_y$  but a maximum exists for  $\delta_x$  and  $\delta_z$ .

For the case of fixed-guided boundary conditions, if  $d$  is the direction of the test force,  $k_d = \frac{F_d}{\delta_d}$  when  $\delta$  in all other perpendicular directions and the rotation  $\theta_r$  is fixed at zero. Due to the nature of vascular pulsation and respiration, only motion in the radial  $y$ -direction needs to be considered. Applying (6.1) to (6.7) and solving the system of equations yields:

$$\delta_y = \frac{F_y N R^3}{E I_z} (\theta_s (\sin^2 \theta_1 + \frac{1}{2}) - \frac{3}{2} \sin(2\theta_1) - g(\theta_1, N)) \quad (6.13)$$

where

$$g(\theta_1, N) = \frac{(-2 \cos^2 \theta_1 + (\pi - 2\theta_1) \sin \theta_1 \cos \theta_1)^2}{\frac{-\sin 2\theta_1 + \pi - 2\theta_1}{2} + \cos^2 \theta_1 \frac{(\pi - 2\theta_1)(N^2 - 1)}{3}}$$

for even  $N$ , and

$$g(\theta_1, N) = \frac{(-2 \cos \theta_1 + (\pi - 2\theta_1) \sin \theta_1)^2}{N^2(\pi - 2\theta_1)}$$

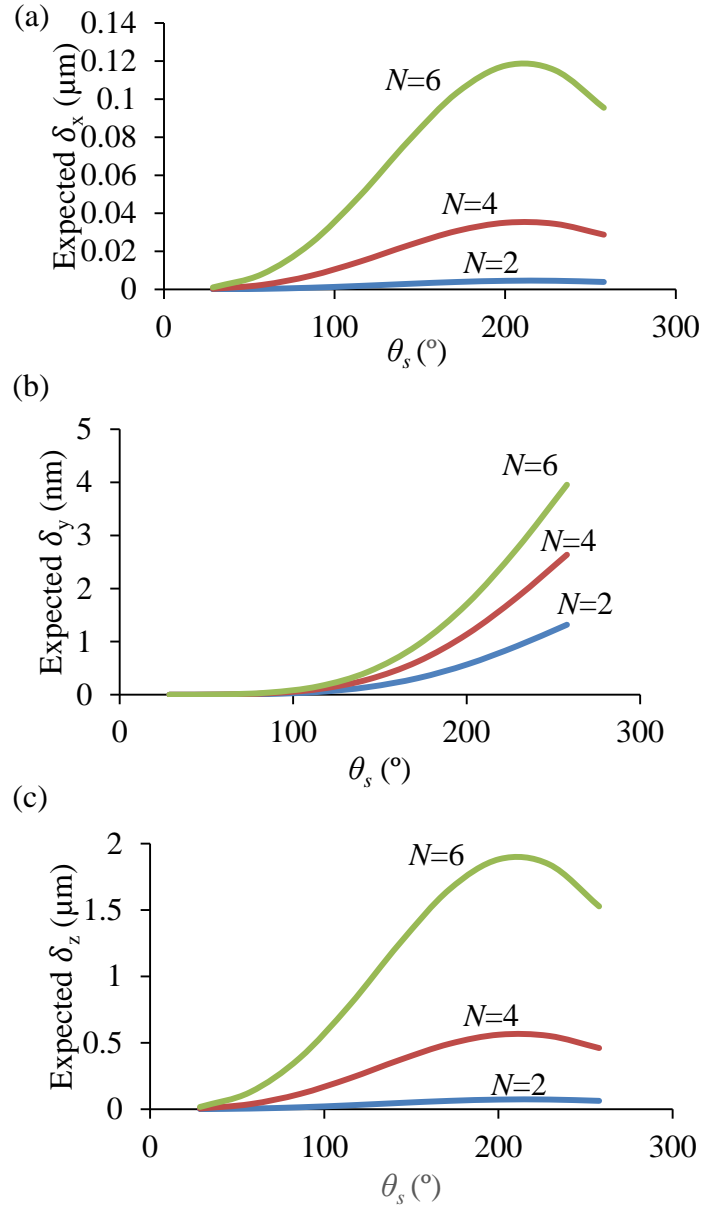


Figure 6-3: Calculated displacements in the  $x$ ,  $y$  and  $z$  directions when  $R = 100 \mu\text{m}$ ,  $t = 2.5 \mu\text{m}$ ,  $w = 10 \mu\text{m}$  for different  $\theta_s$  and  $N$  under a test force of  $10^{-10}$  N in the respective directions.

for odd  $N$ .

Based on (6.13), Figure 6-4 illustrates that for large  $N$ ,  $\delta_y$  under fixed-guided conditions approaches  $\delta_y$  under fixed-free conditions since  $g(\theta_1, N)$  approaches zero. Since neural probes are typically much longer in the  $y$ -direction than in the  $x$ -direction, this condition holds true and thus, for the purposes of this work, it is only necessary to consider the simpler fixed-free expression during the design of the structure.

### 6.1.2 Simulation of spring constants

Simulations are done in COMSOL Multiphysics using the following parameters:  $\theta_s = 0.5$  to 4.5 radians (steps of 0.5 radians),  $R = 100$ -1000  $\mu\text{m}$  (steps of 100  $\mu\text{m}$ ),  $N = 2$ -6 (steps of 2),  $E = 4$  GPa,  $t = 2.5$   $\mu\text{m}$ ,  $w = 10$   $\mu\text{m}$ . The rms error in simulations versus theoretical analysis for  $k_x$  is 2.1% across all parameters simulated. For  $k_z$ , the rms error is 3.3%.

Figure 6-5 shows the error in simulations of  $k_y$  as compared with that obtained from theoretical analysis. As seen, for small  $R$  and  $\theta_s$ , there is a very large difference between the simulated and theoretical results. This is attributed to the increased ratio of axial strain energy to bending energy for small  $R$  and  $\theta_s$ . By including the axial strain energy,

$$U_{axial} = \int \frac{F_y^2 \sin^2 \theta}{2AE} r d\theta \quad (6.14)$$

where  $A$  is the cross sectional area of the structure, the additional displacement due to the axial strain energy can be found using

$$\delta_{y,axial} = \frac{dU_{axial}}{dF_y} = \frac{F_y R}{2AE} ((\pi - 2\theta_1) + \sin(2\theta_1)) \quad (6.15)$$

By including the axial strain energy, the difference between simulated and theoretical results for  $k_y$  across all the parameters used is less than 0.5%.

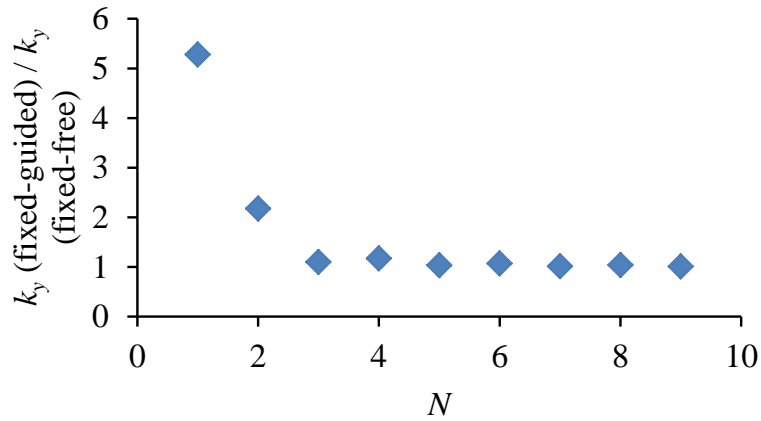


Figure 6-4: Ratio of spring constant under the fixed-guided boundary condition to the fixed-free boundary condition when  $\theta_s = \pi$ . The ratio approaches 1 as  $N$  increases. Non-monotonicity results from different equations for odd  $N$  and even  $N$ .

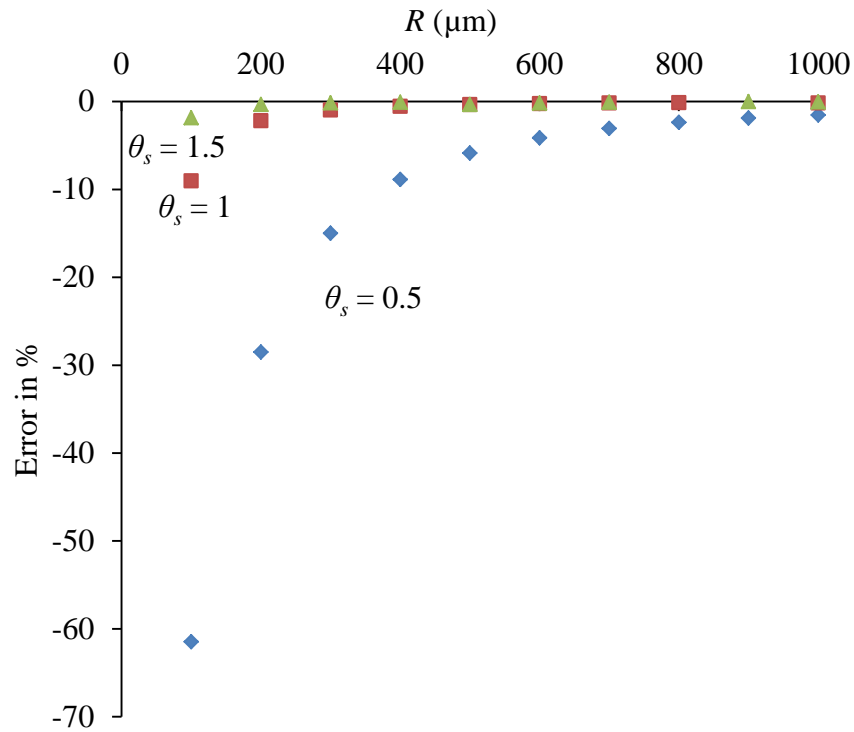


Figure 6-5: Error in simulations of  $k_y$  as compared with theoretical analysis. Meanders which are less curved (small  $R$  and  $\theta_s$ ) have larger errors because the analysis does not include axial strain energy.

### 6.1.3 Constrained optimization of $k_y$ for a single electrode wire

For a probe integrated with a delivery vehicle (*i.e.*, a dissolvable needle)[108], it is necessary to place constraints on the probes in order to fit the probe in the delivery vehicle as shown in Figure 6-6(a). The target length  $L$  is determined by the depth in the brain of the target neural population that the probe is meant to sense and the maximum width  $W_{max}$  is determined by the minimum width of the delivery vehicle to avoid buckling during insertion into neural tissue. Under the assumption that a more compliant probe would yield longer more reliable recordings, it is desired to minimize the spring constant in the  $y$ -direction,  $k_y$ , under these constraints.

Increasing  $R$  and decreasing  $N$  by the same factor keeps the target length  $L$  constant but reduces  $k_y$  since  $k_y$  is inversely proportional to  $NR^3$ . This increases the compliance without changing the target length  $L$  but requires larger  $W_{max}$ . Therefore, the larger  $W_{max}$  is, the larger is the maximum obtainable compliance. Hence, the constraints are expressed as:

$$L = 2RN \sin\left(\frac{\theta_s}{2}\right) \quad (6.16)$$

$$W_{max} = 2R\left(1 - \cos\left(\frac{\theta_s}{2}\right)\right) + w \quad (6.17)$$

There are additional constraints due to the finite wiring pitch for a physically realizable device that limits the maximum possible  $\theta_s$  and is discussed shortly. In addition, these constraints are for the case where there is one electrode per needle. The case with multiple electrodes is discussed in Section 6.1.4.

The two constraints, (6.16) and (6.17), can be combined to obtain equations that define the design space  $(N, R, \theta_s)$  under these constraints:

$$\theta_s = 4 \operatorname{atan}\left(\frac{N(W_{max} - w)}{L}\right) \quad (6.18)$$

$$R = \frac{W_{max} - w}{2(1 - \cos(\theta_s/2))} \quad (6.19)$$

$$N = L \tan\left(\frac{\theta_s}{4(W_{max} - w)}\right) \quad (6.20)$$

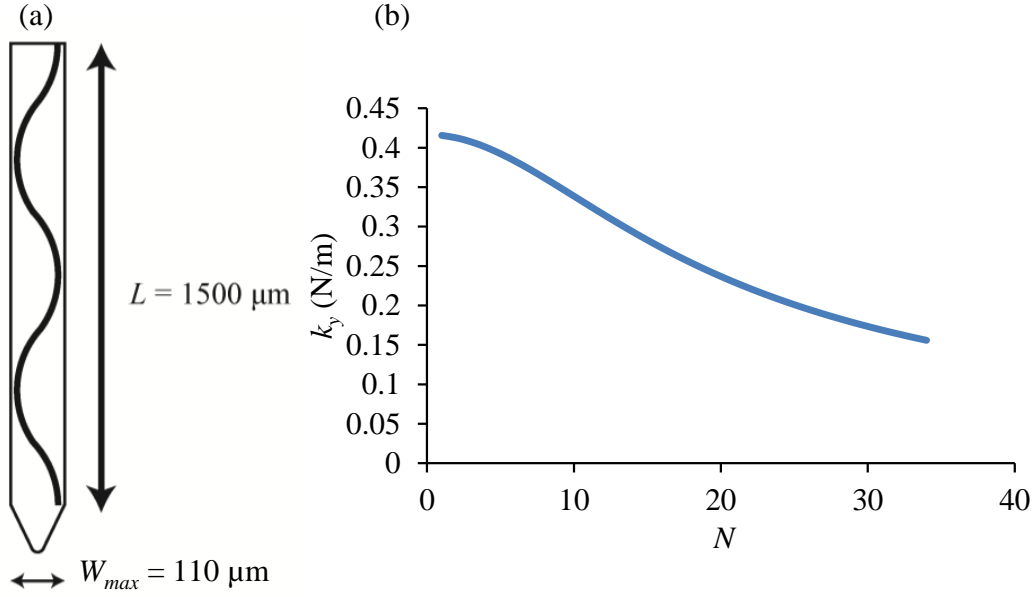


Figure 6-6: (a) Constraints imposed by a delivery vehicle of length  $L = 1500 \mu\text{m}$  and width  $W_{max} = 110 \mu\text{m}$ . (b) Fixed-free  $k_y$  under the constraint of  $L = 1500 \mu\text{m}$  and  $W_{max} = 110 \mu\text{m}$ . Increasing  $N$  reduces the spring constant. No stationary point exists.

The two constraints, (6.16) and (6.17), reduce the three-dimensional space to a one-dimensional one. There are no stationary points under these constraints in  $k_y$  and thus, the optimal solutions are at the end points of the set of possible solutions. In addition,  $\theta_s$  is limited by the need to avoid meander overlap as shown in Figure 6-7(d). This also limits the maximum  $N$  because  $N$  increases with  $\theta_s$  from (6.20). From (6.19), increasing  $\theta_s$  also reduces  $R$ .

For the case  $\theta_s < \pi$ , the minimum spacing between adjacent meanders is

$$s = 2\left(R - \frac{w}{2}\right) \cos \theta_1 \quad (6.21)$$

For the case  $\theta_s > \pi$ ,

$$s = 4(R - R \cos \theta_1) - w \quad (6.22)$$

Under the constraints (6.16) and (6.17),

$$s = 2 \frac{L - (N + 1)R}{N - 1} - w \quad (6.23)$$

For the case with  $L = 1500 \text{ }\mu\text{m}$  and  $W_{max} = 110 \text{ }\mu\text{m}$ , typical values of an insertion vehicle for small animal brain studies[209]. As seen from (6.18), probes with larger  $N$  have larger  $\theta_s$ . Figure 6-7 shows three probes that satisfy  $L = 1500 \text{ }\mu\text{m}$  and  $W_{max} = 110 \text{ }\mu\text{m}$ .

Figure 6-6(b) shows the fixed-free spring constant in the  $y$ -direction under the applied constraints. Since increasing  $N$  under the applied constraints increases compliance,  $N$  should be as large as possible. However,  $N$  is constrained by (6.23) since  $s$  is constrained by lithographic resolution. For example, if there is a lithographic limit of  $s_{min}=1 \text{ }\mu\text{m}$  between two adjacent structures, minimizing  $k_y$  gives a value of 44 for  $N$ , which gives a value of 0.12 N/m for  $k_y$ .

#### **6.1.4 Constrained optimization of $k_y$ for multiple electrode wires**

Another important factor to consider in probe design is the probe packing density. Given the lack of information about the exact location of individual neurons and the desire to obtain recordings from as many neurons as possible, it is desirable to have high electrode counts and electrode spacing matching the extent of individual neuron signals on each implant. In other words, for a target depth  $L$  in the brain, it is desired to maximize the number of electrodes. Increasing the number of electrodes imposes additional constraints to the design space that is considered in this work.

##### **6.1.4.1 Minimizing spacing between multiple electrode wires**

If the fabrication of these structures is performed using 2D planar MEMS fabrication processes, maximizing probe packing density is equivalent to minimizing the horizontal spacing,  $d$ , between two adjacent probes given the lithographic process constraint of  $s_{min}$ . This minimal horizontal spacing between probes,  $d_{min}$ , also imposes additional constraints to the shape of an individual meander. For optimal density, probes should be arrayed horizontally with no vertical displacement as shown in Figure 6-8(a). If a vertical displacement exists, the minimum gap size is reduced as shown in

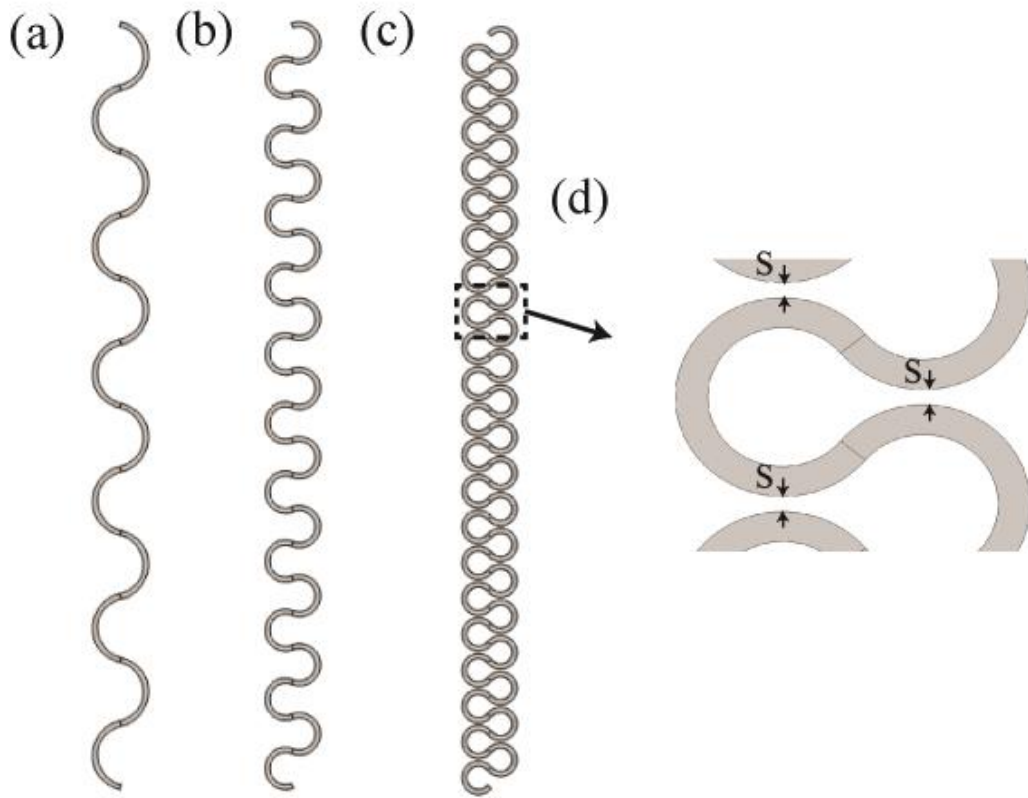


Figure 6-7: Three probes satisfying the conditions  $L = 1500 \mu\text{m}$  and  $W_{max} = 110 \mu\text{m}$ .  $w$  is set to  $10 \mu\text{m}$ . (a)  $N = 12$ , (b)  $N = 22$  and (c)  $N = 42$ . Large  $N$  results in more compliant probes but is limited by the need to avoid meander overlap. In addition, a minimum spacing is required because of lithographic resolution. (d) Minimum spacing for the probe with  $N = 42$ .

Figure 6-8(a). If there is no vertical displacement, as shown in Figure 6-8(b), using trigonometry, for any  $\theta_s$ , an array of probes with distance  $d$  between the probes will result in a minimum distance between the probes

$$g = \sqrt{R^2 + d^2 + 4Rd \cos\left(\frac{\theta_s}{2}\right)} - R - w \quad (6.24)$$

In other words, if there is a lithographic constraint on the minimum value of  $g$ ,  $s_{min}$ , the probes should be spaced apart with a distance

$$d = \sqrt{(s_{min} + w)^2 + 4R(s_{min} + w) + 4R^2 \cos^2\left(\frac{\theta_s}{2}\right)} - 2R \cos\left(\frac{\theta_s}{2}\right) \quad (6.25)$$

For the multielectrode case,  $d$  effectively plays the role of  $W_{max}$  in the single electrode case in constraining the width of the individual structures. Substituting (6.17) into the expression for  $d$  yields

$$d = \sqrt{(s_{min} + w)^2 + 4R(s_{min} + w) + 4\left(R - \frac{W_{max} - w}{2}\right)^2} - 2\left(R - \frac{W_{max} - w}{2}\right) \quad (6.26)$$

This implies that if  $R$  is increased,  $d$  is reduced and hence, the probe packing density is increased. However, based on analysis in the previous section, under the constraints, increasing  $R$  reduces  $N$  and  $\theta_s$  based on and also reduces the mechanical compliance of the structure.

#### 6.1.4.2 Maximizing compliance given a fixed probe density

If a particular number of electrodes,  $M$ , is desired in a single needle, a new constraint can replace (6.17) for the single electrode case:

$$Md + w = W_{max}. \quad (6.27)$$

By substituting (6.26) into (6.27), for each value of  $M$ , an additional constraint on  $R$  is obtained. Using the constraints of  $L = 1500 \mu\text{m}$ ,  $W_{max} = 110 \mu\text{m}$ ,  $s_{min} = 1 \mu\text{m}$

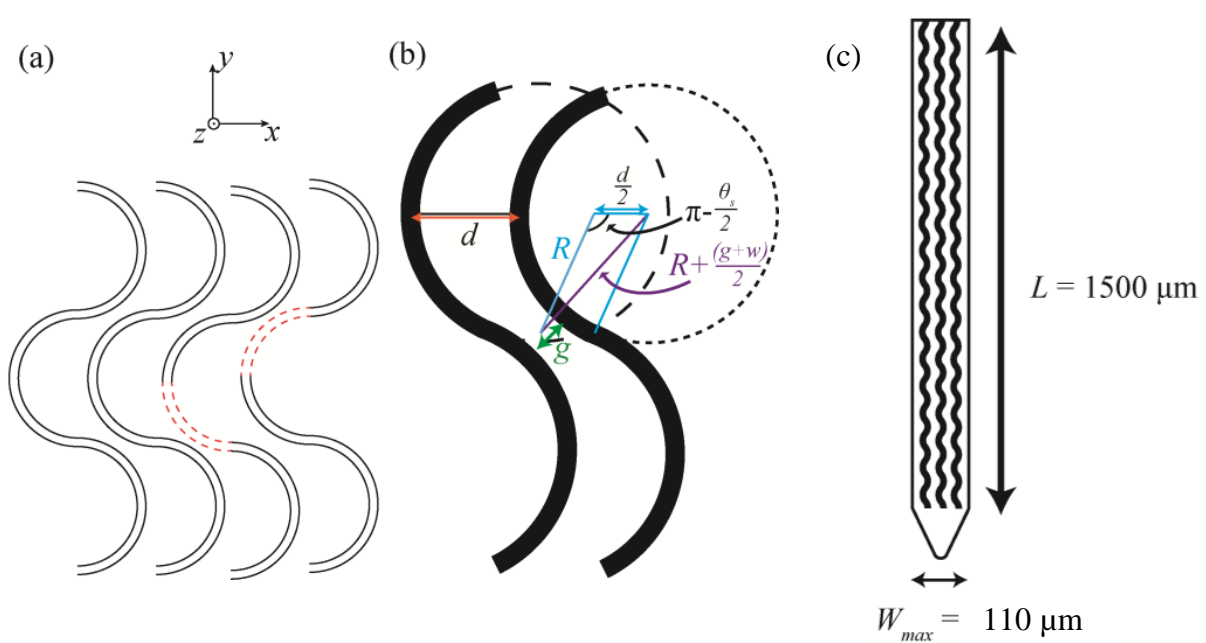


Figure 6-8: (a) Maximum probe density arises when probes are arrayed with no vertical displacement. Segment with limiting spacing is shown with dotted red lines. (b) Minimum spacing,  $g$ , between two identical circular probes shifted horizontally by distance  $d$ . (c) shows the case of 3 probes in the delivery vehicle ( $M = 3$ )

imposed by a delivery vehicle as shown in Figure 6-8(c), a graph showing optimized fixed-free  $k_y$  over  $M$  is shown in Figure 6-9. The other parameters used are  $w = 10 \mu\text{m}$ ,  $t = 2.5 \mu\text{m}$  and  $E = 4 \text{ GPa}$ .

As shown from Figure 6-9, fitting a larger number of probes,  $M$ , in a single delivery vehicle, results in larger spring constants and hence, less compliant probes. Ultimately, the optimum solution depends on the requirements of the application, and the weight placed on the compliance versus the probe density during the optimization process.

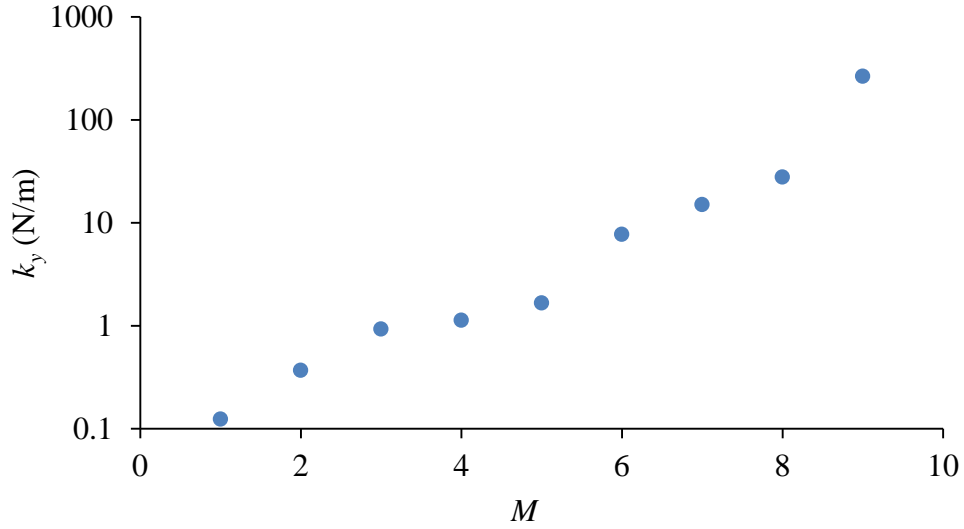


Figure 6-9: (a) Maximum probe density arises when probes are arrayed with no vertical displacement. Segment with limiting spacing is shown with dotted red lines. (b) Minimum spacing,  $g$ , between two identical circular probes shifted horizontally by distance  $d$ . (c) shows the case of 3 probes in the delivery vehicle ( $M = 3$ )

## 6.2 Design of probe cabling

Peripheral nerves are typically tougher than brain tissue. For example, in [210], rat sciatic nerve is found to have a Young's modulus of approximately 580 kPa. This is compared to a Young's modulus of 1 kPa for gray matter and 2 kPa for white matter of the mammalian brain[211]. Hence, in this thesis, peripheral probes are designed to be mechanically robust as shown in Figure 6-10. The probes consist of a long cable region that allows for easy handling, a transition or stress-relief region and the needle region which is inserted into the nerve. The stress-relief region provides a gradual transition from the wider cable region to the narrower needle region so that stress concentration is reduced. The parameterized design of the transition region is shown in Figure 6-11 and consists of four circular sectors with radius  $r$  and sector angle  $\theta$ . The width of the cable region  $w_c$  and the width of the needle region  $w_n$  are constrained by other considerations. This leads to the constraint

$$2r(1 - \cos(\theta)) = w_c - w_n \quad (6.28)$$

Hence, for a larger radius,  $r$ , the angle  $\theta$  has to be smaller.

Simulations are performed as shown in Figure 6-12 with  $w_c = 5$  mm and  $w_n = 1$  mm. The needle end is taken to be fixed and a 1 mN force is applied on the cable end. With  $\theta$  set to  $\frac{\pi}{4}$  as seen in Figure 6-12(a), lower stress is seen in the stress concentration regions along the curves compared to the case when  $\theta$  is set to  $\frac{\pi}{2}$ . This is expected since using a smaller  $\theta$  results in a more gradual transition. The smallest  $\theta$  possible is limited by the length of the transition region which is given by

$$L_t = (w_c - w_b) / \tan(\theta) \quad (6.29)$$

For the design used in the fabrication of devices,  $w_n = 255$   $\mu\text{m}$ ,  $w_c = 4$  mm,  $L_t = 10$  mm,  $r = 15.2$  mm and  $\theta = 41^\circ$ . A mechanical simulation with a 1 nN boundary load of the transition region along with the needle region is shown in Figure 6-13. The Young's modulus of the parylene-C regions is taken to be 4 GPa, which is based on the measurement of the Young's modulus of thin film parylene-C performed in Chapter 2 and is within the range of values of parylene-C reported in literature as listed in Table 2.1. The Young's modulus of Pt is taken to be 168 GPa based on the bulk Young's modulus of Pt[177].

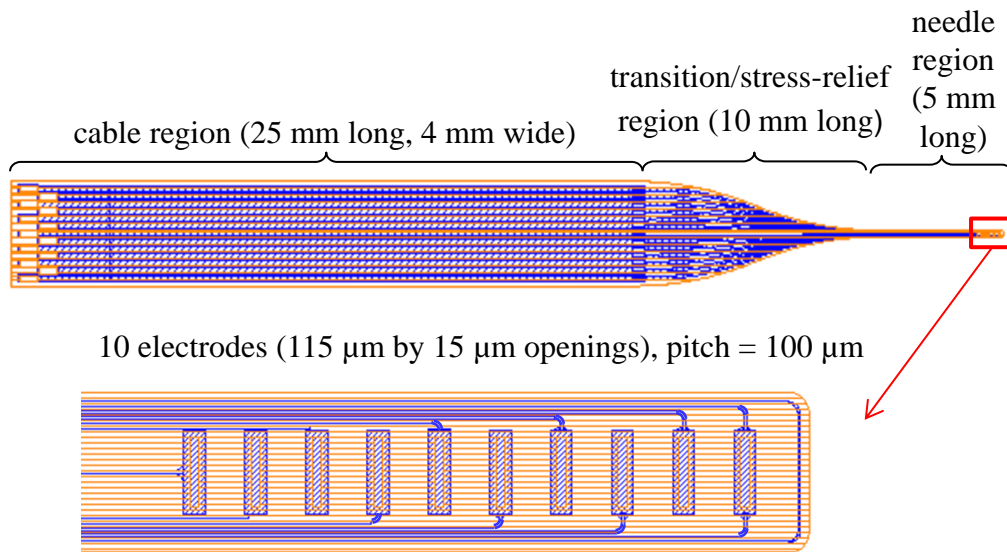


Figure 6-10: Design of a peripheral probe

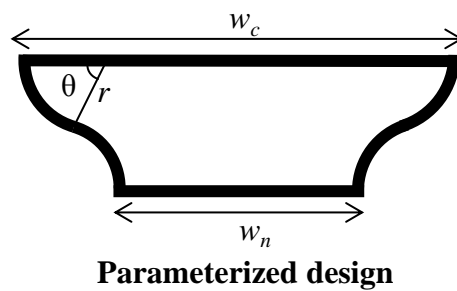


Figure 6-11: Parameterized design of transition region.

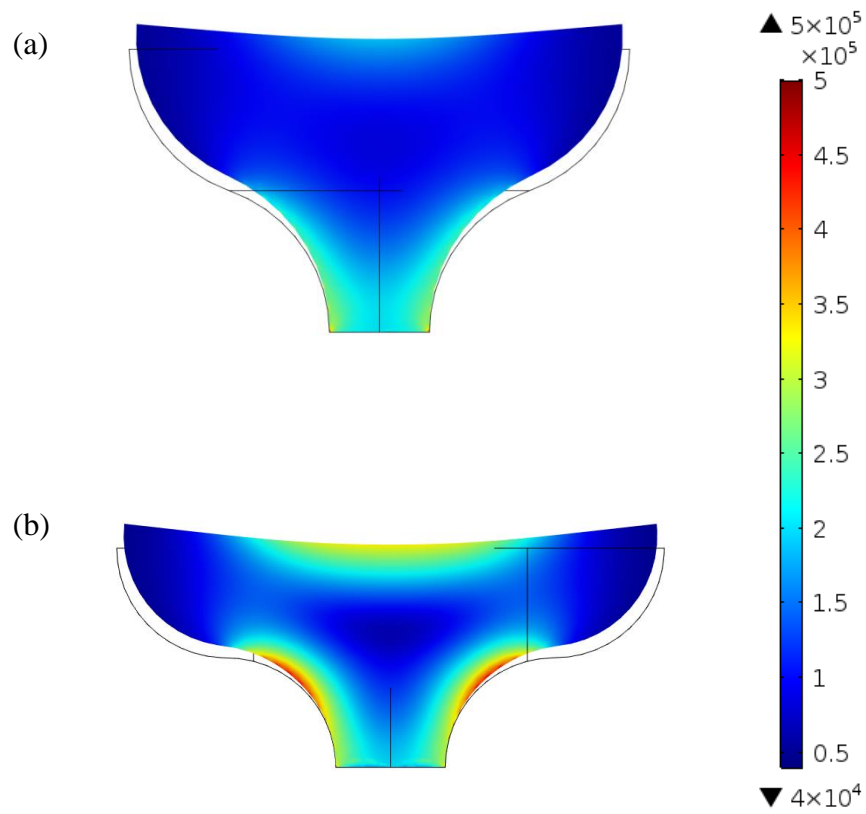


Figure 6-12: Mechanical simulation of two transition region designs within the proposed design parameter space. (a)  $\theta = \pi/4$ . (b)  $\theta = \pi/2$ .

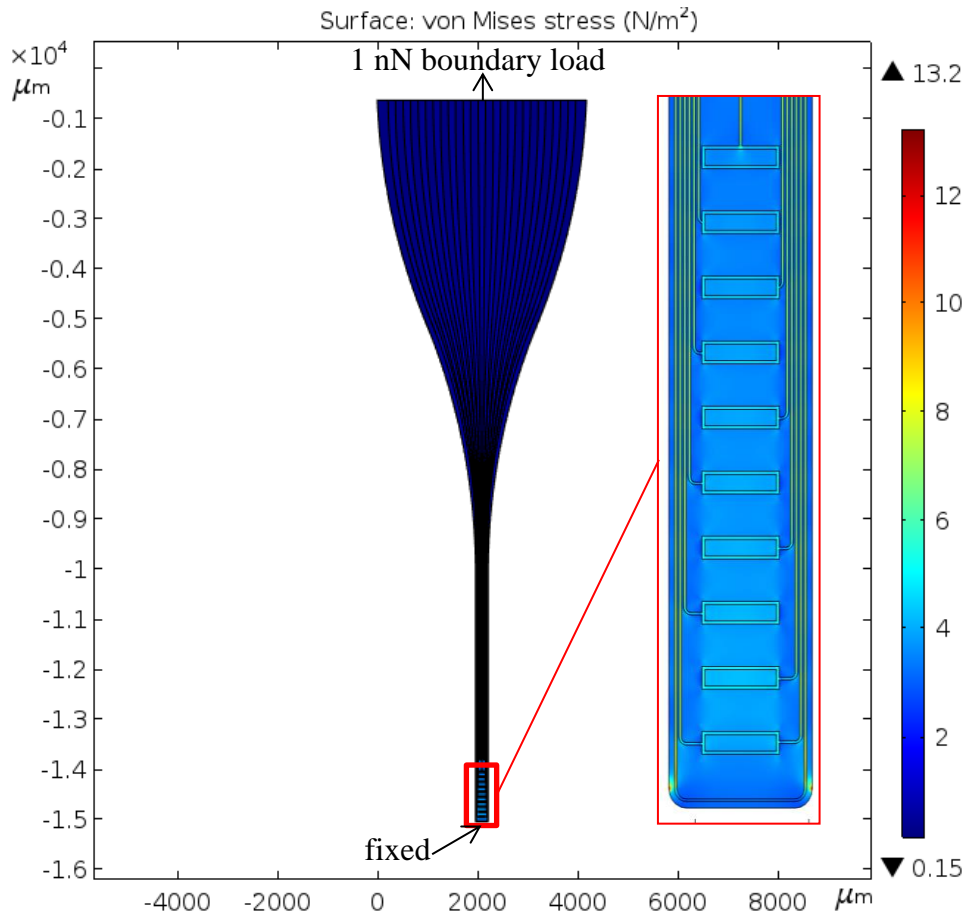


Figure 6-13: Mechanical simulation of fabricated design with needle.

### 6.3 *In vivo* experiments of implantable Si neural probes and ultra-compliant probes integrated with biodissolvable needles

In this section, process development to fabricate Si probes is guided by the desire to emulate the size, structure and material of parylene-C based probes that will eventually be integrated with a biodissolvable needle. These probes are used as a tool to compare with probes integrated with dissolvable material. Since the purpose of this study is to evaluate the acute *in vivo* properties of the probe integrated with the biodissolvable needle, a simpler design of the probe is used as shown in Figure 6-15(a). Using the meander design in Section 6.1 can result in significant initial movement of the probes that are integrated with a biodissolvable needle due to fluidic effects during dissolution unless certain insertion protocols such as flooding the insertion area with saline is followed [212].

The process emulates soft probes made only out of parylene-C and allows testing of the interface between the two layers of parylene-C. The silicon probe thus serves as a tool to investigate the encapsulation properties in parylene-C based probes. Using parylene-C as the only dielectric simplifies the process as only one etch is required to define the dielectric pattern. Furthermore, the use of a bonding wax (BGL7080, AI Technologies, NJ) as an adhesive to a handle wafer potentially allows the process to be expanded to much thinner wafers by integration of the wafer thinning process with the rest of the fabrication steps. The use of wet Si etchants like KOH is shown to be detrimental to parylene-C adhesion[213]. Hence, a dry process is developed using DRIE to define the Si probe.

#### 6.3.1 Fabrication of Si probes

The condensed process to fabricate Si probes is described in Figure 6-14. 2.2  $\mu\text{m}$  of parylene-C is first deposited on a 4 inch,  $250 \pm 25 \mu\text{m}$ -thick Si wafer (Polishing Corporation of America, Santa Clara, CA) that has been treated with A174 silane

(Sigma-Aldrich, St. Louis, MO). 127 nm of Pt is then patterned by lift-off as shown in Figure 6-14(a). A second layer of 2.2  $\mu\text{m}$  parylene-C is then deposited. A 20 nm thick chromium (Cr) mask is then deposited and patterned using Chromium Etchant 1020 (Transene, Danvers, MA) as shown in Figure 6-14(b). Both parylene-C layers are then etched using a 50 W  $\text{O}_2$  RIE using a Phantom II (Trion Technology, AZ) for 40 min. Following the etch, the Cr mask and any remaining resist is removed using Chromium Etchant 1020 and acetone respectively as shown in Figure 6-14(c). A protective resist is then spun on the wafer before the wafer is diced. All photoresist development and strip steps are followed by a 1 min, 100 W  $\text{O}_2$  plasma descum using a barrel etcher (International Plasma Corporation, Hayward, CA).

Following dicing, the protective resist is stripped off the fabricated chips using acetone. The chips are then heated at 300°C for 3 hours in a 10 mT nitrogen environment in order to improve the adhesion between the two parylene-C layers[105]. The fabricated chips are then bonded onto a handle glass slide with BGL7080 as an adhesive. BGL7080 is first spun onto the glass slide at 1500 rpm for 30 s giving a film thickness of 6  $\mu\text{m}$ . The glass slide is then heated at 90°C for 5 min to remove the solvent in the BGL7080. The chip is then bonded at 115°C, 40 N onto the BGL7080 coated glass slide using a M9A Device Bonder (Besi, The Netherlands) as shown in as shown in Figure 6-14(c). In order to define the Si needle geometry, a 50 nm layer of Cr as a hard mask is first deposited using a 2400-8L (Perkin-Elmer, Waltham, MA). The Cr hard mask is then patterned using AZ4210 resist and etched with Chromium Etchant 1020 as shown in Figure 6-14(d). The Si is then etched using a Multiplex ICP RIE (Surface Technology Systems, UK). Following photoresist and Cr removal using acetone and Chromium Etchant 1020 respectively, the structure is then immersed in isopropyl alcohol (IPA) to remove the BGL7080 adhesive in order to release the neural probes as shown in Figure 6-14(e). A 1 min 50 W  $\text{Ar}^+$  mill is performed using the Phantom II (Trion Technology, Tempe, AZ) in order to remove the surface oxidation as described in Chapter 2.

Optical images of fabricated probes are shown in Figure 6-15. The successful fabrication of probes using this method indicates that it possible to perform photolithog-

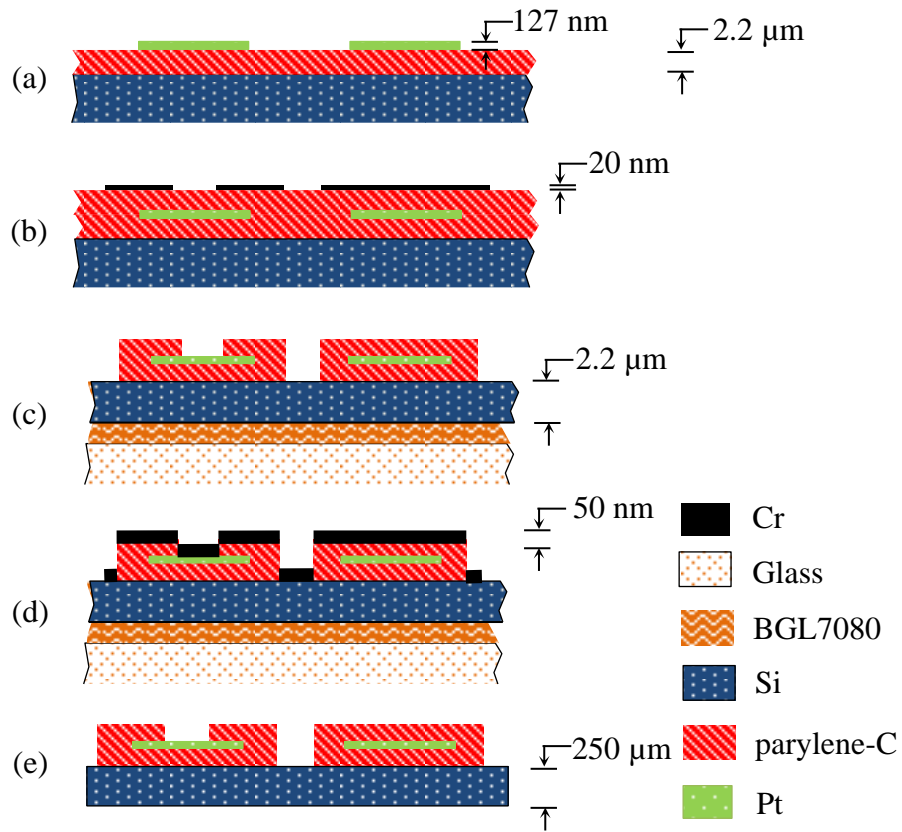


Figure 6-14: Fabrication steps to pattern Si needle using BGL7080 as an adhesive. (a) Parylene-C is deposited. Pt is patterned by lift off. (b) Second layer of parylene-C is deposited. Cr is deposited and patterned. (c) Parylene-C is etched with O<sub>2</sub> plasma. Si is bonded to glass using BGL7080 adhesive. (d) Cr is deposited and patterned. (e) Si is etched using DRIE. Device is released in IPA.

raphy on substrates adhered to a handle wafer using BGL7080. Since BGL7080 is a bonding wax that is meant for use as an adhesive during backgrinding, thinner devices can be made by performing the bonding step on an unprocessed Si wafer followed by a backgrinding step. The parylene-C and platinum processing can then be done on the bonded wafer.

Following fabrication, anisotropic conductive film (ACF) is used to interface the chips with a flat flexible cable (FFC). The bonding is performed by Mats Forssell. ACF 7379 (3M, MN) is pre-tacked to a polyimide FFC 0150150423 (Molex, IL) which is then bonded to the chip using the M9A device bonder applying  $\sim 40$  N of force for 2 min while heating the assembly at  $165^{\circ}\text{C}$  from the chip side and  $145^{\circ}\text{C}$  from the cable side. The resulting yield is low, with only three pads successfully connected out of 13. There are 13 pads but only 10 electrodes because three of the pads are used for self-test loops. In order to improve connection yield, other ACFs or alternative techniques like wire bonding could be explored. The FFC is then connected to a custom built printed circuit board (PCB) through a 502598-2391 zero insertion force (ZIF) clip (Molex, IL) mounted on the PCB. The PCB interfaces the ZIF clip with a A79042-001 connector (Omnetics, MN).

### 6.3.2 *In vitro* experiments

In order to characterize the electrodes and validate performance for *in vivo* studies, electrochemical impedance spectroscopy (EIS) is performed using a PGSTAT302N potentiostat (Metrohm Autolab, Netherlands) in 1X phosphate buffered saline (PBS) diluted from 10X PBS (Fisher BioReagents, NH) with a MF-2052 Ag/AgCl reference (BASi, IN) and a MW-1033 Pt coil counter electrode (BASi, IN). A 30 mV sinusoidal excitation voltage is applied with frequency ranging from 0.1 Hz to 100 kHz.

The EIS performed on one of the electrodes is plotted in Figure 6-16. The impedance of the electrode measured at 1 kHz is  $\sim 80$  k $\Omega$ , indicating that it is possible to detect extracellular neural recordings.

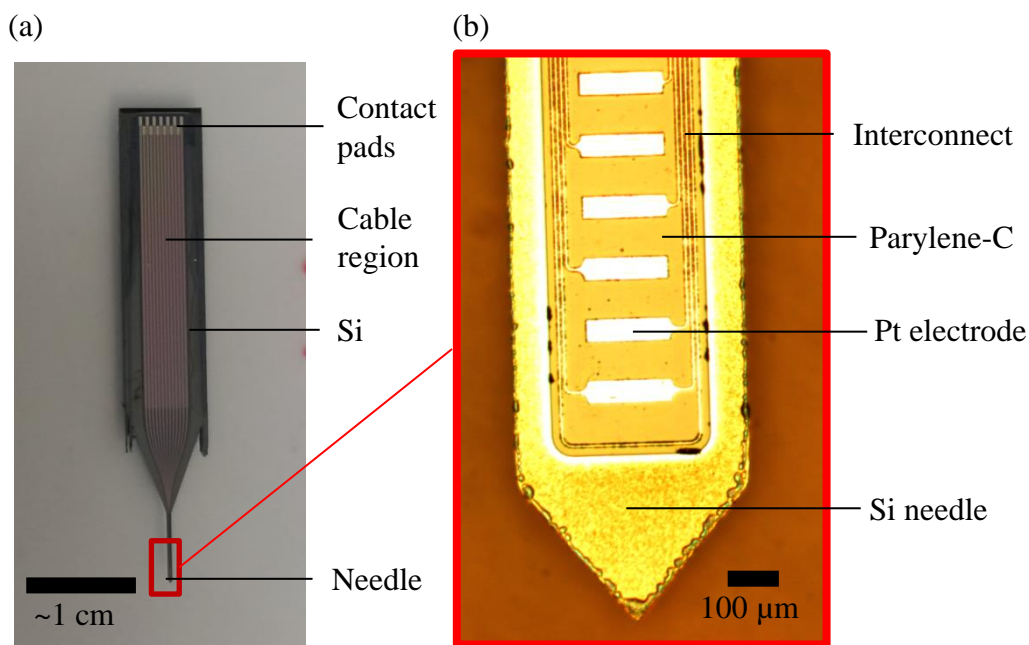


Figure 6-15: (a) Optical image of a fabricated probe. (b) Zoomed-in image of the tip of a fabricated probe.

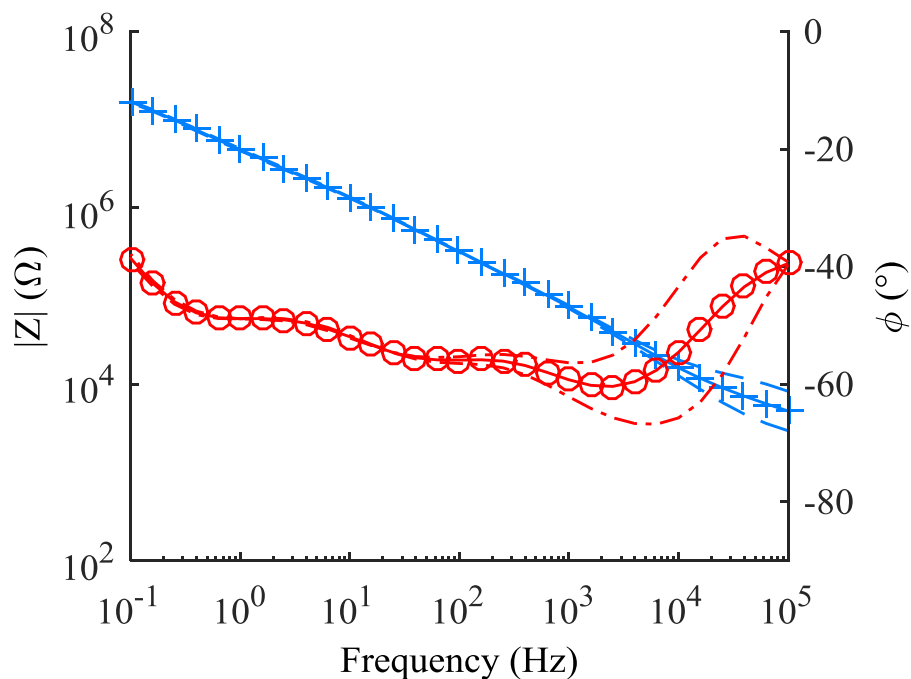


Figure 6-16: Bode plot of Electrochemical Impedance Spectroscopy (EIS) performed on  $115 \mu\text{m}$  by  $15 \mu\text{m}$  electrodes in saline ( $n = 2$ ). Measured impedance at 1 kHz is  $\sim 80 \text{ k}\Omega$ . The red circles denote the average phase and the blue crosses the average magnitude. Standard deviations are indicated by the dashed lines. Measurement is performed by Mats Forssell.

### 6.3.3 *In vivo* experiments

In order to test recording capability, neural probes are fabricated and inserted into the substantia nigra area of a mouse brain. The substantia nigra is located approximately 5 mm deep inside the brain in a mouse. It contains sparsely spaced dopaminergic neurons that influence many behavioral aspects such as motivation and learning[214]. The loss of dopamine neurons is also correlated with Parkinson's disease[215], making it an important region in the brain in the study of Parkinson's disease. The insertion set up is shown in Figure 6-17. No recordings are obtained after insertion of fabricated neural probes integrated with needles made of CMC-glucose even 1 hour after insertion. Evidence from histology indicates that swelling of the CMC-glucose damages the surrounding tissue and could be a cause for the lack of recordings. Another hypothesis is that the swelled CMC-glucose separates the electrode from the neurons, resulting in no signal under acute conditions. Swelling of CMC-glucose is also observed when CMC-glucose needles are inserted in agar tissue phantoms. In order to reduce the amount of damage and swelling, different types of dissolvable materials are being explored by the Ozdoganlar group in the Mechanical Engineering Department as part of the overall neural probe project. In addition, other designs of probes that reduce the size of the needles may lead to proper electrode function.

In order to test probe functionality without the presence of the biodissolvable material, the Si probes are inserted into a mouse targeting the substantia nigra region of the brain. The surgery and *in vivo* test is performed in Prof. Aryn Gittis' lab by Amanda Willard. The setup to insert the Si probes is shown in Figure 6-17. In preparation for the probe insertion, a C57BL/6J mouse is anesthetized with ketamine/xylazine (100mg/kg: 30 mg/kg, intraperitoneal) and placed on a stereotaxic frame (David Kopf Instruments, Tujunga, California, USA) and maintained throughout surgery using 1-2% isoflurane. Bilateral 0.75 mm  $\times$  0.75 mm craniotomies are drilled into the skull centered over  $-3.0$  mm posterior and  $\pm 1.5$  mm lateral from bregma to target the substantia nigra. The dura is removed and a stainless steel head bar is adhered to a section of the intact skull in front of the craniotomies using dental

cement and superglue. The animal is permitted to fully recover prior to being placed on the wheel. Experiments are conducted in accordance with the guidelines from the National Institutes of Health and with approval from Carnegie Mellon University Institutional Animal Care and Use Committee.

Head restraint is employed by positioning the stainless steel head bar within a set of clamps positioned above the running wheel. The probe is then inserted using a MPC200 micromanipulator system (Sutter Instrument, CA) to a depth below the surface of the brain between  $-4.0$  mm and  $-4.5$  mm for neural recordings. Neural recordings are obtained using an OmniPlex D Neural Data Acquisition System (Plexon, TX) and analyzed offline using NeuroExplorer (Plexon, TX). After recordings are completed, the animal is sacrificed and the brain is sectioned at  $300$   $\mu\text{m}$ . Tissue damage is observed by Amanda Willard around the insertion site, which indicates that the probes have been inserted into the substantia nigra region. An image of the mouse brain histology is shown in Figure 6-18.

Spikes are successfully recorded from the three functional electrodes as shown in Figure 6-19. Comparatively, for parylene-C probes integrated with carboxymethyl-cellulose needles with the same design as the silicon insertion device, no spikes are observed even 1 hour after insertion, possibly caused by the swelling of the biodegradable needle material.

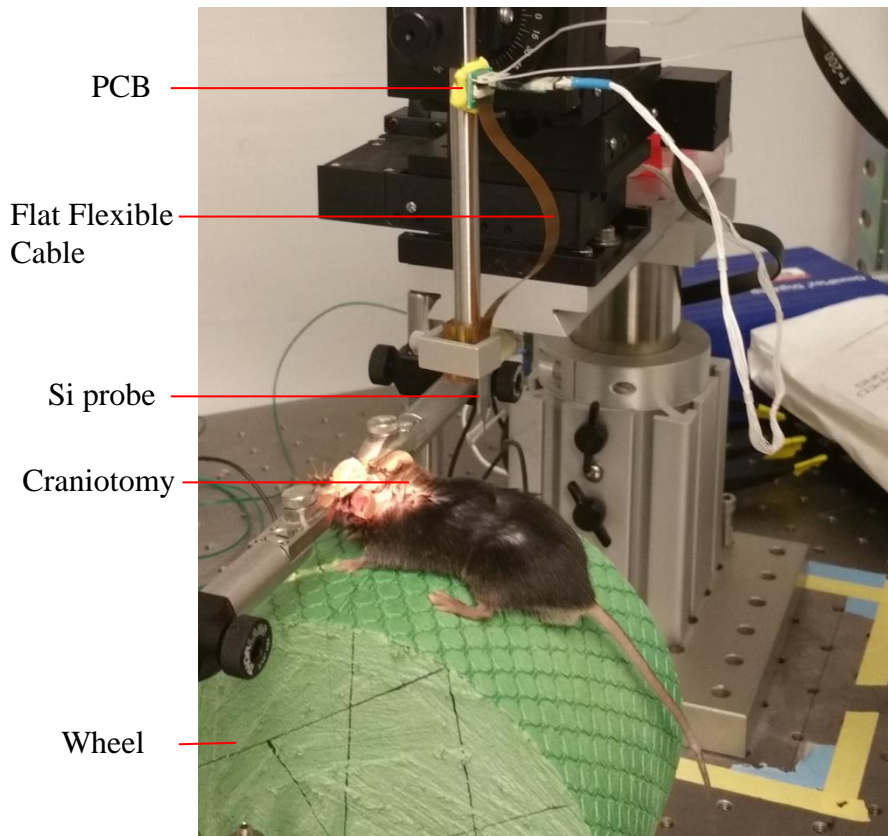


Figure 6-17: Insertion setup for acute *in vivo* experiment in a mouse.

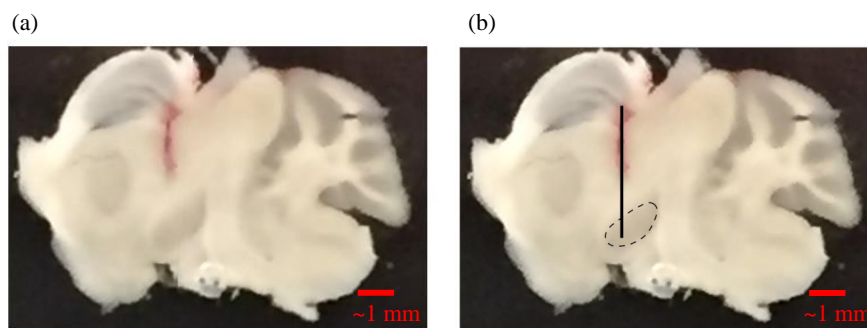


Figure 6-18: (a) Image of mouse brain after post-insertion histology. (b) Image of histology with annotations. Dotted lines represent the substantia nigra region. Probe trace is marked by bold lines. Histology indicates that probe is inserted successfully into target region.

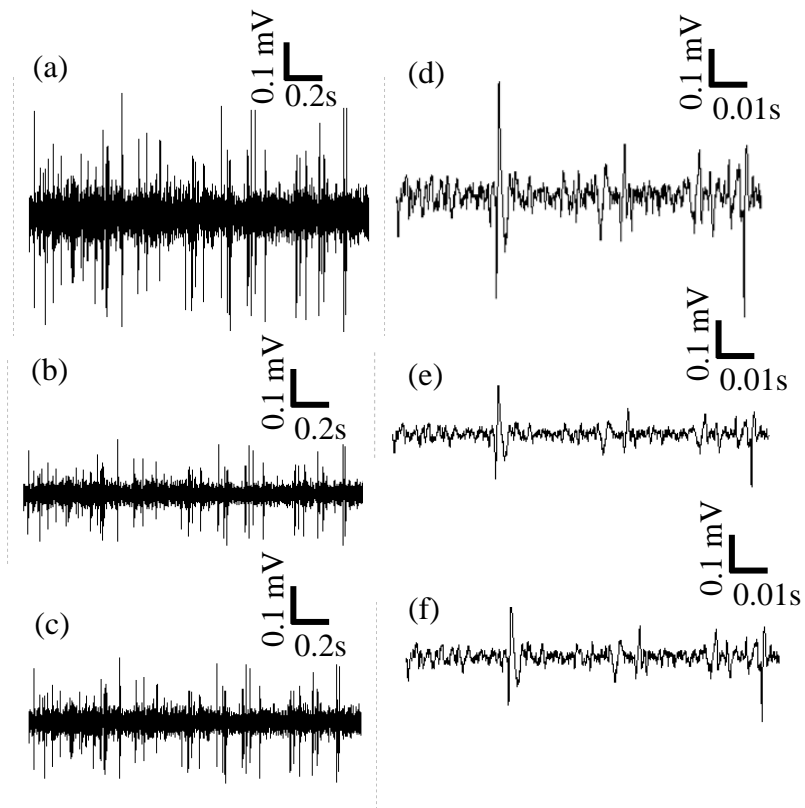


Figure 6-19: Recorded spike data from three different electrodes. (a-c) are data from 3 separate electrodes. (d-f) are plots that are zoomed-in to individual spikes.

## 6.4 Actuation of neural probes using light-sensitive liquid crystals

In the previous chapters, it is emphasized that proximity of the electrodes to the site of interest is important to ensure good quality recordings and stimulation. The methods employed to achieve this are however, passive; Once the probe is inserted, the location of the electrodes is fixed. This remains a problem for probes as the percentage of electrodes that record sortable single-units in reported cortical experiments is only around 25%[53]. Hence, preliminary work on an active approach through the use of actuation is provided in this section.

Actuation is achieved using light-sensitive nematic liquid-crystal polymers synthesized in Prof. Ravi Shankar's lab in the University of Pittsburgh by Dr. Arul Clement. Actuation tests are done with the assistance of Junfeng Gao.

Nematic liquid-crystals have no positional order but have long-range directional order, with the molecules pointing, on average, in the direction known as the director[202]. The director of the liquid crystal can be controlled for example, by using an electric field, which allows for applications such as the creation of liquid crystal displays (LCDs)[216]. This anisotropy can also be exploited to allow for controlled actuation using light since nematic liquid-crystals contract along the direction of the local director and expand in the perpendicular direction when irradiated with light at certain frequencies[217][218].

### 6.4.1 Controlling orientation of liquid-crystal molecules on parylene-C

In order to control the bending of the polymer when irradiated, it is necessary to control the alignment of the liquid crystal molecules. For simple alignment schemes, such as for the case where the alignment of the entire region is desired to be uniform, mechanical stretching and magnetic fields can be used[218]. For more complicated schemes, grooves can be created on the surface prior to coating of the liquid crystal

by rubbing, using an atomic force microscopy tip or by using photolithography to pattern the surface[218]. Of these, photolithography is a more reliable method since it does not generate particles, scratches or static charges[218]. However, it is important to maximize the liquid crystal anchoring strength to ensure successful alignment, which is dependent on the geometry of the grooves and surface chemistry[218]. In this present work, liquid-crystals are integrated into parylene-C to demonstrate that actuation is possible in parylene-C probes.

To allow for actuation, it is necessary to have an effective stress gradient along the thickness of the film. This can be achieved by controlling the alignment of the liquid crystal along the thickness of the film. For example, if grooves are patterned on parylene-C, the grooves control the orientation of the liquid crystal so that the directors of the liquid crystal will be facing in-plane within the grooves. Away from the grooves, the director will be facing out-of-plane. Since liquid crystals contract along the director and expand perpendicular to the director when exposed to light[218], a stress gradient is produced along the thickness of the liquid crystal.

Polarized optical microscopy (POM) is used to determine if the liquid crystal is aligned successfully. In POM, the liquid crystal sample is placed between two polarizers that are orthogonal to each other. Polarizers configured in this way are called crossed polarizers. Malus' law states:

$$I = I_0 \cos^2 \theta_i \tag{6.30}$$

where  $I$  is the intensity of light that leaves the polarizer,  $I_0$  is the initial intensity of light and  $\theta_i$  is the angle between the light's polarization direction and the axis of the polarizer. The intensity of light leaving the two polarizers is zero if no sample is placed between the two polarizers. However, the anisotropy of the liquid crystal leads to the birefringence property where light entering the liquid crystal is split into two rays: the ordinary ray and the extraordinary ray whose polarization are perpendicular to each other[219] unless the angle between the polarization direction of the light and the director is  $0^\circ$  or  $90^\circ$ . Hence, this means that some of the light will be able to

pass through the second polarizer at certain angles and this property can be used to determine the alignment of the grown liquid crystal.

To demonstrate parylene-C based devices that actuate, 1  $\mu\text{m}$  deep grooves are created in 9  $\mu\text{m}$ -thick parylene-C using photolithography using 1.6  $\mu\text{m}$  of patterned AZ4210 photoresist over a Cr hard mask followed by  $\text{O}_2$  RIE timed etching at 50 W, 14.2 sccm  $\text{O}_2$  gas flow for 50 mins using the Phantom Reactive Ion Etch (RIE) System (Trion Technology, Tempe, AZ). The groove pattern consists of 1  $\mu\text{m}$  lines with 2  $\mu\text{m}$  pitch shown in Figure 6-20. As seen from Chapter 4, this  $\text{O}_2$  etch results in a hydrophillic surface of the remaining parylene-C. Since the surface chemistry can affect the ability to align the liquid crystal, for some samples, a 1 min  $\text{SF}_6$  plasma treatment is performed to make the surface hydrophobic as seen from Chapter 4. The groove pattern consists of 1  $\mu\text{m}$  lines with 2  $\mu\text{m}$  pitch shown in Figure 6-20.

After the parylene-C is patterned, a 35  $\mu\text{m}$ -deep parallel-plate gap between the patterned parylene-C, which is on a glass substrate, and a second glass slide is created using spacers. The liquid crystal, which consists of a mixture of 2-Methyl-1,4-phenylene-bis[4[6(acryloyloxy)hexyloxy]benzoate] (RM82), 4,4'-(di(8-(acryloyloxy)octyloxy)azobenzene and photoinitiator (Irgacure 784) (molar ratio = 89:10:1), is fed into the gap using capillary action at  $120^\circ\text{C}$  to ensure homogeneous mixing. The setup is then cooled to the nematic phase temperature of the mixture ( $90^\circ\text{C}$ ). The liquid crystal is then inspected using crossed polarizers to confirm alignment. Photopolymerization is then performed using irradiation from a MI-150 high-intensity illuminator (Edmund Optics, Barrington, NJ) with a cutoff filter ( $\lambda \geq 420$  nm) for 1 h.

From the POM images shown in Figure 6-21 and Figure 6-22, alignment is unsuccessful for the liquid crystal on the hydrophillic sample but successful for the liquid crystal on the hydrophobic sample. This is evidenced by the low intensity of light passing through the hydrophobic sample oriented at  $0^\circ$  with respect to the polarizer and, conversely, a high intensity of light passing it when it is oriented at  $45^\circ$  with respect to the polarizer. The groove patterns are also seen in the hydrophobic sample when the sample is oriented at  $45^\circ$  with respect to the polarizer, indicating that the

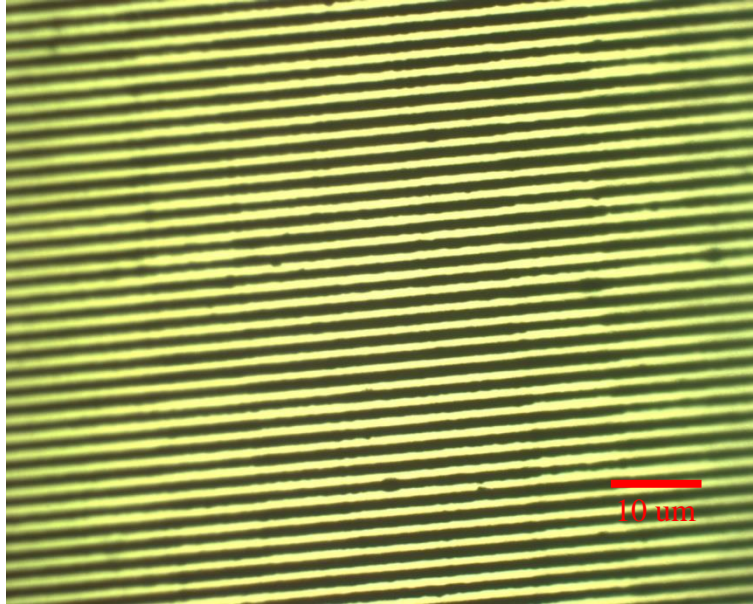


Figure 6-20: Optical image of mask used to fabricate groove patterns.

groove patterns successfully patterned the alignment of the liquid crystal. However, for the hydrophillic sample, there is no observed difference in the POM image when the sample is oriented at  $0^\circ$  and  $45^\circ$  indicating lack of alignment.

Hence, to integrate the liquid crystal into parylene-C based probes, an  $\text{SF}_6$  plasma treatment is used for all devices used in the actuation experiments so that alignment of the liquid crystal is achieved.

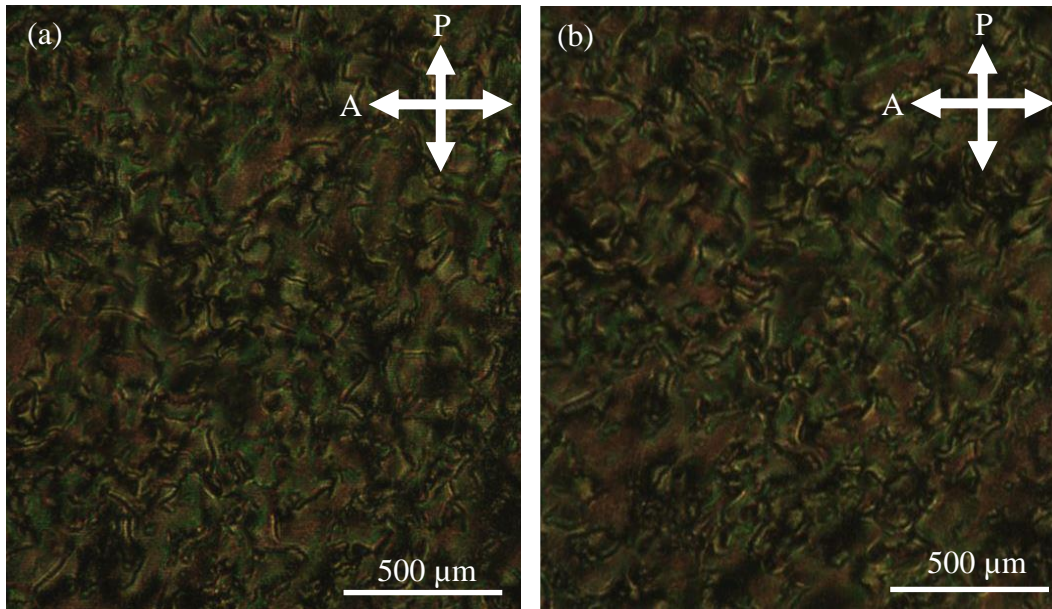


Figure 6-21: POM images of azobenzene on grooved hydrophilic parylene-C with (a) sample oriented  $0^\circ$  with respect to polarizer and (b) sample oriented  $45^\circ$  with respect to polarizer. The orientation of the polarizer (the first polarizer) and the analyzer (the second polarizer) is denoted by P and A.

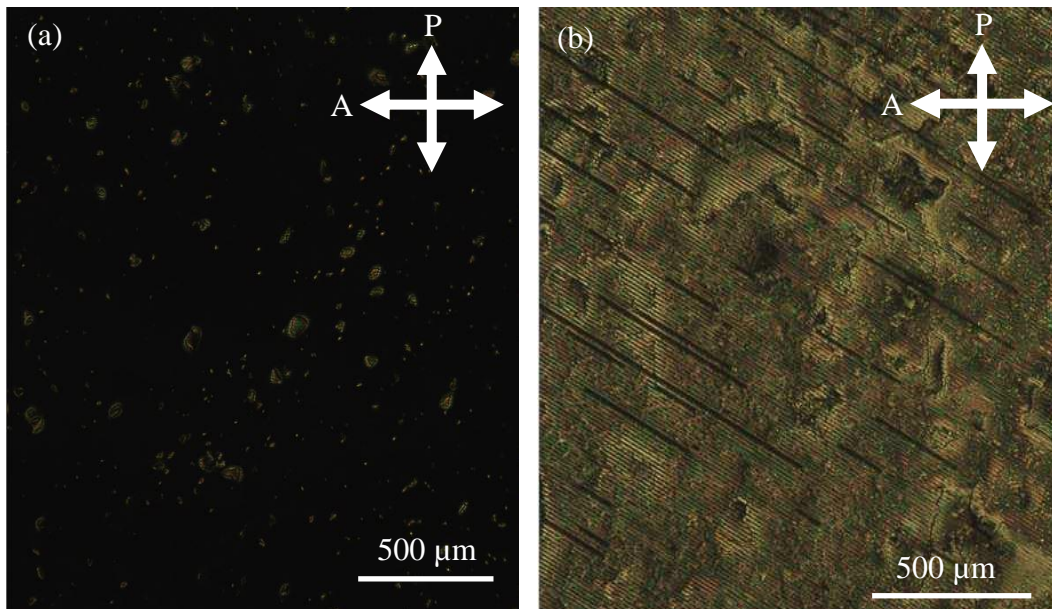


Figure 6-22: POM images of azobenzene on grooved hydrophobic parylene-C with (a) sample oriented  $0^\circ$  with respect to polarizer and (b) sample oriented  $45^\circ$  with respect to polarizer. The orientation of the polarizer (the first polarizer) and the analyzer (the second polarizer) is denoted by P and A.

## 6.4.2 Actuation experiments

To verify that actuation is achieved with the aligned samples, experiments are done in air and in 0.5% agar. 0.2% to 0.6% agar has similar properties as brain tissue and is used as a brain tissue phantom[220]. The experiment in air is performed using 375 nm 100 mW/cm<sup>2</sup> intensity UV laser focused on the device. In agar, a 375 nm 1000 mW/cm<sup>2</sup> intensity UV LED flood lamp is used instead because it is not possible to focus the UV laser through the agar onto the device. Due to absorption and spreading of the light through the glass and agar, the intensity of light reaching the device in agar is expected to be low. Due to equipment limitations, it is not possible to increase the intensity of the UV LED flood lamp further.

As seen in Figure 6-23, in air, the device is initially bent with about 500  $\mu\text{m}$  tip displacement and moves in the out-of-plane direction by a further 600  $\mu\text{m}$  after 49 min. The length of the beam is  $\sim 2.5$  mm and the width of the device is  $\sim 0.5$  mm. In the experiment with the device in agar, the length of the device inserted is  $\sim 850$   $\mu\text{m}$  and the width of the device is  $\sim 0.5$  mm. As seen in Figure 6-24, the device moves by 10  $\mu\text{m}$  after 5 s and reaches a steady state. The device moves a lower distance in agar because of the low intensity of light that reaches the device and the mechanical effects of the agar. Despite the low range of motion achievable, this amount of movement is expected to be sufficient for regions such as the cortical or hippocampus regions of the brain where the density of neurons is high and a typical spacing between neurons is  $13.6 \pm 3.8$   $\mu\text{m}$ [221]. It is expected that with more efficient methods of transferring light energy such as the use of waveguides, it will be possible to increase the range of motion of the device.

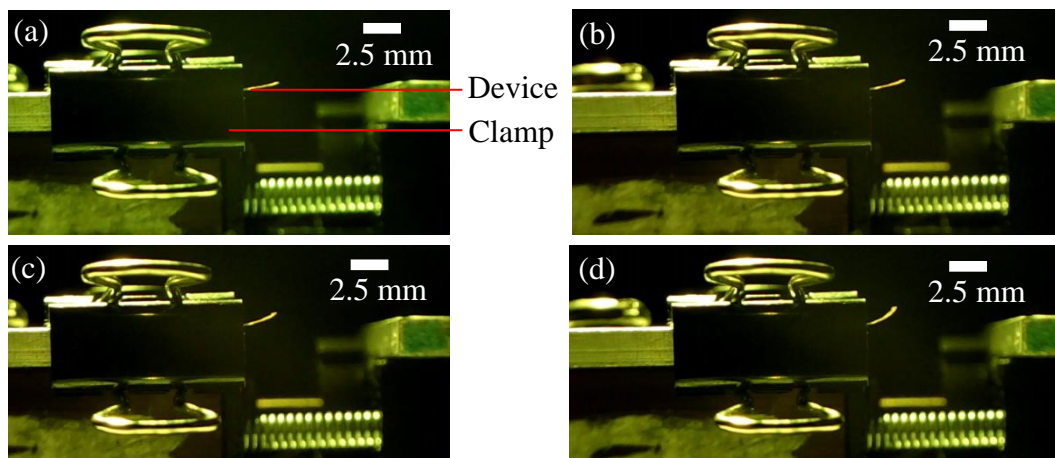


Figure 6-23: A liquid crystal on parylene-C sample exposed to UV laser in air. (a) Sample prior to UV laser exposure. Sample after (b) 7 min, (c) 16 min, and (d) 49 min of UV exposure.

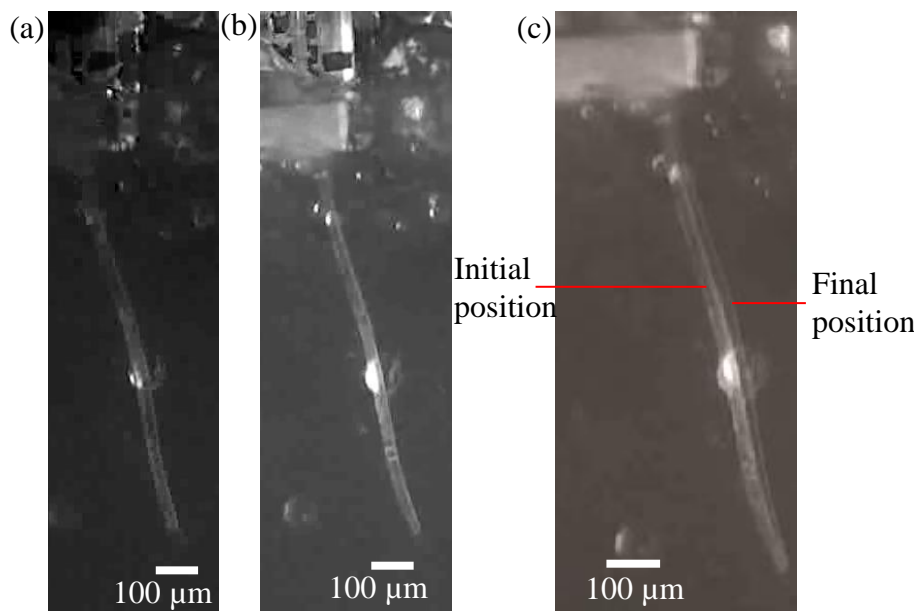


Figure 6-24: A liquid crystal on parylene-C sample exposed to UV from an LED lamp in 0.5% agar. (a) Sample prior to UV exposure. (b) Sample after 5 s of UV exposure. (c) Images of (a) and (b) overlaid to show movement.

## 6.5 Summary

Mechanical design and sizing of probes and their cabling is essential to meet application specifications and to maximize compliance for chronic use. Circular meanders improve the mechanical compliance of implantable neural probes. The design of gradual transition in cable width between the cable connector and needle reduces stress concentration. Parameterized design equations enable optimization under constraints for each specific application needs.

The parylene-C surrogate process with a Si needle provides a path to validate the parylene-C probe while removing the swelling effects of biodissolvable material. *In vivo* results show successful recordings in Si probes but not in probes integrated with biodissolvable material up to 1 hour after insertion. Hence, to determine the time required before recordings are possible, chronic experiments have to be performed in the future.

Preliminary work on actuation in neural probes is also performed using light sensitive liquid crystals, indicating successful integration of liquid crystals in parylene-C and actuation in air and in a brain tissue phantom.

# Chapter 7

## Conclusions and Future Work

The design concepts and process technologies detailed in this thesis represent important progress toward realizing ultra-compliant probes for neural prostheses that meet the necessary capabilities for chronic applications, including elimination of deleterious glial tissue buildup, insulation that lasts a lifetime, and low-impedance electrodes that effectively contact neurons. The additional capability of insertion of compliant probes is a challenge for applications requiring penetration of the probe into neural tissue. Probe integration with a biodissolvable needle is the solution taken up in this work, which motivates development of the probe transfer processes.

The key contributions presented in this work fall into categories of probe design concepts, device-level processes, and processes in support of final probe assembly. In device-level processing, contributions include:

- 1) identifying that the oxidation of the surface of Pt due to  $O_2$ -RIE used to define electrodes is detrimental to electrode performance and that  $Ar^+$  ion milling removes the surface oxidation,
- 2) finding that  $O_2$  plasma provides the best surface pre-treatment for improving parylene-C to parylene-C adhesion out of the treatments studied,
- 3) interleaving layers of two different ALD ceramics to form a nanolaminate to improve the encapsulation performance of the probe without compromising compliance,
- 4) reducing the distance between the electrode and the site-of-interest by devel-

oping a gray-scale lithography based technique to fabricate protruding electrodes, and

5) creating probes that improve electrode yield through electrically controlled actuation formed by integrating liquid crystal polymers into the parylene-C probe structure.

In processes in support of final probe assembly (e.g., integrating the biodissolvable needle with the probe), key contributions include:

6) developing a peel-based process that controls the adhesion between parylene-C to Si using different HMDS conditions, and

7) A probe transfer process flow that enables high-temperature annealing or other additional harsh processes to occur prior to final probe-needle assembly.

Contributions in probe design concepts include:

8) developing a generalized design of neural probes using meandering interconnect and structures, and

9) developing a robust design for cables using curved tapered structures. Further detailed conclusions stemming from these contributions are given below.

The conventional method of O<sub>2</sub>-RIE etching parylene-C to define the electrodes, degrades the electrode performance by forming a layer of oxidized platinum on the surface. A subsequent Ar<sup>+</sup> ion etch removes this layer of oxidized Pt, in agreement with the literature where it is reported that O<sub>2</sub>-RIE degrades the performance of Pt electrodes, and methods such as electrochemical cleaning are employed to achieve better performing electrodes. The XPS measurements show that the cause of the electrode performance degradation is oxidation of the surface layer Pt and that using Ar<sup>+</sup> ion etching can remove the 3 nm layer of oxidized Pt. This step is much simpler compared with the other methods described in literature and reduces process complexity and cost. Electrochemical cleaning is not possible with probes embedded in biodissolvable needles because such cleaning requires immersion of the device in an aqueous solution. By incorporating the Ar<sup>+</sup> step, the performance of the Pt electrodes, as measured by the magnitude of impedance at 1 kHz from electrochemical impedance spectroscopy (EIS), is improved by 23 times from 2.3 MΩ to 100 kΩ. This

significant reduction in impedance is critical to ensure sufficient spatial selectivity while maintaining signal-to-noise ratio.

Exploration of different treatments (plasma fluorination, oxygen plasma, ion mill and A174 chemical treatments) to improve parylene-C to parylene-C layer adhesion led to the conclusion that oxygen plasma treatment, along with a 300°C anneal, provides the best adhesion based on EIS measurement results where impedance is maintained even after 2000 h in saline. Furthermore, there is no correlation found between the hydrophobicity of the tests and insulation performance, indicating that the improvement in encapsulation is due to chemical bonding. This study provides a means of improving adhesion for all parylene-C based devices, and also provides a means of excluding intermediate processes such as ion-milling, which can be detrimental to parylene-C adhesion, unless a further O<sub>2</sub> plasma treatment is performed.

Ceramics inherently have better water vapor transmission as compared to parylene-C (or to any polymer). Hence, one way to improve the lifetime of compliant neural probes even further is to combine ceramics with parylene-C. Thin ALD-deposited ceramics achieve encapsulation without compromising flexibility, but require appropriate layering to provide adequate adhesion and chemically resistant properties. Al<sub>2</sub>O<sub>3</sub> / TiO<sub>2</sub> nanolaminate is resistant to etching in saline and is not electrically conductive, while Al<sub>2</sub>O<sub>3</sub> alone etches and TiO<sub>2</sub> alone is electrically conductive. Incorporation of a TiO<sub>2</sub> adhesion layer solves the issue of poor adhesion of Al<sub>2</sub>O<sub>3</sub>-TiO<sub>2</sub> nanolaminate to parylene-C. The nanolaminate performs well, maintaining a high  $\sim 10^{11}\Omega$  impedance at 0.1 Hz even after 500 h at 60°C in saline.

Protruding electrodes, developed using grayscale lithography, improve on an inherent flaw with surface microfabricated neural probes: having a thicker insulation means a larger electrode recess that increases the distance between the neuronal site of interest and the electrode. The protruding electrode property should improve electrode yield (the number of electrodes that successfully record single-unit action potentials) through this hypothesis remains to be proven through *in vivo* studies. The process of creating the protrusion roughens the electrode and improves its impedance to saline at 1 kHz from 70 k $\Omega$  to 21.6 k $\Omega$  for 115  $\mu\text{m}$  by 15  $\mu\text{m}$  electrodes. The mechanical

stability of the electrode is not compromised since the parylene-C is roughened prior to Pt deposition rather than the Pt surface itself. Poor mechanical stability is a problem for rough electrodes such as platinum black electrodes. This process concept to fabricate protruding electrodes for *in vivo* use is new in the literature. Existing protruding electrodes used for *in vitro* studies are created by electrodepositing thick electrode material.

Incorporating water-soluble materials such as carboxymethylcellulose-glucose (CMC-glucose) into MEMS-based processes is challenging because of the need to use wet chemicals and various plasma chemistries that destroy or change the properties of the material. Integration of CMC-glucose needles with compliant probes motivates development of processes to modulate the adhesion of the probe on its handle wafer and to transfer probes onto a second handle wafer. In a peel-based process flow (i.e., peeling the probe from its handle substrate), different surface coverage of HMDS using different vapor prime conditions effectively controls the adhesion between parylene-C and the substrate. Successful peeling of devices is demonstrated; however, there is large variation in the work of adhesion using this method. In addition, although the peel-based process is simple and cost effective, it is incompatible with high-temperature annealing, which is critical for maintaining the insulation of parylene-C probes.

In order to address these issues, the subsequently developed probe-transfer technique allows for the transfer of strongly adhered structures. The key to this process is the complete removal of the original handle substrate (made of Si), which is necessary to remove the dependence of parylene-C to Si adhesion. The wax, BGL7080, provides suitable characteristics to act as the bonding agent for transfer of the probe to the second handle substrate. The ability of BGL7080 to act as a sacrificial material to release the probe with isopropyl alcohol allows maintenance of the properties of the attached CMC-glucose needle. In addition, the ability to reflow the wax without the use of solvents is critical in ensuring a high yield process, since the formation of bubbles due to any residual solvent exposure would result in probe damage. The versatility of the transfer process allows it to be extended to other applications that involve

assembly of materials that otherwise would be incompatible with microfabrication temperatures or chemistries. Probes that have been annealed have been transferred successfully using this process. In addition, by bonding prefabricated needles to the probes in order to reduce stress on the probes during molding, devices fabricated using this technique have been demonstrated to maintain similar impedance before and after incorporation of the biodissolvable needles, indicating that insulation quality is maintained by this process. Comparatively, stresses arising in the prior direct molding process for incorporation of CMC-based needles degrades the probe leakage impedance by two orders of magnitude.

For the design of probes, geometric parameterization of curved meander interconnect leads to optimization for the maximum probe compliance given realistic constraints imposed by the biodissolvable needle size. Parameterization of the design space enables a generalized design methodology for widely varying applications, leading to rapid optimal mechanical design of probes. Using this methodology, the least compliant direction of the neural probe is optimized. Analyzing the trade-off between probe density and mechanical compliance informs decisions for each application.

The design of a smooth mechanical transition region in the parylene-C cables connecting the electrodes to the pad minimizes stress concentration and improves robustness. The analysis extends to other probes since all penetrating neural probes (at least all such probes today) require a transition from a larger cable region to an electrode region on the scale of individual neurons. The design of the transition region involves structures that gradually taper from the relatively wide (1 cm scale) cable to the relatively narrow (0.1 mm scale) needle region. The more gradual is the transition, the less is the stress concentration as determined by FEA. By reducing the stress concentration region, cable robustness improves since areas of high stress are minimized in the event of manual handling or the presence of other external mechanical factors.

Finally, the preliminary work on probes that actuate using liquid crystal polymers shows promise for future probes having manipulation capability. Controlling the hydrophobicity of parylene-C using SF6 plasma treatment and etching grooves into the

parylene-C successfully aligned the liquid crystal directors. Parylene-C incorporated with the liquid crystal polymer moves 600  $\mu\text{m}$  in air and 10  $\mu\text{m}$  in 0.5% agar, which is used as a brain tissue phantom. This initial experiment illustrates the potential to integrate the liquid polymers into parylene-C to instill manipulation capabilities into compliant probes. The amount of movement in agar is comparable to the typical spacing between neurons in regions such as the cortical or hippocampus regions of the brain and hence, the ability to actuate can be used to improve electrode yield or track multiple neurons.

## 7.1 Future Work

The interest in microfabricated neural probes spans a very broad and application specific set of needs. New challenges in design and processing will arise when probes for new applications are developed. However, the basic principles and constraints in design and processing of compliant parylene-C neural probes maintain their relevance irrespective of the specific application. The techniques and technologies presented in this thesis have broad utility and can benefit new neural probe applications as they arise.

As is true of almost all research efforts, the work in this thesis points toward many future extensions. Given the practically infinite number of possible ALD materials, it is expected that even more effective encapsulant coatings can be developed. Coatings should have very strong adhesion, be mechanically compliant, chemically inert to various chemicals found in the body, be biocompatible and have very low water vapor transmission. The material should also have very low dielectric constant to reduce capacitive coupling across the material. The methods used in this thesis extend to such other ALD materials. Future development of these new materials may, one day, lead to commercially available compliant neural probes that last for a human lifetime.

The preliminary work on liquid-crystal polymer integration with neural probes for actuation is promising and inspires further research. Although currently only 10  $\mu\text{m}$  of movement in 0.5% agar is demonstrated, the experiment is performed with an

external source of light. By integrating the probes with waveguides, for example, it may be possible to actuate probes *in vivo* and demonstrate the ability to move and improve electrode yield.

More research may also lead to even better biodissolvable needle materials. The ideal biodissolvable material has minimal swelling and dissolves quickly within the body. These properties allow for minimal initial damage to cells around the body and rapid acquisition of neural recordings.



# Bibliography

- [1] Janczuk, Białopiotrowicz, and Zdziennicka, “Some Remarks on the Components of the Liquid Surface Free Energy,” *Journal of Colloid and Interface Science*, vol. 211, pp. 96–103, Mar 1999.
- [2] L. A. Geddes and R. Roeder, “Criteria for the selection of materials for implanted electrodes,” *Annals of Biomedical Engineering*, vol. 31, pp. 879–890, Jul 2003.
- [3] F. López-Muñoz, J. Boya, and C. Alamo, “Neuron theory, the cornerstone of neuroscience, on the centenary of the Nobel Prize award to Santiago Ramón y Cajal,” *Brain Research Bulletin*, vol. 70, no. 4-6, pp. 391–405, 2006.
- [4] S. C. Sherrington, *The Integrative Action of the Nervous System. Classics in psychology*, vol. 20. 1906.
- [5] A. L. Hodgkin and A. F. Huxley, “A Quantitative Description of Membrane Current and its Application to Conduction and Excitation in Nerves,” *J. Physiol.*, vol. 117, pp. 500–544, 1952.
- [6] A. Nemri, “Santiago Ramón y Cajal,” *Scholarpedia*, vol. 5, p. 8577, Dec 2010.
- [7] M. F. Glasser, S. M. Smith, D. S. Marcus, J. L. R. Andersson, E. J. Auerbach, T. E. J. Behrens, T. S. Coalson, M. P. Harms, M. Jenkinson, S. Moeller, E. C. Robinson, S. N. Sotiropoulos, J. Xu, E. Yacoub, K. Ugurbil, and D. C. Van

- Essen, “The Human Connectome Project’s neuroimaging approach,” *Nature Neuroscience*, vol. 19, pp. 1175–1187, Aug 2016.
- [8] C. Stosiek, O. Garaschuk, K. Holthoff, and A. Konnerth, “In vivo two-photon calcium imaging of neuronal networks.,” *Proceedings of the National Academy of Sciences of the United States of America*, vol. 100, no. 12, pp. 7319–24, 2003.
- [9] K. L. Rogers, S. Picaud, E. Roncali, R. Boisgard, C. Colasante, J. Stinnakre, B. Tavitian, and P. Brûlet, “Non-Invasive In Vivo Imaging of Calcium Signaling in Mice,” *PLoS ONE*, vol. 2, p. e974, Oct 2007.
- [10] E. S. Boyden, F. Zhang, E. Bamberg, G. Nagel, and K. Deisseroth, “Millisecond-timescale, genetically targeted optical control of neural activity,” *Nature Neuroscience*, vol. 8, pp. 1263–1268, Sep 2005.
- [11] J. L. Collinger, B. Wodlinger, J. E. Downey, W. Wang, E. C. Tyler-Kabara, D. J. Weber, A. J. C. McMorland, M. Velliste, M. L. Boninger, and A. B. Schwartz, “High-performance neuroprosthetic control by an individual with tetraplegia.,” *Lancet (London, England)*, vol. 381, pp. 557–64, Feb 2013.
- [12] L. Greenemeier, “FDA Approves First Retinal Implant,” *Nature*, Feb 2013.
- [13] C. Pandarinath, P. Nuyujukian, C. H. Blabe, B. L. Sorice, J. Saab, F. R. Willett, L. R. Hochberg, K. V. Shenoy, and J. M. Henderson, “High performance communication by people with paralysis using an intracortical brain-computer interface,” *eLife*, vol. 6, p. e18554, Feb 2017.
- [14] J. Gardner, “A history of deep brain stimulation: Technological innovation and the role of clinical assessment tools,” *Social Studies of Science*, vol. 43, pp. 707–728, Oct 2013.
- [15] V. S. Polikov, P. A. Tresco, and W. M. Reichert, “Response of brain tissue to chronically implanted neural electrodes.,” *Journal of neuroscience methods*, vol. 148, pp. 1–18, Oct 2005.

- [16] S. Sommakia, H. C. Lee, J. Gaire, and K. J. Otto, “Materials approaches for modulating neural tissue responses to implanted microelectrodes through mechanical and biochemical means,” *Current Opinion in Solid State and Materials Science*, vol. 18, pp. 319–328, Dec 2014.
- [17] S. M. Bowyer, “Coherence a measure of the brain networks: past and present,”
- [18] Y.-H. Chen, M. Op de Beeck, L. Vanderheyden, E. Carrette, V. Mihajlović, K. Vanstreels, B. Grundlehner, S. Gadeyne, P. Boon, and C. Van Hoof, “Soft, comfortable polymer dry electrodes for high quality ECG and EEG recording,” *Sensors (Basel, Switzerland)*, vol. 14, pp. 23758–80, Dec 2014.
- [19] J. Viventi, D.-H. Kim, L. Vigeland, E. S. Frechette, J. a. Blanco, Y.-S. Kim, A. E. Avrin, V. R. Tiruvadi, S.-W. Hwang, A. C. Vanleer, D. F. Wulsin, K. Davis, C. E. Gelber, L. Palmer, J. Van der Spiegel, J. Wu, J. Xiao, Y. Huang, D. Contreras, J. a. Rogers, and B. Litt, “Flexible, foldable, actively multiplexed, high-density electrode array for mapping brain activity in vivo.,” *Nature neuroscience*, vol. 14, no. 12, pp. 1599–605, 2011.
- [20] A. A. Schendel, K. W. Eliceiri, and J. C. Williams, “Advanced materials for neural surface electrodes,” *Current Opinion in Solid State and Materials Science*, vol. 18, no. 6, pp. 301–307, 2014.
- [21] J. R. Wolpaw and E. W. Wolpaw, *Brain-computer interfaces : principles and practice*. Oxford University Press, 2012.
- [22] G. Rios, E. V. Lubenov, D. Chi, M. L. Roukes, and A. G. Siapas, “Nanofabricated neural probes for dense 3-D recordings of brain activity,” *Nano Letters*, vol. 16, pp. 6857–6862, Nov 2016.
- [23] P. K. Campbell, K. E. Jones, R. J. Huber, K. W. Horch, and R. A. Normann, “A silicon-based, three-dimensional neural interface: manufacturing processes for an intracortical electrode array,” *IEEE Transactions on Biomedical Engineering*, vol. 38, pp. 758–68, Aug 1991.

- [24] K. Najafi, K. Wise, and T. Mochizuki, “A high-yield IC-compatible multichannel recording array,” *IEEE Transactions on Electron Devices*, vol. 32, pp. 1206–1211, Jul 1985.
- [25] MicroProbes, “Microprobes for Life Science,” <https://microprobes.com/>, Accessed: 2017-05-17.
- [26] P. J. Gilgunn, X. C. Ong, S. N. Flesher, A. B. Schwartz, and R. A. Gaunt, “Structural analysis of explanted microelectrode arrays,” in *International IEEE/EMBS Conference on Neural Engineering, NER*, pp. 719–722, 2013.
- [27] A. Prasad, Q.-S. Xue, R. Dieme, V. Sankar, R. C. Mayrand, T. Nishida, W. J. Streit, and J. C. Sanchez, “Abiotic-biotic characterization of Pt/Ir microelectrode arrays in chronic implants,” *Frontiers in neuroengineering*, vol. 7, p. 2, Jan 2014.
- [28] J. K. Nguyen, D. J. Park, J. L. Skousen, A. E. Hess-Dunning, D. J. Tyler, S. J. Rowan, C. Weder, and J. R. Capadona, “Mechanically-compliant intracortical implants reduce the neuroinflammatory response,” *Journal of neural engineering*, vol. 11, p. 056014, Oct 2014.
- [29] T. Ware, D. Simon, D. E. Arreaga-Salas, J. Reeder, R. Rennaker, E. W. Keefer, and W. Voit, “Fabrication of Responsive, Softening Neural Interfaces,” *Advanced Functional Materials*, vol. 22, pp. 3470–3479, Aug 2012.
- [30] W. Shen, L. Karumbaiah, X. Liu, T. Saxena, S. Chen, R. Patkar, R. V. Bellamkonda, M. G. Allen, M. Velliste, S. Perel, M. Spalding, J. Williams, R. Rennaker, D. Kipke, C. Nordhausen, E. Maynard, R. Normann, J. Donoghue, M. Nicolelis, A. Schwartz, L. Hochberg, M. Serruya, G. Friehs, K. Lee, J. He, A. Singh, J. Kuo, B. Kim, S. Hara, J. Subbaroyan, D. Martin, D. Kipke, A. Sridharan, J. Nguyen, J. Capadona, D. O’Brien, T. Nichols, M. Allen, P. Rousche, R. Normann, P. Chen, M. Jorfi, J. Skousen, C. Weder, C. Weder, J. Capadona, K. Shanmuganathan, K. Potter-Baker, J. Capadona, R. Bellamkonda, S. Pai,

- P. Renaud, S. Goldstein, M. Salcman, V. Polikov, P. Tresco, W. Reichert, S. Chen, M. Allen, J. Sanes, U. Rauch, D. Tonge, J. Golding, M. Edbladh, R. Labrador, M. Butí, X. Navarro, W. He, G. McConnell, R. Bellamkonda, Y. Chen, C. Hsieh, C. Tsai, M. Tibbitt, K. Anseth, V. Mukhatyar, L. Karumbaiah, J. Yeh, M. Abidian, D. Martin, T. Kozai, N. Langhals, P. Patel, W. He, G. McConnell, T. Schneider, X. Cui, J. Wiler, M. Dzaman, S. D. Faveri, E. Maggolini, E. Miele, N. Naik, V. Kumar, E. Chaikof, J. Caves, V. Kumar, W. Xu, B. Gillette, J. Jensen, B. Tang, J. Phillips, S. Bunting, S. Hall, L. Karumbaiah, T. Saxena, D. Carlson, T. Saxena, L. Karumbaiah, E. Gaupp, A. Gautieri, S. Vesentini, A. Redaelli, S. Rebscher, A. Hetherington, B. Bonham, G. McConnell, H. Rees, A. Levey, S. Soofi, J. Last, S. Liliensiek, H. Ching, D. Choudhury, M. Nine, B. Rashid, M. Destrade, M. Gilchrist, K. Chawla, S. Lee, B. Lee, J. Muthuswamy, R. Saha, A. Gilletti, R. Parenteau-Bareil, R. Gauvin, F. Berthod, S. Grad, M. Loparic, R. Peter, M. Plainfosse, P. Hatton, A. Crawford, R. Ritter, E. Quate, G. Gillies, H. Zhang, P. Patel, and Z. Xie, "Extracellular matrix-based intracortical microelectrodes: Toward a microfabricated neural interface based on natural materials," *Microsystems and Nanoengineering*, vol. 1, p. 15010, Jun 2015.
- [31] A. Lecomte, V. Castagnola, E. Descamps, L. Dahan, M. C. Blatché, T. M. Dinis, E. Leclerc, C. Egles, and C. Bergaud, "Silk and PEG as means to stiffen a parylene probe for insertion in the brain: toward a double time-scale tool for local drug delivery," *Journal of Micromechanics and Microengineering*, vol. 25, p. 125003, Dec 2015.
- [32] Z. Xiang, S.-C. Yen, N. Xue, T. Sun, W. M. Tsang, S. Zhang, L.-D. Liao, N. V. Thakor, and C. Lee, "Ultra-thin flexible polyimide neural probe embedded in a dissolvable maltose-coated microneedle," *Journal of Micromechanics and Microengineering*, vol. 24, p. 065015, Jun 2014.
- [33] D. Lewitus, K. L. Smith, W. Shain, and J. Kohn, "Ultrafast resorbing polymers for use as carriers for cortical neural probes," *Acta Biomaterialia*, vol. 7,

- pp. 2483–2491, Jun 2011.
- [34] F. Ceysens, K. van Kuyck, B. Nuttin, and R. Puers, “Neural Implants Containing a Resorbable Chitosan Matrix,” *Procedia Engineering*, vol. 47, pp. 688–689, 2012.
- [35] S. Felix, K. Shah, D. George, V. Tolosa, A. Tooker, H. Sheth, T. Delima, and S. Pannu, “Removable silicon insertion stiffeners for neural probes using polyethylene glycol as a biodissolvable adhesive,” in *2012 Annual International Conference of the IEEE Engineering in Medicine and Biology Society*, pp. 871–874, IEEE, Aug 2012.
- [36] S. Takeuchi, D. Ziegler, Y. Yoshida, K. Mabuchi, T. Suzuki, J. P. Donoghue, D. P. O’Brien, T. R. Nichols, M. G. Allen, S. Takeuchi, T. Suzuki, K. Mabuchi, H. Fujita, S. Takeuchi, I. Shimoyama, E. V. Goodall, T. M. Lefurge, K. W. Horch, T. Lefurge, E. Goodall, K. Horch, L. Stensaas, A. Schoenberg, D. Pappageorgiou, S. C. Bledsoe<sup>1</sup>, M. Gulari, J. F. Hetke, D. J. Anderson, K. D. Wise, S. Metz, A. Bertsch, D. Bertrand, P. Renaud, L. Licklider, X.-Q. Wang, A. Desai, Y.-C. Tai, T. D. Lee, H.-S. Noha, Y. Huang<sup>b</sup>, P. J. Hesketh<sup>a</sup>, D. H. Szarowski, M. D. Andersen, S. Retterer, A. J. Spence, M. Isaacson, H. G. Craighead, J. N. Turner, and W. Shain, “Parylene flexible neural probes integrated with microfluidic channels,” *Lab on a Chip*, vol. 5, no. 5, p. 519, 2005.
- [37] V. Castagnola, “Implantable microelectrodes on soft substrate with nanostructured active surface for stimulation and recording of brain activities,”
- [38] E. G. Kim, J. K. John, H. Tu, Q. Zheng, J. Loeb, J. Zhang, and Y. Xu, “A hybrid silicon-parylene neural probe with locally flexible regions,” *Sensors and Actuators B: Chemical*, vol. 195, pp. 416–422, May 2014.
- [39] M. Chamanzar, D. J. Denman, T. J. Blanche, and M. M. Maharbiz, “Ultra-compact optoflex neural probes for high-resolution electrophysiology and optogenetic stimulation,” in *2015 28th IEEE International Conference on Micro Electro Mechanical Systems (MEMS)*, pp. 682–685, IEEE, Jan 2015.

- [40] A. Weltman, H. Xu, K. Scholten, T. Berger, D. Song, and E. Meng, “Deep brain targeting strategy for bare parylene neural probe arrays,” in *Technical Digest*, (Hilton Head Island, SC), Solid-State Sensors, Actuators and Microsystems Workshop, 2016.
- [41] R. Khilwani, P. J. Gilgunn, T. D. Y. Kozai, X. C. Ong, E. Korkmaz, P. Gunalan, X. T. Cui, G. K. Fedder, and O. B. Ozdoganlar, “Ultra-Miniature Ultra-Compliant Neural Probes with Dissolvable Delivery Needles: Fabrication and Characterization,” *Biomedical Microdevices*, vol. 18, no. 6, p. 97, 2016.
- [42] A. C. Barnett, “Tissue cutting mechanics of dynamic needle insertion,” *Ph.D. Thesis*, 2016.
- [43] R. H. Quarles, W. B. Macklin, and P. Morell, “Myelin Formation, Structure and Biochemistry,” *Basic Neurochemistry: Molecular, Cellular and Medical Aspects*, pp. 51–71, 2006.
- [44] I. L. Arancibia-Carcamo and D. Attwell, “The node of Ranvier in CNS pathology,” *Acta neuropathologica*, vol. 128, pp. 161–75, Aug 2014.
- [45] C. Gold, “On the Origin of the Extracellular Action Potential Waveform: A Modeling Study,” *Journal of Neurophysiology*, vol. 95, no. 5, pp. 3113–3128, 2006.
- [46] L. Lapicque, “Recherches quantitatives sur l’excitation électrique des nerfs traitée comme une polarisation,” *J. Physiol. Pathol. Gen*, vol. 9, pp. 620 – 635, 1907.
- [47] D. Boinagrov, J. Loudin, and D. Palanker, “Strength-duration relationship for extracellular neural stimulation: numerical and analytical models,” *Journal of neurophysiology*, vol. 104, pp. 2236–48, Oct 2010.
- [48] D. R. Merrill, M. Bikson, and J. G. Jefferys, “Electrical stimulation of excitable tissue: design of efficacious and safe protocols,” *Journal of Neuroscience Methods*, vol. 141, pp. 171–198, Feb 2005.

- [49] D. R. McNeal, "Analysis of a Model for Excitation of Myelinated Nerve," *IEEE Transactions on Biomedical Engineering*, vol. BME-23, no. 4, pp. 329–337, 1976.
- [50] F. Rattay, "Analysis of Models for External Stimulation of Axons," *IEEE Transactions on Biomedical Engineering*, vol. BME-33, no. 10, pp. 974–977, 1986.
- [51] L. Tung, "The Generalized Activating Function," in *Cardiac Bioelectric Therapy*, pp. 111–132, Boston, MA: Springer US, 2009.
- [52] S. D. Stoney, W. D. Thompson, and H. Asanuma, "Excitation of pyramidal tract cells by intracortical microstimulation: effective extent of stimulating current.," *Journal of Neurophysiology*, vol. 31, no. 5, 1968.
- [53] L. Luan, X. Wei, Z. Zhao, J. J. Siegel, O. Potnis, C. A. Tuppen, S. Lin, S. Kazmi, R. A. Fowler, S. Holloway, A. K. Dunn, R. A. Chitwood, and C. Xie, "Ultra-flexible nanoelectronic probes form reliable, glial scar-free neural integration," *Science Advances*, vol. 3, p. e1601966, Feb 2017.
- [54] V. N. Vernekar, D. K. Cullen, N. Fogleman, Y. Choi, A. J. García, M. G. Allen, G. J. Brewer, and M. C. LaPlaca, "SU-8 2000 rendered cytocompatible for neuronal bioMEMS applications," *Journal of Biomedical Materials Research Part A*, vol. 89, pp. 138–51, Apr 2008.
- [55] K. V. Nemani, K. L. Moodie, J. B. Brennick, A. Su, and B. Gimi, "In vitro and in vivo evaluation of SU-8 biocompatibility.," *Materials Science and Engineering: C, Materials for Biological Applications*, vol. 33, pp. 4453–9, Oct 2013.
- [56] E. M. Schmidt, J. S. McIntosh, and M. J. Bak, "Long-term implants of parylene-C coated microelectrodes," *Medical and Biological Engineering and Computing*, vol. 26, pp. 96–101, Jan 1988.
- [57] T. G. Yuen, W. F. Agnew, and L. A. Bullara, "Tissue response to potential neuroprosthetic materials implanted subdurally," *Biomaterials*, vol. 8, pp. 138–141, Mar 1987.

- [58] A. Lecomte, A. Degache, E. Descamps, L. Dahan, and C. Bergaud, “Biostability Assessment of Flexible Parylene C-based Implantable Sensor in Wireless Chronic Neural Recording,” *Procedia Engineering*, vol. 168, pp. 189–192, 2016.
- [59] S.-J. Kim, D.-S. Lee, I.-G. Kim, D.-W. Sohn, J.-Y. Park, B.-K. Choi, and S.-W. Kim, “Evaluation of the biocompatibility of a coating material for an implantable bladder volume sensor,” *The Kaohsiung Journal of Medical Sciences*, vol. 28, no. 3, pp. 123–129, 2012.
- [60] D. S. Lee, S. J. Kim, J. H. Sohn, I. G. Kim, S. W. Kim, D. W. Sohn, J. H. Kim, and B. Choi, “Biocompatibility of a PDMS-coated micro-device: Bladder volume monitoring sensor,” *Chinese Journal of Polymer Science*, vol. 30, pp. 242–249, Mar 2012.
- [61] S. Watkins, D. Gandhi, and P. J. Rousche, “Biocompatibility of polyimide-based neural interfaces for chronic implant applications,” *Journal of Undergraduate Research*, vol. 1, no. 36, 2007.
- [62] T. Stieglitz, H. Beutel, M. Schuettler, and J.-U. Meyer, “Micromachined, Polyimide-Based Devices for Flexible Neural Interfaces,” *Biomedical Microdevices*, vol. 2, no. 4, pp. 283–294, 2000.
- [63] C. Shih, T. Harder, and Y. Tai, “Yield strength of thin-film parylene-C,” *Microsystem Technologies*, vol. 10, pp. 407–411, Aug 2004.
- [64] T. A. Harder, T.-J. Yao, Q. He, C.-Y. Shih, and Y.-C. Tai, “Residual stress in thin-film parylene-c,” in *Proceedings on the 15th IEEE Conference on Microelectromechanical Systems (MEMS) 2002*, (Las Vegas, NV), pp. 435–438, IEEE, 2002.
- [65] D. Wright, B. Rajalingam, J. M. Karp, S. Selvarasah, Y. Ling, J. Yeh, R. Langer, M. R. Dokmeci, and A. Khademhosseini, “Reusable, reversibly sealable parylene membranes for cell and protein patterning,” *Journal of Biomedical Materials Research Part A*, vol. 85, pp. 530–8, May 2008.

- [66] H.-S. Noh, K.-S. Moon, A. Cannon, P. J. Hesketh, and C. P. Wong, “Wafer bonding using microwave heating of parylene intermediate layers,” *Journal of Micromechanics and Microengineering*, vol. 14, pp. 625–631, 2004.
- [67] X. C. Ong, G. K. Fedder, and P. J. Gilgunn, “Modulation of Parylene-C to silicon adhesion using HMDS priming,” *Journal of Micromechanics and Microengineering*, vol. 24, p. 105001, Oct 2014.
- [68] C. J. Robin, A. Vishnoi, and K. N. Jonnalagadda, “Mechanical Behavior and Anisotropy of Spin-Coated SU-8 Thin Films for MEMS,” *Journal of Microelectromechanical Systems*, vol. 23, pp. 168–180, Feb 2014.
- [69] T. Xu, J. H. Yoo, S. Babu, S. Roy, J.-B. Lee, and H. Lu, “Characterization of the mechanical behavior of SU-8 at microscale by viscoelastic analysis,” *Journal of Micromechanics and Microengineering*, vol. 26, p. 105001, Oct 2016.
- [70] J. Gao, L. Guan, and J. Chu, “Determining the Young’s modulus of SU-8 negative photoresist through tensile testing for MEMS applications,” in *Proceedings on the Sixth International Symposium on Precision Engineering Measurements and Instrumentation*, p. 754464, SPIE, Aug 2010.
- [71] MicroChem (Woburn; MA), “SU-8 Permanent Photoresists Resist Description,” <http://www.microchem.com/pdf/SU-8-table-of-properties.pdf>, Accessed: 2017-06-06.
- [72] J. C. Lötters, W. Olthuis, P. H. Veltink, and P. Bergveld, “The mechanical properties of the rubber elastic polymer polydimethylsiloxane for sensor applications,” *Journal of Micromechanics and Microengineering*, vol. 7, pp. 145–147, Sep 1997.
- [73] A. Mata, A. J. Fleischman, and S. Roy, “Characterization of Polydimethylsiloxane (PDMS) Properties for Biomedical Micro/Nanosystems,” *Biomedical Microdevices*, vol. 7, pp. 281–293, Dec 2005.

- [74] J. B. Fortin and T.-M. Lu, "Film Properties," in *Chemical Vapor Deposition Polymerization*, pp. 57–82, Boston, MA: Springer US, 2004.
- [75] Momentive (Waterford; NY), "Element14\* PDMS 350-J," <http://www.momentive.com/products/show-technical-datasheet.aspx?id=25653>, Accessed: 2017-06-07.
- [76] A. Kachroudi, S. Basrour, L. Rufer, A. Sylvestre, and F. Jomni, "Dielectric properties modelling of cellular structures with PDMS for micro-sensor applications," *Smart Materials and Structures*, vol. 24, p. 125013, Dec 2015.
- [77] Dupont Kapton (Wilmington; DE), "Dupont Kapton Summary of Properties," <http://www.dupont.com/content/dam/dupont/products-and-services/membranes-and-films/polyimide-films/documents/DEC-Kapton-summary-of-properties.pdf>, Accessed: 2017-06-07.
- [78] E. Meng, P.-Y. Li, and Y.-C. Tai, "Plasma removal of Parylene C," *Journal of Micromechanics and Microengineering*, vol. 18, p. 045004, Apr 2008.
- [79] E. Meng and Y.-C. Tai, "Parylene etching techniques for microfluidics and bioMEMS," pp. 568–571, 2005.
- [80] H. C. Koydemir, H. Kulah, and C. Ozgen, "Solvent Compatibility of Parylene C Film Layer," *Journal of Microelectromechanical Systems*, vol. 23, no. 2, pp. 298–307, 2014.
- [81] T. Adrega and S. P. Lacour, "Stretchable gold conductors embedded in PDMS and patterned by photolithography: fabrication and electromechanical characterization," *Journal of Micromechanics and Microengineering*, vol. 20, p. 055025, May 2010.
- [82] W. F. Gorham, "A New, General Synthetic Method for the Preparation of Linear Poly-p-xylylenes," *Journal of Polymer Science Part A-1: Polymer Chemistry*, vol. 4, no. 12, pp. 3027–3039, 1966.

- [83] E. Charlson, E. Charlson, and R. Sabeti, "Temperature selective deposition of Parylene-C," *IEEE Transactions on Biomedical Engineering*, vol. 39, pp. 202–206, Feb 1992.
- [84] C. J. Mitchell, G.-R. Yang, and J. J. Senkevich, "Adhesion aspects of poly(p-xylylene) to SiO<sub>2</sub> surfaces using  $\gamma$ -methacryloxypropyltrimethoxysilane as an adhesion promoter," *Journal of Adhesion Science and Technology*, vol. 20, no. 14, pp. 1637–1647, 2006.
- [85] N. Faucheux, R. Schweiss, K. Lützow, C. Werner, and T. Groth, "Self-assembled monolayers with different terminating groups as model substrates for cell adhesion studies," *Biomaterials*, vol. 25, no. 14, pp. 2721–2730, 2004.
- [86] J. N. Israelachvili, *Intermolecular and Surface Forces: Revised Third Edition*. Academic Press, Jul 2011.
- [87] T. Young, "An Essay on the Cohesion of Fluids," *Philosophical Transactions of the Royal Society of London*, vol. 95, pp. 65–87, Jan 1805.
- [88] D. K. Owens and R. C. Wendt, "Estimation of the surface free energy of polymers," *Journal of Applied Polymer Science*, vol. 13, no. 8, pp. 1741–1747, 1969.
- [89] F. M. Fowkes, "Determination of interfacial tensions, contact angles, and dispersion forces in surfaces by assuming additivity of intermolecular interactions in surfaces," *The Journal of Physical Chemistry*, vol. 66, pp. 382–382, Feb 1962.
- [90] M. Chaudhury, "Interfacial interaction between low-energy surfaces," *Materials Science and Engineering: R: Reports*, vol. 16, pp. 97–159, Mar 1996.
- [91] D. E. Packham, *Handbook of Adhesion*. John Wiley and Sons, Feb 2006.
- [92] I. Kamyab and E. H. Andrews, "Interfacial and Bulk Contributions to Peeling Energy," *The Journal of Adhesion*, vol. 56, pp. 121–134, Apr 1996.

- [93] G. Gervason, J. Ducom, and H. Cheradame, "Relationship between surface energy and adhesion strength in polyethylene-paper composites," *British Polymer Journal*, vol. 21, pp. 53–59, Jan 1989.
- [94] K. Kendall, "Thin-film peeling—the elastic term," *Journal of Physics D: Applied Physics*, vol. 8, no. 13, pp. 1449–1452, 1975.
- [95] C. Hassler, R. P. von Metzen, P. Ruther, and T. Stieglitz, "Characterization of parylene C as an encapsulation material for implanted neural prostheses," *Journal of Biomedical Materials Research Part B: Applied Biomaterials*, vol. 93B, no. 1, pp. 266–274, 2010.
- [96] W. Franks, I. Schenker, P. Schmutz, and A. Hierlemann, "Impedance characterization and modeling of electrodes for biomedical applications," *IEEE Transactions on Biomedical Engineering*, vol. 52, pp. 1295–302, Jul 2005.
- [97] H. Cesiulis, N. Tsyntsar, A. Ramanavicius, and G. Ragoisha, "The study of thin films by electrochemical impedance spectroscopy," in *Nanostructures and Thin Films for Multifunctional Applications*, pp. 3–42, 2016.
- [98] C. Pang, "Parylene Technology for Neural Probes Applications," *Ph.D. Thesis*, Department of Electrical Engineering, California Institute of Technology, 2008.
- [99] M. Heim, B. Yvert, and A. Kuhn, "Nanostructuring strategies to enhance microelectrode array (MEA) performance for neuronal recording and stimulation," *Journal of Physiology-Paris*, vol. 106, pp. 137–145, May 2012.
- [100] E. M. Kelliher and T. L. Rose, "Charge Utilization in Anodic Rhodium Oxide Films Pulsed in Carbonate-Buffered Saline," *Journal of The Electrochemical Society*, vol. 136, p. 1765, Jun 1989.
- [101] R. V. Shannon, "A Model of Safe Levels for Electrical Stimulation," *IEEE Transactions on Biomedical Engineering*, vol. 39, no. 4, pp. 424–426, 1992.

- [102] D. B. McCreery, W. F. Agnew, T. G. H. Yuen, and L. Bullara, "Charge density and charge per phase as cofactors in neural injury induced by electrical stimulation," *IEEE Transactions on Biomedical Engineering*, vol. 37, no. 10, pp. 996–1001, 1990.
- [103] S. F. Cogan, K. A. Ludwig, C. G. Welle, and P. Takmakov, "Tissue damage thresholds during therapeutic electrical stimulation," *Journal of Neural Engineering*, vol. 13, p. 021001, Apr 2016.
- [104] S. F. Cogan, T. D. Plante, and J. Ehrlich, "Sputtered iridium oxide films (SIROFs) for low-impedance neural stimulation and recording electrodes," *Conf Proc IEEE Eng Med Biol Soc.*, vol. 6, pp. 4153–6, 2004.
- [105] R. P. von Metzen and T. Stieglitz, "The effects of annealing on mechanical, chemical, and physical properties and structural stability of parylene C," *Biomedical Microdevices*, vol. 15, pp. 727–35, Oct 2013.
- [106] National Institute of Standards and Technology, "NIST X-ray Photoelectron Spectroscopy Database, Version 4.1," 2012.
- [107] E. Slavcheva, R. Vitushinsky, W. Mokwa, and U. Schnakenberg, "Sputtered Iridium Oxide Films as Charge Injection Material for Functional Electrostimulation," *Journal of The Electrochemical Society*, vol. 151, p. E226, Jul 2004.
- [108] P. Gilgunn, R. Khilwani, T. D. Y. Kozai, D. J. Weber, X. T. Cui, G. Erdos, O. B. Ozdoganlar, and G. K. Fedder, "An ultra-compliant, scalable neural probe with molded biodissolvable delivery vehicle," in *2012 IEEE 25th International Conference on Micro Electro Mechanical Systems (MEMS)*, (Paris, France), pp. 56–59, IEEE, Jan 2012.
- [109] R. Huang and Y. Tai, "Parylene to silicon adhesion enhancement," in *TRANSDUCERS 2009 - 14th International Solid-State Sensors, Actuators and Microsystems Conference*, pp. 1027–1030, IEEE, Jun 2009.

- [110] J. P. Seymour, N. B. Langhals, D. J. Anderson, and D. R. Kipke, “Novel multi-sided, microelectrode arrays for implantable neural applications.,” *Biomedical microdevices*, vol. 13, pp. 441–51, Jun 2011.
- [111] B. J. Kim, C. B. M. Gupta, and E. Meng, “Formation of three-dimensional parylene C structures via thermoforming,” *Journal of Micromechanics and Microengineering*, vol. 24, p. 9, 2014.
- [112] A. Carlson, A. M. Bowen, Y. Huang, R. G. Nuzzo, and J. A. Rogers, “Transfer printing techniques for materials assembly and micro/nanodevice fabrication.,” *Advanced materials (Deerfield Beach, Fla.)*, vol. 24, pp. 5284–318, Oct 2012.
- [113] C. H. Lee, D. R. Kim, and X. Zheng, “Fabricating nanowire devices on diverse substrates by simple transfer-printing methods.,” *Proceedings of the National Academy of Sciences of the United States of America*, vol. 107, pp. 9950–5, Jun 2010.
- [114] M. A. Meitl, Z.-T. Zhu, V. Kumar, K. J. Lee, X. Feng, Y. Y. Huang, I. Adesida, R. G. Nuzzo, and J. A. Rogers, “Transfer printing by kinetic control of adhesion to an elastomeric stamp,” *Nature Materials*, vol. 5, pp. 33–38, Dec 2005.
- [115] P. G. Jung, I. D. Jung, S. M. Lee, and J. S. Ko, “A micropatterned metal embedding process for the formation of metal lines in flexible electronics,” *Journal of Micromechanics and Microengineering*, vol. 18, p. 035017, Mar 2008.
- [116] X. C. Ong, R. Khilwani, M. Forssell, O. B. Ozdoganlar, and G. K. Fedder, “A transfer process to fabricate ultra-compliant neural probes in dissolvable needles,” *Journal of Micromechanics and Microengineering (In Review)*.
- [117] X. C. Ong, A. Willard, M. Forssell, A. Gittis, and G. K. Fedder, “A silicon neural probe fabricated using DRIE on bonded thin silicon,” in *2016 38th Annual International Conference of the IEEE Engineering in Medicine and Biology Society (EMBC)*, pp. 4885–4888, IEEE, Aug 2016.

- [118] J. Jeong, N. Chou, and S. Kim, "Fabrication of flexible electrode array based on PDMS for long-term in-vivo use," in *2013 6th International IEEE/EMBS Conference on Neural Engineering (NER)*, pp. 911–914, IEEE, Nov 2013.
- [119] X. C. Ong, M. Forssell, and G. K. Fedder, "Processing of platinum electrodes for parylene-C based neural probes," in *The 29th IEEE International Conference on Micro Electro Mechanical Systems (MEMS 2016)*, (Shanghai, China), pp. 509–512, 2016.
- [120] D.-H. Kim, J. Viventi, J. J. Amsden, J. Xiao, L. Vigeland, Y.-S. Kim, J. A. Blanco, B. Panilaitis, E. S. Frechette, D. Contreras, D. L. Kaplan, F. G. Omenetto, Y. Huang, K.-C. Hwang, M. R. Zakin, B. Litt, and J. A. Rogers, "Dissolvable films of silk fibroin for ultrathin conformal bio-integrated electronics.," *Nature materials*, vol. 9, pp. 511–7, Jun 2010.
- [121] B. Bediz, E. Korkmaz, R. Khilwani, C. Donahue, G. Erdos, L. D. Faló, and O. B. Ozdoganlar, "Dissolvable microneedle arrays for intradermal delivery of biologics: fabrication and application.," *Pharmaceutical research*, vol. 31, pp. 117–35, Jan 2014.
- [122] J.-C. Tsai and Y.-S. Hsu, "Profile of microlens fabricated by the thermal reflow process," *IEEE Transactions on Magnetics*, vol. 47, pp. 598–601, Mar 2011.
- [123] A. Oláh and G. J. Vancso, "Characterization of adhesion at solid surfaces: development of an adhesion-testing device," *European Polymer Journal*, vol. 41, pp. 2803–2823, Dec 2005.
- [124] SPI Supplies Division, "Crystalbond<sup>TM</sup> 509," [http://www.2spi.com/catalog/documents/GHS-SDS-05110-Crystalbond\\_509.pdf](http://www.2spi.com/catalog/documents/GHS-SDS-05110-Crystalbond_509.pdf), Accessed: 2015-12-31, 2013.
- [125] T. Fujii, "PDMS-based microfluidic devices for biomedical applications," *Microelectronic Engineering*, vol. 61-62, pp. 907–914, Jul 2002.

- [126] W. Zhang, G. Ferguson, and S. Tatic-Lucic, "Elastomer-supported cold welding for room temperature wafer-level bonding," in *2004 IEEE 17th International Conference on Micro Electro Mechanical Systems (MEMS)*, (Maastricht, The Netherlands), pp. 741–744, IEEE, 2004.
- [127] L. Xiong, P. Chen, and Q. Zhou, "Adhesion promotion between PDMS and glass by oxygen plasma pre-treatment," *Journal of Adhesion Science and Technology*, vol. 28, pp. 1046–1054, Mar 2014.
- [128] R. W. R. L. Gajasinghe, S. U. Senveli, S. Rawal, A. Williams, A. Zheng, R. H. Datar, R. J. Cote, and O. Tigli, "Experimental study of PDMS bonding to various substrates for monolithic microfluidic applications," *Journal of Micromechanics and Microengineering*, vol. 24, p. 075010, Jul 2014.
- [129] AZ Electronic Materials, "AZP4000 thick film photoresist," [http://www.microchemicals.com/micro/AZ\\_P4000\\_Phototresist.pdf](http://www.microchemicals.com/micro/AZ_P4000_Phototresist.pdf), Accessed: 2016-05-01.
- [130] MicroChemicals, "Softbake of photoresist films," [http://www.microchemicals.com/technical\\_information/softbake\\_photoresist.pdf](http://www.microchemicals.com/technical_information/softbake_photoresist.pdf), Accessed: 2016-05-01.
- [131] Electron Microscopy Sciences, "Crystalbond<sup>TM</sup> wafer-mount embedding media for the materials sciences," <https://www.emsdiasum.com/microscopy/products/materials/adhesives.aspx>, Accessed: 2016-01-09.
- [132] Aremco Products Inc., "Crystalbond 509 MSDS," <http://grover.mirc.gatech.edu/data/msds/542.pdf>, Accessed: 2015-01-01.
- [133] Pelco, "Crystalbond adhesives," [https://www.tedpella.com/technote\\_html/821-1-2-3-4-6-TN.pdf](https://www.tedpella.com/technote_html/821-1-2-3-4-6-TN.pdf), Accessed: 2015-02-09, p. 2.

- [134] Adriamed, “Cephalopods age determination by statoliths reading: A technical manual,” <http://www.faoadriamed.org/pdf/publications/web-td-22.pdf>, Accessed: 2016-02-03.
- [135] H. H. Gatzert, V. Saile, and J. Leuthold, *Micro and nano fabrication: tools and processes*. Berlin - Heidelberg: Springer-Verlag, 2015.
- [136] SpillTech, “Chemical compatibility guide for polyurethane items,” <https://www.spilltech.com/wcsstore/SpillTechUSCatalogAssetStore/Attachment/documents/ccg/POLYURETHANE.pdf>, Accessed: 2016-05-01.
- [137] AI Technology Inc, “Spin-coating temporary bonding IPA-soluble wax solutions,” <https://www.aitechnology.com/products/tapes/wax-coating-and-film/>, Accessed: 2016-05-02.
- [138] D. Malleo, J. T. Nevill, A. van Ooyen, U. Schnakenberg, L. P. Lee, and H. Morgan, “Note: Characterization of electrode materials for dielectric spectroscopy,” *Review of Scientific Instruments*, vol. 81, p. 016104, Jan 2010.
- [139] S. Butun, F. G. Ince, H. Erdugan, and N. Sahiner, “One-step fabrication of biocompatible carboxymethyl cellulose polymeric particles for drug delivery systems,” *Carbohydrate Polymers*, vol. 86, pp. 636–643, Aug 2011.
- [140] H. Feng, “Preparation, characterization, and applications of polysaccharide-stabilized metal nanoparticles for remediation of chlorinated solvents in soils and groundwater,” *Ph.D. Thesis*, Auburn University, 2007.
- [141] L. T. Cuba-Chiem, L. Huynh, J. Ralston, and D. A. Beattie, “In situ particle film ATR-FTIR studies of CMC adsorption on talc: the effect of ionic strength and multivalent metal ions,” *Minerals Engineering*, vol. 21, pp. 1013–1019, Nov 2008.
- [142] D. Pasqui, M. De Cagna, and R. Barbucci, “Polysaccharide-based hydrogels: the key role of water in affecting mechanical properties,” *Polymers*, vol. 4, pp. 1517–1534, Aug 2012.

- [143] K. Pal, A. K. Banthia, and D. K. Majumdar, “Development of carboxymethyl cellulose acrylate for various biomedical applications.,” *Biomedical materials (Bristol, England)*, vol. 1, pp. 85–91, Jun 2006.
- [144] H. Fang, J. Zhao, K. J. Yu, E. Song, A. B. Farimani, C.-H. Chiang, X. Jin, Y. Xue, D. Xu, W. Du, K. J. Seo, Y. Zhong, Z. Yang, S. M. Won, G. Fang, S. W. Choi, S. Chaudhuri, Y. Huang, M. A. Alam, J. Viventi, N. R. Aluru, J. A. Rogers, and J. M. Desimone, “Ultrathin, transferred layers of thermally grown silicon dioxide as biofluid barriers for biointegrated flexible electronic systems,” *Proceedings of the National Academy of Sciences*, vol. 113, no. 42, pp. 11682–11687, 2016.
- [145] A. R. Johnson and J. Kanicki, “Low Temperature Encapsulation for OLEDs and PLEDs,” [http://vhosts.eecs.umich.edu/omelab/downloads/AJ\\_Vehicle\\_and\\_Photons\\_Symp\\_Digest\\_2006.pdf](http://vhosts.eecs.umich.edu/omelab/downloads/AJ_Vehicle_and_Photons_Symp_Digest_2006.pdf), Accessed: 2017-06-11.
- [146] X. Xie, L. Rieth, L. Williams, S. Negi, R. Bhandari, R. Caldwell, R. Sharma, P. Tathireddy, and F. Solzbacher, “Long-term reliability of Al<sub>2</sub>O<sub>3</sub> and Parylene C bilayer encapsulated Utah electrode array based neural interfaces for chronic implantation,” *Journal of Neural Engineering*, vol. 11, p. 026016, Apr 2014.
- [147] B. H. Lee, B. Yoon, A. I. Abdulagatov, R. A. Hall, and S. M. George, “Growth and Properties of Hybrid Organic-Inorganic Metalcone Films Using Molecular Layer Deposition Techniques,” *Advanced Functional Materials*, vol. 23, pp. 532–546, Feb 2013.
- [148] M. Vähä-Nissi, P. Sundberg, E. Kauppi, T. Hirvikorpi, J. Sievänen, A. Sood, M. Karppinen, and A. Harlin, “Barrier properties of Al<sub>2</sub>O<sub>3</sub> and alucone coatings and nanolaminates on flexible biopolymer films,” *Thin Solid Films*, vol. 520, no. 22, pp. 6780–6785, 2012.
- [149] A. V. Vasenkov, “Atomistic modeling of parylene-metal interactions for surface micro-structuring,” *Journal of Molecular Modeling*, vol. 17, pp. 3219–3228, Dec 2011.

- [150] H.-s. Noh, K.-s. Moon, A. Cannon, P. J. Hesketh, and C. P. Wong, "Wafer bonding using microwave heating of parylene intermediate layers," *Journal of Micromechanics and Microengineering*, vol. 14, p. 625, Apr 2004.
- [151] L. H. Kim, K. Kim, S. Park, Y. J. Jeong, H. Kim, D. S. Chung, S. H. Kim, and C. E. Park, "Al<sub>2</sub>O<sub>3</sub>/TiO<sub>2</sub> nanolaminate thin film encapsulation for organic thin film transistors via plasma-enhanced atomic layer deposition," *ACS Applied Materials and Interfaces*, vol. 6, pp. 6731–6738, May 2014.
- [152] J. H.-C. Chang, B. Lu, and Y.-C. Tai, "Adhesion-enhancing surface treatments for parylene deposition," in *2011 16th International Solid-State Sensors, Actuators and Microsystems Conference*, pp. 390–393, IEEE, Jun 2011.
- [153] H. Kim and K. Najafi, "Wafer bonding using parylene and wafer-level transfer of free-standing parylene membranes," in *Transducers 2003. 12th International Conference on Solid-State Sensors, Actuators and Microsystems. Digest of Technical Papers (Cat. No.03TH8664)*, vol. 1, pp. 790–793, IEEE.
- [154] D. Ziegler, T. Suzuki, and S. Takeuchi, "Fabrication of flexible neural probes with built-in microfluidic channels by thermal bonding of parylene," *Journal of Microelectromechanical Systems*, vol. 15, pp. 1477–1482, Dec 2006.
- [155] R. Huang and Y. Tai, "Parylene to silicon adhesion enhancement," in *TRANSDUCERS 2009 - 2009 International Solid-State Sensors, Actuators and Microsystems Conference*, pp. 1027–1030, IEEE, Jun 2009.
- [156] A. Amirudin and D. Thieny, "Application of electrochemical impedance spectroscopy to study the degradation of polymer-coated metals," *Progress in Organic Coatings*, vol. 26, no. 1, pp. 1–28, 1995.
- [157] X.-P. Bi, N. L. Ward, B. P. Crum, and W. Li, "Plasma-treated switchable wettability of parylene-C surface," in *2012 7th IEEE International Conference on Nano/Micro Engineered and Molecular Systems (NEMS)*, pp. 222–225, IEEE, Mar 2012.

- [158] M. Golda, M. Brzychczy-Wloch, M. Faryna, K. Engvall, and A. Kotarba, “Oxygen plasma functionalization of parylene C coating for implants surface: Nanotopography and active sites for drug anchoring,” *Materials Science and Engineering: C*, vol. 33, pp. 4221–4227, Oct 2013.
- [159] X. Bi, B. P. Crum, and W. Li, “Super hydrophobic parylene-C produced by consecutive O<sub>2</sub> and SF<sub>6</sub> plasma treatment,” *Journal of Microelectromechanical Systems*, vol. 23, pp. 628–635, Jun 2014.
- [160] V. S. Smentkowski, ed., *Surface Analysis and Techniques in Biology*. Cham: Springer International Publishing, 2014.
- [161] R. K. Hanson, “Lecture 6: Spectral Lineshapes,” <https://cefrc.princeton.edu/sites/cefrc/files/Files/2015%20Lecture%20Notes/Hanson/pLecture6.pdf>, Accessed: 2017-06-18.
- [162] S. Roger, M. Stewart, B. Mike, and B. Igor, “X-ray Photoelectron Spectroscopy,” [http://mmrc.caltech.edu/SS\\_XPS/XPS\\_PPT/XPS\\_Slides.pdf](http://mmrc.caltech.edu/SS_XPS/XPS_PPT/XPS_Slides.pdf), Accessed: 2017-06-18.
- [163] T. Weckman and K. Laasonen, “First principles study of the atomic layer deposition of alumina by TMA-H<sub>2</sub>O-process,” *Physical Chemistry Chemistry Physics*, vol. 17, no. 26, pp. 17322–17334, 2015.
- [164] S. M. George, “Atomic Layer Deposition: An Overview,” *Chemical Reviews*, vol. 110, pp. 111–131, Jan 2010.
- [165] R. Caldwell, H. Mandal, R. Sharma, F. Solzbacher, P. Tathireddy, and L. Rieth, “Analysis of Al<sub>2</sub>O<sub>3</sub>-parylene C bilayer coatings and impact of microelectrode topography on long term stability of implantable neural arrays,” *Journal of Neural Engineering*, vol. 14, p. 046011, Aug 2017.
- [166] B. Visweswaran, “Encapsulation of Organic Light Emitting Diodes,” *Ph.D. Thesis*, Princeton University, Dept. of Electrical Engineering, 2014.

- [167] Z. Wu, L. Wang, C. Chang, and Y. Qiu, "A hybrid encapsulation of organic light-emitting devices," *Journal of Physics D: Applied Physics*, vol. 38, pp. 981–984, Apr 2005.
- [168] D. S. Wu, W. C. Lo, C. C. Chiang, H. B. Lin, L. S. Chang, R. H. Horng, C. L. Huang, and Y. J. Gao, "Water and oxygen permeation of silicon nitride films prepared by plasma-enhanced chemical vapor deposition," *Surface and Coatings Technology*, vol. 198, no. 1-3, pp. 114–117, 2004.
- [169] E. Cianci, S. Lattanzio, G. Seguni, S. Vassanelli, and M. Fanciulli, "Atomic layer deposited TiO<sub>2</sub> for implantable brain-chip interfacing devices," *Thin Solid Films*, vol. 520, pp. 4745–4748, 2012.
- [170] D. S. Finch, T. Oreskovic, K. Ramadurai, C. F. Herrmann, S. M. George, and R. L. Mahajan, "Biocompatibility of atomic-deposited alumina thin films," *Journal of Biomedical Materials Research Part A*, vol. 87, no. 1, pp. 100–6, 2008.
- [171] A. I. Abdulagatov, Y. Yan, J. R. Cooper, Y. Zhang, Z. M. Gibbs, A. S. Cavanagh, R. G. Yang, Y. C. Lee, and S. M. George, "Al<sub>2</sub>O<sub>3</sub> and TiO<sub>2</sub> atomic layer deposition on copper for water corrosion resistance," *ACS Applied Materials and Interfaces*, vol. 3, pp. 4593–4601, Dec 2011.
- [172] J. R. Decker, K. Kolari, and R. Puurunen, "Inductively coupled plasma etching of amorphous Al<sub>2</sub>O<sub>3</sub> and TiO<sub>2</sub> mask layers grown by atomic layer deposition," *Journal of Vacuum Science and Technology B: Microelectronics and Nanometer Structures*, vol. 24, no. 5, pp. 2350–2355, 2006.
- [173] W. M. Moreau, "Subtractive etching," in *Semiconductor Lithography*, pp. 631–777, Boston, MA: Springer US, 1988.
- [174] J. J. Yang, N. P. Kobayashi, D. A. A. Ohlberg, Z. Li, and R. S. Williams, "Engineering oxygen vacancies in atomic layer deposited TiO<sub>2</sub> films for Memristive switches."

- [175] I. Iatsunskiy, E. Coy, R. Viter, G. Nowaczyk, M. Jancelewicz, I. Baleviciute, K. Załęski, and S. Jurga, “Study on structural, mechanical, and optical properties of Al<sub>2</sub>O<sub>3</sub>-TiO<sub>2</sub> nanolaminates prepared by atomic layer deposition,” *The Journal of Physical Chemistry C*, vol. 119, pp. 20591–20599, Sep 2015.
- [176] M. Berdova, T. Ylitalo, I. Kassamakov, J. Heino, P. T. Törmä, L. Kilpi, H. Ronkainen, J. Koskinen, E. Hægström, and S. Franssila, “Mechanical assessment of suspended ALD thin films by bulge and shaft-loading techniques,” *Acta Materialia*, vol. 66, pp. 370–377, Mar 2014.
- [177] ESPI Metals, “Platinum,” <http://www.espimetals.com/index.php/technical-data/186-platinum>, Accessed: 2017-06-22.
- [178] VP-Scientific, “Parylene Properties & Characteristics,” [http://www.vp-scientific.com/parylene\\_properties.htm](http://www.vp-scientific.com/parylene_properties.htm), Accessed: 2017-06-22.
- [179] AZO Materials, “Properties: Alumina - Aluminium Oxide - Al<sub>2</sub>O<sub>3</sub> - A Refractory Ceramic Oxide,” <http://www.azom.com/properties.aspx?ArticleID=52>, Accessed : 2017-06-22.
- [180] AZO Materials, “Properties: Titanium Dioxide - Titania (TiO<sub>2</sub>),” <http://www.azom.com/properties.aspx?ArticleID=1179>, Accessed: 2017-06-22.
- [181] S. S. Rangaraj and S. B. Bhaduri, “A modified rule-of-mixtures for prediction of tensile strengths of unidirectional fibre-reinforced composite materials,” *Journal of Materials Science*, vol. 29, no. 10, pp. 2795–2800, 1994.
- [182] J. Du, M. L. Roukes, and S. C. Masmanidis, “Dual-side and three-dimensional microelectrode arrays fabricated from ultra-thin silicon substrates,” *Journal of Micromechanics and Microengineering*, vol. 19, pp. 75008–7, 2009.
- [183] J. T. W. Kuo, B. J. Kim, S. A. Hara, C. D. Lee, C. A. Gutierrez, T. Q. Hoang, and E. Meng, “Novel flexible parylene neural probe with 3D sheath structure for enhancing tissue integration,” *Lab on a Chip*, vol. 13, pp. 554–61, Feb 2013.

- [184] A. L. S. Loke and A. L. Sun, "Process integration issues of low-permittivity dielectrics with copper for high-performance interconnects," *Ph.D. Thesis*, Stanford University, Dept. of Electrical Engineering, 1999.
- [185] J. Norman, B. Muratore, P. Dyer, D. Roberts, and A. Hochberg, "New OM-CVD precursors for selective copper metallization," in *1991 Proceedings Eighth International IEEE VLSI Multilevel Interconnection Conference*, pp. 123–129, IEEE, 1991.
- [186] J. S. Cho, H.-K. Kang, S. S. Wong, and Y. Shacham-Diamand, "Electroless Cu for VLSI," *MRS Bulletin*, vol. 18, pp. 31–38, Jun 1993.
- [187] C. Q. Cui and K. Pun, "Cu fully filled ultra-fine blind via on flexible substrate for high density interconnect," in *2006 Thirty-First IEEE/CPMT International Electronics Manufacturing Technology Symposium*, pp. 13–19, IEEE, Nov 2006.
- [188] P. Ledochowitsch, R. J. Felus, R. R. Gibboni, A. Miyakawa, S. Bao, and M. M. Maharbiz, "Fabrication and testing of a large area, high density, parylene MEMS," in *2011 IEEE 24th International Conference on Micro Electro Mechanical Systems*, pp. 1031–1034, IEEE, Jan 2011.
- [189] M. O. Heuschkel, M. Fejtl, M. Raggenbass, D. Bertrand, and P. Renaud, "A three-dimensional multi-electrode array for multi-site stimulation and recording in acute brain slices," *Journal of Neuroscience Methods*, vol. 114, no. 2, pp. 135–148, 2002.
- [190] A. Hai, J. Shappir, and M. E. Spira, "Long-Term, multisite, parallel, in-cell recording and stimulation by an array of extracellular microelectrodes," *Journal of Neurophysiology*, vol. 104, no. 1, 2010.
- [191] D. Egert, R. L. Peterson, and K. Najafi, "Parylene microprobes with engineered stiffness and shape for improved insertion," in *Transducers 2011 - 16th International Solid-State Sensors, Actuators and Microsystems Conference*, pp. 198–201, IEEE, Jun 2011.

- [192] J. W. Clancey, A. S. Cavanagh, R. S. Kukreja, A. Kongkanand, and S. M. George, "Atomic layer deposition of ultrathin platinum films on tungsten atomic layer deposition adhesion layers: Application to high surface area substrates," *Journal of Vacuum Science and Technology A: Vacuum, Surfaces, and Films*, vol. 33, no. 1, p. 01A130, 2015.
- [193] S. L. Aristizabal, G. A. Cirino, A. N. Montagnoli, A. A. Sobrinho, J. B. Rubert, M. Hospital, and R. D. Mansano, "Microlens array fabricated by a low-cost grayscale lithography maskless system," *Optical Engineering*, vol. 52, p. 125101, Dec 2013.
- [194] C. Waits, R. Ghodssi, M. Ervin, and M. Dubey, "MEMS-based gray-scale lithography," in *2001 International Semiconductor Device Research Symposium. Symposium Proceedings (Cat. No.01EX497)*, pp. 182–185, IEEE, 2001.
- [195] J. Gao, "Large stroke electrostatic pump for an electrocaloric micro-cooler," *Ph.D. Thesis*, Carnegie Mellon University, Dept. of Electrical and Computer Engineering, 2015.
- [196] D. Liu, "Fabrication of 3-D nanoscale structures of arbitrary shape by a single-step E-beam grayscale lithographic process," *Ph.D. Thesis*, Auburn University, Dept. of Materials Engineering, 2010.
- [197] C. McKenna, K. Walsh, M. Crain, and J. Lake, "Maskless direct write grayscale lithography for MEMS applications," in *2010 18th Biennial University/Government/Industry Micro/Nano Symposium*, pp. 1–4, IEEE, Jun 2010.
- [198] K. Hanai, T. Nakahara, S. Shimizu, and Y. Matsumoto, "Fabrication of three-dimensional structures by image processing," *Sensors and Materials*, vol. 18, no. 1, pp. 49–61, 2006.
- [199] L. Mosher, C. M. Waits, B. Morgan, and R. Ghodssi, "Double-exposure grayscale photolithography," *Journal of Microelectromechanical Systems*, vol. 18, no. 2, 2009.

- [200] Y. Hirai, Y. Inamoto, K. Sugano, T. Tsuchiya, and O. Tabata, "Moving mask UV lithography for three-dimensional structuring," *Journal of Micromechanics and Microengineering*, vol. 17, pp. 199–206, Feb 2007.
- [201] G. S. May and C. J. Spanos, *Fundamentals of semiconductor manufacturing and process control*. IEEE, 2006.
- [202] I. R. Minev and S. P. Lacour, "Mechanically Compliant Neural Interfaces," pp. 257–273, Springer, Cham, 2016.
- [203] H. S. Sohal, A. Jackson, R. Jackson, G. J. Clowry, K. Vassilevski, A. O'Neill, and S. N. Baker, "The sinusoidal probe: a new approach to improve electrode longevity.," *Frontiers in Neuroengineering*, vol. 7, no. April, p. 10, 2014.
- [204] J. Muthuswamy, A. Gilletti, T. Jain, and M. Okandan, "Microactuated neural probes to compensate for brain micromotion," *2003 Annual International Conference of the IEEE Engineering In Medicine and Biology Society*, vol. 2, pp. 1941–1943, 2003.
- [205] J.-U. Meyer, D. Edell, L. Rutten, and J. Pine, "Chronically implantable neural information transducers," *Proceedings of 18th Annual International Conference of the IEEE Engineering in Medicine and Biology Society*, vol. 5, pp. 2139–2141, 1996.
- [206] W. Zhang, Z. Li, M. Gilles, and D. Wu, "Mechanical simulation of neural electrode -brain tissue interface under various micromotion conditions," *Journal of Medical and Biological Engineering*, vol. 34, no. 4, pp. 386–392, 2014.
- [207] V. Sankar, J. C. Sanchez, E. McCumiskey, N. Brown, C. R. Taylor, G. J. Ehlert, H. A. Sodano, and T. Nishida, "A highly compliant serpentine shaped polyimide interconnect for front-end strain relief in chronic neural implants," *Frontiers in Neurology*, vol. 4 SEP, 2013.

- [208] G. K. Fedder, "Simulation of microelectromechanical systems," *Ph.D. Thesis*, University of California at Berkeley, Dept. of Electrical Engineering and Computer Science, 1994.
- [209] T. D. Kozai, Z. Gugel, X. Li, P. J. Gilgunn, R. Khilwani, O. B. Ozdoganlar, G. K. Fedder, D. J. Weber, and X. T. Cui, "Chronic tissue response to carboxymethyl cellulose based dissolvable insertion needle for ultra-small neural probes," *Biomaterials*, vol. 35, no. 34, pp. 9255–9268, 2014.
- [210] G. H. Borschel, K. F. Kia, W. M. Kuzon, and R. G. Dennis, "Mechanical properties of acellular peripheral nerve," *The Journal of Surgical Research*, vol. 114, pp. 133–9, Oct 2003.
- [211] S. Budday, R. Nay, R. De Rooij, P. Steinmann, T. Wyrobek, T. C. Ovaert, and E. Kuhl, "Mechanical properties of gray and white matter brain tissue by indentation," *Journal of the Mechanical Behavior of Biomedical Materials*, vol. 46, pp. 318–330, Jun 2015.
- [212] W. F. H. Rakuman, X. C. Ong, H. S. Tetikol, R. Khilwani, X. T. Cui, O. B. Ozdoganlar, G. K. Fedder, and P. J. Gilgunn, "Ultra-compliant neural probes are subject to fluid forces during dissolution of polymer delivery vehicles," in *2013 35th Annual International Conference of the IEEE Engineering in Medicine and Biology Society (EMBC)*, vol. 2013, pp. 1550–1553, IEEE, Jul 2013.
- [213] J. Charmet, J. Bitterli, O. Sereda, M. Liley, P. Renaud, and H. Keppner, "Optimizing parylene C adhesion for MEMS processes: potassium hydroxide wet etching," *Journal of Microelectromechanical Systems*, vol. 22, no. 4, pp. 855–864, 2013.
- [214] A. M. Willard and A. H. Gittis, "Mapping neural circuits with CLARITY," *eLife*, vol. 4, p. e11409, Oct 2015.

- [215] A. Willard, R. Bouchard, and A. Gittis, “Differential degradation of motor deficits during gradual dopamine depletion with 6-hydroxydopamine in mice,” *Neuroscience*, vol. 301, pp. 254–267, Aug 2015.
- [216] S. Agamanolis, “Liquid Crystal Displays: Past, Present, and Future,” <http://web.media.mit.edu/~stefan/liquid-crystals/liquid-crystals.html>, Accessed: 2017-10-24, 1995.
- [217] Y. L. Yu, M. Nakano, and T. Ikeda, “Directed bending of a polymer film by light - Miniaturizing a simple photomechanical system could expand its range of applications,” *Nature*, vol. 425, no. 6954, p. 145, 2003.
- [218] Y. Xia, G. Cedillo-Servin, R. D. Kamien, and S. Yang, “Guided folding of nematic liquid crystal elastomer sheets into 3D via patterned 1D microchannels,” *Advanced Materials*, vol. 28, no. 43, pp. 9637–9643, 2016.
- [219] S.-T. Wu, U. Efron, and L. D. Hess, “Birefringence measurements of liquid crystals,” *Applied Optics*, vol. 23, no. 21, p. 3911, 1984.
- [220] R. Pomfret, G. Miranpuri, and K. Sillay, “The substitute brain and the potential of the gel model,” *Annals of Neurosciences*, vol. 20, pp. 118–22, Jul 2013.
- [221] T. Quan, T. Zheng, Z. Yang, W. Ding, S. Li, J. Li, H. Zhou, Q. Luo, H. Gong, and S. Zeng, “NeuroGPS: automated localization of neurons for brain circuits using L1 minimization model,” *Scientific Reports*, vol. 3, p. 1414, 2013.

# Appendix A

## Process Flow for Parylene-C Process

No.	Process	Process Steps	Equipment	Materials	Comments
1	Clean wafer	Load wafers into Spin-Rinse-Dry (SRD) machine and press run.	Semitoool spin rinse dryer	100 mm Si wafer or 100 mm glass wafer	Each parylene-C deposition run allows for 3 wafers. Prepare 3 wafers at one go.
2	A174 Adhesion Promotion	Mix IPA, DI water and A174 in the ratio 100:100:1. For three 4" wafers, use 1000 ml DI water, 1000 ml IPA, 10 ml A174. Measure volume of A174 using a syringe. Cure this solution overnight.	4000 mL beaker		

3	Parylene-C deposition	Turn on chiller. Load parylene-C dimer. Load wafers. Start machine.	SCS Labcoter Parylene Deposition System	Parylene-C Dimer	Deposition rate is controlled by amount of dimer placed into the machine. 4 g = 2.2 $\mu\text{m}$ of parylene-C. 8 g of parylene-C dimer is used for 4.5 $\mu\text{m}$ runs. Set points for parylene-C: 175 degrees C Vaporizer, Pyrolysis heater set point 690 degrees C. If base pressure does not get below 20 mT, please inform nanofab staff.
4	Spin coat AZ5214E	Load wafer using the appropriate 4" wafer chuck. For patterns with large ( $> 4 \mu\text{m}$ features) Spread speed = 600 rpm for 6s. Spin speed = 2000 rpm for 30 s giving 2 $\mu\text{m}$ thick photoresist. For patterns with small features $< 4 \mu\text{m}$ ) Spread speed =	Solitec spinner		

		600 rpm for 6s. Spin speed = 4000 rpm for 30s giving about 1.4 $\mu\text{m}$ thick photoresist.			
5	Soft Bake	Place wafer on hotplate using a manual timer for 1 minute at 100 degrees C.	Hotplate		

6	Expose	Intensity = 5 mW/cm <sup>2</sup> 40s for soda lime glass masks with 1.4 μm photoresist. 60 s for soda lime glass masks with 2 μm photoresist. 80 s for plastic masks, regardless of resist thickness.	Karl-Suss MA6		Contact alignment mode.
7	Reversal Bake	115 degrees C for 2 minutes	Hotplate		This is a critical step. Please ensure that the wafer is centered on the hot plate and time it very carefully.
8	Flood Expose	80 s for all steps.	Karl-Suss MA6		Use flood exposure mode. No glass mask should be placed.

9	Development	Mix AZ developer, (2 AZ developer:1 DI water by volume). Immerse the wafer slanted to prevent the wafer from floating. Agitate and ensure no bubbles stick to the surface of the wafer. Time is 1 minute.	Glassware	AZ Developer DI water	Have a second glass container ready to quench the process prior to rinsing in DI water.
10	Inspect	Ensure complete development	Olympus MX-80 Microscope		If development is incomplete, continue development for 0.2 minutes and inspect again. Repeat until development is complete. Look in narrow regions with steep curvatures.
11	Descum	1 min, 100 W, 1 T O2 plasma	International Plasma Corporation (IPC) Barrel Etcher		Tune reflected power to 0.

12	Deposit Pt	5 mins, 50 W DC, 65 sccm Ar, 20 mT	Perkin-Elmer 2400-6J		20 minutes gives 500 nm. For lift-off processes typically 5 mins is used which gives 125-128 nm. 20 mT of Ar gives low stress Pt. Ensure base pressure is below $5e-7$ T. Using 5 mT, 25 sccm Ar results in high stress film.
13	Lift-off	Immerse in beaker acetone for 2 hours. Change the bath and apply ultrasonic in the new acetone beaker for a further 2 hours.	Ultrasonic Bath		Wafer should be facing down.
14	Descum	1 min, 100 W, 1 T O <sub>2</sub> plasma	International Plasma Corporation (IPC) Barrel Etcher		Tune reflected power to 0.

15	Parylene-C deposition	Turn on chiller. Load parylene-C dimer. Load wafers. Start machine.	SCS Labcoter Parylene Deposition System	Parylene-C Dimer	Deposition rate is controlled by amount of dimer placed into the machine. 4 g = 2.2 $\mu\text{m}$ of parylene-C. 8 g of parylene-C dimer is used for 4.5 $\mu\text{m}$ runs. Set points for parylene-C: 175 degrees C Vaporizer, Pyrolysis heater set point 690 degrees C. If base pressure does not get below 20 mT, please inform nanofab staff.
16	Cr deposition	3 mins, 30 W DC, 65 sccm Ar, 20 mT.	Perkin-Elmer 2400-8L		3 minutes gives 20 nm of Cr. Use 20 mT for low stress Cr. Use 5 minutes (33 nm Cr) for etching 9 $\mu\text{m}$ thick parylene-C. Note: maximum thickness is determined by the opacity of the Cr. The underlying features have to be visible for alignment. Ensure base pressure is below 5e-7 T. Process using 5 mT, 25 sccm Ar has high stress.

17	Spin Coat AZ4210				Note: Cr is susceptible to stress. After spin coating AZ4210, please complete exposure and development, Cr etching and parylene-C etching immediately after. Leaving AZ4210 overnight can cause the Cr and underlying parylene-C to crack.
18	Soft Bake	20 minutes in the 90 degrees C oven.	Oven		
19	Expose	Intensity = 5 mW/cm <sup>2</sup> 120 s using glass mask, 170 s with transparency mask.	Karl-Suss MA6		Contact alignment mode.
20	Development	Use pure AZ developer. Immerse the wafer slanted to prevent the wafer from floating. Agitate and ensure no bubbles stick to the surface of	Glassware	AZ developer	Have a second glass container ready to quench the process prior to rinsing in DI water.

		the wafer. Time is 1 minute.			
21	Inspect	Ensure complete development	Olympus MX-80 Microscope		If development is incomplete, continue development for 0.2 minutes and inspect again. Repeat until development is complete. Look in narrow regions with steep curvatures.
22	Descum	1 min, 100 W, 1 T O <sub>2</sub> plasma	International Plasma Corporation (IPC) Barrel Etcher		Tune reflected power to 0.
23	Etch Cr	Immerse in Transene Chromium Etchant 1020 for about 20 to 30s. The change in color is observable.	Glassware	Transene Chromium Etchant 1020	

		Allow for 5 s additional etch time after end point is observed.			
24	Descum	1 min, 100 W, 1 T O <sub>2</sub> plasma	International Plasma Corporation (IPC) Barrel Etcher		Tune reflected power to 0.
25	Etch parylene-C	14.2 sccm O <sub>2</sub> , 50 W	Trion Phantom II RIE		This is not a timed etch. So a longer time is used than necessary. 40 minutes is used to etch 4.5 μm of parylene-C. 80 minutes is used to etch 9 μm of parylene-C.
26	Strip resist	Immerse in acetone. Spray acetone using a spray bottle.	Glassware		
27	Descum	1 min, 100 W, 1 T O <sub>2</sub> plasma	International Plasma Corporation (IPC) Barrel		Tune reflected power to 0.

			Etcher		
28	Etch Cr	Immerse in Transene Chromium Etchant 1020 for about 1 minute. The change in color is observable. Allow for 5 s additional etch time after end point is observed.	Glassware	Transene Chromium Etchant 1020	
29	Spin protective photoresist	600 rpm spread at 6s, 3000 rpm at 30s AZ4620			
30	Soft bake	1 min, 100 degrees C	Hotplate		
31	Dice		Kulicke and Soffa dicing saw		

# Appendix B

## Process Flow for Parylene-C/Nanolaminate Process

No.	Process	Process Steps	Equipment	Materials	Comments
1	Clean wafer	Load wafers into Spin-Rinse-Dry (SRD) machine and press run.	Semitoool spin rinse dryer	100 mm Si wafer or 100 mm glass wafer	Each parylene-C deposition run allows for 3 wafers. Prepare 3 wafers at one go.
2	A174 Adhesion Promotion	Mix IPA, DI water and A174 in the ratio 100:100:1. For three 4" wafers, use 1000 ml DI water, 1000 ml IPA, 10 ml A174. Measure volume of A174 using a syringe. Cure this solution overnight.	4000 mL beaker		

3	Parylene-C deposition	Turn on chiller. Load parylene-C dimer. Load wafers. Start machine.	SCS Labcoter Parylene Deposition System	Parylene-C Dimer	Deposition rate is controlled by amount of dimer placed into the machine. 4 g = 2.2 $\mu\text{m}$ of parylene-C. 8 g of parylene-C dimer is used for 4.5 $\mu\text{m}$ runs. Set points for parylene-C: 175 degrees C Vaporizer, Pyrolysis heater set point 690 degrees C. If base pressure does not get below 20 mT, please inform nanofab staff.
---	-----------------------	---	---	------------------	--

4	ALD Ceramic Deposition	<p>Precursor used for alumina: trimethyl-aluminum (TMA) and water H<sub>2</sub>O. Precursor used for TiO<sub>2</sub>: tetrakis(dimethylamido) titanium (IV) (TDMA-Ti) and H<sub>2</sub>O.</p> <p>Precursors used for NL: TMA, O<sub>2</sub> plasma, TDMA-Ti, O<sub>2</sub> plasma. Temperature is 150 degrees C. Pressure is held at 200 mT.</p>	Fiji ALD (Cambridge Nanotech)	<p>The platen is large enough to load two 4" wafers. Please load at least one 1" Si test piece to ensure that there is nothing wrong with the deposition. Problems that can happen include: Ar<sup>+</sup> gas runs low, resulting in a gradual drop in pressure. Precursor runs out etc. etc. The color of the film deposited on the Si piece gives a very good indication of whether anything went wrong during the process. Deposition rates: 500 cycles for TMA-H<sub>2</sub>O process gives 48 nm of Al<sub>2</sub>O<sub>3</sub>. 100 cycles for TDMA-Ti and H<sub>2</sub>O gives 42 nm of TiO<sub>2</sub>. 550 cycles of TMA-O<sub>2</sub>-TDMATi-O<sub>2</sub> gives 78 nm of Al<sub>2</sub>O<sub>3</sub>-TiO<sub>2</sub>.</p>
---	------------------------------	--	-------------------------------------	---

5	Spin coat AZ5214E	<p>Load wafer using the appropriate 4" wafer chuck.</p> <p>For patterns with large (&gt; 4 <math>\mu\text{m}</math> features)          Spread speed = 600 rpm for 6s. Spin speed = 2000 rpm for 30 s giving 2 <math>\mu\text{m}</math> thick photoresist.</p> <p>For patterns with small features &lt; 4 <math>\mu\text{m}</math> )          Spread speed = 600 rpm for 6 s. Spin speed = 4000 rpm for 30s giving about 1.4 <math>\mu\text{m}</math> thick photoresist.</p>	Solitec spinner		
6	Soft Bake	Place wafer on hotplate using a manual timer for 1 minute at 100 degrees C.	Hotplate		

7	Expose	Intensity = 5 mW/cm <sup>2</sup> 40s for soda lime glass masks with 1.4 μm photoresist. 60 s for soda lime glass masks with 2 μm photoresist. 80 s for plastic masks, regardless of resist thickness.	Karl-Suss MA6		Contact alignment mode.
8	Reversal Bake	115 degrees C for 2 minutes	Hotplate		This is a critical step. Please ensure that the wafer is centered on the hot plate and time it very carefully.
9	Flood Expose	80 s for all steps.	Karl-Suss MA6		Use flood exposure mode. No glass mask should be placed.
10	Development	Mix AZ developer, (2 AZ developer:1 DI water by volume). Immerse the wafer slanted to prevent the wafer from floating. Agitate and ensure no bubbles stick to the surface of the wafer. Time is 1 minute.	Glassware	AZ Developer DI water	Have a second glass container ready to quench the process prior to rinsing in DI water.

11	Inspect	Ensure complete development	Olympus MX-80 Microscope		If development is incomplete, continue development for 0.2 minutes and inspect again. Repeat until development is complete. Look in narrow regions with steep curvatures.
12	Descum	1 min, 100 W, 1 T O <sub>2</sub> plasma	International Plasma Corporation (IPC) Barrel Etcher		Tune reflected power to 0.
13	Deposit Ti/Pt/Ti	5 mins, 50 W DC, 65 sccm Ar, 20 mT. Use 37 s, 100 W DC for each Ti layer.	Perkin-Elmer 2400-6J		20 minutes gives 500 nm. For lift-off processes typically 5 mins is used which gives 125-128 nm. 20 mT of Ar gives low stress Pt. Ensure base pressure is below 5e-7 T. Using 5 mT, 25 sccm Ar results in high stress film.
14	Lift-off	Immerse in beaker acetone for 2 hours. Change the bath and apply ultrasonic in the new acetone beaker for a further 2 hours.	Ultrasonic Bath		Wafer should be facing down.

15	Descum	1 min, 100 W, 1 T O <sub>2</sub> plasma	International Plasma Corporation (IPC) Barrel Etcher		Tune reflected power to 0.
16	ALD Ceramic Deposition	<p>Precursor used for alumina: trimethyl-aluminum (TMA) and water H<sub>2</sub>O. Precursor used for TiO<sub>2</sub>: tetrakis(dimethylamido) titanium (IV) (TDMA-Ti) and H<sub>2</sub>O.</p> <p>Precursors used for NL: TMA, O<sub>2</sub> plasma, TDMA-Ti, O<sub>2</sub> plasma. Temperature is 150 degrees C. Pressure is held at 200 mT.</p>	Fiji ALD (Cambridge Nanotech)		<p>The platen is large enough to load two 4" wafers. Please load at least one 1" Si test piece to ensure that there is nothing wrong with the deposition. Problems that can happen include: Ar+ gas runs low, resulting in a gradual drop in pressure. Precursor runs out etc. etc. The color of the film deposited on the Si piece gives a very good indication of whether anything went wrong during the process. Deposition rates: 500 cycles for TMA-H<sub>2</sub>O process gives 48 nm of Al<sub>2</sub>O<sub>3</sub>. 1100 cycles for TDMA-Ti and H<sub>2</sub>O gives 42 nm of TiO<sub>2</sub>. 550 cycles of TMA-O<sub>2</sub>-TDMATi-O<sub>2</sub></p>

					gives 78 nm of Al <sub>2</sub> O <sub>3</sub> -TiO <sub>2</sub> . For process with TiO <sub>2</sub> adhesion layer, combine the recipes.
17	Spin Coat AZ4210	Spread = 600rpm for 6s Spin = 4000 rpm for 1 minute	Solitec spinner		
18	Bake	90 degrees C, 20 minutes	Oven		
19	Expose	Intensity = 5 mW/cm <sup>2</sup> . 120 s using glass mask. 170 s with transparency mask.	Karl-Suss MA6		

20	Development	Use pure AZ developer. Immerse the wafer slanted to prevent the wafer from floating. Agitate and ensure no bubbles stick to the surface of the wafer. Time is 1 minute.	Glassware	AZ developer	Have a second glass container ready to quench the process prior to rinsing in DI water.
21	Descum	1 min, 100 W, 1 T O <sub>2</sub> plasma	International Plasma Corporation (IPC) Barrel Etcher		Tune reflected power to 0.
21	Etch	Cl <sub>2</sub> ICP-RIE. 35 sccm Cl <sub>2</sub> , 15 sccm Ar, 3 mT, Bias power = 100 W, ICP power = 600 W. Electrode temperature = 25 degrees C. Lid temperature = 170 degrees C. Spool temperature = 120 degrees C. Liner temperature = 70 degrees C.	Plasma-Therm Versaline ICP RIE		Etch rate is about 40 nm/min for TiO <sub>2</sub> , 50 nm/min for Al <sub>2</sub> O <sub>3</sub> , 30 nm/min for NL.

22	Strip Resist	Immerse in acetone. Spray acetone using a spray bottle.	Glassware		
23	Descum	O <sub>2</sub> -RIE. 14.2 sccm O <sub>2</sub> , 50 W, 5 mins	Trion Phantom II RIE		This descum is necessary to remove the resist which becomes very hard to remove after Cl <sub>2</sub> ICP-RIE. Acetone alone or O <sub>2</sub> barrel etch is found to be insufficient and using piranha results in low yield. Other methods could be attempted such as more toxic materials like post-etch remover. However, O <sub>2</sub> RIE is found to be effective.
20	Parylene-C deposition	Turn on chiller. Load parylene-C dimer. Load wafers. Start machine.	SCS Labcoter Parylene Deposition System	Parylene-C Dimer	Deposition rate is controlled by amount of dimer placed into the machine. 4 g = 2.2 μm of parylene-C. 8 g of parylene-C dimer is used for 4.5 μm runs. Set points for parylene-C: 175 degrees C Vaporizer, Pyrolysis heater set point 690 degrees C. If base

					pressure does not get below 20 mT, please inform nanofab staff.
21	Cr deposition	3 mins, 30 W DC, 65 sccm Ar, 20 mT.	Perkin-Elmer 2400-8L		3 minutes gives 20 nm of Cr. Use 20 mT for low stress Cr. Use 5 minutes (33 nm Cr) for etching 9 $\mu\text{m}$ thick parylene-C. Note: maximum thickness is determined by the opacity of the Cr. The underlying features have to be visible for alignment. Ensure base pressure is below $5\text{e-}7$ T. Process developed using 5 mT, 25 sccm Ar which has high stress.

22	Spin Coat AZ4210				Note: Cr is susceptible to stress. After spin coating AZ4210, please complete exposure and development, Cr etching and parylene-C etching immediately after. Leaving AZ4210 overnight can cause the Cr and underlying parylene-C to crack.
23	Soft Bake	20 minutes in the 90 degrees C oven.	Oven		
24	Expose	Intensity = 5 mW/cm <sup>2</sup> 120 s using glass mask, 170 s with transparency mask.	Karl-Suss MA6		Contact alignment mode.
25	Development	Use pure AZ developer. Immerse the wafer slanted to prevent the wafer from floating. Agitate and ensure no bubbles stick to the surface of the wafer. Time is 1 minute.	Glassware	AZ developer	Have a second glass container ready to quench the process prior to rinsing in DI water.

26	Inspect	Ensure complete development	Olympus MX-80 Microscope		If development is incomplete, continue development for 0.2 minutes and inspect again. Repeat until development is complete. Look in narrow regions with steep curvatures.
27	Descum	1 min, 100 W, 1 T O <sub>2</sub> plasma	International Plasma Corporation (IPC) Barrel Etcher		Tune reflected power to 0.
28	Etch Cr	Immerse in Transene Chromium Etchant 1020 for about 20 to 30s. The change in color is observable. Allow for 5 s additional etch time after end point is observed.	Glassware	Transene Chromium Etchant 1020	
29	Descum	1 min, 100 W, 1 T O <sub>2</sub> plasma	International Plasma Corporation (IPC) Barrel Etcher		Tune reflected power to 0.

30	Etch parylene-C	14.2 sccm O <sub>2</sub> , 50 W	Trion Phantom II RIE		This is not a timed etch. So a longer time is used than necessary. 40 minutes is used to etch 4.5 μm of parylene-C. 80 minutes is used to etch 9 μm of parylene-C.
31	Strip resist	Immerse in acetone. Spray acetone using a spray bottle.	Glassware		
32	Descum	1 min, 100 W, 1 T O <sub>2</sub> plasma	International Plasma Corporation (IPC) Barrel Etcher		Tune reflected power to 0.
33	Etch Cr	Immerse in Transene Chromium Etchant 1020 for about 1 minute. The change in color is observable. Allow for 5 s additional etch time after end point is observed.	Glassware	Transene Chromium Etchant 1020	
34	Spin protective photoresist	600 rpm spread at 6s, 3000 rpm at 30s AZ4620			
35	Soft bake	1 min, 100 degrees C	Hotplate		

36	Dice		Kulicke and Soffa dicing saw		
----	------	--	------------------------------------	--	--

# Appendix C

## Process Flow for Parylene-C on Si Needles Process

No.	Process	Process Steps	Equipment	Materials	Comments
1	Clean wafer	Load wafers into Spin-Rinse-Dry (SRD) machine and press run.	Semitoool spin rinse dryer	100 mm Si wafer or 100 mm glass wafer	Each parylene-C deposition run allows for 3 wafers. Prepare 3 wafers at one go.
2	A174 Adhesion Promotion	Mix IPA, DI water and A174 in the ratio 100:100:1. For three 4" wafers, use 1000 ml DI water, 1000 ml IPA, 10 ml A174. Measure volume of A174 using a syringe. Cure this solution overnight.	4000 mL beaker		

3	Parylene-C deposition	Turn on chiller. Load parylene-C dimer. Load wafers. Start machine.	SCS Labcoter Parylene Deposition System	Parylene-C Dimer	Deposition rate is controlled by amount of dimer placed into the machine. 4 g = 2.2 $\mu\text{m}$ of parylene-C. 8 g of parylene-C dimer is used for 4.5 $\mu\text{m}$ runs. Set points for parylene-C: 175 degrees C Vaporizer, Pyrolysis heater set point 690 degrees C. If base pressure does not get below 20 mT, please inform nanofab staff.
5	Spin coat AZ5214E	Load wafer using the appropriate 4" wafer chuck. For patterns with large ( $> 4 \mu\text{m}$ features) Spread speed = 600 rpm for 6s. Spin speed = 2000 rpm for 30 s giving 2 $\mu\text{m}$ thick photoresist. For patterns with small features $< 4 \mu\text{m}$ ) Spread speed =	Solitec spinner	AZ5214E	

		600 rpm for 6s. Spin speed = 4000 rpm for 30s giving about 1.4 $\mu\text{m}$ thick photoresist.			
6	Soft Bake	Place wafer on hotplate using a manual timer for 1 minute at 100 degrees C.	Hotplate		

7	Expose	Intensity = 5 mW/cm <sup>2</sup> 40s for soda lime glass masks with 1.4 μm photoresist. 60 s for soda lime glass masks with 2 μm photoresist. 80 s for plastic masks, regardless of resist thickness.	Karl-Suss MA6	Glass mask, or transparency mask manually attached to a blank glass mask	Contact alignment mode.
8	Reversal Bake	115 degrees C for 2 minutes	Hotplate		This is a critical step. Please ensure that the wafer is centered on the hot plate and time it very carefully.
9	Flood Expose	80 s for all steps.	Karl-Suss MA6		Use flood exposure mode. No glass mask should be placed.

10	Development	Mix AZ developer, (2 AZ developer:1 DI water by volume). Immerse the wafer slanted to prevent the wafer from floating. Agitate and ensure no bubbles stick to the surface of the wafer. Time is 1 minute.	Glassware	AZ Developer DI water	Have a second glass container ready to quench the process prior to rinsing in DI water.
11	Inspect	Ensure complete development	Olympus MX-80 Microscope		If development is incomplete, continue development for 0.2 minutes and inspect again. Repeat until development is complete. Look in narrow regions with steep curvatures.
12	Descum	1 min, 100 W, 1 T O2 plasma	International Plasma Corporation (IPC) Barrel Etcher		Tune reflected power to 0.

13	Deposit Pt	5 mins, 50 W DC, 65 sccm Ar, 20 mT	Perkin-Elmer 2400-6J		20 minutes gives 500 nm. For lift-off processes typically 5 mins is used which gives 125-128 nm. 20 mT of Ar gives low stress Pt. Ensure base pressure is below $5e-7$ T. Using 5 mT, 25 sccm Ar results in high stress film.
14	Lift-off	Immerse in beaker acetone for 2 hours. Change the bath and apply ultrasonic in the new acetone beaker for a further 2 hours.	Ultrasonic Bath		Wafer should be facing down.
15	Descum	1 min, 100 W, 1 T O <sub>2</sub> plasma	International Plasma Corporation (IPC) Barrel Etcher		Tune reflected power to 0.

17	Parylene-C deposition	Turn on chiller. Load parylene-C dimer. Load wafers. Start machine.	SCS Labcoter Parylene Deposition System	Parylene-C Dimer	Deposition rate is controlled by amount of dimer placed into the machine. 4 g = 2.2 $\mu\text{m}$ of parylene-C. 8 g of parylene-C dimer is used for 4.5 $\mu\text{m}$ runs. Set points for parylene-C: 175 degrees C Vaporizer, Pyrolysis heater set point 690 degrees C. If base pressure does not get below 20 mT, please inform nanofab staff.
18	Cr deposition	3 mins, 30 W DC, 65 sccm Ar, 20 mT.	Perkin-Elmer 2400-8L		3 minutes gives 20 nm of Cr. Use 20 mT for low stress Cr. Use 5 minutes (33 nm Cr) for etching 9 $\mu\text{m}$ thick parylene-C. Note: maximum thickness is determined by the opacity of the Cr. The underlying features have to be visible for alignment. Ensure base pressure is below 5e-7 T. 5 mT, 25 sccm Ar has high stress.

19	Spin Coat AZ4210			AZ4210	Note: Cr is susceptible to stress. After spin coating AZ4210, please complete exposure and development, Cr etching and parylene-C etching immediately after. Leaving AZ4210 overnight can cause the Cr and underlying parylene-C to crack.
20	Soft Bake	20 minutes in the 90 degrees C oven.	Oven		
21	Expose	Intensity = 5 mW/cm <sup>2</sup> 120 s using glass mask, 170 s with transparency mask.	Karl-Suss MA6	Glass mask, or transparency mask manually attached to a blank glass mask	Contact alignment mode.
22	Development	Use pure AZ developer. Immerse the wafer slanted to prevent the wafer from floating. Agitate and ensure no bubbles stick to the surface of	Glassware	AZ developer	Have a second glass container ready to quench the process prior to rinsing in DI water.

		the wafer. Time is 1 minute.			
23	Inspect	Ensure complete development	Olympus MX-80 Microscope		If development is incomplete, continue development for 0.2 minutes and inspect again. Repeat until development is complete. Look in narrow regions with steep curvatures.
24	Descum	1 min, 100 W, 1 T O <sub>2</sub> plasma	International Plasma Corporation (IPC) Barrel Etcher		Tune reflected power to 0.
25	Etch Cr	Immerse in Transene Chromium Etchant 1020 for about 20 to 30s. The change in color is observable.	Glassware	Transene Chromium Etchant 1020	

		Allow for 5 s additional etch time after end point is observed.			
26	Descum	1 min, 100 W, 1 T O <sub>2</sub> plasma	International Plasma Corporation (IPC) Barrel Etcher		Tune reflected power to 0.
27	Etch parylene-C	14.2 sccm O <sub>2</sub> , 50 W	Trion Phantom II RIE		This is not a timed etch. So a longer time is used than necessary. 40 minutes is used to etch 4.5 μm of parylene-C. 80 minutes is used to etch 9 μm of parylene-C.
28	Strip resist	Immerse in acetone. Spray acetone using a spray bottle.	Glassware		
29	Descum	1 min, 100 W, 1 T O <sub>2</sub> plasma	International Plasma Corporation (IPC) Barrel		Tune reflected power to 0.

			Etcher		
30	Etch Cr	Immerse in Transene Chromium Etchant 1020 for about 1 minute. The change in color is observable. Allow for 5 s additional etch time after end point is observed.	Glassware	Transene Chromium Etchant 1020	
31	Spin protective photoresist	600 rpm spread at 6s, 3000 rpm at 30s AZ4620			
32	Soft bake	1 min, 100 degrees C	Hotplate		
33	Dice		Kulicke and Soffa dicing saw		
34	Remove photoresist	Acetone. Immerse in acetone and use a spray bottle	Glassware	Acetone	

35	Anneal	Heat at 300 degrees C, 10 mT N2 for 3 hours	Custom built annealer		Allow temperature to rise gradually to 300 degrees C (This takes about 15 minutes or so). Start timing once 300 degrees C is reached. After 3 hours, turn off the heat. It will take about 2 hours for temperature to ramp down to room temperature. Maintain N2 pressure at 10 mT throughout ramp up and cool down.
36	Clean glass slide	Acetone, IPA	Use the squeeze bottle. Dry using N2 gun.		
37	Spin coat BGL7080	1500 rpm, 30s, about 6 $\mu$ m thickness on the glass slide. No spread step.	Solitec spinner		
38	Bake	To remove IPA solvent, bake at 90 degrees C for at least 5 mins	Oven		
39	Bond	115 degrees C, 40 N force for 1 hour	M9A Device Bonder (Besi, The		Chips are facing upwards for this process.

			Netherlands)		
40	Cr deposition	7.5 mins, 30 W DC, 65 sccm Ar, 20 mT.	Perkin-Elmer 2400-8L		50 nm of Cr is used. as a hard mask. Use 20 mT for low stress Cr. Use 5 minutes (33 nm Cr) for etching 9 μm thick parylene-C. Note: maximum thickness is determined by the opacity of the Cr. The underlying features have to be visible for alignment. Ensure base pressure is below 5e-7 T. 5 mT, 25 sccm Ar has high stress.
41	Spin coat AZ4210	600 rpm for 6 s spread, 3000 rpm spin coat	Solitec spinner		
42	Bake	20 minutes in the 90 degrees C oven.	Oven		
43	Expose	5 mW/cm <sup>2</sup> for 170 s with transparency mask.	Karl-Suss MA6	Transparency mask manually attached to a blank glass mask	Contact alignment mode.

44	Development	Pure AZ developer. Immerse the wafer slanted to prevent the wafer from floating. Agitate and ensure no bubbles stick to the surface of the wafer. Time is 1 minute.	Glassware	AZ developer	Have a second glass container ready to quench the process prior to rinsing in DI water.
43	Descum	1 min, 100 W, 1 T O <sub>2</sub> plasma	International Plasma Corporation (IPC) Barrel Etcher		Tune reflected power to 0.
44	Etch Cr	Immerse in Transene Chromium Etchant 1020 for about 1 minute. The change in color is observable. Allow for 5 s additional etch time after end	Glassware	Transene Chromium Etchant 1020	

		point is observed.			
45	Etch Si using DRIE	About 300 cycles used. Anisotropic etch used. Passivate time: 8s. Etch time: 12s. C4F8 pressure is 85 sccm (passivate). SF6 pressure is 130 sccm (etch). O2 pressure is 13 sccm (etch). RF Coil power is 600W for both passivate and etch. 12 W platen power only for etch.		STS-ASE	Bond the glass slide onto a 4" Si wafer using heat release tape. Etch rate is about 1 $\mu\text{m}$ per cycle. Process name is called "stdaniso"
46	Remove photoresist	Spray with acetone			

47	Descum	1 min, 100 W, 1 T O <sub>2</sub> plasma	International Plasma Corporation (IPC) Barrel Etcher		Tune reflected power to 0.
48	Etch Cr	Immerse in Transene Chromium Etchant 1020 for about 1 minute. The change in color is observable. Allow for 5 s additional etch time after end point is observed.	Glassware	Transene Chromium Etchant 1020	
49	Release	Immerse in IPA for 2 hours to dissolve BGL	Glassware		Immerse until the device comes off easily i.e. a very gentle nudge will get the entire device off. Do not force the device off!
50	Anneal	300 degrees C for 3 hours, 10 mT N <sub>2</sub>	Custom Built Annealer		
51	Ar <sup>+</sup> etch	1 min 50 W	Trion Phantom II RIE		To remove surface oxidation of Pt

